The Molecular Structure of Herbig-Haro Objects, Outflows and Jets from Young Stellar Objects

Christopher John Davis

Doctor of Philosophy

University of Edinburgh

1992

This thesis is my own composition,
except where specifically indicated
in the text.

May 1992

To my parents, for
their love and support.

Abstract

The observations discussed in this thesis are of regions of star-formation where outflow is believed to be occurring. Specifically, radio, millimeter/sub-millimeter and infrared observations are made to illustrate the molecular structure of outflows and related phenomena.

CO J=2-1 observations of the molecular outflow from the infrared reflection nebulae GGD27 IRS complement earlier CO J=1-0 observations and further allow us to revise previous estimates of the outflow mass and energetics. The mass derived here is comparable to mass estimates for other outflows from similarly luminous sources, though it is a factor of $\sim$ 10 less than that derived from the earlier CO 1-0 observations. This difference is due to the choice of excitation temperature used in deriving the outflow mass; here combining CO 2-1 observations with the 1-0 studies allows us to calculate T_{ex} more precisely. I also show that the conical outflow overlaps the plane of the sky, and find that the observed *molecular* flow is not powerful enough to excite the associated HH nebulae HH80/81.

Studies of the molecular environment around the HH objects HH1 and 2, and towards the optical jet/HH bow-shock system HH34 reveal the presence of dense, quiescent molecular material associated with all three HH objects. The presence of such stationary, molecular clumps, particularly evident in HH2 and HH34, does not support current popular HH models.

Observations of these regions in a number of molecular species also show how contrasting and sometimes misleading observations in different molecular gas tracers can be: In HH2 peaks seen in NH_3 (1,1) do not coincide with the well resolved clump observed in HCO^+ J=3-2, whilst the $C^{18}O$ J=2-1 emission shows no clear peak at all. These contrasting morphologies are thought to be due to the differing excitation requirements of the observed lines. However, in HH34 chemical abundance variations are also significant: Towards the exciting source of the optical stellar jet and HH bow-shock, the NH_3 is underabundant. Indeed, in many other outflow sources, a similar NH_3 depletion is observed towards the central source. Instead, the NH_3 delineates a toroidal structure that encircles the central gas-density peak and the outflow source.

I also show how near-IR imaging of the shocked H_2 emission from molecular outflows (particularly those embedded within molecular clouds) may be used to search for infrared counterparts to optical stellar jets. The H_2 structure in L1448 is thought to illustrate the interface between the molecular outflow and an associated stellar wind. These observations thus support the idea that CO

(molecular) outflows result from an entrainment process as an atomic stellar wind shocks ambient cloud gas. Moreover, they represent the first steps towards observing collimated stellar jets in most, if not all, CO outflows.

Future millimeter/sub-millimeter and infrared observations and pertinent questions concerning the outflow process are also discussed.

Acknowledgements

This thesis would not have been possible without the guidance and patience of my supervisors, Bill Dent and Peter Brand. I'd particularly like to thank Bill for his efforts, even after escaping, or so he thought, to the other side of the planet (sorry chapter 3 was so long – have you read it yet !?).

Of the many friends at the Observatory/Department of Astronomy in Edinburgh I'd like to thank John Lightfoot for his time and rigorous efforts, and Alistair Glasse and Jocelyn Bell Burnell for their moral support and (in Alistair's case) the witty banter over the photocopier. Also Stuart Lumsden and later Dave Buckley for their help in bringing me and the R.O.E. Vax closer together, and Richard (Rijdat) Dixon for introducing me to the IRCAM reduction software.

I'd also like to acknowledge the SERC for their generous financial support, and the support staff (the unsung heros) at each of the telescopes I've visited, particularly for their efforts in the small hours. Of my visits abroad, most memorable was the food at the A.A.O. (and the food in Japan, though for different reasons!), the spiders at the A.A.O. (if you ever visit avoid walk 4 of the guide of walks on Siding Spring mountain), the pain in my nose whilst up Mauna Kea, Bill's jeep, rush-hour in Tokyo, midnight in Rome (homeless) and particularly the sight of an often fog/mist/rain-bound Edinburgh on my return.

A big *cheers* to the Soccerladz for the pain, sweat and tears, the staff of *Sneeky Pete's* for the early days, Penny for our porta-chats, Mike for the photos and Bob for services on the 7th (I'm sure we'd still be waiting for that taxi!).

I finally reserve my biggest thank you for my wife Caroline for her love and support (through thick and thin). She has contributed to this thesis in many ways. Little did I realise how fruitful my frequent visits to the Visitor Centre would be (T-minus 3 months...)!

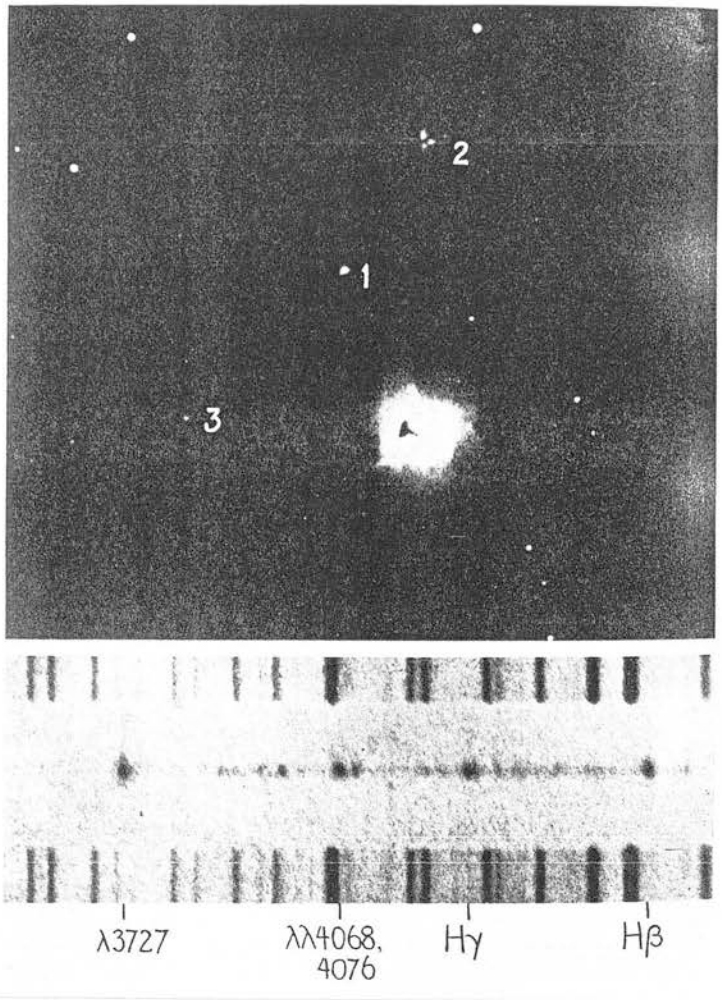

First observed Herbig-Haro objects
(HH1-2; by G. Herbig [1951]).

Contents

Chapter 1

Introduction

1.1 INTRODUCTION

How does a star form by actually *losing* mass? How can a star simultaneously undergo infall and outflow? These perplexing questions (and many subsequent queries) have prompted a great surge in the study of mass outflows from young stellar objects. Indeed, with the advent of ever-more sensitive line and continuum receivers at millimeter and sub-millimeter wavelengths, and with the recent advances in near-infrared imaging and spectroscopy we have over the last 10 or so years come a long way toward understanding this remarkable process. However, these detailed studies yield not only answers, but additional questions, and so there remains much to be done before a coherent and universal model for outflow is reached.

Here I present line-observations and imaging at centimeter, millimeter/sub-millimeter and near-infrared wavelengths, studies which illustrate the processes associated with outflow. I also discuss the techniques used to observe and quantify these phenomena and argue the pros and cons of simple models which may account for many of the observed features.

1.2 MOLECULAR OUTFLOWS

Molecular outflows from young stars are predominantly observed in the rotational lines of CO. The majority of known outflows are bipolar and almost all are associated with embedded infrared sources — known as *Class I* sources or *protostars* (Lada 1991), though a small number of *Class II* stars (e.g. *T-Tauri* stars) also possess similar outflows. These latter, often optically visible sources are thought to represent the later stages of a star's early life. It has thus been suggested on statistical grounds that molecular outflows correspond to an evolutionary status prior to the Class II or T-Tauri period (Lada 1985). Surveys of T-Tauri stars have uncovered molecular outflows towards only $\sim$10% of the observed sources, whilst surveys of more embedded infrared sources find molecular outflows towards nearly 80% of the candidate objects. Furthermore, it seems likely that the outflow period of a star's early evolution lasts for only a fraction of the time associated with the T-Tauri phase (Fukui 1989). Typically an outflow size of $\sim$ 1pc and velocity of 10 km s^{-1} corresponds to a dynamical time scale for the flow of

$\sim 10^5$ years; a value roughly 1/10th the apparent life-span of a T-Tauri star (Cohen & Kuhi 1979).

Bolometric luminosities of known outflow sources range from $\sim$ 1 to 10^5 $L_\odot$; collimated mass loss therefore appears to be a universal stage in the formation and early evolution of all stars.

Fukui (1989) has catalogued 144 molecular outflows, and has studied in detail 48 IRAS point sources in the dark cloud L1641. From the observed 25 μm excess Fukui infers that outflow sources possess more massive circumstellar dust envelopes than T-Tauri stars in the same region, once again supporting the above association of outflows with very early stages of star formation. He further shows that outflow sources appear far more luminous, by a factor of $\sim$10, than the observed T-Tauri stars. He attributes the excess luminosity to gravitational energy release during the accretion of material onto the protostellar core. In addition, since the accretion time-scale ($t_{accr} = \dot{M}/M_{core}$) is typically 10^5 years for his sample of low mass stars in L1641, outflow must be taking place over almost the entire accretion phase.

The source and mechanism for powering such outflows represents a considerable challenge to theorists. The derived momenta and kinetic energies of molecular outflows are indeed huge (see table 1.1). Bally & Lada (1983) find that, over the dynamical time scales of observed flows each central source has radiated sufficient luminous energy to drive the flow. Typically, the ratio of mechanical luminosity (the *energy supply rate*, $MV^3/2R = \dot{M}V^2/2$) to radiant luminosity is $\sim$0.002–0.02 (figure 1.1). However, on considering the *momentum supply rate*, $\dot{M}V$ of the flow and comparing this with the force exerted on the gas by *radiation pressure*, L_*/c, in all cases $\dot{M}V \gg L_*/c$ (figure 1.2). It seems that for the outflows to be driven by stellar radiation each photon would need to be scattered 100-1000 times before escaping from the outflow environment. This would only be possible very close to the embedded source, where dust opacities could be as high as 100.

Table 1.1: Molecular outflow statistics taken from recent CO observations.
References: 1. Yamashita *et al.* 1989, 2. Wolf *et al.* 1990, 3. Cabrit *et al.* 1988, 4. Fukui 1989, 5. Moriarty-Schieven & Snell 1989, 6. Mitchell & Hasegawa 1991, 7. Shultz *et al.* 1989., 8. chapter 2 of this thesis, 9. Knee 1992.
[a]Full extent of outflow (blue and red lobe).
[b]Assuming a distance of 3kpc.

Source	[a]Length (pc)	Veloc. (km s^{-1})	Mass ($M_\odot$)	MV ($M_\odot$ km s^{-1})	Kinetic Energy ($\times 10^{39}$ J)	Mechan. Lumin. ($L_\odot$)
[1]GGD27-IRS	1.5	13	460	5300	8	6
[8]GGD27-IRS	–	–	>60	>185	2.7	1.7
[2]Mon R2	3.8	24	202	2400	29	16
[6]NGC7538	~ 1	~ 8	50	400	4	40
[3]RNO43	~ 1.4	~ 5	13	134	1.3	0.8
[7]V645-Cyg[b]	$\sim$1	16	10	$\sim$160	2.7	3
[4]Ori-KL	0.04	<60	5	<300	0.2	0.04
[9]HH52-53	~ 0.2 –	2.4	7.5	0.03	0.033	
[9]HH54	–	–	0.68	1.6	0.004	0.01
[5]B335	~ 0.9	~ 5	0.13	1.3	0.02	–
[5]L723	~ 0.6	~ 12	0.18	1.0	0.007	–

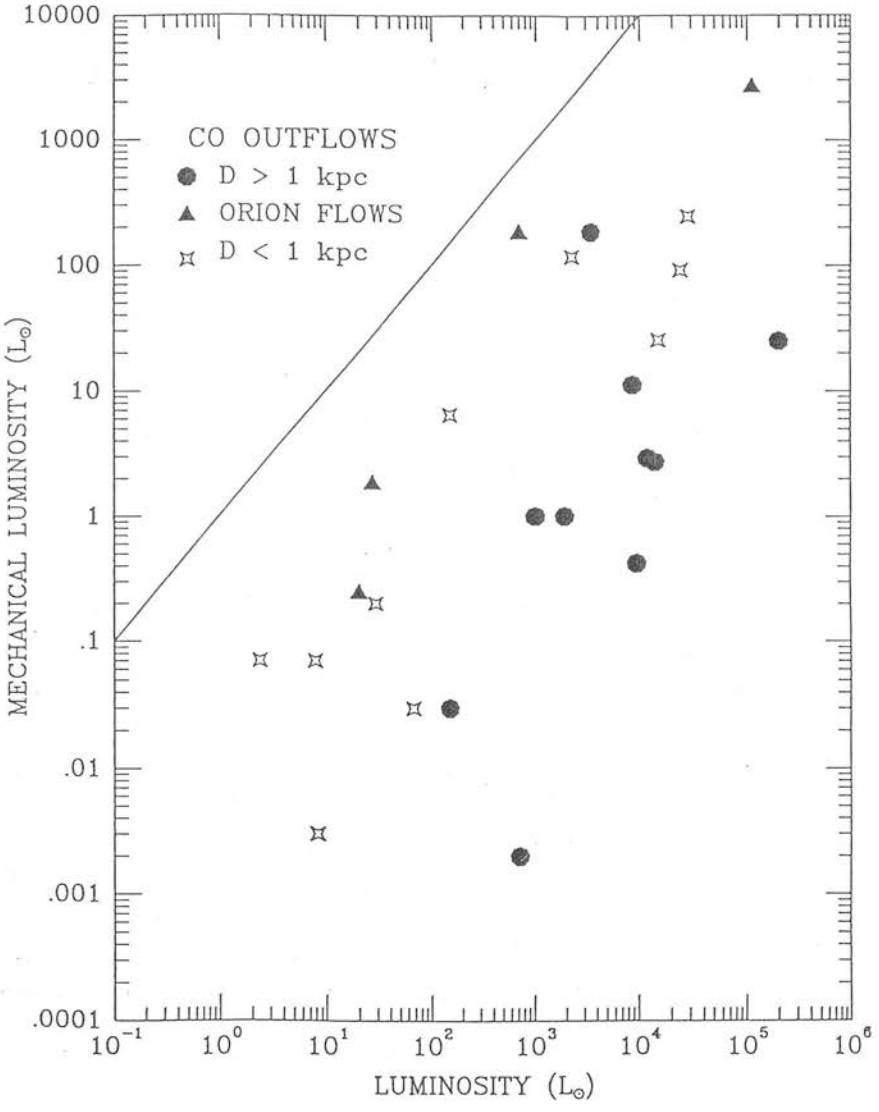

Figure 1.1: A plot of *mechanical luminosity*, $\dot{M}V^2/2$, against *source luminosity*, L_* for a number of outflows (from Bally & Lane 1991). On the diagonal line the mechanical luminosity equals the radiative luminosity.

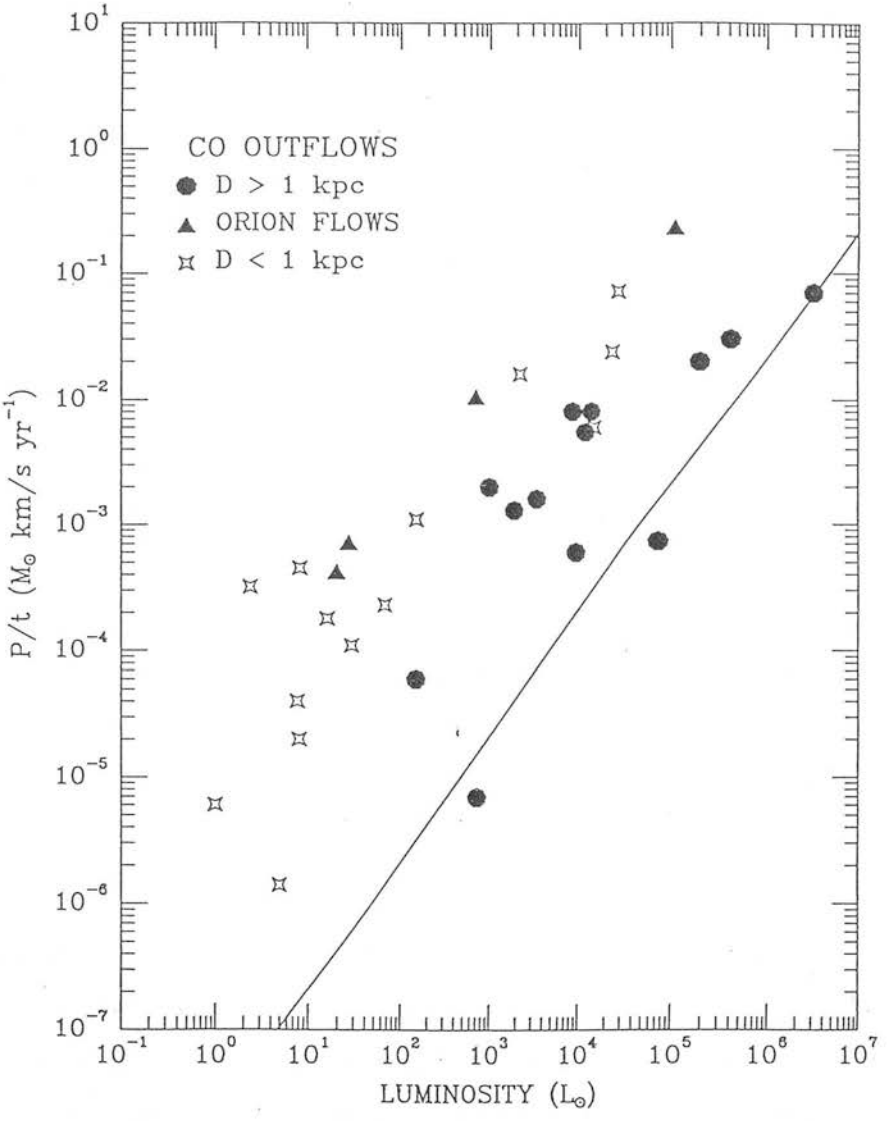

Figure 1.2: A plot of *momentum supply rate, $\dot{M}V$,* against *source luminosity, L_** for the same sample of outflows as in figure 2.1 (from Bally & Lane 1991). The diagonal line shows the *radiation pressure, L_** exerted by the radiation field from the source.

Conversely, the observed flow of molecular material may be driven by an internal "stellar wind" or "jet", the CO outflow thus being ambient molecular material that has been swept up into a hollow shell. Infra-red spectroscopy towards heavily obscured, luminous young stellar objects reveals compact regions of hydrogen recombination line emission, emission that is too luminous to be due to compact HII regions around zero-age main sequence stars (ZAMS) of the same luminosity (Thompson 1981). Also, line widths are greater ($\sim$ 100 km s^{-1}) than expected for thermal motions ($\sim$ 30 km s^{-1}), and high-resolution radio continuum studies show peaks towards outflow sources that are extended along the flow axis (Rodriguez *et al.* 1990b, Rodriguez & Reipurth 1990). The evidence thus points strongly towards the existence of an ionised wind component in molecular outflows.

We may estimate the force of an ionised wind, $(\dot{M}V)_{wind}$, from radio continuum observations (which give $\dot{M}$, Panagia 1988) and from IR-line observations (giving V) and compare these with the momentum supply rates of the associated CO outflows. In virtually all cases, $(\dot{M}V)_{wind} \ll (\dot{M}V)_{CO}$. Evidently the observed ionised winds cannot directly drive swept-up molecular gas in a molecular outflow. This has led theorists to postulate that winds may be time variable, or only partially ionised so that a predominantly neutral component carries most of the wind momentum and energy: Evidence for a neutral wind associated with the molecular outflow in HH7-11 has recently been presented by Lizano *et al.* (1988).

There is also observational evidence that molecular outflows are hollow: In L1551 the lowest velocity molecular gas, observed in CO, lies along the periphery of the flow, whilst the highest velocity gas is found towards the outflow axis (Snell & Schloerb 1985). Model fits to the data predict that the CO lies in a (molecular) shell that is both expanding and moving radially away from the source. Such a shell-like CO structure has however only been observed towards a small number of outflows, though this may be due to a lack of angular resolution.

The characteristics of a number of outflows are listed in table 1.1: Clearly, what is commonly termed a *high velocity molecular outflow* represents an extremely massive (1-100 $M_\odot$) flow of cold (10-90K), low to moderate density molecular material (Lada

1985) from an often heavily embedded young stellar object.

1.3 HERBIG-HARO OBJECTS

Often found to be associated with molecular outflows are the rather peculiar emission nebulae known as Herbig-Haro objects. First detected independently by G. Herbig and G. Haro during Hα emission line star surveys in the early 50s (Herbig 1951, Haro 1952), much has since been learnt of these objects, in many cases by the aforementioned astronomers, via high-resolution imaging and spectroscopy at optical and, in more recent years, infrared wavelengths. The optical spectra of HHs are typically dominated by hydrogen Balmer emission lines but also by low-excitation lines of [OI], [SII], [NI], [FeII], and to a lesser extent [OII], [NII] and [OIII]. The relative strengths of these emission lines over hydrogen recombination lines distinguish HHs from HII regions; the ionisation in HHs was recognised early on as being due to a process other than photo-ionisation by stellar radiation (Böhm 1956, Osterbrock 1958). Species such as oxygen, carbon and nitrogen within an HII region are mostly stripped of their electrons, so atoms, or singly or doubly ionised particles such as OI and NII will only exist within a thin shell between the HII region and the molecular surroundings. Emission from these ions will consequently be relatively weak with respect to that from hydrogen recombination from within the Strömgren sphere, and so the optical spectra of HII regions differ greatly from those of HHs.

The prototype objects HH1,2 and 3, located near NGC 1999 in Orion, show structure on scales smaller than 0.01pc; similar clumping has been seen since in other sources (e.g. Bührke *et al.* 1988, Raga, Barnes & Mateo 1990). These HH objects also appear to be moving rapidly away from nearby IR sources. Optical emission lines are often shifted by as much as $\sim$ 100km s^{-1} whilst proper motions approach 200-400 km s^{-1} (e.g. for HH1/2 see Hartmann & Raymond 1984 and Herbig & Jones 1981). The observed optical and IR lines are also rather wide, typically of the order 100 and 50 km s^{-1} FWHM respectively. It is these high velocities, and the apparent association with outflows from embedded sources that link HHs with the early stages of star formation. Indeed, HH objects are now thought to represent visible shocks, produced when outflowing material from an IR source or T-Tauri star encounters the ambient

medium. Herbig-Haro objects are thus powerful tools that enable us to examine the interaction between energetic outflows and the ambient cloud envelope.

Early attempts to explain the optical spectra of HH objects were based on plane-parallel shock models, though to some extent these failed to account for the observed UV and visible line strengths (Dopita 1978, Raymond 1979): Because low-excitation emission lines are frequently accompanied by bright lines from highly ionised species such as OIII and CIV, later work instead modeled HH spectra using bow-shaped shocks. The oblique shock-angles (and so low shock velocities) in the wings of such a bow-shock, together with the higher shock velocities produced at the head of the bow-shock, were more successful in accounting for the mixture of observed low and high-excitation emission lines (Hartigan, Raymond & Hartmann 1987). These bow-shocks further explain the wide and often double-peaked line profiles observed in most HH nebulae.

At the same time, theorists were developing dynamical models which might produce these HH bow-shocks (reviewed in Dyson 1987): Schwartz (1978) considered the effects of a continuous flow impacting dense, stationary clumps in the ambient cloud, whilst Norman & Silk (1979) proposed a model where the line emission derives from rapidly moving clumps or "bullets" within the outflow (essentially the inverse of Schwartz's model). These bullets were thought to result from Rayleigh-Taylor instabilities which develop in the cloud envelope as it collapses onto the central source. The bullets are subsequently swept up and accelerated by the outflow; as they travel supersonically through the slower-moving (or stationary) molecular surroundings, the resulting bow-shock produces the observed line emission. Recent high-resolution imaging has shown that a number of HHs actually consist of a cluster of small, optical knots, such as might be produced by either scenario. However, the former "shocked cloudlet" model (Schwartz 1978) does not account for the high proper motions seen in HH objects. The radiating bow-shock around a stationary cloudlet would itself be at rest, and although acceleration of the cloudlet would alleviate this problem, it would at the same time reduce the shock velocity (since $v_{bs} = v_{wind} - v_{cloudlet}$) and so less outflow kinetic energy would be transported to luminous energy.

A third model has been proposed by Cantó (1980), linking HHs with a more contin-

uous outflow phenomenon: He firstly considered the effects of a spherically symmetric stellar wind on a uniform ambient cloud medium (Cantó 1980). Initially an expanding spherical cavity is produced. The cavity is bounded by an inner shock which decelerates the wind and an outer shock that accelerates the ambient cloud gas. Ultimately however, a static configuration is reached where the ram pressure of the stellar wind equals the gas pressure in the surrounding cloud envelope. In this way a spherical cavity of unshocked wind gas bounded by a shock is produced.

The addition of a density gradient to the ambient cloud in Cantó's model produces an *ovoidal* cavity, with the longer shock radius occurring in the direction of decreasing cloud density (Cantó & Rodriguez 1980). The stellar wind is now refracted by the oblique shock angles produced by this geometry and so it runs along the walls of the cavity. At increased distances from the source, the ambient gas pressure exceeds the ram-pressure of the wind; the previously expanding cavity thus begins to narrow down until ultimately the annular stream running along the cavity wall shocks against itself (at the point in the cavity farthest from the source). The authors identify the HH object with this latter shock, where part of the kinetic energy of the gas flowing over the cavity wall is converted to radiated energy (Cantó, Tenorio-Tagle & Rozyczka [1988] have also recently identified the flow of shocked gas from the tip of the ovoidal cavity, away from the source, with the optical jets discussed below). The optical emission from the shock along the cavity wall is thought to be associated with the faint nebulosity often found to surround HH nebulae and their exciting sources.

In this way, the Cantó model accounts for the small solid angles subtended by the HH objects with respect to the associated source. Further, since a large fraction of momentum and kinetic energy in the stellar wind is deposited at the HH, the model also alleviates the need for unrealistically powerful stellar winds, though because it describes a steady-state situation, the HH objects are expected to be near-stationary. As previously mentioned, this latter requirement contradicts more recent observations of a number of HH systems (e.g. Herbig & Jones 1981).

Whilst the above models each go some way to accounting for the observed features in some Herbig-Haro objects, it is never-the-less unlikely that any one scenario will account

for all HH objects. Indeed, very recent imaging has linked some HHs with yet another excitation process: A number of HH objects are now known to be associated with faint though optically visible jets and bow-shocks produced by stellar winds emerging from cloud envelopes (discussed in more detail below).

1.4 OPTICAL JETS

Over the past six or seven years, optical CCD imaging has identified a number of "jet-like" nebulae associated with low to moderate luminosity ($L = 1-100\,L_{\odot}$) T-Tauri stars and infra-red sources (Mundt *et al.* 1987). These jets are seen to be highly collimated – with aspect ratios typically greater than 10:1 (as compared to the relatively poorly collimated molecular outflows, where the ratio is more often less than 5:1) – and they are frequently optically bipolar. The jets are seen to consist of many small knots (knot spacings of the order 10^{15} cm, Mundt *et al.* 1990) and whilst on a large scale they appear quite straight and well aligned with the associated source, they also exhibit small-scale "wiggling" (Mundt 1988).

Optical jets are thought to be closely related to Herbig-Haro objects (Mundt 1988); both HHs and jets exhibit the same type of low-excitation optical emission line spectrum predicted by radiative shock models (Raymond 1979). Also akin to HHs, optical spectroscopy and proper motion studies assign radial velocities of 100–400 km s^{-1} to the knotty structures within these jets. Indeed, several long-known HHs have recently been identified as being the brightest knots within erstwhile unobserved jets (Mundt 1988).

In approximately 60% of known cases, the optical jets are seen to terminate in a bow-shaped (HH-like) nebula (see HH34 and HH111 for perhaps the most striking examples; Buhrke *et al.* 1988, Reipurth 1989). These bow-shocks are thought to represent the point where the jet terminates, the shock structure being produced by the jet as it burrows through the ambient gas.

Modelling aimed at accounting for the above collimated jet structures has been conducted by a number of theorists (Dyson 1984, Falle *et al.* 1987, Tenorio-Tagle 1989, Königl 1982, reviewed in Raga 1989). Initially, the jet is thought to be overpressured

with respect to the local environment, which (unlike Canto's model above) is assumed to be homogeneous. The jet expands (approximately in a Mach cone) until the jet pressure drops below the ambient gas pressure. The resulting underpressured though still supersonic flow is then recollimated by a shock (the *incident shock*) after which the flow reconverges towards the axis of symmetry. The converging flow eventually collides on itself; a conical or *collimator* shock is produced at this point which funnels the now overpressured flow along the symmetry axis. Further downstream the jet again expands and the cycle is repeated. A series of incident and collimator shocks is thus produced along the flow; these shocks are identified with some HH objects and the knots in optical jets.

However, these initially very promising models again describe a steady-state situation; once again they fail to account for the high proper motions of both the HH objects *and* the knots in stellar jets (Eiseloeff, private communication, Reipurth 1989). This severe flaw has led Raga, Canto *et al.* (1990) to consider the effects of stellar jets from intrinsically varying sources. The resulting variable ejection velocities produce non-stationary internal working surfaces within the flow which go some way to explaining the observed high proper motions.

Are these optical jets linked to molecular flows? Whilst a small number of jets derive from embedded infrared sources, the majority seem to be associated with T-Tauri stars, in contrast to their molecular counterparts. Moreover, a large number of known optical jets have no observable associated molecular flow. Both findings are most probably subject to selection effects; jets are more readily observed towards T-Tauris where the optical extinction is relatively low (perhaps only 5–10 magnitudes), whilst at the same time this *lack* of a molecular environment is not conducive to the entrainment of molecular material and so the formation of an observable CO outflow. Conversely, towards the more heavily embedded IR sources where the molecular envelope *is* sufficient to produce an observable CO outflow, any associated jet would most likely be too heavily extinctioned to be visible.

Table 1.2: Optical Jet statistics.
References: 1. Mundt *et al.* 1987, 2. Mundt *et al.* 1990.
[a] Heliocentric radial velocities.
[b] A comparison is made here between the jet mass outflow rate and that measured for any associated molecular outflow.

Source	Length (pc)	[a]Veloc. (km s^{-1})	$\dot{M}_j$ ($\times 10^{-8}$ $M_\odot$ yr^{-1})	[b]$\dot{M}_{CO}$ ($\times 10^{-8}$ $M_\odot$ yr^{-1})	Mechanical Luminosity ($L_\odot$)	A_v to source (mag)
[1]L1551	0.015	-70 to -350	0.3	40-70	0.02	$\sim$20
[1]HH7-11	0.1	-35 to -170	0.4	400	0.03	> 20
[1]HH34	0.05	-60 to -135	≤ 0.1	-	≤ 0.008	5
[1]HH1/2	0.15	$\sim$-3	2.6	-	0.2	> 20
[2]HL Tau	0.04	120 to 180	0.03	-	0.001	-
[2]XZ Tau	0.008	45 to 77	0.05	-	0.002	-

From their sample of optical jets, Mundt *et al.* (1987) estimate that for each source the mechanical luminosity of the jet is typically 10^{-3} the bolometric luminosities of the associated source. However, as was the case for molecular flows, the source radiation pressure remains insufficient to power the observed jets.

Do these optical jets represent the driving mechanism for the more extensive molecular outflows? The momentum supply rate, or ram pressure of optical jets from low to intermediate mass stars is typically $0.1 - 4 \times 10^{-6}\,M_{\odot}\ yr^{-1}\ km\ s^{-1}$ (Mundt *et al.* 1987), a factor of 10-100 less than that measured for equivalent molecular outflows (Edwards & Snell 1984). It therefore remains uncertain as to whether optical jets power molecular flows, though a number of jet parameters are not known accurately and once again one should not exclude the possible presence of a neutral stellar wind component. The characteristics of a number of jets are listed in table 1.2.

A number of excellent reviews exist which discuss present theories of star formation (Lada & Shu 1991, Lada 1991, Shu & Adams 1987, Pudritz 1986), molecular outflows (Bachiller & Gomez-Gonzales 1991, Fukui 1989, Lada 1985) and HH objects and optical jets (Reipurth 1989, Raga 1989, Dyson 1987, Mundt 1988).

1.5 SHOCKS IN STELLAR JETS AND HH OBJECTS

1.5.1 Perfect Gas, B=0

Shock waves within molecular clouds are driven by a variety of processes including stellar winds from embedded IR sources and T-Tauri stars. Indeed, as discussed above Herbig-Haro objects and optical jets are most probably manifestations of shocks produced in this way. A shock will develop when the sound speed of the ambient medium is less than the velocity of the gas that is impacting or expanding into it. We have seen that emission lines from HHs and optical jets greatly exceed the likely sound speed of the cold ambient cloud envelope (few $km\ s^{-1}$). The effect of such a shock will be to compress, heat, chemically alter and accelerate the ambient gas (Hollenbach & McKee

1989).

In order to understand the conditions associated with such shocks, it is constructive to consider the interaction of a plane parallel flow, which is constant in time, with a homogeneous ambient medium (Raymond 1979). It is further desirable to operate in a frame of reference where the shock is stationary, i.e. by following a parcel of gas as it passes through the shock, and also to treat the gas as a single fluid. The shock "region" may be split up into four areas;

1) a radiative precursor in which the ambient gas ahead of the shock is moderately heated and partially ionised by UV photons produced in the shocked layer.

2) the *adiabatic* shock front, a thin layer in which the ambient gas is accelerated, heated and compressed.

3) a much broader layer where inelastic collisions produce radiative cooling, emission, recombination, and further compression downstream from the front.

4) a final region further downstream from the shock where the gas has cooled to essentially the ambient, pre-shock temperature.

The rapid transition between regions 1 and 2 occurs within a distance equivalent to several mean free paths of the particles in the gas, typically $\sim 10^{-5} - 10^{-7}$pc ($10^{-2} - 10^{-4}$ arcseconds in Orion at a distance of 460pc) for an ambient gas density, $\rho_1 \sim 1000 - 10\text{cm}^{-3}$. Physical changes depend on the following Rankine-Hugoniot "jump" conditions (Landau & Lifshitz 1987, Bowers & Deeming 1984);

$$\rho_1 v_1 = \rho_2 v_2 \tag{1.1}$$

$$P_1 + \rho_1 v_1^2 = P_2 + \rho_2 v_2^2 \tag{1.2}$$

$$\frac{1}{2}\rho_1 v_1^3 + P_1 v_1 + U_1 \rho_1 v_1 = \frac{1}{2}\rho_2 v_2^3 + P_2 v_2 + U_2 \rho_2 v_2 \tag{1.3}$$

where U is the internal energy of the gas, P the pressure and v the velocity of the parcel of gas. Simply, mass, momentum and energy fluxes are continuous across the adiabatic

shock. I shall assume that Herbig-Haro shocks are *strong*, i.e. the Mach number of the gas entering the shock is high, $M_1 = v_1/c_1 >> 1$. Following Bowers & Deeming (1984), the above equations give

$$\frac{v_2}{v_1} = \frac{\rho_1}{\rho_2} = \frac{\gamma - 1}{\gamma + 1} \tag{1.4}$$

For a diatomic gas, the ratio of specific heats $\gamma = 7/5$. The shocked ambient gas may therefore be compressed to $\sim 6\times$ its original density whilst being accelerated to 1/6 the shock velocity.

The increase in gas temperature and pressure behind the adiabatic shock may further be obtained from

$$P_2 = \frac{2\rho_1 v_1^2}{\gamma + 1} = \frac{5}{6}\rho_1 v_1^2 \tag{1.5}$$

$$T_2 = 2\frac{(\gamma - 1)}{(\gamma + 1)^2}\frac{\mu_H m_{H2}}{k} v_1^2 = \frac{5}{36}\frac{\mu_H m_{H2}}{k} v_1^2 \tag{1.6}$$

where μ_H is the mean molecular weight of the molecular gas (~ 1.3) and m_{H2} is the mass of an H_2 molecule. Thus, directly behind a planar, diatomic shock of $v \sim 20$km s^{-1}, the gas is compressed and heated to $T_2 \sim 10^3$K; at higher shock velocities $v \sim$ 200km $s^{-1}, T_2 \sim 10^6$K. Modeling of recombination-line emission spectra predict that the velocity of shocks associated with HHs and optical jet features lie within this range (Hartigan *et al.* 1987).

This hot, shocked transition is followed by cooling, further compression and radiative energy losses — region 3. Although mass and momentum remain conserved (equations 1.1 and 1.2), we must adjust equation 1.3 to account for this latter process (Shull & Draine 1987)

$$\frac{d}{dx}\left[\frac{1}{2}\rho_3 v_3^3 + P_3 v_3 + U_3 \rho_3 v_3\right] = -\Lambda \tag{1.7}$$

Here Λ is the net cooling rate per unit volume. Contributions to Λ will depend on the temperature of the post-shock gas: Behind rapid shocks, Λ is almost entirely due

to electron excitation of ions of typically C, N, O and Ne, since these have excited levels a few volts above the ground level. These levels are collisionally populated at temperatures $\sim 10^4$K, the cross-sections exceed those of radiative capture by about 10^5, and so they provide a very powerful cooling mechanism (Spitzer 1978). Behind lower velocity shocks, $v_{shock} \equiv v_1 \leq 25$ km s^{-1}, or more oblique shocks (we take v_1 as the velocity component perpendicular to the shock front), molecular dissociation does not occur. Here we must consider radiative and dissociative cooling from molecules, specifically H_2, but also CO and H_2O (Shull & Draine 1987).

The cooling in region 3 results also in a large compression, though the total pressure $(P + \rho v^2)$ remains constant throughout all regions, 1–4. Ultimately, we may regard the transition between the initial preshock material and the final, cool, compressed layer (region 4) as being *isothermal*; thus $\gamma = 1$ and so the thermal pressure term $P = \rho c^2$. Again by assuming that our HH shock is strong, equation 1.2 reduces to (Spitzer 1978, p. 221, Bowers & Deeming 1984, p. 440)

$$\frac{\rho_4}{\rho_1} = \frac{v_1^2}{c^2} = M_1^2 \tag{1.8}$$

For strong shocks a large overall increase in gas density is therefore possible, perhaps by a factor of 100 or more.

We may finally make a crude estimate of the cooling time t_c in region 3 by simply equating the thermal energy to be radiated away to the cooling rate (for say 10^5K gas) $\times t_c$:

$$n_{H2} \times \frac{3}{2} k T_k \sim \Lambda t_c \tag{1.9}$$

Taking $\Lambda / n_H^2 \sim 10^{-32}$ J cm^3 s^{-1} as a lower limit (Spitzer 1978, p 143), then for a fast shock, $v_1 \sim 100$ km s^{-1} impacting a dense ambient medium $n_{H2} \sim 10^4$ cm^{-3} the gas will cool from $T_k \sim 4 \times 10^5$K to $\sim 10^2$K in $\sim 10^9$ seconds. This corresponds to cooling within $\leq 10^{-3}$ pc of the shock front and compares to an *adiabatic* shock width of $\sim 10^{-8}$ pc ($\sim$ a few mean-free-paths) in region 2. Clearly, resolving either the adiabatic shock or the radiative layer in either HHs or optical jet shocks is beyond current observational capabilities.

1.5.2 The Effect of a B-field: Hydromagnetic Shocks

The presence of a magnetic field B modifies our treatment of an HH-type shock. Assuming the field is perpendicular to the flow, a sufficient level of ionisation assures that B is coupled to the matter, leading to "flux freezing" in which vB and B/ρ are constant. An additional pressure term, $B^2/8\pi$ thus appears on both sides of equation 1.2. As the shocked gas cools and ρ increases, the magnetic pressure ($\propto \rho^2$) eventually dominates the momentum flux ($\propto \rho$) so that the maximum compression in the post shock gas (region 4) is now limited not by thermal pressure but by magnetic pressure; by $\rho_1 v_1^2 \simeq B_4^2/8\pi$ (Shull & Draine 1987). As $B_4/\rho_4 = B_1/\rho_1$, then

$$\frac{\rho_4}{\rho_1} = \left(\frac{8\pi\rho_1 v_1^2}{B_1^2}\right)^{1/2} = 2^{1/2}\frac{v_1}{v_{A1}} \tag{1.10}$$

Here $v_{A1} = (B_1^2/4\pi\rho_1)^{1/2}$ is the Alfvén velocity. However, observed B-fields in star-forming clouds are relatively weak, ~few $\times 10^{-6}$Gauss. Consequently, the compression in the post-shock flow may still approach that predicted earlier (with B=0). Because outflow velocities and proper motions of HH shocks are high, the gas is (at least to a first approximation) likely to be "super-Alfvénic" as well as supersonic; i.e. $v_1 \gg v_{A1}$.

1.6 MOLECULAR LINE EMISSION

Optically the most obvious feature of interstellar molecular clouds is the extinction of background starlight, caused by the presence of interstellar dust. However, 99% of the mass of a cloud is in the form of gaseous hydrogen, of which $> 60\%$ is molecular. Molecular clouds are certainly not uniform, but although gas densities increase from diffuse values of $10 - 10^3 \mathrm{cm}^{-3}$ to densities in excess of $10^4 - 10^5 \mathrm{cm}^{-3}$ near sites of active star formation (Williams & Harquist 1990, Bally 1989) the most abundant species, H_2, remains all but invisible.

H_2 is a homonuclear molecule, so only quadrupole transitions are allowed between different vibrational *(v)* and rotational *(J)* states within the ground electronic state (figure 1.3; discussed in detail in Shull & Beckwith 1982). Transitions obey the selection rule $\Delta J = 0, \pm 2$, with $0 - 0$ forbidden. There is no restriction on Δv. The $J = 2$ level

lies at $\sim$ 512K above the ground state; transitions with $\Delta v = \pm 1$ have higher energies $\sim$ 0.5eV ($\sim$6000K); and the first excited electronic state lies at $\sim$ 11.2eV ($\sim$130,000 K) above the ground level. Consequently, observable H_2 line emission becomes significant only when the gas kinetic temperature exceeds $\sim$500K. Since the ambient gas in molecular clouds remains at a temperature < 100K, and most often < 40K, IR line emission from H_2 is only produced behind low-velocity shocks or via UV excitation (Sternberg 1988). Therefore one must often use the other molecular cloud constituents as tracers of the more elusive H_2. The merits of a number of molecular tracers are discussed below.

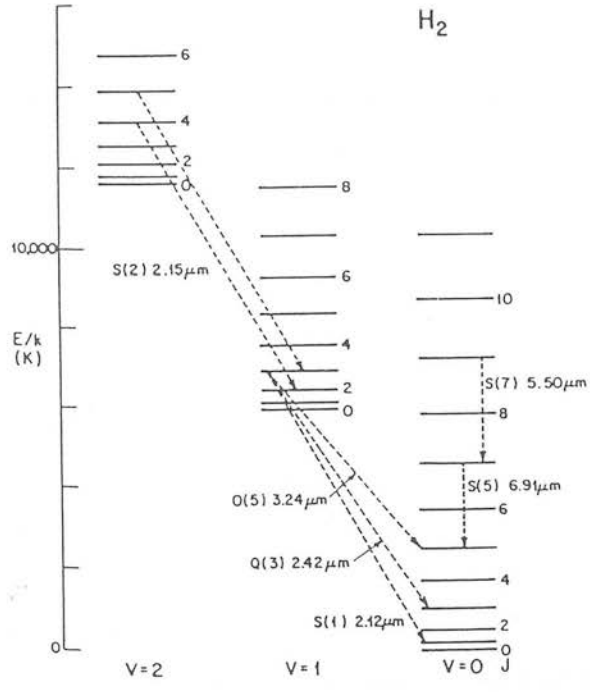

Figure 1.3: Ro-vibrational transitions in H_2 (from Shull & Beckwith 1982).

Molecular line observations have certain advantages over dust continuum studies: In addition to providing velocity information, different molecules and rotational transitions may be used to probe the differing excitation conditions in and around areas of star formation. However, as will be discussed in more detail later, molecular abundance variations in the turbulent regions near outflows, jets and IR sources complicate the

use of molecules as probes of the overall H_2 conditions.

The rotational transitions of many molecules lie at radio, millimeter and sub-millimeter wavelengths. In radio astronomy, the brightness (or radiation) temperature, T_b (or T_R), is used to measure the intensity of the source, $I_\nu = B_\nu(T_b)$, where $B_\nu(T_b)$ may be expressed using the Planck law. A further simplification is made using the Rayleigh-Jeans approximation (since at radio wavelengths, $h\nu \ll kT_b$);

$$I_\nu = \frac{2h\nu^3}{c^2}\frac{1}{(exp(\frac{h\nu}{kT})-1)} \tag{1.11}$$

$$\simeq \frac{2\nu^2}{c^2}kT_b \tag{1.12}$$

However, at mm and sub-mm wavelengths, we have the situation where $h\nu \ll kT_b$ does not apply. Thus, strictly speaking equation 1.12 should instead be written in terms of an *equivalent* brightness temperature, $J_\nu(T_b)$;

$$I_\nu = \frac{2\nu^2}{c^2}kJ_\nu(T_b)$$

where $J_\nu(T) = h\nu/k(\exp(h\nu/kT)-1)^{-1}$. $J_\nu(T_b)$ is known as the Rayleigh-Jeans equivalent brightness temperature. It is still useful however to define a temperature scale which is proportional to the radiation intensity, I_ν: At the telescope, sub-mm and mm observations are calibrated by comparing the observed source with a black body at a known temperature, thus producing a scale where the intensity varies *linearly* with temperature. At these shorter wavelengths the approximation in equation 1.12 is therefore still assumed valid; i.e. the line brightness temperature of the mm/sub-mm observations still applies in equation 1.12 (though one should never-the-less be aware that this calibration process has been used).

Re-arranging equation 1.12 gives the following expression for brightness temperature:

$$T_b = \frac{c^2}{2k\nu^2}I_\nu \tag{1.13}$$

The radiation emitted by a source will often be attenuated by intervening molecular material – (some of the photons emitted from the centre of a molecular cloud for example will be scattered or absorbed and re-emitted by molecules in the outer layers). This attenuation is governed by the probability of scattering or absorption, termed the absorption coefficient, κ_ν, such that over a distance ds, $dI_\nu = -I_\nu \kappa_\nu ds = -I_\nu d\tau_\nu$. Here $d\tau_\nu$ is the optical thickness of the gas to radiation of frequency ν; it is the ratio of the distance travelled by a photon in the medium to the photon's mean free path. Thus, when $\tau_\nu = \int \kappa_\nu . ds \gg 1$, where the integration is over the thickness of the intervening molecular cloud, the gas is optically thick and each photon will have been scattered and absorbed many times; conversely, when $\tau_\nu \ll 1$, the gas is optically thin.

The observed intensity will also be "contaminated" by the background radiation field, at a black body temperature, $T_{bg} = 2.7$K (Kutner 1984). The brightness temperature thus becomes

$$T_b = \frac{c^2}{2k\nu^2}[I_\nu(T_{ex}) - I_\nu(T_{bg})](1 - \exp(-\tau_\nu)) \tag{1.14}$$

where T_{ex}, the excitation temperature of the observed transition j to i, is defined by

$$\frac{n_j}{n_i} = \frac{g_j}{g_i} \exp(-h\nu/kT_{ex}) \tag{1.15}$$

Here n_j is the level population of the jth level and g_j the statistical weight. Equation 1.14 is also sometimes written in terms of the Rayleigh-Jeans equivalent brightness temperature;

$$T_b = [J_\nu(T_{ex}) - J_\nu(T_{bg})](1 - \exp(-\tau_\nu)) \tag{1.16}$$

T_b is also subject to the efficiencies of the observing system (Kutner & Ulrich 1981). The signal measured at the telescope, the *antenna temperature*, T_A^*, the quantity which is used throughout this thesis, has already been corrected for the ohmic (resistive) losses of the antenna and for atmospheric attenuation. However, to establish the true brightness temperature of the source we need to first correct for the *beam efficiency* of the telescope antenna, η_b.

The response of the antenna as a function of angular offset from the telescope axis is given by the antenna pattern. This pattern consists of a main beam or "lobe" and a large number of "sidelobes" (the angular resolution of the telescope is determined by the half power beam width (HPBW), θ_m, of the main lobe of the antenna pattern). The beam efficiency of the antenna is thus a measure of the power lost in these sidelobes and is equal to the ratio of the main lobe solid angle, Ω_m, to the *total* beam solid angle, Ω_a, the angle through which all the power from a transmitting antenna would stream if the power (per unit solid angle) was constant over this angle and equal to the maximum value (Kraus 1986). Division of T_A^* by η_b results in the telescope main beam brightness temperature, T_{mb}. For large telescopes η_b is usually calibrated with standard sources of known flux densities, and any contribution to the antenna temperature received in the sidelobes is removed when an off-source observation is subtracted.

Also, since T_{mb} is a measure of the average temperature over the telescope beam, for very small sources the observed temperature must be divided by an additional beam dilution or beam filling factor, $\eta_f = \Omega_s/\Omega_m$, where Ω_s is the source solid angle. If both the main beam of the antenna *and* the source brightness distribution approximate to a gaussian, then $\eta_f = \theta_s^2/\theta_m^2$ (where θ_s and θ_m are the widths at half power of the source distribution and the main telescope beam, measured often in arcseconds). For extended sources, $\eta_f = 1$.

We may therefore relate T_A^* to T_b by;

$$T_b = \frac{T_A^*}{\eta_f \eta_b} \tag{1.17}$$

1.6.1 Linear Molecules; CO, CS, HCO^+, HCN

After H_2, CO is the most abundant molecule found in a molecular cloud (abundance $\sim 10^{-4}\times$ that of H_2). The low dipole moment of CO ($\mu = 0.112$ Debyes) allows for the excitation of the low-J rotational levels in relatively diffuse, cool environments ($few \times 10$K; H_2 density, $n(H_2) \geq 10^3$ cm^{-3}). For the $J = 1$ level, $h\nu/k = T_0$ =5.5 K. Hence the usefulness of the CO $J = 1 - 0$, 2-1 and 3-2 transitions, at 2.6mm, 1.3mm and 0.86mm respectively in tracing the molecular outflows discussed above.

If we assume, as is often the case (Bally 1989), that in molecular cloud cores typical of star forming regions the gas density is greater than $10^3 \mathrm{cm}^{-3}$, then the low-J levels of CO will be thermalised. In other words, the excitation temperature that describes the populations of the low-J levels will approach the gas kinetic temperature, T_k. If the observed line is also optically thick ($\tau \gg 1$) then we may use the CO as a gas thermometer (Evans 1980). Substituting the Planck function for $I_\nu(T_{ex})$ and $I_\nu(T_{bg})$, and replacing T_b in equation 1.14 yields a relationship between T_A^* and T_{ex}. However, as pointed out by Evans (1980), care should be taken that these conditions *are* fulfilled. The gas density may be too low to thermalise the observed transition, and although generally $\tau \gg 1$, this may not be the case in high velocity molecular outflows.

However, molecular outflows are usually observed in CO. Thus if we are to calculate the outflow mass and energetics accurately then we need to know the opacity of the outflowing gas; the optical depth in the CO linewings. We may calculate τ by observing the flow in a second CO isotope (most commonly ^{13}CO), though in the same rotational transition (e.g. Wolf *et al.* 1990). We assume equal excitation temperatures for each isotope and an abundance ratio of $^{12}\mathrm{C}/^{13}\mathrm{C} \sim 89$ (solar abundances). The average optical depth in the line wings is obtained from the ratio of the ^{12}CO and ^{13}CO wing integrated intensities;

$$\frac{\int_{wings} T_A^*(^{12}CO).dv}{\int_{wings} T_A^*(^{13}CO).dv} = \frac{1-\exp(-89\tau_{13})}{1-\exp(-\tau_{13})} = \frac{89(1-\exp(-\tau_{12}))}{\tau_{12}} \qquad (1.18)$$

Having established the optical depth in the line wings, we may then go on to calculate the column density of CO in the wings (in the outflow) and so eventually the mass of the outflow. See appendix A for a calculation of molecular column densities.

A more accurate measure of dense molecular cloud structure associated with star formation and outflow may be obtained by observing the radiation from molecules such as HCO^+, CS and HCN. The high dipole moments of these molecules (μ = 4.07, 1.96 and 2.98 Debyes, for HCO^+, CS and HCN respectively) and their relatively low abundances (typically $< 10^{-8}\times$ that of H_2; Irvine & Knacke 1988) mean that the millimeter and sub-millimeter lines from the low-J transitions require high densities for excitation and are often optically thin. Further, these molecules are sensitive to

a *wide range* of gas densities in the denser core regions ($10^3 < n_{H2} < 10^8$ cm^{-3}). For these reasons they illustrate very well the dense, quiescent cores within molecular clouds ($n(H_2) \geq 10^6 - 10^7 \mathrm{cm}^{-3}$). Column density estimates (again refer to appendix A) further lead to mass estimates for individual cloud features. The merits of the individual tracers will be discussed in more detail in subsequent chapters of this thesis.

1.6.2 Symmetric Top Molecules; NH_3

The ammonia molecule is another useful probe of gas densities and temperatures within molecular clouds. NH_3 however differs from the above linear molecules in that it is able to rotate about *two* axes, described by two principal quantum numbers, J and K (with transitions obeying the dipole selection rules $\Delta K = 0, \Delta J = 0, \pm 1$; Townes & Schawlow 1975). As shown in figure 1.4, the rotational energy levels in NH_3 may be represented in terms of independent K ladders, since transitions between these ladders are forbidden (though vibration of the molecule can give rise to very slow $\Delta K = \pm 3$ transitions). Within these ladders, the low $J = K$ levels decay very slowly and are regarded as *metastable*, whilst the higher $J > K$ states decay far more rapidly, and are known as *nonmetastable*. These higher states are difficult to populate under normal conditions, requiring densities of the order of $10^8 \mathrm{cm}^{-3}$. Levels within the $K = 3$ ladder are similarly hard to fill, and consequently interstellar ammonia exists primarily in the $J, K = 1,1$ and 2,2 rotational states.

The NH_3 molecule also undergoes an additional *observable* transition, where the N-atom penetrates the plane formed by the three H-atoms. This produces a splitting of the rotational J, K levels into *inversion doublets*. Inversion transitions within a doublet occur at $\sim$ 24GHz, and so are observable at radio wavelengths. Moreover, because the $J, K = 1,1$ and $2,2$ states are quite independent, we may treat these metastable states as independent, two level systems.

Each inversion transition (between the two levels in a doublet) is additionally split due to hyperfine interactions between electronic, nuclear and molecular spins. These result in two pairs of *satellite* hyperfines at $\sim$ 1MHz and $\sim$ 2MHz either side of the main line component (figure 1.5). These satellite lines in turn allow us to calculate the optical depth of the main (central) hyperfine component. The ratio of the peak

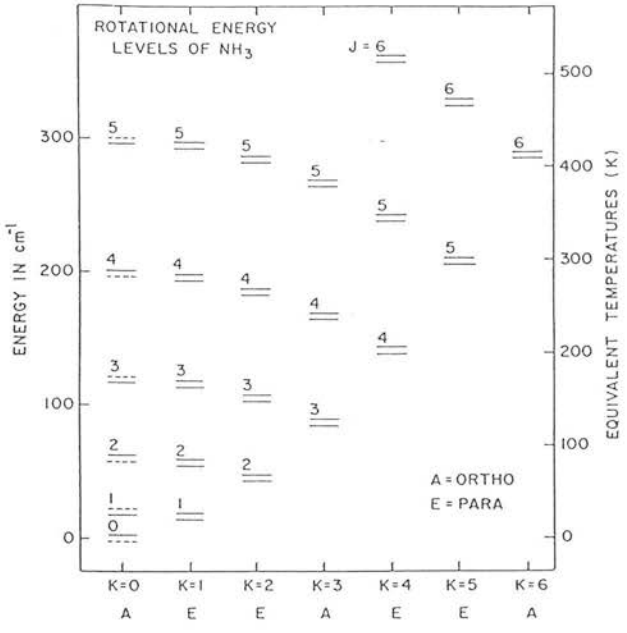

Figure 1.4: Rotational energy states in NH_3 (from Ho & Townes 1983).

antenna temperatures, T_A^*, of the main and satellite hyperfines of for example the (1,1) inversion line lead to the optical depth $\tau_{1,1}$ (Barrett et al. 1977) via equation 1.14.

$$\frac{T_A^*(1,1,m)}{T_A^*(1,1,s)} \simeq \frac{1-exp(-\tau_{1,1})}{1-exp(-a\tau_{1,1})} \tag{1.19}$$

where the equilibrium ratio of main and inner hyperfine optical depths, a, is a known quantity; 0.28 (Martin & Barrett 1978). As for CO, this treatment is a powerful one, since η_b, η_f and the excitation temperatures may be assumed equal due to the very close energy separations between main and hyperfine components. We may similarly apply these arguments to the J,K = 1,1/2,2 ratio, to obtain $\tau_{2,2}$.

Observation of the $J, K = 2, 2$ transition also allows the observer to estimate the gas kinetic temperature via an estimate of $T_R(2,2;1,1)$, the rotational temperature that describes the relative populations of the (1,1) and (2,2) metastable states. $T_R(2,2;1,1)$

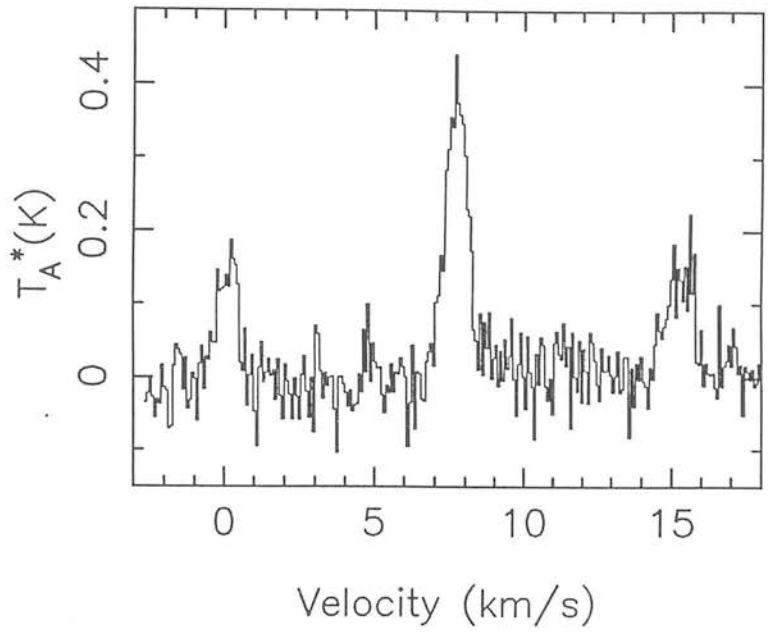

Figure 1.5: NH_3 (1,1) in L1551-IRS; the inner hyperfines are clearly detected, the outer hyperfines (not shown) occur at $v_{LSR} \sim -12$ and 27 km s^{-1}.

is widely regarded as a good indicator of T_k (Ho & Townes 1983, Martin & Barrett 1978), since the low $J = K$ levels achieve a near Boltzman population distribution via collisions with H_2. From equation 1.14 (applied to the (1,1) and (2,2) transitions), and in the optically thin limit, the ratio of optical depths gives

$$\frac{\tau_{2,2}}{\tau_{1,1}} = \frac{\mathcal{Q}(2,2)}{\mathcal{Q}(1,1)} \frac{\nu^2(2,2)}{\nu^2(1,1)} \frac{\mid \mu(2,2) \mid^2}{\mid \mu(1,1) \mid^2} \frac{\Delta\nu(1,1)}{\Delta\nu(2,2)} \frac{T_{1,1}}{T_{2,2}} \times \exp\left(\frac{-\Delta E(2,2;1,1)}{kT_R(2,2;1,1)}\right) .$$

We thus arrive at an equation for $T_R(2,2;1,1)$

$$T_R(2,2;1,1) = \frac{-41.5}{\ln(0.282\ \tau_{2,2,}/\tau_{1,1})} \leq T_k \tag{1.20}$$

In the above, $\mid \mu(J,K) \mid^2 = \mu^2 K^2/[J(J+1)]$ is the dipole matrix element and ν and $\Delta\nu$ are the line rest frequency and line width respectively. Note, however, that $T_R(2,2;1,1)$ may slightly underestimate T_k, because of downward relaxations from the non-metastable states and the slow collisional coupling between K ladders (Ho & Townes 1983).

Finally, treating the (1,1) metastable state alone as a two level system, balancing collisions and stimulated emission against spontaneous emission leads to a relation between the density, excitation temperature and kinetic temperature (Ho & Townes 1983).

$$n_{H2} = \frac{A_{1,1}}{(\sigma_c \times \overline{v})} \left[\frac{J(T_{1,1}) - J(T_{bg})}{J(T_K) - J(T_{1,1})}\right] \left[1 + \frac{J(T_K)}{h\nu/k}\right] \tag{1.21}$$

where $J(T)$ is the Rayleigh-Jeans equivalent brightness temperature, $A_{1,1}$ is the Einstein coefficient for spontaneous emission and $(\sigma_c \times \overline{v})$ is the collision rate.

Chapter 2

GGD27 IRS: A Molecular Outflow Source

SUMMARY: CO J=1-0 observations of the outflow from the luminous, infrared reflection nebula GGD27 IRS imply that it is one of the most massive molecular outflows known. Further, the associated optical nebulae HH80 and HH81 are two of the brightest HH objects yet discovered. Within the following chapter I present CO and ^{13}CO J=2-1 observations of this outflow, and discuss the techniques used to calculate the mass and energetics of the blue and red-shifted outflow lobes. Significantly, contour plots of the low-velocity and high-velocity outflowing gas, when compared, imply that the flow lies very near to the plane of the sky; the low-velocity blue-shifted contours overlap the high-velocity red-shifted lobe and vice-versa. This structure is interpreted in terms of an outflow with an opening angle that is greater than twice the angle between the flow axis and the plane of the sky. Also, the mass and energetics derived here are roughly a factor of 10 less than values obtained from the CO 1-0 observations; this difference is due to the careful calculation of the excitation temperature made here.

2.1 INTRODUCTION

Found by Yamashita *et al.* (1987) during a polarimetric survey, GGD27 IRS lies at the south-west edge of a dark lane extending NW-SE in Sagittarius. GGD27 IRS also appears in the IRAS catalogue and is often considered to be a prototype infra-red reflection nebula — a source in a star-forming region that is associated with diffuse, polarised near-infrared emission. Low-resolution near-IR imaging has revealed a distinct bipolar, dumbbell-like structure, orientated approximately north-south (Aspin *et al.* 1991, Yamashita *et al.* 1987), a morphology that is consistent with the hollow-shell structure proposed for CO outflows. Indeed, subsequent mapping in CO J=1-0 has revealed a molecular outflow that is attributed to GGD27 IRS, and which extends in the same north-south direction towards the HH objects HH80 and HH81. (Yamashita *et al.* 1989).

These associated HH nebulae were identified as two of the brightest known HH objects by Reipurth & Graham (1988). Detailed, high-resolution, optical spectroscopy has also revealed velocity structure over a remarkable 700 km s^{-1} whilst radio continuum observations show emission peaks, elongated along the CO outflow direction, associated with both the GGD27 IRS source and the HH objects (Rodriguez & Reipurth 1990, Reipurth 1989). These radio studies have further confirmed the high proper motions of HH80 and HH81, and again are consistent with a shell-like/ionised wind-driven molecular outflow scenario as discussed in chapter 1.

2.2 OBSERVATIONS

Sub-millimeter observations of the outflow in GGD27 IRS and towards the associated HH nebulae HH80-81 were carried out using the James Clerk Maxwell telescope on Mauna Kea, Hawaii with the heterodyne receiver A and a wide band acousto-optic spectrometer. We observed both the ^{12}CO (hereafter written CO) and ^{13}CO J=2-1 transitions at 230.5380 GHz and 220.3987 GHz respectively; the spectral resolution of the AOS was 0.25 MHz or 0.32 km s^{-1} (though the local oscillator is known to smear and move the emission on a scale of $\sim$ 0.6 km s^{-1}). Two visits to Mauna Kea were required to complete this project, since our initial 3-night observing run

during March 1990 was hampered by thick cloud and heavy snow; when observing was possible, system temperatures were typically 3000 - 5000 K! Improved conditions were encountered in March 1991, and a $T_{sys} \sim 940$ K was maintained throughout the two nights. The JCMT beam at 230 GHz measures 22 arcsecs and the beam efficiency is 0.65. Mapping in both CO and ^{13}CO was conducted with 15 arcsecond spacings, whilst chopping 5 arcminutes in declination provided a reference position for each source position. To enable large-scale mapping we restricted our on-source integration time to 1 minute per point, though towards the central position 8 individual scans with longer integrations were obtained and averaged, culminating in a total on-source integration time of 18 minutes for the CO 2-1 spectrum in figure 2.3. The pointing was checked hourly against IRC+10216; the rms error measured $\sim 5''$ during bad weather and better than $\sim 2''$ during our second observing run. The distance to GGD 27 IRS and HH80-81 is $\sim$ 1.7 kpc (Rodriguez *et al.* 1980b).

2.3 RESULTS AND DISCUSSION

2.3.1 A Molecular Outflow from GGD 27 IRS

The CO and ^{13}CO J=2-1 spectra observed towards GGD 27 IRS are shown in the grid maps of figures 2.1 and 2.2. The lines observed in both isotopes towards the central map position (towards GGD 27 IRS) are presented in figure 2.3. The emission in CO and ^{13}CO is clearly optically thick and high-velocity wings are evident on both spectra.

The central portion of each CO spectrum represents emission from the surrounding cloud envelope. The line profile function of this ambient cloud component is often well represented by a gaussian and so virtually all of the emission beyond $v_o \pm$ FWHM (full width at half the maximum line intensity), where v_o is the velocity of the line peak, will be from high-velocity gas (Liseau & Sandell 1986). Unfortunately, the CO 2-1 spectra here are heavily self-absorbed and so it is difficult to measure the true FWHM of the underlying gaussian line profile. With this in mind, the blue wing emission in the CO and ^{13}CO spectra is judged to extend from 10.5 km s^{-1} and the red from 14.5 km s^{-1} (though I recognise that this velocity range may also include emission from the ambient cloud). In ^{13}CO the blue wing emission is lost in the noise at $\sim$ 6 km s^{-1}, the red at

$\sim$ 19 km s^{-1}. However, wing emission is observed out to ~ -12 km s^{-1} and $\sim$ 37km s^{-1} in CO. I shall therefore treat these two wing components separately; a *low-velocity* inner wing component that is seen here in CO and ^{13}CO J=2-1 — corresponding to the outflow observed in CO J=1-0 by Yamashita *et al.* (1989), and a *high-velocity* outer wing component detected only in CO J=2-1.

From the spectra in figure 2.1 the distribution of both low- and high-velocity CO wing components is shown in figure 2.4 as contour plots. The map of low-velocity wing emission in figure 2.4*a* is similar to that of the earlier CO J=1-0 observations of Yamashita *et al.* (1989); the blue wing emission peaks within 10-20$\widehat{''}$ of the source, with a slight easterly offset, whilst the red-shifted component extends south of GGD27 IRS. However, the distribution of the high-velocity gas, shown in figure 2.4*b*, is inversely orientated; this time the red-shifted component peaks $\sim 30\widehat{''}$ north of the source, whilst the blue wing emission extends to the south.

The sketch in figure 2.5 shows an outflow structure that would result in similar contour plots, where low-velocity blue-shifted gas overlaps high-velocity red-shifted emission, and vica-versa. Here, half the full opening angle of the flow is greater than the angle between the outflow and the plane of the sky. The radial component of the flow velocity in the rear side of the blue lobe is consequently slightly red-shifted, whilst the front side of the red lobe is similarly blue-shifted. Cabrit (1989) has considered in detail the structure of contour maps that would result from different outflow geometries. The CO 2-1 results here of the outflow from GGD27 IRS agree best with the *idealised* case 3 in Cabrit (1989), where the outflow is almost in the plane of the sky; because of the divergence of the flow, the front side of the red lobe is approaching the observer whilst the rear side of the blue lobe is receding from him/her.

2.3.2 The Optical Depth in the CO Outflow

Before an estimation of the optical depth and excitation temperature in the ^{13}CO line wings, and subsequently the mass and energetics of the low-velocity flow may be made, we must first outline the assumptions which are to be made:

i) We assume that the outflow gas is in local thermodynamic equilibrium and that the

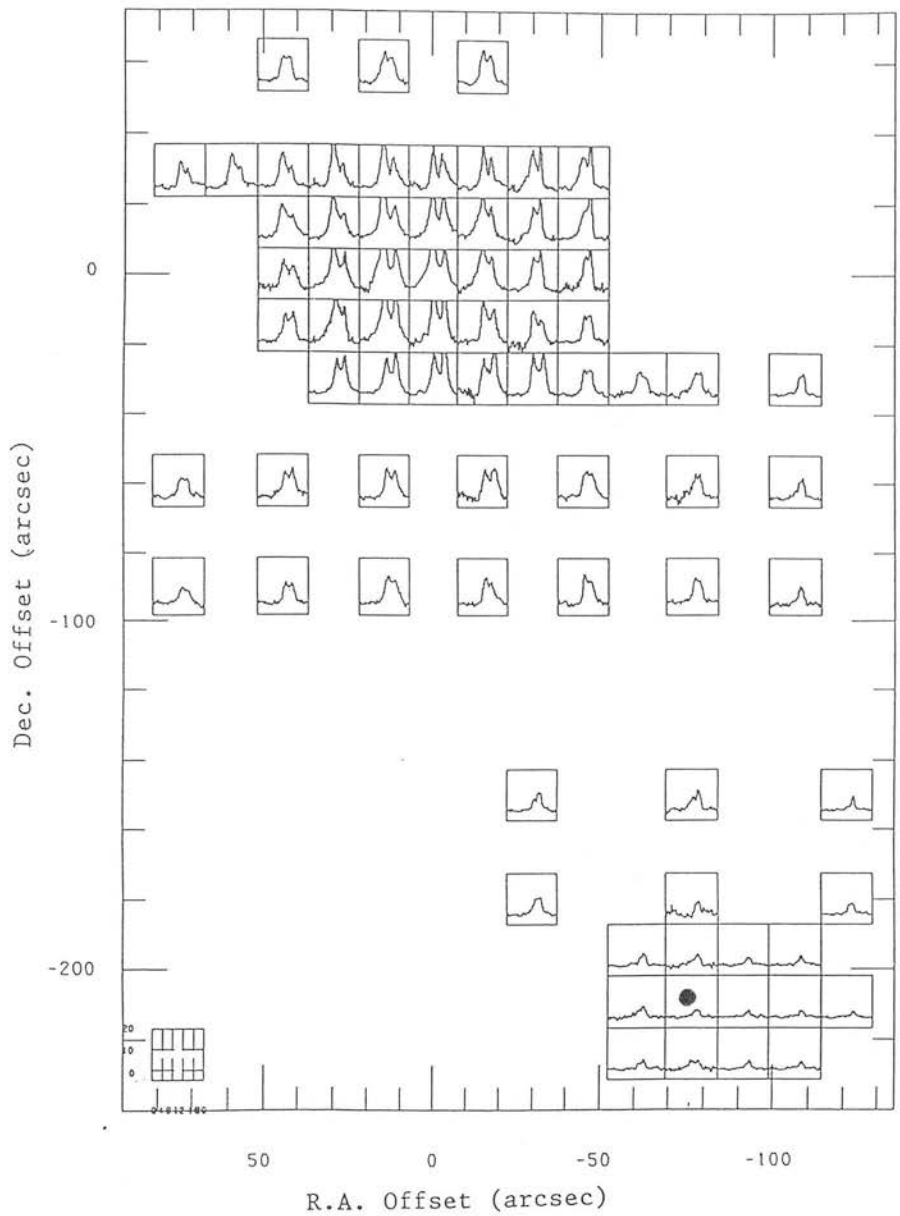

Figure 2.1: CO J=2-1 spectra observed near to the IR source GGD27 IRS. Note the temperature scale is the antenna temperature, T_A^*, uncorrected for the telescope beam efficiency. The map centre: RA(1950): $18^h16^m13^s.0$, DEC(1950): $-20^o48'49''$, corresponds to the position of GGD27 IRS. HH81 is marked by a filled circle; HH80 occurs at offsets (-83$\widehat{m}$, -260$\widehat{m}$).

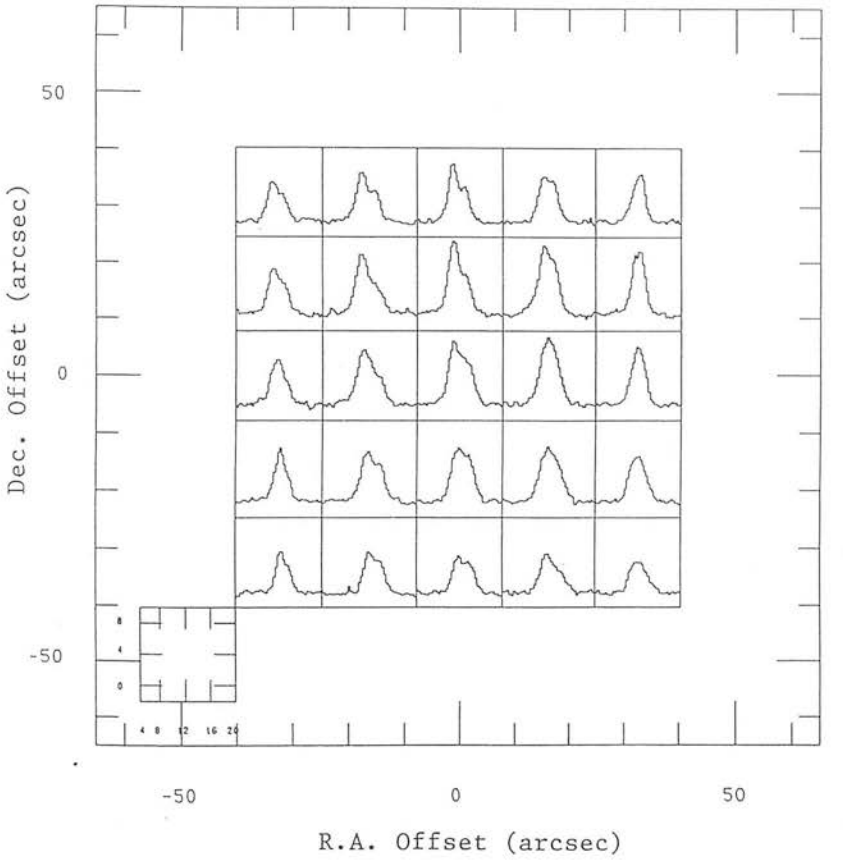

Figure 2.2: ^{13}CO J=2-1 spectra observed around GGD27 IRS. Again the temperature scale is T_A^* and the map centre is as for figure 2.1.

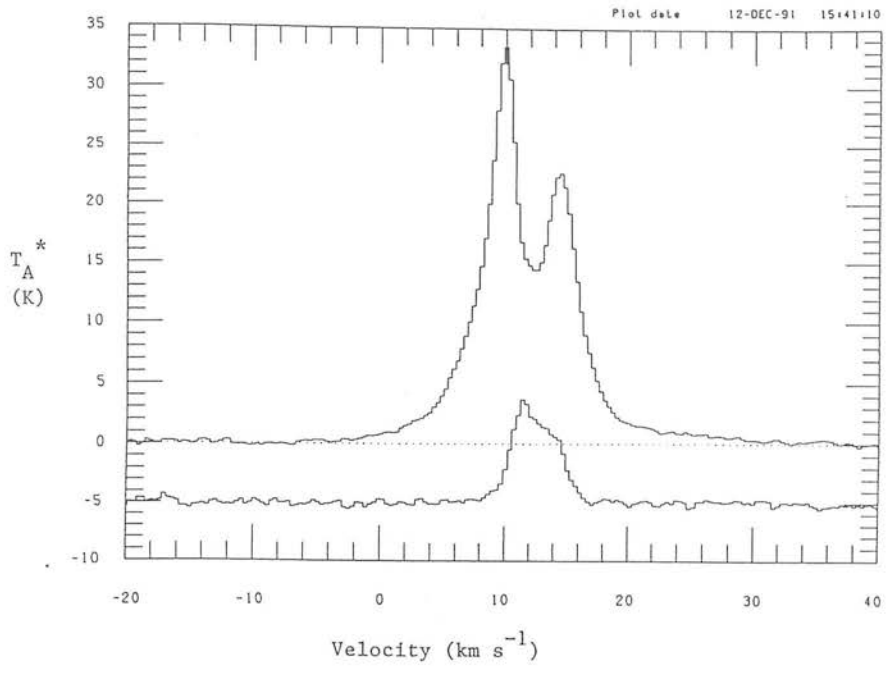

Figure 2.3: CO and ^{13}CO J=2-1 spectra, taken from figures 2.1 and 2.2, towards the source GGD27 IRS (the central map position).

excitation temperature is the same for the J=2-1 and 1-0 transitions of both isotopes.
ii) The isotopic abundance ratio is assumed to remain constant along the outflow, at a terrestrial value of CO/^{13}CO = 89.
iii) I shall additionally assume that the CO and ^{13}CO emission derives from the same gas, and that the beam filling factor is the same for both isotopes (though note that the beam size for the 2-1 observations is 5 arcseconds larger than that used by Yamashita *et al.* (1989) for the 1-0 observations).

Having made these assumptions, then from the CO and ^{13}CO observations of both J=2-1 and 1-0 transitions towards the source of the outflow (figure 2.3 and figure 1 in Yamashita *et al.* 1989), we may estimate the optical depth in the ^{13}CO line wings. A curve was drawn by eye through the noise in the ^{13}CO 2-1 and 1-0 line wings. Values of the antenna temperature (the main beam brightness temperature for the CO and ^{13}CO J=1-0 lines) were subsequently measured and are listed in table 2.1. It is then a simple matter to calculate the optical depth in the 2-1 and 1-0 lines of ^{13}CO at specific

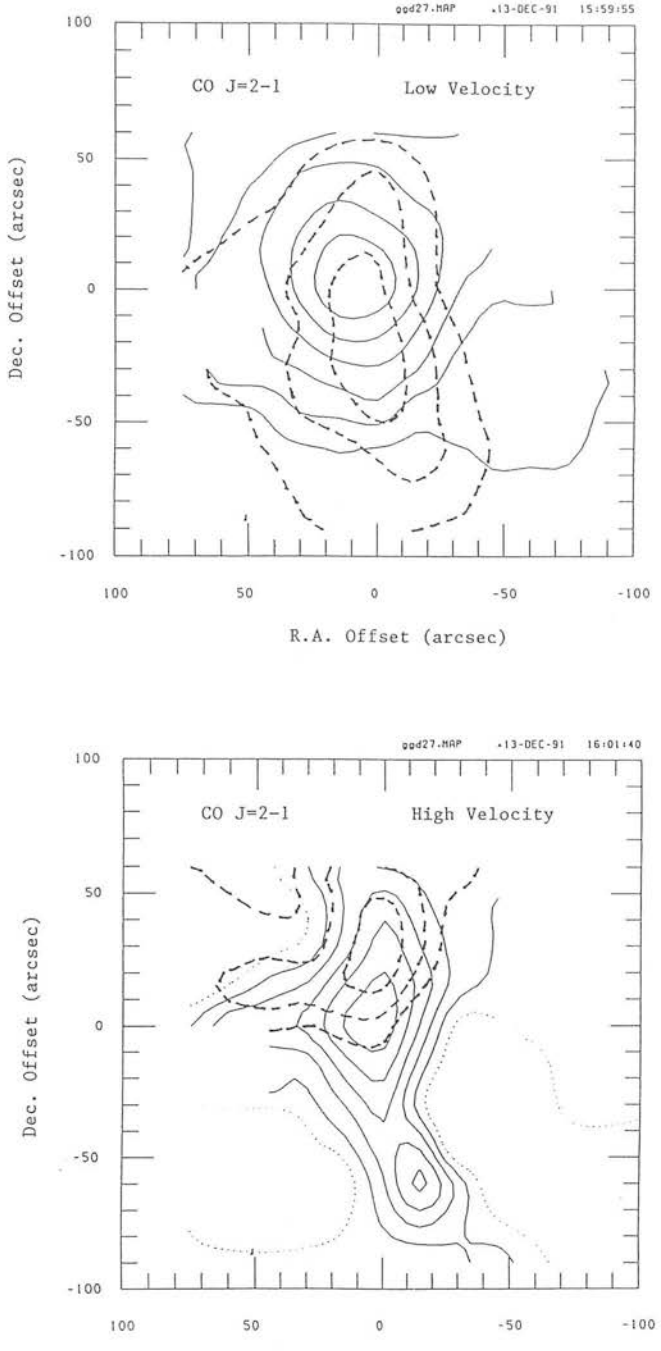

Figure 2.4: Contour plots showing the angular distribution of the *a)* low-velocity CO wing emission; blue component filled (6 – 10.5 km s^{-1}) and red dashed (14.5 – 19 km s^{-1}) and *b)* the high-velocity CO gas; again with the blue component filled (-12 – 6 km s^{-1}) and the red dashed (19 – 37 km s^{-1}). In *a)* the contours increase from 10 K km s^{-1} in steps of 10 K km s^{-1}; in *b)* the contour interval is 3 K km s^{-1} from a base level of 0 K km s^{-1}. Map centre as for figure 2.1.

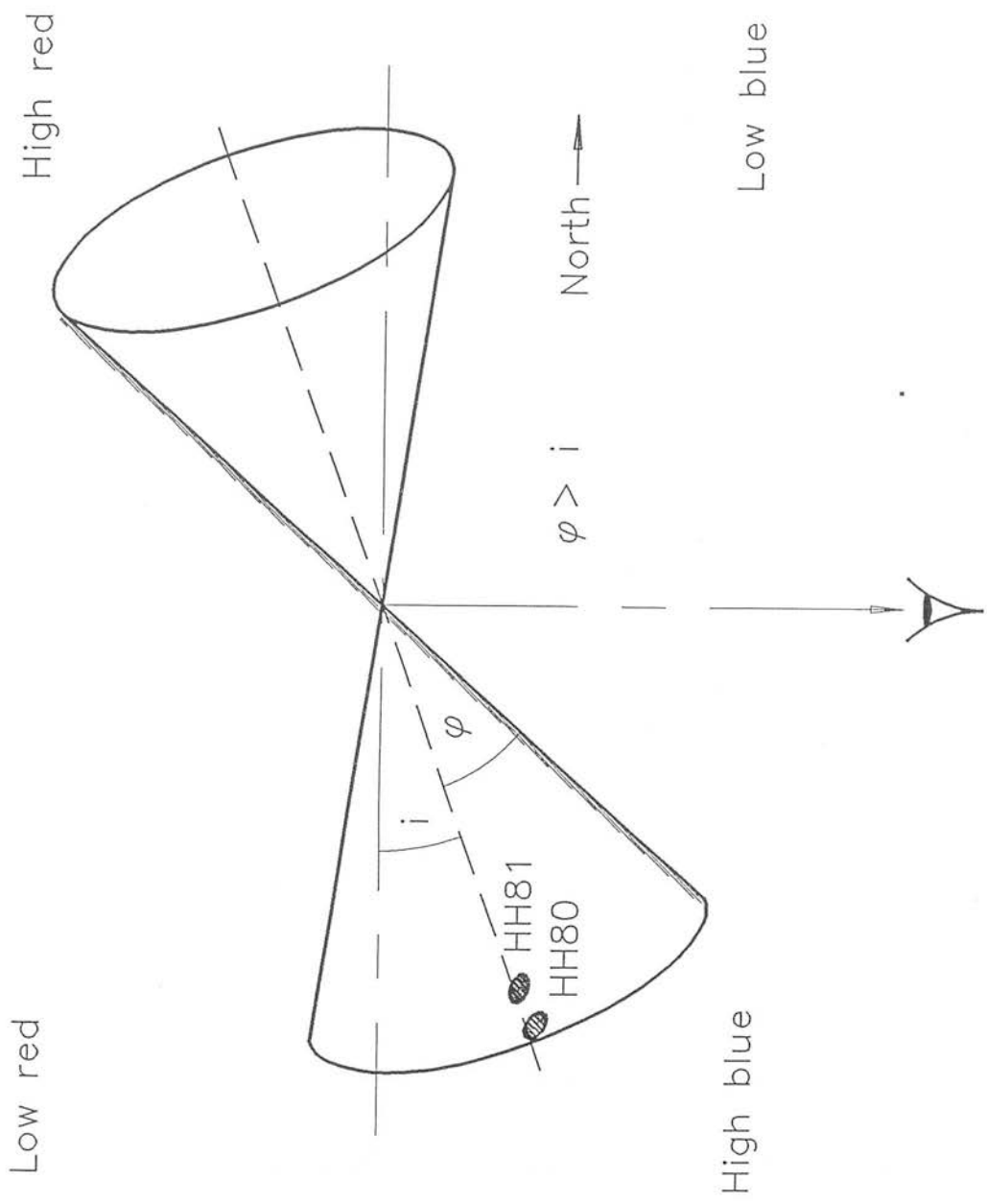

Figure 2.5: An outflow geometry that would account for the contour plots in figure 2.4

velocities in the low velocity blue (6 to 10.5 km s^{-1}) and red (14.5 to 19 km s^{-1}) line wings via equation 1.18. These values are also listed in table 2.1 and are shown in figure 2.6.

Error bars have not been drawn on the points since the optical depth calculated in this way is subject to our choice of an isotopic abundance ratio. However, at low outflow velocities the error in the ratio of antenna temperatures due to the noise level and velocity resolution of the observations is judged to be $\sim$ 15%, though this error will increase with increasing velocity from line centre. Regardless, the optical depth in both 2-1 and 1-0 line-wings exhibits a smooth decrease with increasing velocity from line centre. The ^{13}CO emission is clearly optically thin at all velocities sampled.

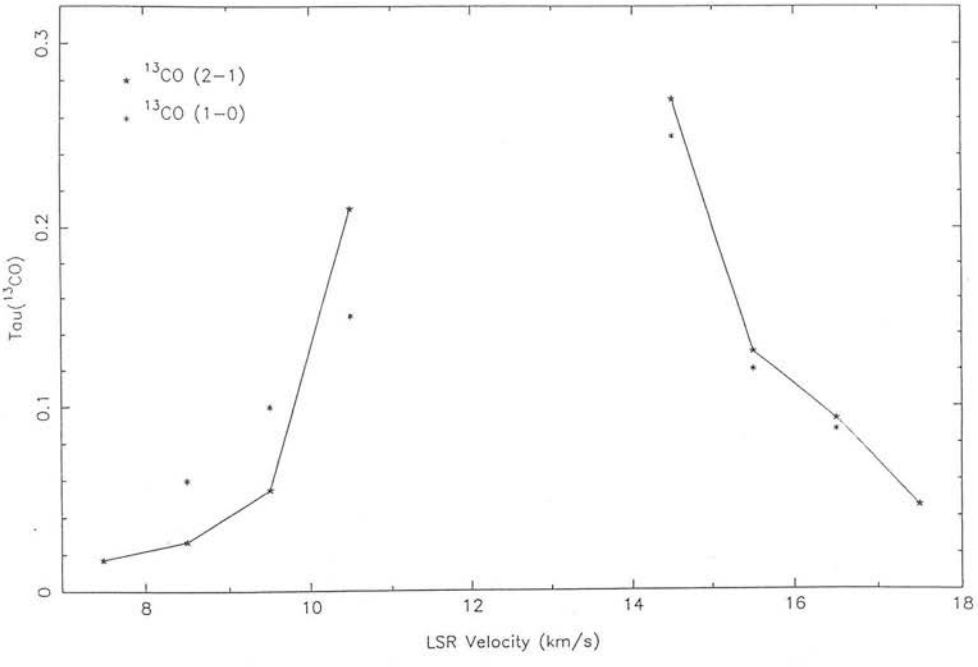

Figure 2.6: The ^{13}CO optical depth in the J=2-1 and 1-0 (Yamashita *et al.* 1989) line wings.

The *average* optical depths of the low-velocity gas can also be estimated, from the ratio of *integrated* intensities over the velocity intervals defined above. Further, since we have observed a grid of 25 ^{13}CO spectra around the source (figure 2.2) we may calculate these average optical depths at different positions in the flow. The plots in figure 2.7

Table 2.1: ^{13}CO Optical depth at various velocities in the 2-1 and 1-0 line wings. The 1-0 observations are taken from Yamashita *et al.* (1989), where $T_{mb} = T_A^*/\eta_b$.

	V_{LSR} (km s^{-1})	T_A^*(CO) (2-1)	$T_A^*(^{13}CO)$ (2-1)	$\tau_{13}(2-1)$
Blue wing	10.5	34	6.5	0.21
	9.5	28	1.5	0.055
	8.5	17	0.5	0.027
	7.5	11.5	0.25	0.017
	6.5	8.0	<0.25	<0.03
Red wing	14.5	23	5.5	0.27
	15.5	16.5	2.0	0.13
	16.5	9.0	0.8	0.093
	17.5	5.5	0.25	0.046
	18.5	3.5	<0.25	<0.074

	V_{LSR} (km s^{-1})	T_{mb}(CO) (1-0)	$T_{mb}(^{13}CO)$ (1-0)	$\tau_{13}(1-0)$
Blue wing	10.5	28.0	4.0	0.15
	9.5	15.5	1.6	0.10
	8.5	8.5	0.5	0.06
	7.5	4.5	<0.5	<0.12
	6.5	2.5	–	–
Red wing	14.5	20	4.5	0.25
	15.5	13	1.5	0.12
	16.5	6	0.5	0.087
	17.5	2.5	<0.5	< 0.22
	18.5	1.0	–	–

show the variation in τ_{13} along and perpendicular to the outflow; in a north-south and east-west direction.

From the top figure; the optical depth of the blue wing emission in an east-west direction across the source shows little variation, though notably the optical depth in the red-shifted gas increases markedly towards and to the west of GGD27 IRS. This latter increase may be due to an intervening molecular clump at the same LSR velocity. From the bottom figure; as one might expect, the optical depth in the low velocity red-shifted gas increases to the south of the source, where we see the red-shifted lobe in the contour plot of figure 2.4*a*. Similarly, to the north, towards the blue-shifted outflow lobe, the blue-wing optical depth increases.

Finally, the CO 2-1 wing emission beyond this low-velocity component (from the *high*-velocity outflowing gas), traced *only* in CO 2-1 (figure 2.3), is assumed to be optically thin in my later estimate of the high-velocity outflow mass, since no ^{13}CO wing emission is detected here. This assumption does not seem unreasonable; the opacity in the low-velocity blue and red wings in ^{13}CO 2-1 clearly decreases with increasing outflow velocity (figure 2.6). Because $\tau_{12}/\tau_{13} = 89$, we may therefore be certain that $\tau_{12} \ll 1.5$ and 4 in the high-velocity CO 2-1 blue and red line wings.

2.3.3 The Excitation Temperature

I shall later use the ^{13}CO J=2-1 observations to calculate the mass of the low-velocity outflow because the emission suffers less than the CO 2-1 from optical depth effects. However, we still require an estimate of the excitation temperature in the ^{13}CO line wings. Indeed, the equation used below (equation 2.1) to calculate the ^{13}CO column density is strongly dependent upon our choice of T_{ex}. As we now however have ^{13}CO J=2-1 observations to complement the 1-0 spectra of Yamashita *et al.* (1989) we may calculate T_{ex} at different velocities in both the blue and red ^{13}CO line wings (as was previously done for the opacity).

One may calculate the excitation temperature in the line wings from a ratio of ^{13}CO optical depths (the equation relating τ_{13} to T_{ex} is derived from the equation for the absorption coefficient, κ_ν, equation A.2., applied to the 2-1 and 1-0 transitions;

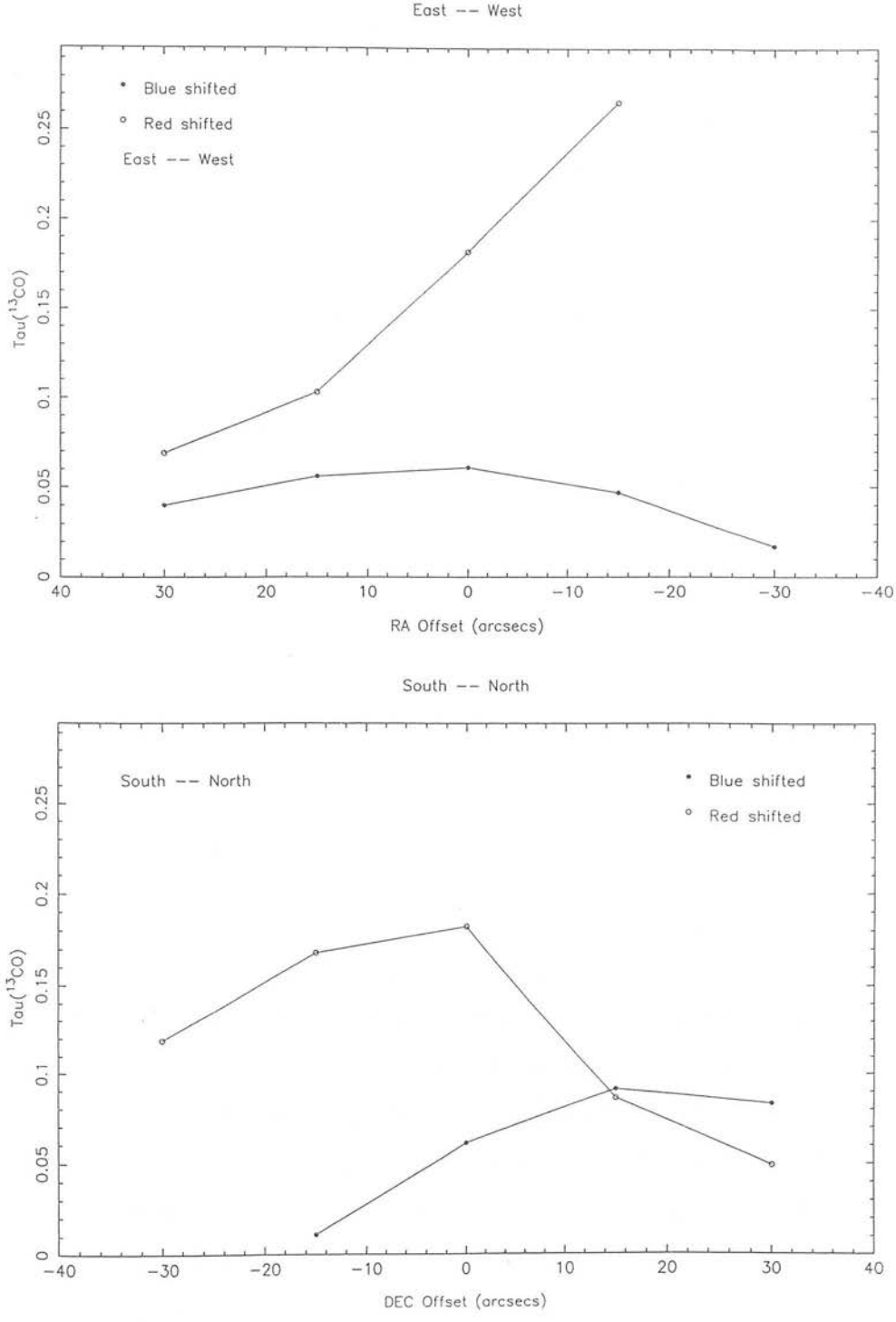

Figure 2.7: Plots showing the variation in the *mean* ^{13}CO 2-1 optical depth in the low-velocity gas; *(top)* in an east-west direction across the source, and *(bottom)* along the outflow.

Margulis & Lada 1985). However, estimates of T_{ex} obtained in this way for the outflow from GGD27 IRS are found to be below 10K. These values are considerably lower than the observed antenna temperatures in the CO line wings, and so are unphysical. Clearly, one or more of the assumptions listed above is breaking down: Either the true isotopic abundance ratio is substantially less than 89 or the CO and ^{13}CO emission (used to calculate τ) does not derive from the *same* gas. Fortunately, we may calculate the excitation temperature in the low-velocity outflow gas without having to make this latter assumption, or without having prior knowledge of the C/^{13}C ratio. We may estimate T_{ex} solely from the ^{13}CO observations.

Having already established that the ^{13}CO emission is optically thin in the line wings, then *in this limit*, the brightness of the emission in the outflowing gas (in Joules m^{-2} s^{-1} sterad.$^{-1}$ Hz^{-1}) is proportional to the energy per unit bandwidth produced by spontaneous emission (Goldsmith 1972). i.e.

$$\begin{aligned} I_\nu &= \frac{A_{ji} n_j h\nu_{ji}}{4\pi\Delta\nu\kappa_\nu}(1-\exp(-\kappa_\nu L)) \\ &\simeq \frac{A_{ji} n_j h\nu_{ji} L}{4\pi\Delta\nu} \end{aligned}$$

where n_j is the population of the jth rotational state, A_{ji} is the Einstein coefficient for spontaneous emission, κ_ν the absorption coefficient, $\Delta\nu$ the line width (in Hz) and L the length (Scoville & Solomon 1974, Martin & Barrett 1978). Replacing $(\nu/\Delta\nu)$ with $(c/\Delta v)$, where Δv is the doppler broadened velocity spread of the molecules, leads to $I_\nu(thin) \propto A_{ji} n_j$, and since I_ν is related to the observed antenna temperature via equations 1.13 and 1.17, then $T_A^*(thin) \propto A_{ji} n_j \nu_{ji}^{-2}$ (note that $I_\nu(T_{bg})$ is assumed to be negligable). Thus, at any given velocity in the ^{13}CO line wings, the ratio of the 2-1 to 1-0 antenna temperatures is related to the relative populations of the $J = 2$ and $J = 1$ levels and, assuming LTE, the excitation temperature for the 2-1 transition. Substituting for n_2/n_1 (via the Boltzman equation) gives

$$\frac{T_{mb}(2-1)}{T_{mb}(1-0)} = \frac{g_2 A_{21}\nu_{10}^2}{g_1 A_{10}\nu_{21}^2}\exp\left(\frac{-h\nu_{21}}{kT_{ex}}\right)$$

$$= 4.0 \exp\left(\frac{-h\nu_{21}}{kT_{ex}}\right)$$

Here g_2 and g_1 are the statistical weights ($g_j = 2j + 1$) and $A_{ji} \propto |\mu_{ji}|^2 \nu_{ji}^3$; the dipole matrix element is related to the dipole moment μ by $|\mu_{ji}|^2 = \mu^2(i+1)/[2i+3]$ where j is the upper rotational state (Townes & Schawlow 1975).

From the single ^{13}CO J=1-0 spectrum observed towards GGD27 IRS (Yamashita *et al.* 1989) and the ^{13}CO J=2-1 line observed in the same position (figure 2.3) we may therefore calculate T_{ex} at specific velocities in the ^{13}CO line wings (table 2.2).

Table 2.2: The ^{13}CO excitation temperature at various velocities in the line wings.
[a] $T_{mb} = T_A^*/\eta_b$, where $\eta_b = 0.65$ for the JCMT.
[b] from Yamashita *et al.* (1989).

	V_{LSR} (km s^{-1})	[a] $T_{mb}(^{13}CO)$ (2-1)	[b] $T_{mb}(^{13}CO)$ (1-0)	T_{ex} (K)
Blue wing	10.5	10.0	4.0	23
	9.5	2.3	1.6	10
	8.5	0.77	0.5	11
	7.5	0.38	<0.5	>6
Red wing	14.5	8.5	4.5	14
	15.5	3.1	1.5	16
	16.5	1.2	0.5	21
	16.5	0.77	<0.5	>6

Although the excitation temperatures derived in this way are greater than the previous estimations of <10K, they are still notably lower than the T_{ex} = 40K used by

Yamashita *et al.* (1989) in their calculation of the GGD27 IRS outflow mass and energetics, and (of more concern) also still lower than the observed main beam brightness temperatures ($T_{mb} = T_A^*/0.65$) in the CO line wings. This latter discrepancy may be due to beam filling factors which are less than unity and subsequently not equal for the 2-1 and 1-0 observations.

Although in calculating T_{ex} it has not been necessary to accept assumptions *ii)* and *iii)* above, we have never-the-less assumed that the beam filling factors for the ^{13}CO 2-1 and 1-0 observations are the same. The J=1-0 observations of Yamashita *et al.* (1989) were conducted with a 16 arcsecond beam, the 2-1 observations with a 22 arcsecond beam. Thus, if the outflow gas, traced in ^{13}CO, is clumpy and confined to an outflow width smaller than the 1-0 beam, then the 2-1 observations will suffer from a greater degree of beam dilution than will the 1-0 studies. The confinement of the flow near to the source by a circumstellar dust disk or molecular toroid (Rodriguez 1987), to scales of less than 0.1 pc, $\sim$ 10 arcseconds at 1.7 kpc, would produce this. Indeed, multiplying the ratio of main beam brightness temperatures $T_{mb}(2-1)/T_{mb}(1-0)$ by the ratio of telescope beam solid angles $= \theta_{21}^2/\theta_{10}^2 = 1.89$ does increase our estimates of T_{ex} to values of the order of 100K. However, this correction is not made here for two reasons. Firstly, the outflow appears to be extended in both CO 2-1 and 1-0 contour maps, and secondly, the plots in figure 2.7 show no evidence for a decrease in the mean optical depth in the ^{13}CO line wings (in the outflow gas) over a distance of $\sim 60\widehat{''}$ from east to west of the source.

Furthermore, if the CO and ^{13}CO emission does indeed derive from different gas components — the CO emission may come from warmer, more diffuse gas whilst the more optically thin ^{13}CO emission may be produced in cooler clumps or filaments within the flow — then this would serve to increase the T_A^* in the CO line wings relative to the ^{13}CO wing emission. The excitation temperatures derived here would then be *correct* for the ^{13}CO line wings.

2.3.4 The Mass of the Molecular Outflow

Having therefore established the optical depths and excitation temperatures in the ^{13}CO line-wings, we may go on to estimate the mass and energetics of the outflow.

The mass of the gas in the low-velocity red and blue wings is calculated from the ^{13}CO opacity (appendix A): Assuming thermalised level populations, we may derive an expression for the total column density of ^{13}CO (from equation A.9);

$$N_{13CO} = 1.20 \times 10^{14} \frac{T_{ex} \exp(5.29/T_{ex})}{[1 - \exp(-10.57/T_{ex})]} \tau_{13} \, \delta v \qquad (2.1)$$

Here the column density is in particles cm^{-2} and δv is the width of the low-velocity line wing in km s^{-1}. The above applies to the J=2-1 line only. I shall assume that the excitation temperatures and optical depths derived above (towards the source) apply to the entire outflow (note that we did not map the whole outflow, as illustrated by the CO 1-0 observations of Yamashita *et al.* 1989); the optical depths in the red and blue-shifted ^{13}CO calculated from the central spectrum are thus used to find N_{13CO}.

Since I have calculated optical depths and excitation temperatures at 1 km s^{-1} intervals in the low-velocity line wings, listed in tables 2.1 and 2.2, we may also calculate the column density, $N_{13CO}(v)$, per 1 km s^{-1} velocity-slice: Equation 2.1 gives values for $N_{13CO}(v)$, with δv = 1km s^{-1}. The *total* column density of ^{13}CO towards the source at all velocities in the low-velocity outflow is then obtained by summing these values; $N_{13CO} = \sum N_{13CO}(v)$. We may convert N_{13CO} to an H_2 column density, N_{H2}, using a ratio [^{13}CO]/[H_2] $\sim 1.1 \times 10^{-6}$ (Irvine & Knacke 1988). The mass of the low-velocity outflow is then found by multiplying N_{H2} by $\beta = 1.3 \times Area \times m_{H2}$, where m_{H2} is the mass of an H_2 molecule and 1.3 takes into account the mass contribution of Helium at 10% by number.

The area of each low-velocity outflow lobe is taken from figure 2.4*a*; the extent of the blue lobe measured from the FWHM of the observed peak is approximately ($105\widehat{''} \times 100\widehat{''}$), at 1.7 kpc a total area of 6.4 $\times$ 10^{36}cm^2. For the red lobe the area is ($130\widehat{''} \times 80\widehat{''}$), at the same distance a total area of 4.8 $\times$ 10^{36}cm^2. I therefore estimate masses for the low-velocity blue (6 to 10.5km s^{-1}) and red-shifted (14.5 to 19 km s^{-1}) outflow gas of 30 $M_\odot$ and 31 $M_\odot$ respectively.

We should also consider the outflow mass contained in the CO wings below 6 km s^{-1} and above 19 km s^{-1}. Since only the CO J=2-1 wing emission is detected at these

high outflow velocities, the mass of this component is obtained from the integrated line intensity in these high velocity CO wings; we must assume the emission is thermalised and optically thin. Since we have no direct way of measuring T_{ex}, the mean value of T_{ex} in each low-velocity outflow lobe is used here; from table 2.2, T_{ex}(blue) = 15K, T_{ex}(red) = 17K. From appendix A., the CO column density in the line wings may be calculated from;

$$N_{CO} = 1.15 \times 10^{14} \frac{\exp(5.53/T_{ex})}{[1 - \exp(-11.06/T_{ex})} \int T_b.dv \qquad (2.2)$$

The beam filling factor is assumed to be unity, though note that ultimately this assumption will not affect the outflow mass estimate. Again the mass of each high-velocity outflow lobe, illustrated in figure 2.4b, is calculated by multiplying the column density in each high-velocity CO line wing by the extent of the flow. I therefore estimate masses of 0.3 $M_\odot$ and 0.03 $M_\odot$ for the high-velocity blue (6 to -12 km s^{-1}) and red-shifted (19 to 37 km s^{-1}) outflow components.

The total mass of the outflow, some 60 $M_\odot$, is in accordance with other intermediate-to-high mass outflows (listed here in table 1.1, and also in Lada 1985, Bally & Lada 1983), though it is considerably lower than the value derived by Yamashita *et al.* (1989) for the outflow from GGD27 IRS. From their CO 1-0 observations they calculate a total outflow mass of 460 $M_\odot$.

The outflow mass derived above from the CO 2-1 data should be regarded as an underestimate for two reasons:
i) I have not taken into account orientation effects: For outflows which lie in (or near to) the plane of the sky, the emission from the outflowing material which has a radial velocity (V_{LSR}) equal to that of the ambient cloud will be covered by the ambient gas component in each line profile (see figure 2.3). Thus, this low *radial* velocity gas will not contribute to the brightness of the line wings, nor to the final mass estimate.
ii) I have only mapped the central portion of the outflow ($\sim$ the central 3 arcminutes). The CO 1-0 outflow mapped by Yamashita *et al.* (1989) extends over approximately 4 arcminutes ($\sim$ 2pc) and so encompasses a larger area (this of course will serve to increase their mass estimate by a factor of a few).

However, these uncertainties do not account for the factor of 10 difference between the mass derived here (from both the CO 2-1 and 1-0 observations) and Yamashita *et al.*'s earlier mass estimate (from only 1-0 observations). Yamashita *et al.* were unable to measure T_{ex} accurately but instead obtained T_{ex} from the peak line brightness temperature. Consequently their outflow mass is *overestimated.*

The use of a higher value of T_{ex} here would similarly enhance the mass estimate: If we use a value of $T_{ex} = 56$K, taken from the peak main-beam brightness temperature of the spectrum in figure 2.3 (and via equation 1.16, assuming $\eta_f = 1$ and with $\tau_{12}(2-1) = \tau_{13}(2-1) \times 89 = 18.7$ at 10.5 km s^{-1}) and use this value for all velocities in the low-velocity line wings, then our 2-1 mass estimate (for the low-velocity outflow component) is much larger; Mass $\sim 180\,M_\odot$ (blue) and $\sim 240\,M_\odot$ (red). These masses are certainly comparable to Yamashita *et al.*'s estimates; as one would expect since this was the method employed by Yamshita *et al.* to calculate T_{ex} from their CO 1-0 observations.

The above treatment thus clearly illustrates the importance of measuring T_{ex} accurately before calculating outflow masses.

2.3.5 The Momentum and Kinetic Energy of the Outflow

The momentum and energy of the outflow gas is also dependent on the orientation of the outflow in space, though actually more so, since we have only measured the radial component of the gas velocity. There is therefore an inherent uncertainty of at least a factor of a few in any estimate of the momentum or energy.

The momentum and kinetic energy at each position in the outflow may be obtained from $\int T_b v.dv/cos\theta$ and $\int T_b v^2.dv/cos^2\theta$, where θ is the angle between the flow axis and the line of sight and the integral is taken over the low-velocity and high-velocity wing components respectively. The total momentum and energy is then obtained by summing the contributions of all points in the outflow. However, since we did not map the entire outflow, we may only calculate the momentum and kinetic energy for the area covered by the CO and ^{13}CO plots of figure 2.3 — i.e. towards the source position,

and then multiply these values by the observed area of the outflow. We must of course also assume that the momentum and kinetic energy remain constant along the flow.

The optical depth in the low-velocity ^{13}CO line wings has been measured to be less than unity. We may therefore express the ^{13}CO column density in terms of the integrated wing brightness temperature. From equation 2.1;

$$N_{13CO} = 1.20 \times 10^{14} \frac{\exp(5.29/T_{ex})}{[1 - \exp(-10.57/T_{ex})} \int T_b.dv \tag{2.3}$$

Replacing $\int T_b.dv$ by $\int T_b v.dv/cos\theta$ and $\int T_b v^2.dv/cos^2\theta$ in equations 2.2 and 2.3 gives equations for the momentum M and energy E, per unit surface area in the flow (cm^{-2}), in both the low-velocity ^{13}CO line wings and the high-velocity CO line wings. The mean values of T_{ex} in the blue and red lobes are used here. Unfortunately we do not know θ; Yamashita *et al.* (1989) think that the flow lies within a few degrees of the sky, though the overlap in the blue and red lobes observed here in CO J=2-1 (figure 2.4) implies a greater angle. Because of my interpretation of the outflow structure (section 2.3.1 and figure 2.5), I use $\theta = 60^o$. As before, the total momentum and kinetic energy is then found by multiplying M and E by $\beta = 1.3 \times Area \times m_{H2}$. The derived outflow parameters are listed in table 2.3.

2.3.6 Momentum and Energy Rates

An estimate of the mean velocity of the gas $< V >$, weighted by mass, may also be determined for each outflow component from the ratio of the momentum to the mass. Also, a measure of the length of each flow lobe leads to an estimate of the dynamical time scale, $\tau_d =< R > / < V >$, though this timescale is subject to a large degree of uncertainty since it is derived from a size parallel to the plane of the sky and a velocity perpendicular to it. Therefore, we may only make here very rough estimates of τ_d and subsequently the momentum flux (momentum/τ_d) and the mechanical luminosity

Table 2.3: Physical parameters of the bipolar flow.

	Mass ($M_\odot$)	Momentum ($M_\odot$ km s^{-1})	Energy ($\times 10^{39}$ J)
LV_{blue}	30	112	1.5
LV_{red}	31	63	0.8
HV_{blue}	0.3	10	0.4
HV_{red}	0.03	0.6	0.02

(energy/τ_d) for the low and high-velocity outflow components. These values are listed in table 2.4.

Although the mass and extent of the outflow is consistent with that derived for other sources of similar luminosities (Lada 1985), the momentum flux and mechanical luminosity of the flow is roughly a factor of 10 less. This is due to the large dynamical time scale derived here for the flow from GGD27 IRS. Together with the relatively large outflow mass, these factors imply an evolved nature for the outflow.

At an assumed distance of 1.7kpc, the absolute luminosity of GGD27 IRS is $\sim 20,000\,L_\odot$ (Rodriguez *et al.* 1980). We may therefore compare the momentum flux and mechanical luminosity with the momentum flux of the stellar photons (L_*/c) and the stellar luminosity (L_*); I find that the ratio of L_M/L_* is of the order 10^{-5} and the ratio $\dot{M}V/(L_*/c)$ is greater than unity. Thus, only a fraction of the luminosity of the central source is transported to the molecular material, but the momentum in the gas

Table 2.4: Additional Outflow Parameters.

	$< V >$ (km s^{-1})	$< R >$ (pc)	τ_d (yrs)	$\dot{M}V$ (M$_\odot$ yr^{-1} km s^{-1})	L_M (L$_\odot$)
LV_{blue}	3.7	0.9	2.3×10^5	4.8×10^{-4}	0.6
LV_{red}	1.5	1.1	7.0×10^5	0.8×10^{-4}	0.1
HV_{blue}	23	1.1	4.5×10^4	2.3×10^{-4}	0.8
HV_{red}	53	0.5	0.9×10^4	0.6×10^{-4}	0.2

at best equals (though probably exceeds, since our mass estimate is a lower limit) the momentum which can be provided by the photons. As previously discussed in chapter 1, it seems unlikely that the outflow could be driven by radiation pressure from the central star.

2.3.7 Are HH80-81 Driven by the Molecular Outflow?

There is certainly compelling evidence that HH80 and HH81 are excited by a stellar wind from GGD27 IRS; the 6cm radio continuum peaks towards GGD27 IRS and both HH objects are plainly extended along the outflow direction and proper motion studies imply that both HH nebulae are moving radially away from the source. However, there is little indication here that the HHs are powered by the molecular outflow: No high *or* low-velocity CO wing emission is detected beyond $\sim$ 100 arcseconds from the source; by approximately half the distance to HH80 and HH81 the integrated intensity contours in figure 2.4 (and so the mass of outflowing gas) have decreased to roughly 1/10th of that measured towards the source. Assuming a constant outflow velocity, then the mechanical luminosity of the outflow that reaches HH80/81 is at best 0.1 L$_\odot$ (from table 2.4). However, from optical and radio studies of HH80/81, Reipurth (1989) estimates

that HH80 and 81 are more luminous than HH1 and 2 by a factor of ~10; the total luminosity of HH1/2 is judged to be $\sim 1\,L_{\odot}$ (Strom *et al.* 1985). Thus, the energy supply rate of the molecular outflow from GGD27 IRS is insufficient to power HH80/81 by a factor of at least 100. Instead, it seems more likely that these HH nebulae are driven by an "invisible" stellar wind component.

2.4 CONCLUSIONS

The detection of high-velocity line-wing emission in CO 2-1 confirms the presence of a molecular outflow from the infrared reflection nebula GGD27 IRS. Moreover, these sensitive observations imply that half the opening angle of the flow is greater than the angle between the plane of the sky and the flow axis; this results in overlapping low and high-velocity blue and red-shifted lobes in contour plots of the outflowing gas.

I have derived the mass and energetics of the outflow; mass $\sim 60\,M_{\odot}$, momentum $\sim 185\,M_{\odot}$ km s^{-1} and energy $\sim 3 \times 10^{39}$ J. These estimates are consistent with values derived for other outflows from similarly luminous sources (Lada 1985), though they are roughly a factor of 10 below values derived by Yamashita *et al.* (1989) from his CO J=1-0 observations. This difference results from the contrasting methods of calculation, particularly because T_{ex} has been calculated more accurately here. Indeed, comparison of the 2-1 and 1-0 observations underlines the importance of adopting as few assumptions as possible when calculating accurate outflow masses and energetics.

Finally, the molecular outflow from GGD27 IRS is not sufficiently powerful to drive the bright HH nebulae, HH80/81, though the radio continuum observations and the proper motion studies discussed above imply an association.

Chapter 3

Herbig-Haro 1/2

SUMMARY: In an attempt to study the molecular environment associated with HH objects, and in particular search for molecular clumping in HHs, observations at cm, mm and sub-mm wavelengths have been made towards a number of outflows with known HHs. The following chapter discusses the results obtained for HH1 and 2. Notably, a quiescent, dense, stationary clump is seen ahead of (south-east of) the advancing optical knots that comprise HH2. This molecular peak is further identified in NH_3 channel maps at the same radial LSR velocity, though peaks in the NH_3 *total* integrated intensity map are *not* found to be coincident with the HCO^+ clump, and additional mapping in $C^{18}O$ shows no clear peak at all. This lack of correlation between the spatial morphologies of each species is thought to be due to the differing excitation requirements of the transitions observed (though additional abundance variations cannot at this stage be ruled out): The HCO^+ (and NH_3 (1,1) channel maps) show a dense, quiescent clump ahead of HH2, whilst the distribution of $C^{18}O$ is more uniform, indicating a non-changing column density of gas over the area mapped. Therefore, in this case and probably in other HHs the sub-mm rotational emission lines of HCO^+ are the preferred tracers of dense clumping associated with optical HH objects.

3.1 INTRODUCTION

Herbig-Haro 1 and 2 are two of the brightest, most extended and consequently most heavily observed HH objects. Optical emission lines from both HH nebulae arise from hot, dense gas, intimated by the wide line profiles (FWHM $\geq$ 50 km s^{-1}) and relative strengths of forbidden lines ([SII], [NII], [OIII]) to hydrogen recombination lines (Hartmann & Raymond 1984, Böhm & Solf 1985). H_2 ro-vibrational emission lines are similarly wide (FWHM $\sim$ 40 km s^{-1}; Zinnecker *et al.* 1989) and proper motion studies of both HHs attribute velocities of between 150 and 350 km s^{-1} to the individual HH condensations (Herbig & Jones 1981).

Data illustrating the molecular outflow that is presumably linked to HH2 (and HH1) has yet to be published, though deep R-band CCD frames indicate the presence of a jet-like feature extending towards HH1 (the blue-shifted half of the HH1-2 system, Strom et al. 1985). Here I show a polaroid taken from a UK Schmidt Red plate (plate no. OR 14052), figure 3.1.

R-band and Radio-interferometric (2, 6, 20cm) imaging also illustrates the clumpiness of each HH nebula , with clump sizes <5 arcseconds (Raga, Barnes & Mateo 1988, Rodriguez *et al.* 1990). The radio continuum observations have further identified the embedded source that probably powers HH1-2 (Pravdo *et al.* 1985). Known as VLA1, Strom *et al.* (1985) have estimated an A_v of between 20 and 90 towards the source, whilst a number of other authors have identified the obscuring structure, apparently disk-like, via ammonia observations (Marcaide *et al.* 1988, Martin-Pintado & Cernicharo 1987).

3.1.1 The Molecular Structure of HH Objects

Up until quite recently, studies of HH objects have been conducted at optical and, to a lesser extent, near-IR wavelengths. HH models have thus been based solely on observations of the hot, shocked HH gas, with little knowledge of the pre-shock molecular cloud environment. However, with the advent of mm and sub-mm astronomy we are now able to observe not only the HH shock-front but also emission from the cool, precursor gas in HH objects, and so obtain a complete picture of the physical and chemical nature of

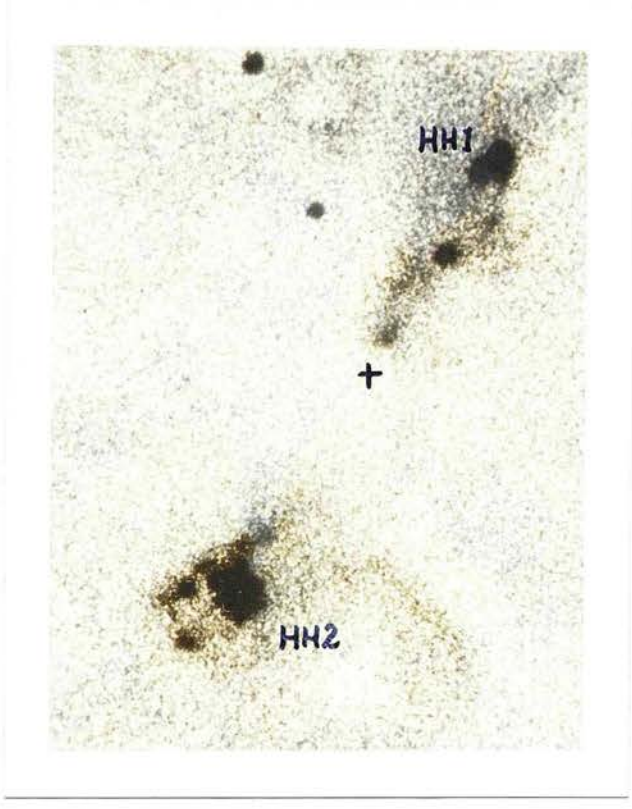

Figure 3.1: An R-band image of HH1-2. Image scale is 2 arcseconds/mm. VLA1 is marked by a cross.

HH objects.

To this end, Rudolph & Welch (1988) made pioneering millimeter-wave observations of the HCO^+ J=1-0 line emission from the HH7-11 system, and subsequently identified stationary, quiescent molecular peaks towards four of the five HH objects. They went on to interpret these results in terms of shocked, stationary molecular cloudlets or clumps within the molecular outflow. We have in turn made similar observations, though in the HCO^+ J=3-2 line, towards a small number of other sources. Although no detection was made for some of the objects studied, HCO^+ was observed in HH1 and HH2, and in the latter a similar cloudlet was mapped (Davis, Dent & Bell Burnell 1990, hereafter DDB). However, since there is a certain degree of controversy regarding the shock chemistry of HCO^+ (discussed in Ziurys *et al.* 1989) I hoped to further confirm the presence of molecular peaks in the HH1-2 system via observations in other molecular gas tracers. Consequently, I present here the original HCO^+ observations, plus additional studies in NH_3 and $C^{18}O$. I also present the first detection of the atomic carbon $^3P_1 - ^3P_0$ line at 492GHz from any HH object.

3.2 OBSERVATIONS

The observations discussed here were obtained using the James Clerk Maxwell 15m sub-mm telescope sited on Mauna Kea, Hawaii during October 1988 and again in January 1991. Additional work was conducted with the Max-Plank-Institut für Radioastronomie 100m radio telescope located at Effelsberg, Germany during December 1989 and with the NRO 45 meter telescope in Nobeyama, Japan during May 1990.

3.2.1 HCO^+

The HCO^+ J=3-2 line emission was measured using the RxA heterodyne receiver and a wide band acousto-optic spectrometer (bandwidth 500MHz with a resolution of 1.0 MHz or 1.1 km s^{-1}) on the JCMT. The HCO^+ J=3-2 rotational transition lies at 267.557GHz; the JCMT main beam HPBW measures $19\widehat{''}$ at this frequency and so mapping was conducted at $15\widehat{''}$ spacings (at 460pc, the distance to HH1-2, $15\widehat{''}$ ~0.04pc). The beam efficiency is 0.79, and typical SSB system temperatures were 800 – 1000K. 10 minutes integration was required for each spectrum.

3.2.2 NH_3

In Effelsberg we observed the NH_3 (1,1) and (2,2) inversion transitions simultaneously, each at approximately 23.7GHz (1.3cm), using the 18 – 26 GHz maser receiver and auto-correlating spectrometer split into two 512 channel wavebands. At these frequencies the HPBW measures 40 arcseconds. We observed initially with a spectral resolution of 48.8 kHz, though lat er this was reduced to 12.2 kHz (0.15km s^{-1}). T_{sys} ~50K throughout. In order to map the entire HH2 environment we restricted the on-source integration time for each point to only 2 minutes, the exception being the central map position (the HCO^+ peak position) where we integrated for a total of 4.5 minutes to improve the signal-to-noise. Chopping (30 arcminutes east) consisted of 2 or 3 on- followed by 1 off-source position. Pointing checks were made every few hours, and the error was generally restricted to < 10 arcseconds. The beam efficiency at 23GHz is 0.45.

3.2.3 CO

The $C^{18}O$ map was made during a second visit to the JCMT. The observations were again made with the heterodyne receiver (RxA) with a wide band acousto-optic spectrometer tuned to the $C^{18}O$ J=2-1 transition at 219.560GHz. Typically SSB system temperatures were ~ 1000 K. A resolution of 0.25MHz (0.3km s^{-1}) was maintained throughout. For the $C^{18}O$ mapping the telescope beam measured 23″. On-source integration times for all observations were generally 2-3 minutes. At 220GHz the JCMT beam efficiency is 0.61.

3.2.4 CI

The CI transition was observed using the new heterodyne receiver C on the JCMT. The IF bandwidth is limited to 1MHz so it is necessary to "sweep" the local oscillator frequency across the line to obtain a spectrum. However, both sidebands are utilised to give a 16 channel (2 MHz resolution) spectrum. The receiver temperature was typically 21,000 K total (for the 16 channels) and so an on-source integration time of 30 minutes was required. The CI beam measures ~ 10 arcseconds, and the beam efficiency at 492 GHz is 0.40.

3.2.5 Other Molecules

The HCO^+ J=1-0, HCN J=1-0 and CS J=2-1 observations were made at the NRO 45 meter telescope. The three lines, at 89.189, 88.632 and 97.981GHz respectively, were observed simultaneously, using the 80GHz Schottky receiver and the 100GHz SIS receiver with a polarization splitter, the 100GHz signal again being split into two sidebands to accommodate the HCN and HCO^+ lines. High spectral resolutions of 37kHz (0.13 km s^{-1}) were maintained throughout, whilst a total on- and off-source integration time of 30 minutes was required to achieve the desired signal to noise. Conditions remained good and so both the T_{sys} and the pointing were kept low at 450-550K and < 5 arcseconds respectively. At 90GHz the telescope HPBW is 19 arcseconds and the beam efficiency is 0.43. Data reduction was performed at the telescope using the LINEPROC facility.

Finally, the near-IR spectrum shown in figure 3.10 was obtained with service time on the UK Infra-Red Telescope Facility on Mauna Kea, using the 7-channel Cooled Grating Spectrometer CGS2. The grating was centred on two positions, the H_2 v=1-0S(1) and v=2-1S(1) ro-vibrational emission lines. The width of each channel on the grating measures $\sim 0.018\,\mu$m at $2\,\mu$m. To achieve a fully-sampled spectrum the grating is *twice* shifted by 1/3 of a channel width. On each occasion the emission is re-observed; thus a resolution of $\sim 0.006\,\mu$m is achieved. The UKIRT/CGS2 beam at $2\,\mu$m measures 5 arcseconds. 2 20 second co-adds were taken towards both positions.

All line intensities (excluding the near-IR observations) are in units of antenna temperature T_A^*; conversion to a brightness temperature T_b is carried out only when required, and is discussed within the text. All data reduction was done using the SPECX and PGPLOT software packages available on STARLINK.

3.3 HCO^+ RESULTS

We searched for HCO^+ in both HH1 and HH2, and obtained an additional spectrum towards the central continuum source, VLA1, now thought to be the exciting source of the HH1-2 system (Pravdo et al. 1985). Grid maps of the observed lines are shown in figure 3.2 and 3.3. The emission from HH1 was found to be relatively weak; lines were

detected towards only a few positions. Further observations, with a higher signal-to-noise are needed to establish clearly the HCO^+ distribution in HH1, though the observer should note that the emission appears to be strongest to the east of the optical and near-IR emission in HH1.

A far clearer picture was obtained for HH2: A compact clump of emission was mapped, the peak of which is situated $\sim 20 - 25\widehat{''}$ south-east of the optical knots that comprise the HH. Notably the HCO^+ emission decreases towards the optical and near-IR emission from HH2, sketched on to figure 3.3 as points and contours respectively.

All the plots obtained for HH1 and HH2 were averaged to give the top two spectra shown in figure 3.4. These plots thus represent the large-scale HCO^+ emission in the two HH regions. Also shown is the single spectrum recorded for VLA1. From these, the peak LSR radial velocities have been measured and recorded in table 3.1. A comparison is made there with the velocities of H_2 and various optical recombination lines. Additionally, table 3.2 shows the HCO^+ FWHM velocities.

Although the individual optical knots that comprise these HH objects possess a range of peak radial velocities, overall HH1 is regarded as being blue-shifted, and HH2 red-shifted, with respect to the observer (this is further supported by the presence of a faint jet-like structure extending towards HH1). The peak velocity shifts are however only a fraction of the proper motion velocities, so the outflow that presumably excites HH1 and 2 is thought to lie within 5-10^o of the plane of the sky (Hartigan *et al.* 1987). Hartmann & Raymond (1984) suggest that the overall blue-shift of the peak LSR velocities of the optical lines with respect to the ambient cloud velocity (observed in CO; Edwards & Snell 1984), shown in table 3.1, is due to the effects of extinction which favour the detection of optical knots on the side of each HH nearest the Earth.

The peak LSR HCO^+ velocities in HH1 and HH2 are within a few km s^{-1} of the ambient cloud velocity (as compared to the large velocity shifts in the optical and H_2 lines). In addition, the HCO^+ lines are much narrower than the H_2 and optical lines. The HCO^+ in HH1 and HH2 therefore seems to represent quiescent, stationary and so presumably pre-shock material; the spatial offset of the HCO^+ in HH2 further supports this scenario. For comparison, molecular studies of the shocked clouds associated with

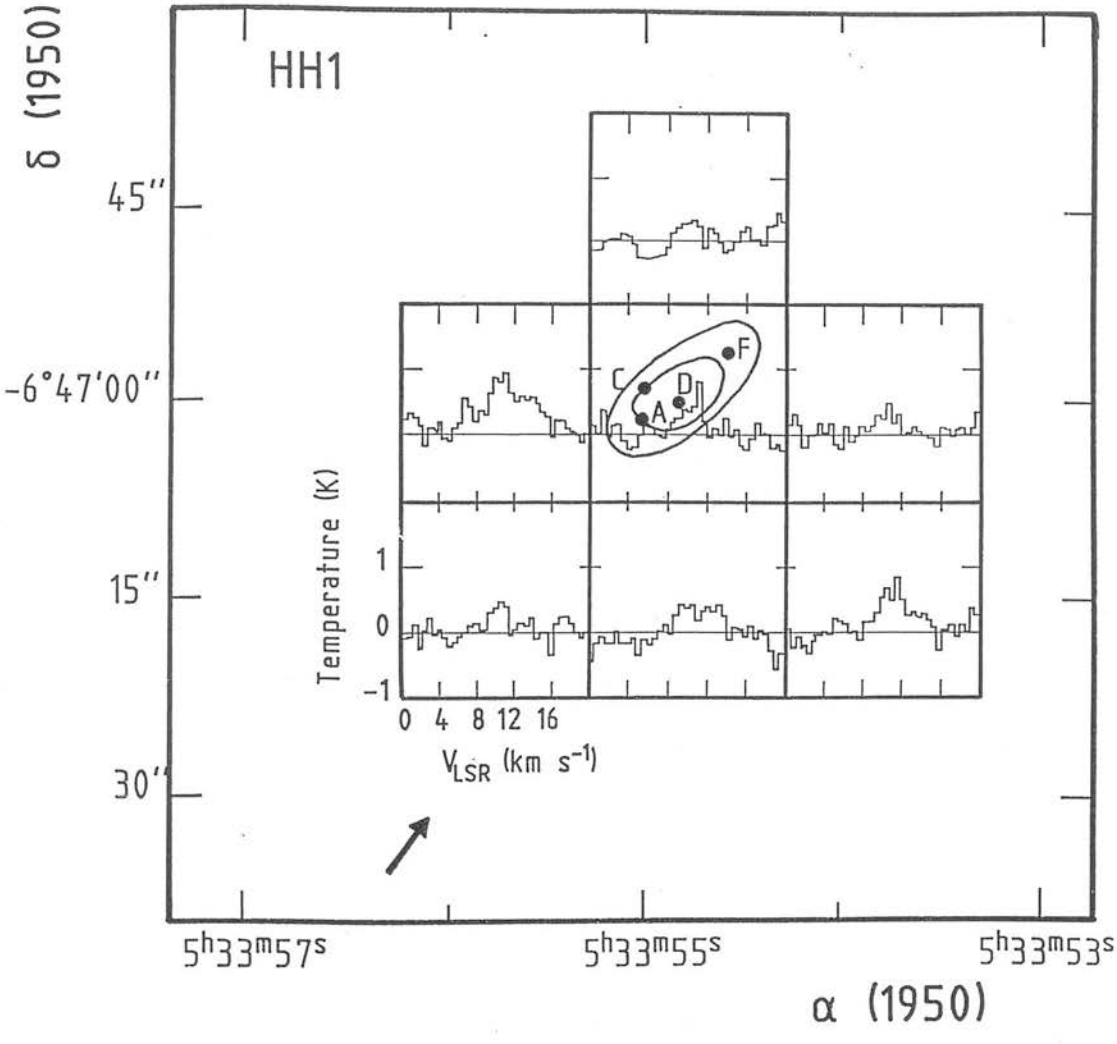

Figure 3.2: A grid map showing the distribution of HCO^+ J=3-2 in HH1. The points correspond to the peaks of optical emission and the contours to molecular hydrogen emission at 2.12 μm (from Harvey *et al.* 1986). The arrow shows the direction of the assumed outflow from the source, VLA1.

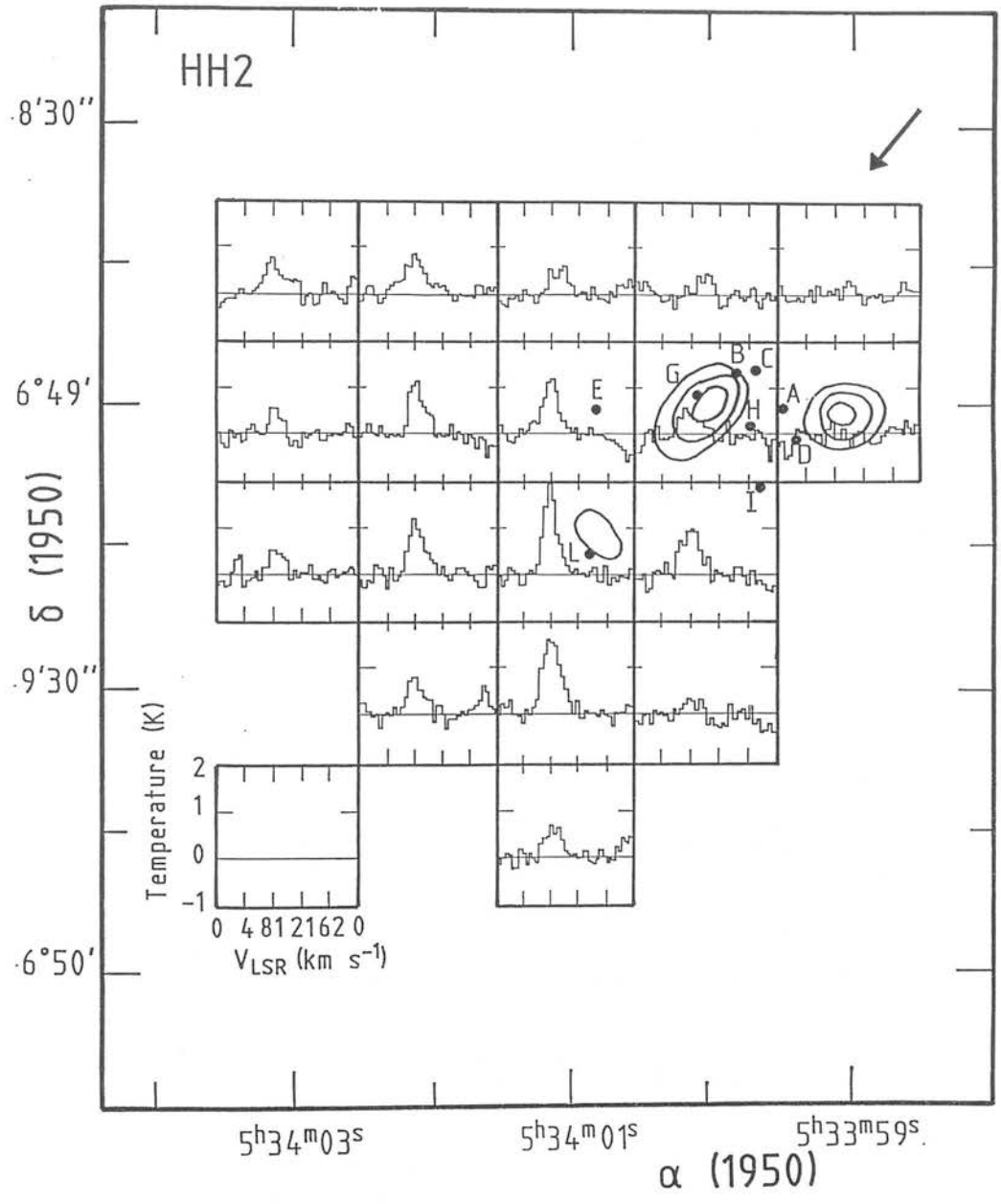

Figure 3.3: The HCO^+ J=3-2 observed in HH2. The points and contours are as for figure 3.2.

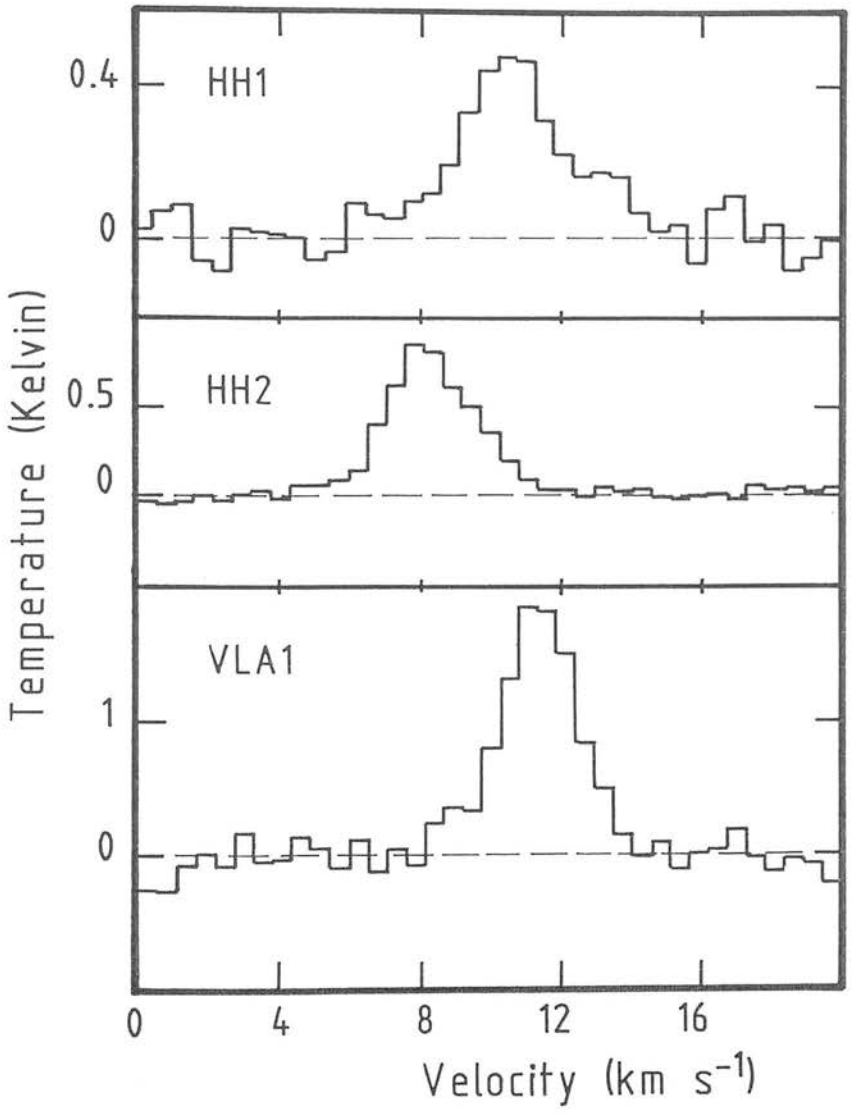

Figure 3.4: HCO^+ J=3-2 from HH1, HH2 and VLA1. The three spectra represent *a)* the average of the 7 spectra shown in the grid map of HH1, *b)* the average of the 18 spectra observed towards HH2, and *c)* the emission from VLA1.

the supernova remnant IC 443 measure HCO^+ line widths of $\sim 20 - 30$ km s^{-1} and line peak velocities shifted by $\sim$ 5-10 km s^{-1}.

Table 3.1: A comparison of peak LSR radial velocities for HH1,HH2 and VLA1. HH2 H_2 velocities correspond to the HH2A clump. Optical velocities have been converted from heliocentric values; all velocities are in km s^{-1}; References: a) Edwards & Snell 1983, b) Hartmann & Raymond 1984, c) Zinnecker et al. 1989.

Source	HCO^+ V_{LSR}	[a]CO V_{LSR}	[b]H_α V_{LSR}	[b][NII] V_{LSR}	[c]H_2 V_{LSR}
HH1	10.5	8.2	-24 to -3	-30 to -9	5
HH2	8.0	8.0	-30 to 13	-40 to 6	7
VLA1	11.0	8.0	–	–	–

3.3.1 Calculation of HCO^+ Column Densities and Source Masses

From the HCO^+ data we may calculate column densities, N_{HCO+}, and masses for the molecular features in HH1, HH2 and towards VLA1. From the calculations in appendix A, and using a dipole moment of 4.07 debyes (Cox et al. 1987) — which converts to an Einstein A coefficient of 2.23×10^{-3} s^{-1} for the J = 3–2 transition (Townes & Schawlow 1975), and by assuming optically thin emission and LTE, the following equation can be used to calculate the column density from each observed J=3-2 line (Dickman 1978):

$$N_{HCO+} = 1.79 \times 10^{11} \frac{\exp^{-12.8/T_{ex}}}{(1 - \exp^{-12.8/T_{ex}})} \int T_b.dv \qquad (3.1)$$

Table 3.2: A comparison of the FWHM line widths for HH1 and HH2. All line widths are in km s^{-1}; References: a) Hartmann & Raymond 1984, b) Zinnecker et al. 1989.

Source	HCO^+	$^aH_\alpha$	^{b}[NII]	$^bH_2$
HH1	2.6	40 to 90	32 – 79	38
HH2	4.8	48 to 125	65 – 99	44

We may also calculate the excitation temperature for the low-J levels in HCO^+ from the J=3-2 and J=1-0 (presented later; figure 3.11) lines observed towards the HCO^+ peak in HH2. Following section 2.3.3, T_{ex} is obtained from the ratio of main beam brightness temperatures.

$$\frac{T_{mb}(3-2)}{T_{mb}(1-0)} = 4.0 \exp\left(\frac{-\Delta E_{31}}{kT_{ex}}\right)$$

Where ΔE_{31} is the difference in energy between the J=3 and J=1 rotational levels. The emission is again assumed to be optically thin and T_{ex} is assumed to be the same for both transitions. Note also that the beam sizes for the 3-2 and 1-0 observations are the same; we may thus be confident that $\eta_f(1-0) = \eta_f(3-2)$. From figures 3.3 and 3.11 then, the ratio $T_{mb}(3-2)/T_{mb}(1-0)$ $(= [T_A^*(3-2)/T_A^*(1-0)] \times [\eta_b(1-0)/\eta_b(3-2)])$ leads to an excitation temperature of $T_{ex} = 9$K.

From the CO line temperatures recorded by Edwards & Snell (1983), molecular gas kinetic temperatures of 17K for HH1 and 16K for HH2 may be calculated (Evans 1980). Also, Martin-Pintado & Cernicharo (1987) measure a rotational temperature of 23K from their NH_3 observations of the HH1-2 region (this NH_3 rotational temperature is assumed to be a lower limit for the gas kinetic temperature). If in HH1 and HH2 the CO and NH_3 is thermalised then these studies suggest a molecular gas kinetic temperature of $\sim$ 20K. However, the low-J rotational levels of HCO^+ are probably not

in LTE — the critical density for the HCO^+ J=3-2 line is of the order $10^6 - 10^7 cm^{-3}$ (see discussion below). Thus I expect $T_{ex}(HCO^+ 3-2) < T_k$; the value of 9K used here seems reasonable. However, doubling the value of T_{ex} used in calculating N_{HCO+} via equation 3.1 would only increase the column density by a factor of a few and so the values derived below are believed to be relatively insensitive to any reasonable error in T_{ex}.

It is now a simple matter to obtain the integrated line intensities, $\int T_{mb}.dv$, corrected for a 0.79 beam efficiency of the 3-2 observations, from the two average plots for HH1 and HH2 and the VLA1 plot (figure 3.4) and so calculate the column densities *averaged* over the areas mapped:

- For HH1, $\int T_{mb}.dv = 2.33$K km s^{-1}; so $N_{HCO+} = 2.3 \times 10^{12} cm^{-2}$,
- For HH2, $\int T_{mb}.dv = 3.27$K km s^{-1}; so $N_{HCO+} = 3.2 \times 10^{12} cm^{-2}$

The map sizes of the HCO^+ sources observed are $(45'' \times 30'') + (15'' \times 15'')$, at 500pc a total area of $8.8 \times 10^{34} cm^2$ for HH1, and $(75'' \times 45'') + (15'' \times 60'')$, at the same distance a total area of $23.8 \times 10^{34} cm^2$ for HH2.

The *peak* column densities are also calculated, from the individual spectra recorded at the coordinates of peak HCO^+ emission (figure 3.2 and 3.3). For HH1 and HH2 the coordinates of the spectrum used were RA(1950): $05^h33^m56^s.0$, DEC(1950): $-06^o47'00''$, and RA: $05^h34^m01^s.0$, DEC: $-06^o49'30''$ respectively.

- For HH1, $\int T_{mb}.dv = 4.14$K km s^{-1}; so $N_{HCO+} = 4.0 \times 10^{12} cm^{-2}$
- For HH2, $\int T_{mb}.dv = 6.35$K km s^{-1}; so $N_{HCO+} = 6.2 \times 10^{12} cm^{-2}$
- For VLA1, $\int T_{mb}.dv = 6.43$K km s^{-1}; so $N_{HCO+} = 6.3 \times 10^{12} cm^{-2}$

Following Rudolph & Welch (1988) the *average* HCO^+ column densities can now be used to estimate overall masses for the "large-scale" HH1 and HH2 regions. The mass of each object is calculated from $M = 1.3 \times N_{HCO+} \times Area \times m_{H2}/X_{HCO+}$, where X_{HCO+} is the abundance of HCO^+ relative to H_2 and m_{H2} the mass of an H_2 molecule.

The factor of 1.3 here takes into account the mass contribution of elements other than hydrogen found in interstellar gas. Assuming a value of 2.3×10^{-9} for X_{HCO+} (Blake *et al.* 1987) the masses of each emission region are thus calculated to be $0.2(\pm 0.08)\,M_{\odot}$ for HH1 and $0.7(\pm 0.1)\,M_{\odot}$ for HH2.

3.3.2 The Gas Density in the HCO^+ Clump

Since we know the excitation temperature for the low-J HCO^+ levels then we can also use this to estimate the gas density. The population of each HCO^+ rotational state, n_i, under steady state conditions, is given by an equation of detailed balance, where collisions and spontaneous transitions into any level are balanced by transitions out of that level. Neglecting stimulated transitions (in the optically thin limit) then for the i'th rotational state;

$$n_{H2} n_i \sum_{j=0}^{j=4} C_{ij} + n_i A_{i,i-1} = n_{H2} \sum_{j=0}^{j=4} n_j C_{ji} + n_{i+1} A_{i+1,i}$$

where n_{H2} is the H_2 number density, C_{ij} the collision rate for the transition $i \rightarrow j$ and A_{ij} the Einstein A coefficient for spontaneous transition. For simplicity we limit the analysis to $J \leq 4$ (not unreasonable for low gas kinetic temperatures). Substituting for the collision rates for HCO^+ at a $T_k = 20$K (from Monteiro 1984 – note that HCS^+ rates are used) and the A coefficients for each level leads to a set of 5 simultaneous equations (1 for each rotational state) from which we may obtain the level populations, n_1, n_2 ... etc.

The excitation temperature derived in section 3.3.1 ($T_{ex} = 9$K) is used to calculate the fraction of HCO^+ ions in each level

$$\frac{n_i}{n_{HCO+}} = \frac{g_i}{Q} \exp\left(\frac{-h\nu_{i0}}{kT_{ex}}\right)$$

Here Q is the partition function (see appendix A) and $n_i/n_{HCO+} = [n_i/n_{H2}]X_{HCO+}$. We thus arrive at the following population distribution for HCO^+;

$$n_0 = 1.45 \times 10^{-3}\ \mathrm{cm}^{-3}$$
$$n_1 = 3.65 \times 10^{-3}\ \mathrm{cm}^{-3}$$

$$n_2 = 3.66 \times 10^{-3} \text{ cm}^{-3}$$
$$n_3 = 2.57 \times 10^{-3} \text{ cm}^{-3}$$
$$n_4 = 1.81 \times 10^{-3} \text{ cm}^{-3}$$

The *total* HCO^+ number density is thus

$$n_{HCO+} = 0.013 \text{ cm}^{-3}$$

From n_{HCO+} we may finally estimate the H_2 gas density in the HCO^+ clump. Again, using an HCO^+/H_2 abundance ratio of $X_{HCO+} = 2.3 \times 10^{-9}$ (Blake *et al.* 1987) then $n_{H2} = 5 \times 10^6$ cm^{-3}.

Evidently the HCO^+ clump in HH2 *does* represent a density peak in the ambient cloud. However, we should also note that *i)* I have here assumed that the excitation temperature used to calculate n_i/n_{HCO+} is the same for each level considered (this may not be the case if the "true" gas density is less than the critical densities quoted in table 3.4) and *ii)* the derived H_2 density is dependent on our choice of X_{HCO+}; if the HCO^+ is overabundant in HH2 then of course the underlying H_2 density would be overestimated.

Also, the characteristic depth of the HCO^+ clump (=HCO^+ column density/n_{HCO+}) measures only $\sim 5 \times 10^{14}$ cm compared to a FWHM diameter of $\sim 10^{17}$ cm. This low characteristic depth would result if the HCO^+ cloud consists of many smaller sub-clumps or again if n_{HCO+} is overestimated. For these reasons I thus treat the H_2 gas density derived here as an upper limit only; $n_{H2} \leq 5 \times 10^6$ cm^{-3}.

3.4 NH_3 RESULTS

Ammonia observations have been made towards the HH1-2 system by a number of astronomers (Marcaide *et al.* 1988, Martin-Pintado & Cernicharo 1987) though to date, no sensitive, high-resolution studies have been directed towards the HH objects themselves, and specifically south-east of the optical HH condensations in HH2. Consequently, we centred our observations on HH2 and mapped extensively around this region.

In figure 3.5 I show the distribution of the NH_3 (1,1) main hyperfine component integrated intensity, combined with dashed contours of the HCO^+ J=3-2 emission discussed above (DDB). The *total* NH_3 emission peaks to the east and south-east of HH2 and appears to form part of an elongated structure that extends down from the north. Indeed, in figure 3 of Marcaide *et al's* paper (1988) we see signs of such a feature to the north-east of HH2, on their total integrated intensity map of emission around VLA1. A ridge of ammonia is also apparent to the west of the HH, similar to that seen here. Clearly however, neither NH_3 peak seen in figure 3.5 here is coincident with the peak in HCO^+. This apparent anti-correlation is discussed in detail in section 3.6.

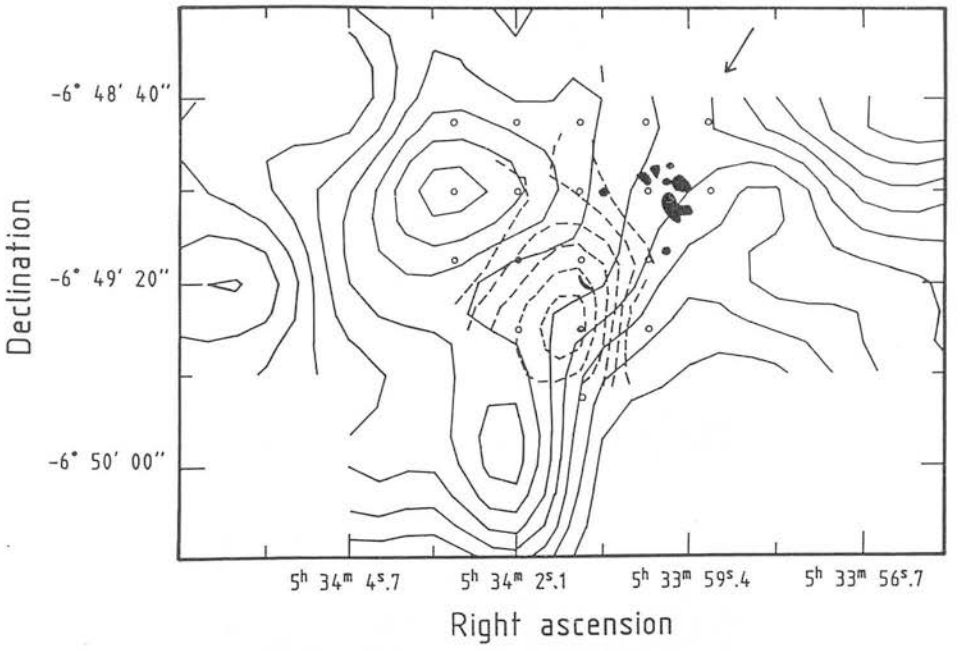

Figure 3.5: NH_3 (1,1) total integrated intensity map (T_A^* integrated from 4 to 12.0 km s^{-1}, contour levels begin at 0.02K km s^{-1} and increase in steps of 0.03K km s^{-1}). Superimposed are dashed contours, showing the distribution of HCO^+ J=3-2 ahead of HH2 (here, T_A^* integrated from 0 to 20 km s^{-1}, maximum contour level at 0.24K km s^{-1}, contours decrease in steps of 0.03K km s^{-1}, from DDB). The optical knots that comprise HH2 are also included, and the arrow indicates the outflow direction from VLA1 (found to the north-west of this diagram). The NH_3 beam measures $40\widehat{''}$, the HCO^+ beam $19\widehat{''}$.

The spectra shown in figure 3.6 correspond to five positions selected from the region

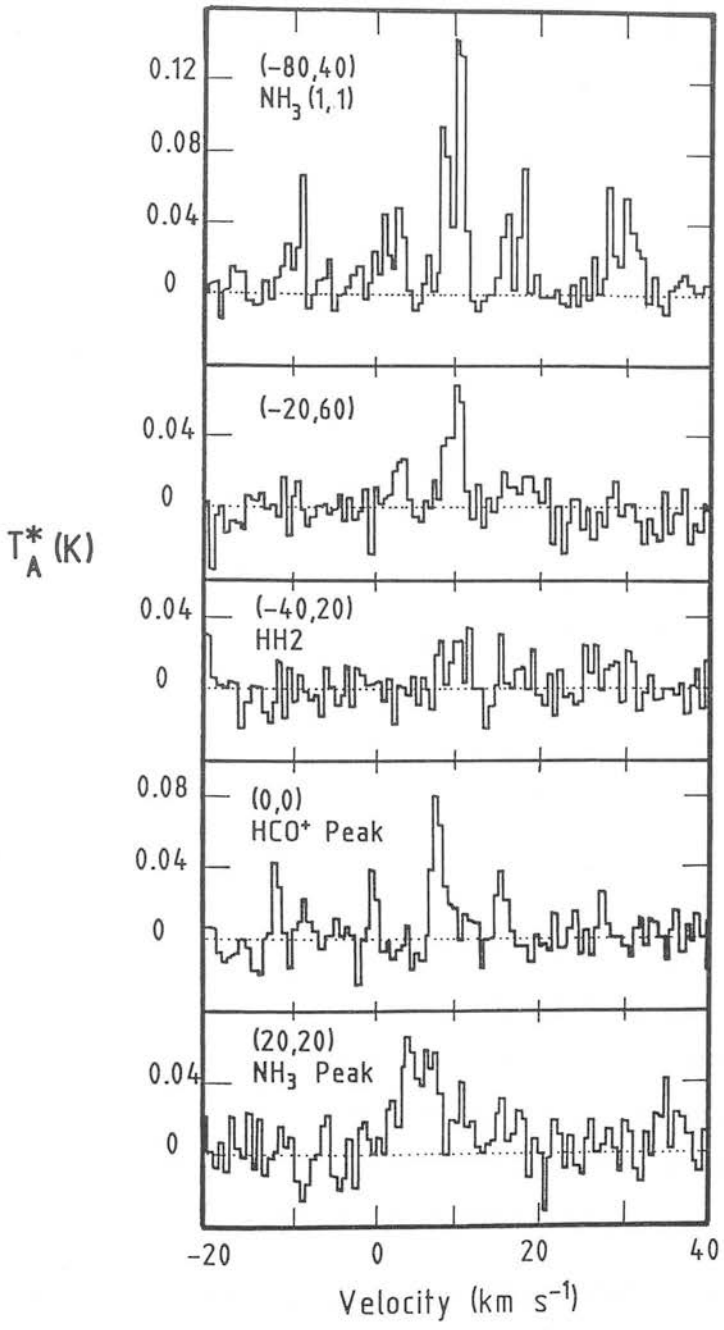

Figure 3.6: NH_3 J,K = 1,1 spectra from five positions around HH2. The offsets from the NH_3 map-centre ($\alpha(1950) = 5^h34^m02^s.1$, $\delta(1950) = -06°49'20''$) are marked in the top-left corner of each plot.

mapped. These spectra illustrate how highly complex the velocity structure of the molecular gas in this region is. The emission seems to consist of at least four distinct components, three of which may contribute to the wide emission line seen towards the easterly NH_3 peak, where the integrated intensity is strongest (figure 3.6, offset [20,20]). The top spectrum in figure 3.6, from the north-west, is more clearly split into two features with peaks at V_{LSR} = 8.6($\pm$0.7) and 10.4($\pm$0.7)km s^{-1}. The splitting, too wide to represent magnetic hyperfine structure (of the order of 40kHz; 0.5km s^{-1}), is also present in the optically thin electric quadrupole hyperfines, and so cannot be due to optical depth effects. Similarly, the gas to the north maintains both velocity components, though now in the form of a peak at 10.4km s^{-1} and a strong blue wing (figure 3.6, offset [-20,60]). The spectrum obtained towards the HCO^+ peak however, at offset (0,0), peaks instead at a third, lower velocity; V_{LSR} = 7.7($\pm$0.7)km s^{-1}.

Marcaide *et al.* (1988) and Martin-Pintado & Cernicharo (1987) have likewise observed line-splitting in ammonia studies of VLA1, the HH1-2 source (VLA1 is found to the north-west of the region we have mapped here; RA: $05^h33^m57^s.0$, DEC: $-06^o47'57''$, Pravdo *et al.* 1985). The main hyperfine component is seen to consist of two definite peaks, at 8.4 and 10.4km s^{-1}, consistent with the top spectrum in figure 3.6. The data is interpreted in terms of a slowly rotating, and infalling (or expanding) disk seen nearly edge on, extending NE–SW about VLA1, that is centrally evacuated (Marcaide *et al.* 1988). The blue and red-shifted components are attributed to the infall (or expansion) of the front and rear of the rotating toroid, whilst the gas at intermediate velocities is thought to illustrate the rotation: Their contour plots, of emission between 8.0 and 8.5km s^{-1}, and 10.0 and 10.5km s^{-1} clearly peak on the source itself, whilst the gas at 8.5 to 9.0 and 9.0 to 10.0km s^{-1} peaks to the north-east and west of VLA1 respectively. No emission was detected for gas at velocities below 8.0, or above 11.0km s^{-1}.

To illustrate the distribution of molecular material in HH2 at these differing velocities I present in figure 3.7 channel maps of the NH_3 emission. The peaks, seen in figure 3.5 to the east and south-east of HH2 (and apparently part of a *tongue* of emission that extends from the north of HH2), are seen at low velocities, 5 – 7 km s^{-1}. However, at slightly higher velocities, $\sim$7 – 9 km s^{-1}, a further feature appears, at the NH_3 map centre and only $\sim$ 5–10 arcseconds (0.02pc) to the north-east of the HCO^+

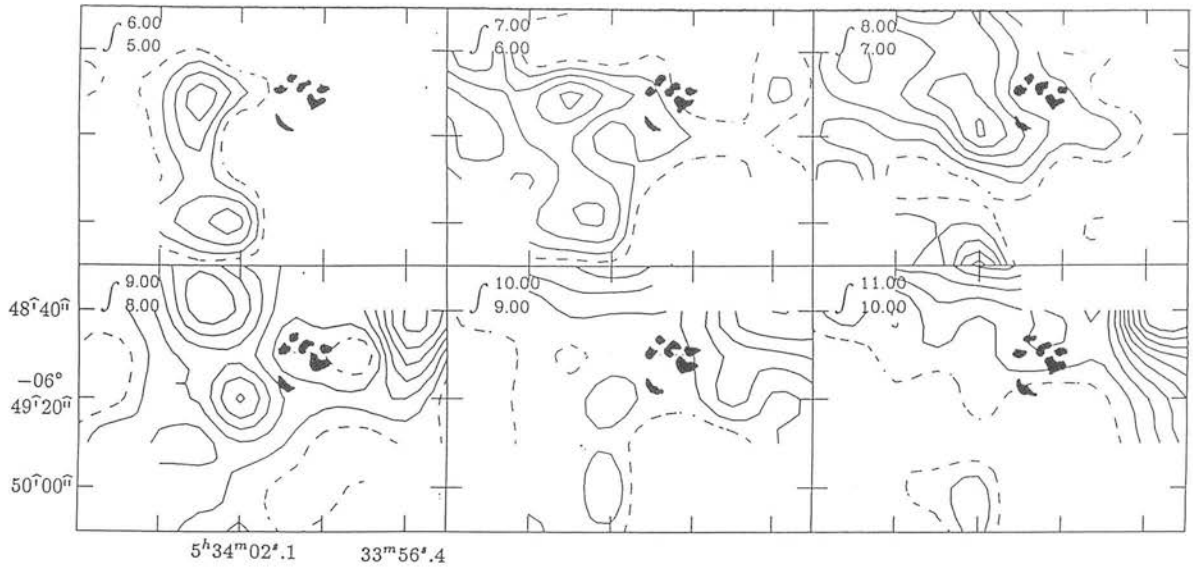

Figure 3.7: Channel maps of the NH_3 (1,1) emission around HH2. Minimum contour level is 0.01K km s^{-1} (dotted), levels increase in steps of 0.01K km s^{-1}. Again, the optical knots that comprise HH2 are sketched on each map.

J=3-2 peak. The near-spatial coincidence of this peak with the HCO^+ clump, within the pointing accuracy of the NH_3 observations (rms error in azimuth and elevation typically < 10 arcseconds), and the fact that it occurs at the same radial V_{LSR} as the HCO^+ peak, implies that both HCO^+ J=3-2 and NH_3 (1,1) peaks represent the same dense, near-stationary clump south-east of HH2.

3.4.1 Further Temperature and Density Estimates Ahead (SE) of HH2

As well as being indicative of the molecular structure in dense clouds, the NH_3 molecule may also be used as both thermometer and densitometer. Although the emission from the HH region is weak, hyperfines have been resolved towards the NH_3 map centre (towards the peak observed in the channel maps at $V_{LSR} \sim 7 - 9$km s^{-1}). We may therefore determine the optical depth of the transition and at the same time set limits on the excitation temperature. The spectrum in figure 3.6 (offset 0,0) is used to represent the molecular clump ahead of – south east of – HH2 (now observed in both HCO^+ and NH_3). These results will then lead to estimates of the gas temperature and density as outlined in chapter 1.

From equation 1.19, and applying this to the ratio of the observed (1,1) and (2,2) maximum antenna temperatures, I calculate optical depths for the 2,2 and 1,1 lines of $\tau_{2,2} = 0.5$ and $\tau_{1,1} = 1.8$. This then leads, via equation 1.20, to a rotational temperature of 16.0($\pm$1.0)K towards the NH_3 map centre (this value is notably higher than the HCO^+ excitation temperature calculated above). We may also calculate the excitation temperature that describes the relative populations of the inversion levels in the $J, K = 1, 1$ rotational state, from the spectrum in figure 3.6 (0,0) using equation 1.16. I find that $T_{1,1} = 2.9$K. This excitation temperature and a value of 20K for the gas kinetic temperature then lead to a lower limit for the molecular hydrogen density of 500 cm^{-3} (equation 1.21, see also the discussion in section 1.6.2). I have assumed here a uniform filling of the beam by the source, $\eta_f = 1$ and have used a value of $\eta_b = 0.45$ for the Effelsberg beam at 23GHz.

We should note that this result may suffer greatly from beam dilution, and so the density of any small scale clumps within the NH_3 beam may be much higher. Indeed, the presence of HCO^+ J=3-2 emission, with a critical density for de-excitation of $10^6 - 10^7$ cm^{-3} at temperatures of 10-20K, implies densities far higher than 500 cm^{-3}. However, now both NH_3 and HCO^+ observations indicate the presence of dense, quiescent molecular gas at $\sim$ 8 km s^{-1} associated with, and predominantly south-east (or ahead of) HH2, whilst the NH_3 observations show an additional feature (a *tongue* of molecular material) further to the east and south-east at a lower LSR velocity, $\sim$ 6km s^{-1}.

3.5 $C^{18}O$ RESULTS AND THE DETECTION OF CI

Further mapping of this region was recently conducted in the optically thin $C^{18}O$ J=2-1 transition using the JCMT. Figure 3.8 shows the $C^{18}O$ spectra observed; superimposed also are the NH_3 (1,1) and HCO^+ J=3-2 contours. The $C^{18}O$ emission is plainly extended across the entire region. No clumping is evident towards either of the NH_3 peaks or the HCO^+ peak. The spectra appear highly structured; line-splitting is seen to the south-west of the region mapped, and individual spectra are strong at random positions that are notably *not* coincident with either of the NH_3 or HCO^+ peaks.

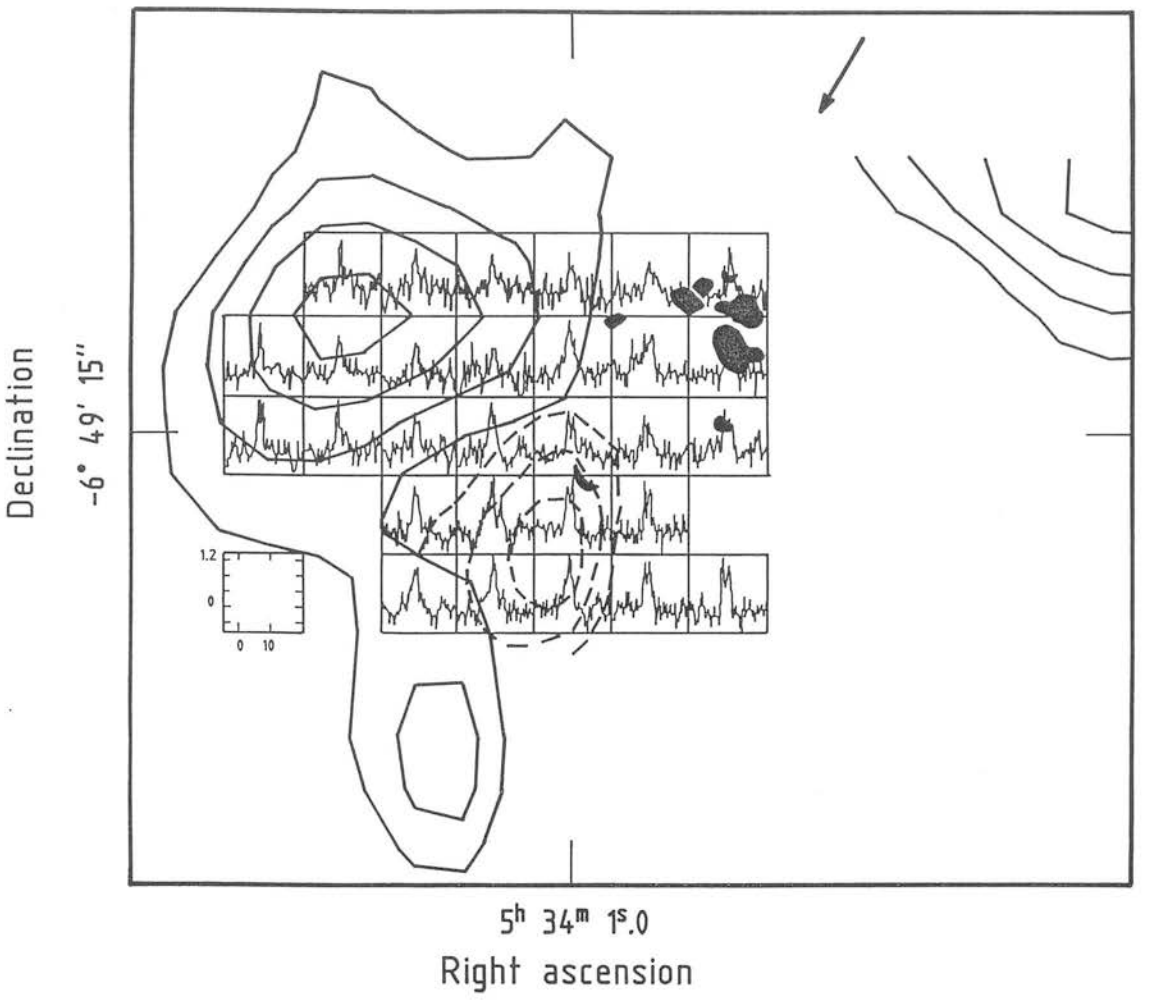

Figure 3.8: The $C^{18}O$ J=2-1 spectra observed towards HH2, and superimposed both the HCO^+ J=3-2 (dotted) and the NH_3 (1,1) (full) total integrated intensity contours, an arrow to indicate the outflow direction and the optical HH2 knots.

I also present the first detection of the $^3P_1 - ^3P_0$ fine structure line of atomic carbon from any HH object. We searched for emission towards two positions; the molecular peak traced in HCO^+ and one of the bright optical knots that comprise HH2. The strongest line was seen towards the latter position, and is shown in figure 3.9. No line was detected towards the HCO^+ peak in figure 3.3 (at RA(1950): $5^h34^m01^s.0$, DEC(1950): $-06°49\hat{}15\hat{''}$) above a noise level of ~ 0.8K.

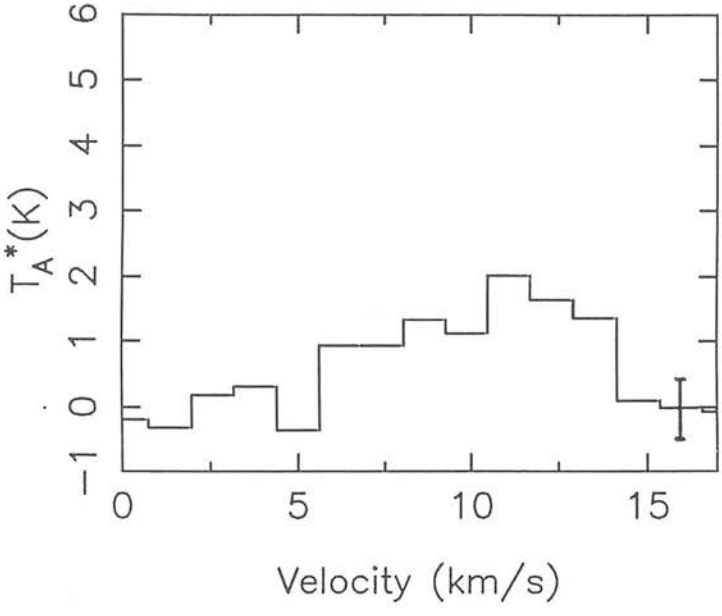

Figure 3.9: CI $^3P_1 - ^3P_0$ in HH2; towards RA(1950): $5^h34^m00^s.0$, DEC(1950): $-06°49\hat{}00\hat{''}$ The error bar has been calculated from the system temperature at the time of the observation and represents the rms noise level (1σ).

It would be premature to assume that the CI line is enhanced towards the optical knots in HH2, or that the CI is associated directly with HH2. CI emission may indeed be widespread throughout the region. However, whilst the CI line appears to extend over the full $C^{18}O$ line width, it is also notably strong at LSR velocities greater than 10 km s^{-1}, i.e. velocities slightly red-shifted from the ambient cloud velocity. Could the CI emission derive from the molecular outflow that is associated with HH2?

From the observed CI and $C^{18}O$ lines we may calculate the CI/CO abundance ratio:

Following appendix A the $C^{18}O$ column density in LTE may be obtained from:

$$N_{C18O} = 1.21 \times 10^{14} \frac{\exp(5.27/T_{ex})}{(1 - \exp(-10.54/T_{ex}))} \int T_b.dv \qquad \text{for } J = 2 - 1 \qquad (3.2)$$

The CI column density is obtained in a similar fashion (and is discussed in detail in Keene *et al.* 1985).

$$\begin{aligned} N_{CI} &= \frac{8\pi\nu_{10}^3}{3c^3 A_{10}} \frac{Q}{T_{ex}} \left[1 - \exp\left(\frac{h\nu_{10}}{kT_{ex}}\right)\right]^{-1} \int T_b.dv \\ &= 9.86 \times 10^{16} \frac{1}{T_{ex}} \left[1 - \exp\left(\frac{-23.6}{T_{ex}}\right)\right]^{-1} \int T_b.dv \qquad \text{for } {}^3P_1 - {}^3P_0 \end{aligned}$$

where $T_b (= T_A^*/[\eta_f \eta_b])$ in each case is measured in K, all velocities are in km s^{-1} and column densities are in cm^{-2}. For CI a value of 2.1 is used for the partition function Q (for a T_k of 20K) and the Einstein-A coefficient $A_{10} = 7.9 \times 10^{-8} s^{-1}$ (Keene *et al.* 1985).

Thus, for total integrated line intensities of 3.03 K km s^{-1} and 10.9 K km s^{-1} for the $C^{18}O$ and CI lines respectively, and assuming $N_{CO}/N_{C18O} \sim 490$ (Martin & Barrett 1978), for $T_{ex} = 16$K (from the CO kinetic temperature from Edwards & Snell [1983] and from the NH_3 rotational temperature measured here, and assuming thermalised level populations) I calculate a ratio of $N_{CI}/N_{CO} \sim 0.1$.

The ${}^3P_1 - {}^3P_0$ CI line, thought to be predominantly excited by collisions with electrons, has also been detected towards photo-ionisation fronts (Keene *et al.* 1985) and in dense, molecular cloud cores ($N_{H2} \geq 10^{23} cm^{-2}$ [Phillips & Huggins 1981], though note that this gas column density is an order of magnitude greater than that measured here for HH2 from the HCO^+ observations). In the former, the CI/CO column density ratio is $\sim 0.1 - 0.2$, in the latter the ratio measures ~ 1. These values differ markedly from early theoretical values (discussed in detail in Keene *et al.* 1985), where CI was thought to be less abundant than CO by a few orders of magnitude (these predictions were based on models where the CI is only found near cloud edges). However, many theories have since been forwarded to account for this *over*-abundance of CI in cloud

cores, including evaporation of grain mantles due to sputtering in shocks (Williams & Hartquist 1984) and the photo-dissociation of CO by UV fields produced also by shocks (Norman & Silk 1980). By comparison then, the results presented here show no enhancement in the abundance of CI in HH2 above that expected at the edge of a cloud.

3.6 THE UNCORRELATED DISTRIBUTIONS OF HCO^+, $C^{18}O$ AND NH_3

Although a molecular clump has been observed in HH2, in the HCO^+ map of figure 3.3 and at the same LSR radial velocity in the NH_3 channel maps of figure 3.7, there is still a distinct lack of correlation between the morphologies of HCO^+, NH_3 and $C^{18}O$ total integrated intensity contour maps. This lack of agreement is due to either; *i)* chemical abundance variations ahead, or south-east of, the HH shock in HH2, or *ii)* the differing excitation conditions favoured by each molecule/transition.

3.6.1 Chemical Abundance Variations

I shall initially consider the HCO^+ J=3-2 and NH_3 (1,1) observations in figure 3.5. South-east of the cluster of optical knots that comprise HH2, though coincident with the HCO^+ peak and the faint optical knot HH2L (Raga, Barnes & Mateo 1989), the NH_3 contours clearly decrease. This decline in the NH_3 main hyperfine integrated line intensity could be attributed to the *preferential dissociation* of NH_3 over HCO^+, or conversely to an increase in the HCO^+ abundance; is the NH_3 underabundant with respect to the HCO^+ (and indeed the underlying H_2 density)? Possible processes that might result in this include a photo-dissociating FUV precursor, produced at the HH shock, or perhaps a further shock or group of shocks coincident with HH2L and the HCO^+ clump.

A UV field has been observed in HH2 (Böhm *et al.* 1987), the spectrum of which was measured from 1950Å to 1250Å (6.4eV to 9.9eV), and although the spectrum appears to peak at 1580Å, it also equally shows a gradual rise into the FUV. Indeed, the spectrum varies only by a factor of $\sim$2.6 over the entire wavelength range. We may therefore, by extrapolation, predict the presence of an FUV precursor in the range

2070Å to 912Å (6eV to 13.6eV), and estimate a *total flux* of FUV photons capable of ionising C ($h\nu \geq$11.26eV); $F_{FUV} \sim 6 \times 10^{-18}$ W cm^{-2} (CII is thought to be an important ion in the chemistry of HCO^+; Elitzur 1983). From the calculated gas column density associated with HH2, I also estimate an $A_v \sim 1$ between HH2 and the HCO^+ peak. This flux and A_v may then be compared to models and observations of photo-dissociation regions (Tielens & Hollenbach 1985, Genzel *et al.* 1988). I find that the likely FUV flux from HH2 is too low, by a factor of $\sim 10^{-4}$, to affect chemical abundances appreciably ahead of the HH. Instead, any abundance variations are more likely to be the product of shocking, as indicated by the following test.

Molecular Hydrogen emission has been observed from HH2 (Harvey *et al.* 1986). The observed v=1-0 S(1) transition derives only from shocked or fluoresced gas (discussed in chapter 1). However, excitation by fluorescence populates the vibrational ladder of H_2. Thus by observing transitions from higher vibrational states, and by comparing line strengths, we may establish whether the emitting gas is shocked or fluoresced. We have therefore observed a single near-IR spectrum towards the HCO^+ peak and the optical knot HH2L in HH2 to test whether the gas here is indeed shocked or fluoresced. The plot in figure 3.10, obtained through service observations on the UKIRT, covers the v=1-0S(1), v=1-0S(0), and the v=2-1S(1) ro-vibrational emission lines of H_2. Shock models predict a v=1-0/v=2-1 S(1) line ratio of ~10 for H_2 emission that derives from shock-excited gas, whilst a ratio of ~2 is expected for the fluorescent case (assuming $n_{H2} < 10^5 - 10^6 cm^{-3}$; Sternberg 1988). The spectrum in figure 3.10 therefore implies shock-heating of the molecular region coincident with the HCO^+ peak *providing the gas density is not too high.* That is to say, *if chemical abundances are affected* in and south-east of HH2, the likely culprit is a shock or group of shocks, rather than an FUV field produced in the HH.

3.6.2 The HCO^+/NH_3 Column Density Ratio in HH2

Is NH_3 Underabundant in HH2?

From the spectrum in figure 3.5d we may calculate the NH_3 column density towards the HCO^+ peak in HH2 and so compare this with the HCO^+ column density evaluated

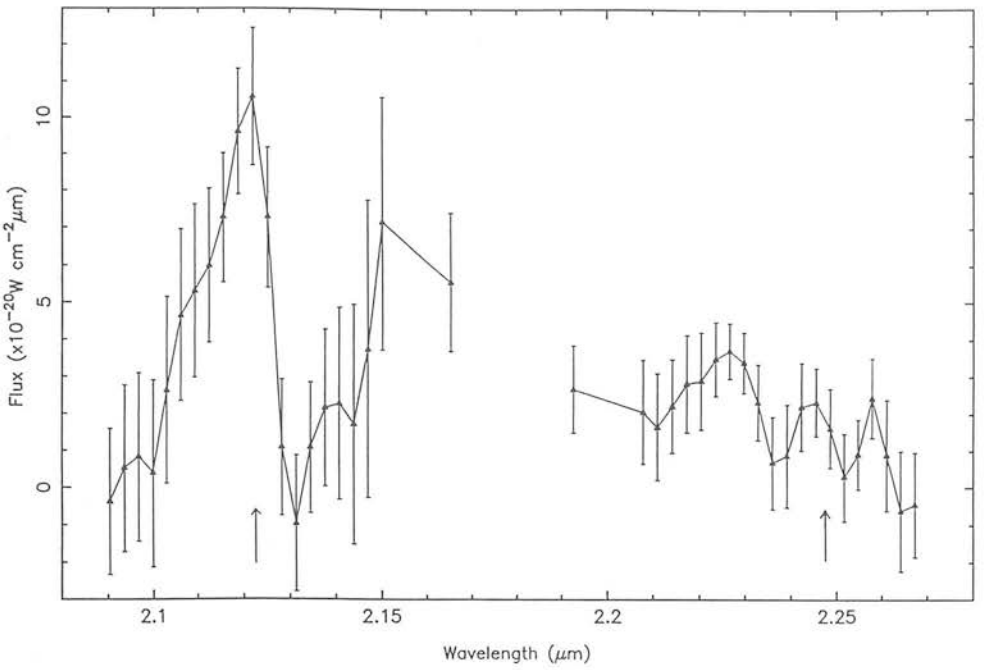

Figure 3.10: Near-IR spectrum observed towards the HCO^+ peak and the optical knot HH2L ($\alpha(1950) = 5^h34^m01^s.0$, $\delta(1950) = -06°49'15''$). Marked with arrows are the positions of the v=1-0S(1) and v=2-1S(1) ro-vibrational lines of H_2; the latter is clearly *not* detected. Beamsize = $5''$.

earlier.

The equation for the absorption coefficient, κ_ν (equation A.2), can be expressed in terms of the optical depth, τ_ν (Martin & Barrett 1978);

$$\tau_{1,1} = \frac{c^2}{8\pi\nu^2}\frac{A_{1,1}}{\delta\nu}\frac{g_j}{g_i}N_i(1,1)[1-\exp(-T_0/T_{1,1})]$$

where the line profile function in A.2, ϕ, integrated over the line width, normalises to unity. g_j and g_i are the statistical weights of the upper and lower levels in the inversion transition, and $N_i(1,1)$ is the column density of molecules in the lower level of the (1,1) rotational state. Consequently, the fraction of molecules in *both inversion levels* in the (1,1) state is given by $f_{1,1} = (N_i(1,1) + N_j(1,1))/N_{NH3}$; via the Boltzmann equation the above may therefore be written;

$$N_{NH3} = 1.48 \times 10^{13}\frac{1+\exp(-T_0/T_{1,1})}{1-\exp(-T_0/T_{1,1})}\frac{\delta v\ \tau_{1,1}}{f_{1,1}}$$

where N_{NH3} is in cm^{-3}, $\delta v = (\delta\nu/\nu)c$ is the linewidth in km s^{-1}, $T_0 = h\nu_{1,1}/k$ and $f_{1,1} = 0.43$ for a T_k of 20K (Martin & Barrett 1978).

I have already calculated the optical depth ($\tau_{1,1} \sim 1.8$) and the excitation temperature of the (1,1) rotational level ($T_{1,1} = 2.9$K – section 3.4.1). We may easily measure the line width at half maximum; from figure 3.6 (0,0), $\delta v = 2(\pm 1)$km s^{-1}. Thus, the ammonia column density towards the HCO^+ peak in HH2 is $N_{NH3} = 6(\pm 3) \times 10^{14}$ cm^{-3}.

We may now compare this value with the average HCO^+ column density calculated above (I use the average value since the HCO^+ beam is much smaller than the NH_3 beam); in HH2 $N_{NH3}/N_{HCO+} = 300$. The cloud chemistry models of Viala (1986) predict a ratio of $\sim 10^2 - 10^3$ for similar conditions, i.e. $n(H_2) = 10^4 - 10^5$, $T_k = 10$K and $A_v = 11$. Earlier cloud models by Mitchell *et al.* (1978) for the centre of a cloud having solar abundances and a mass of 500 $M_\odot$ predict $N_{NH3}/N_{HCO+} \leq 1$ for a diffuse cloud with gas densities $\leq 5 \times 10^3$ cm^{-3}; only at increased densities does the N_{NH3}/N_{HCO+} ratio increase to values anywhere near that observed here in HH2. Thus, I find no direct evidence for the underabundance of NH_3 with respect to HCO^+ in HH2. However, this column density ratio does suggest *higher gas densities* than was measured from the NH_3 observations earlier.

Is HCO^+ Overabundant in HH2?

We may also independently assess whether the HCO^+ is overabundant in HH2, not only with respect to NH_3 but also with respect to other molecular species (and ultimately H_2): The emission from HCO^+ J=1-0, HCN J=1-0 and CS J=2-1 was observed using the NRO 45m mm-wave telescope towards 3 positions in the HH1-2 system (figure 3.11). These observations allow us to calculate HCO^+, HCN and CS column densities, again using equations derived in appendix A (assuming in all cases optically thin emission and LTE):

$$N_{HCO+} = 7.45 \times 10^{10} \frac{\int T_b.dv}{(1 - \exp(-4.28/T_{ex}))} \qquad \text{for } J = 1 - 0 \qquad (3.3)$$

$$N_{HCN} = 1.41 \times 10^{11} \frac{\int T_b.dv}{(1 - \exp(-4.26/T_{ex}))} \qquad \text{for } J = 1 - 0 \qquad (3.4)$$

$$N_{CS} = 8.87 \times 10^{11} \frac{\exp(2.35/T_{ex})}{(1 - \exp(-4.71/T_{ex}))} \int T_b.dv \qquad \text{for } J = 2 - 1 \qquad (3.5)$$

The abundance of HCN is thought to remain relatively unaffected by *weak* shocks (Ziurys *et al.* 1989 and references therein) and so a comparison of the HCO^+ column density with that in HCN may prove a useful indicator of HCO^+ enhancement. Viala's dark cloud models predict $HCO^+/HCN \sim 0.2-0.6$, whilst observations of the quiescent dark cloud TMC-1 record ratios ~ 0.3 for HCO^+/HCN, and ~ 1 for HCO^+/CS (Irvine & Knacke 1988). Observations of the ridge in OMC1 ($N_{H2} = 10^{23}\text{cm}^{-2}$, $n(H_2) \sim 10^4 - 10^6\text{cm}^{-3}$, $T_k \sim 50 - 100\text{K}$), yield a ratio of $HCO^+/HCN \sim 0.5$ and $HCO^+/CS \sim 1$ (Blake 1987, Irvine & Knacke 1988). Here, the column densities, calculated for $T_{ex} = 9\text{K}$ and listed in table 3.3, indicate at best only a slight increase, by a factor of ~2–5 in the abundance of HCO^+ over HCN, towards either the optical knot HH2A or the HCO^+ peak to the south-east of this position. One should also note however the apparent *decrease* in the HCO^+/CS ratio.

Table 3.3: Column Densities (in cm^{-2}) calculated for the HCO^+ J=1-0, HCN J=1-0 and CS J=3-2 Spectra presented in figure 3.11.

	N_{HCO+}	N_{HCN}	N_{CS}	HCO^+/HCN	HCO^+/CS
HH2A	3.4×10^{12}	2.9×10^{12}	1.4×10^{13}	1.1	0.2
HH2-HCO^+	2.5×10^{12}	1.6×10^{12}	1.5×10^{13}	1.6	0.2

It is certainly difficult to come to a firm conclusion with regard to the chemical abundance variations in HH2, particularly with respect to the underlying H_2 abundance. However, at this stage we may conclude that although the HCO^+ appears to be enhanced by a factor of a few with respect to HCN, it is equally underabundant by ~ 5 with respect to CS: there is thus no clear-cut evidence for an enhanced HCO^+ abundance in HH2. Nor do we measure any definite reduction in the NH_3 abundance, though clearly higher resolution, multiple species observations are required of this and other HH objects to investigate the molecular chemistry in HH objects further.

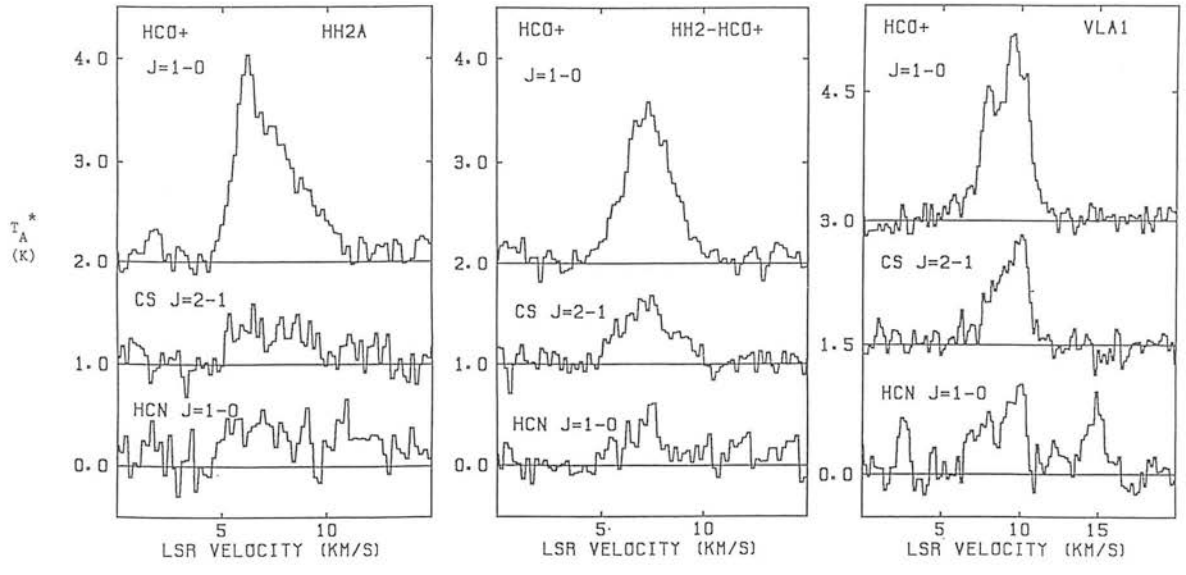

Figure 3.11: The J=1-0 HCO^+, HCN and J=2-1 CS spectra shown represent observations towards 3 positions in HH2; the bright optical knot HH2A, the HCO^+ peak and VLA1. The observations were made towards the following coordinates: HH2A; $\alpha(1950) = 5^h33^m59^s.44$, $\delta(1950) = -06°48'59''.2$ HH2-HCO^+; $\alpha(1950) = 5^h34^m01^s.07$, $\delta(1950) = -06°49'24''.0$ and VLA1 (as in main text).

3.6.3 Differing Excitation Conditions

Instead, the *anti*-correlation between the HCO^+ J=3-2 map and the NH_3 (1,1) total integrated intensity map and also the *non*-correlation with the $C^{18}O$ is most probably

due to the different physical conditions required to excite the observed lines. Listed in table 3.4. are values for the critical density for collisional de-excitation of the molecular transitions observed, calculated for $T_K \sim 10-20$K (Martin & Barrett 1978). Clearly, for the low temperatures associated with dense molecular cloud cores; $T_k \sim 5-20$K, $M \sim 0.1-10\,M_\odot$ (Khersonskii 1989), the n_{crit} values are highest for the HCO^+ lines, and far lower for the $C^{18}O$ and NH_3 transitions. In other words, very high densities ($\sim 10^6-10^7$ cm^{-3}) are required before the HCO^+ J=3-2 transition is thermalised.

Table 3.4: Critical H_2 densities for the excitation of rotational states in a selection of density-tracers (calculated for $T_k \sim 10-20$K).
References: a) Cox et al. 1987, b) Danby et al. 1988, c) Monteiro 1984, d) Martin & Barrett 1978, e) Green & Thaddeus 1974, f) Green & Chapman 1978, g) Schinke et al. 1985, h) Flower 1990.

Species	μ (Debyes)	transition	Frequency (MHz)	A_{ul} (s^{-1})	Collision rate (cm^3s^{-1})	$n(H_2)_{crit}$
HCN	[d] 2.98	J=3-2	265886	1.17×10^{-3}	[e] 1.13×10^{-11}	1×10^8
		J=1-0	88628	7.20×10^{-5}	0.8×10^{-11}	1×10^7
HCO^+	[a] 4.07	J=3-2	267559	2.23×10^{-3}	[c] 1.46×10^{-10}	2×10^7
		J=1-0	89189	1.38×10^{-4}	1.02×10^{-10}	1×10^6
CS	[d] 1.96	J=2-1	97981	1.68×10^{-5}	[f] 2.9×10^{-11}	6×10^5
NH_3	[d] 1.47	J,K=2,2	23723	3.34×10^{-7}	[b] 1.1×10^{-11}	3×10^3
		J,K=1,1	23695	1.67×10^{-7}	8.6×10^{-11}	2×10^3
CO	[d] 0.112	J=3-2	345813	2.59×10^{-6}	[g] 6.76×10^{-11}	3×10^4
		J=2-1	230538	7.15×10^{-7}	5.61×10^{-11}	1×10^4
		J=1-0	115271	7.46×10^{-8}	2.38×10^{-11}	3×10^3
CI	–	$^3P_1 - {}^3P_0$	492160	[h] 7.93×10^{-8}	–	–

In for example a simple two-level system that is in equilibrium (where the emission is again assumed to be optically thin) upward collisions are balanced by downward radiative transitions so that

$$n_{H2} n_1 C_{12} = n_2 A_{21} \qquad \text{if } n_{H2} \ll n_{crit}.$$

However, as n_{H2} increases then downward collisional transitions become increasingly more important until ultimately

$$n_{H2} n_1 C_{12} = n_{H2} n_2 C_{21} \qquad \text{when } n_{H2}\ n_{crit}.$$

Thus the intensity of the emission (and so from equations 1.13 and 1.17 the observed antenna temperature) increases with gas density *squared*; $T_A^*(thin) \propto n_2 A_{21} = n_{H2} n_1 C_{12}$. However, when the H_2 density becomes greater than the critical density, $T_A^*(thin)$ ($\propto n_2 A_{21}$) varies only with density. That is to say, any molecular tracer of H_2 becomes less sensitive to changes in gas density once that density surpasses the critical density of the observed transition. In HH2 then, the HCO^+ J=3-2 has a far wider *dynamic range* than the NH_3 or $C^{18}O$ lines observed (see table 3.4 for critical densities) and so is more effective in picking-out the dense clump associated with HH2 (the $C^{18}O$ observations may additionally suffer from a relatively poor signal-to-noise).

I therefore conclude that the clump seen in HCO^+ and in NH_3 channel maps at $V_{LSR} \sim 7 - 9$km s^{-1} represents a dense, ambient cloud, with $500 < n(H_2) < 5 \times 10^6$ cm^{-3} (the NH_3/HCO^+ column density ratio infers densities in excess of 10^4 cm^{-3}) and $T_k \sim$ 16K. Particularly high densities are expected if the cloud is clumpy. The NH_3 observations additionally show a (double peaked) tongue of molecular material to the east of the HCO^+ clump at $V_{LSR} \sim 5 - 7$km s^{-1}. The density of this feature must be less than that of the clump at $V_{LSR} \sim 7 - 9$km s^{-1} since it is not observed in HCO^+.

3.7 A MODEL FOR HH2

Based on the wealth of observations of HH2 and particularly HH1, many observers and theorists have tended to support Norman & Silk's "interstellar bullet" (1979) or

Dyson's later (1984) "jet" model for these HH objects (Hartigan et al. 1987, Hartmann & Raymond 1984 and Böhm & Solf 1985). These conclusions are based largely on the high proper motions of the optical knots in each HH, the shape of position-velocity diagrams (particularly HH1) and the profiles of the observed emission lines (Hartigan *et al.* 1987). Indeed, in the optical image shown in figure 3.1, the bow-shaped shock that constitutes HH1 is clearly convex on the side farthest from the exciting source of the system. It does not seem unreasonable therefore to postulate that this shock is the result of either *i)* a dense clump or bullet of material ploughing into the ambient cloud, or *ii)* the head or "working surface" of a collimated jet similarly burrowing through the surrounding medium.

However, jet and bullet models require high velocities, since the optical and near-IR emission derives from the cooling flow very near to the shocked and accelerated gas at the head of the bullet or jet working surface. Observed velocities along the line of sight and proper motions studies do indeed imply velocities ranging from 150 to over 350 km s^{-1} for the individual optical knots that comprise many HHs, including both HH1 and HH2 (Herbig and Jones 1981) . However, the presence of low velocity, quiescent HCO^+, observed here in HH1 and 2 and in the HH7-11 system (Rudolph & Welch 1987) does not fit easily into either model (though of course whether the observed emission in HH1 derives from the HH or from some unassociated ambient clump is not clear).

3.7.1 Shocked Cloudlet or Jet Working Surface

I shall here discuss a model for HH2 only, since the molecular observations of HH1 are somewhat limited. However, much of the discussion is directly applicable to HH1 also.

The distinct peak of HCO^+ emission in HH2 is quite clearly ahead of the advancing optical knots, the H_2 peaks and the 6cm bremsstrahlung continuum emission peak. Further, the emission lines are uncommonly narrow, unlike associated H_2 and optical lines. These observations, in conjunction with the earlier optical and infrared studies, therefore support one of two possible scenarios: Either a jet working surface model, as was proposed by Dyson (1984) though where the ambient gas is *denser* than the jet gas (i.e. a "light" jet scenario), or a "shocked cloudlet" model (Schwartz 1978). Both models are shown in figure 3.12.

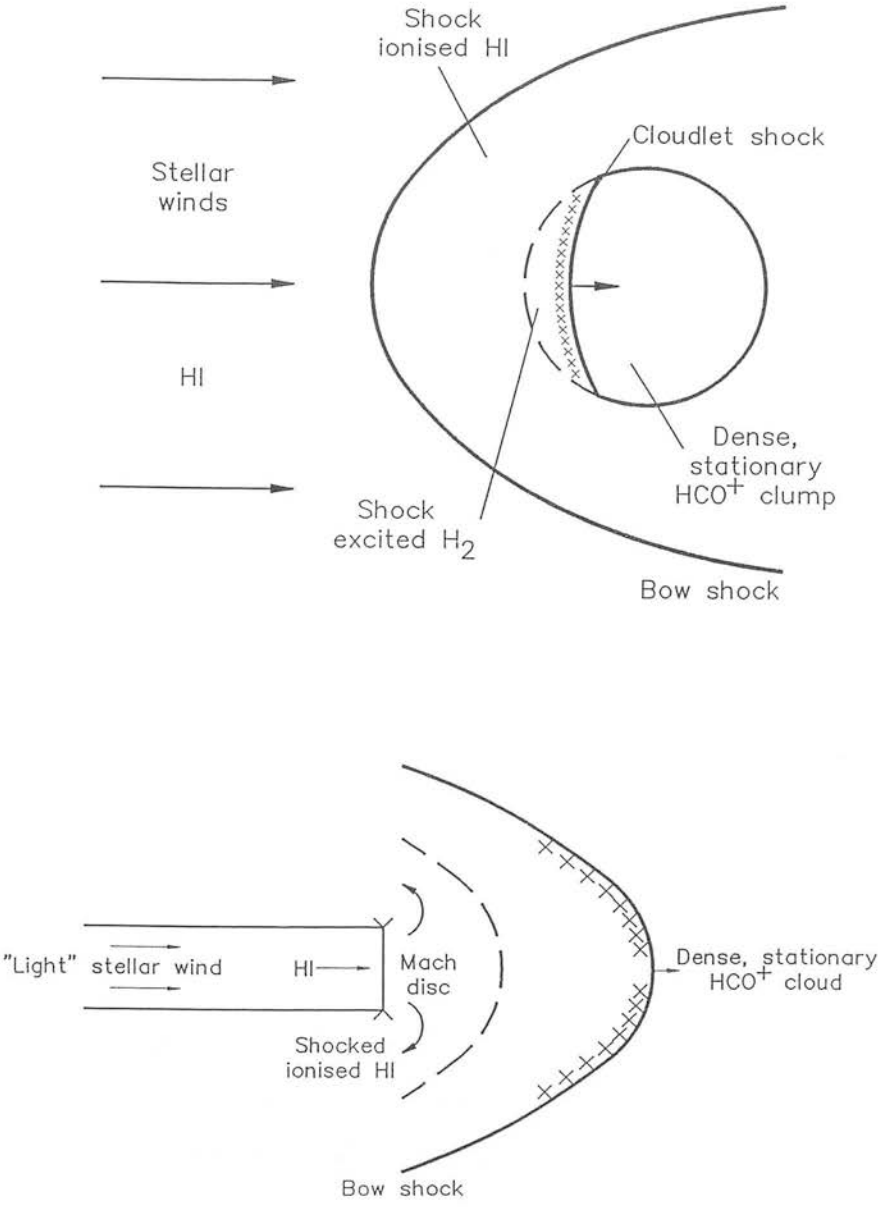

Figure 3.12: Shocked cloudlet (top) and jet working surface (bottom) models for HH objects.

In the latter shocked cloudlet model the HCO^+ emission derives from relatively quiescent, dense, un-shocked, cloudlet gas, positioned *ahead* of the bow and cloudlet shocks. The impact of a high velocity outflow upon such a stationary clump results in an *inverted bow shock* on the side of the clump facing the outflow source — this bow shock is the reverse of that produced by a jet working surface or interstellar bullet. In addition, a second, though far slower *cloudlet shock* propagates into the clump itself, producing a general heating of the cloudlet gas and possibly acceleration of the cloudlet itself (Schwartz 1978); ro-vibrational emission from shocked H_2 will more probably come from this shock, though H_2 may also be seen in the "wings" of the bow-shock, where shock angles are oblique and so shock velocities lower.

The above model is essentially the inverse of Norman & Silk's interstellar bullet model, though now we expect the HCO^+ to be stationary ambient material rather than high-velocity bullet gas. We also expect to observe shock-ionised wind gas, stopped at the *head* of the cloudlet but also flowing around the sides of the cloudlet. This cooling flow, and the bow-shock geometry, thus account for the large line widths seen in the optical and near-IR. However, the bow shock itself would adopt the velocity of the near-stationary cloudlet, and so the model *fails* to explain the observed high proper motions of the optical knots, which in HH2 (and HH1) approach 150–350 km s^{-1} (Herbig & Jones 1981).

Schwartz (1978) envisaged his cloudlets to be only a few arcseconds across (at 460pc) in accordance with the small optical knots that comprise many HH objects; i.e. *cloudlet radius* $\ll$ *outflow radius*. However, the clump of HCO^+ seen in HH2 extends over nearly 1 arcminute, though the HCO^+ column density and HCO^+ number density derived here suggest clumping on scales $\sim 10^{14}$ cm ($0.02\widehat{''}$). Any such clumps would of course be too small to be resolved with the 19 arcsecond beam used in these observations, though each clump individually shocked could produce the observed optical structure in HH2.

If on the other hand the HCO^+ cloud in HH2 is not clumpy but relatively uniform, then one could invoke a *light* jet working-surface model (shown in figure 3.12, bottom). This time the jet radius is much smaller than the HCO^+ clump size. As with the cloudlet shock above, the bow-shock (and indeed the whole working surface of the jet)

moves relatively slowly through the ambient clump, though now the optical emission derives from the cooling flow from the jet shock, or *Mach disc*: Indeed, Hartigan (1989) predicts that for a jet velocity of $\sim$ 200–300 km s^{-1} and for a cloud/jet density ratio ≥ 10, then in H_β the Mach disc will be brighter than the bow-shock. Furthermore, the action of a light jet shocking a dense cloud will produce Rayleigh-Taylor instabilities on scales of 1/100ths of a parsec (a few arcseconds); these instabilities may account for the clumpy structure of this and other HH objects (Blondin *et al.* 1989).

We may calculate the bow-shock velocity (or cloudlet shock velocity in the shocked cloudlet model), and so the velocity with which the working surface penetrates the HCO^+ cloud, from (Blondin *et al.* 1989);

$$V_{bs} = \frac{V_j}{1 + (\rho_c/\rho_j)^{1/2}} \tag{3.6}$$

where V_j, ρ_j, ρ_c and V_{bs} are the jet velocity, the jet and cloud (pre-shock) densities and the cloud shock velocities respectively. Using values of $V_j \sim$ 300km s^{-1} (Pravdo et al. 1985, Mundt *et al.* 1987), $\rho_c \sim 10^3$cm^{-3}, and $\rho_j \sim 100$cm^{-3} (Mundt *et al.* 1987) a $V_{bs} \sim 70$ km s^{-1} is calculated. For $\rho_c \sim 10^5$cm^{-3}, V_{bs} is only ~ 10 km s^{-1}. Alternatively, for higher jet densities, V_{bs} increases, though again if we are to account for the high proper motions in HH2, and so increase the velocity of the working surface, then for a wind ≤ 500 km s^{-1} the jet must be denser than the ambient gas. Otherwise, unrealistically high jet velocities are required (Hartigan 1989).

Clearly we have great difficulty in accounting for both the high precursor-gas densities, inferred particularly by the HCO^+ J=3-2 observations, and the large proper motions of the optical HH knots in HH2 using *any* of the current popular HH models. Further adaptation of these models is thus required.

3.7.2 The Lifetime of the HCO^+ Cloud

We may finally obtain a crude estimate of the lifetime of the cloud in HH2. The gas temperatures behind a jet working-surface bow-shock (or cloudlet shock) will initially be of the order of $5\times10^3 - 10^5$K, hot enough to dissociate HCO^+ and so perhaps also destroy the HCO^+ peak. For a jet working-surface model, the thermal pressure

gradient produced behind the bow shock will result in a flow of the shocked cloud (and jet) material around the head and back down the sides of the jet (Dyson 1987, Hartigan 1989). The lifetime of HH2 may therefore be estimated from the time it takes the jet working surface (traveling at the bow-shock velocity) to traverse the HCO^+ clump. For a diameter of $\sim$ 45 arcsec (0.1pc) for the HCO^+ clump, an approximate lifetime of 10^3 years is calculated for HH2 (a similar analysis in terms of the cloudlet model yields the same result). This value is notably consistent with the dynamical ages of optical jets (200-3000 yrs; Mundt *et al.* 1987), though it is roughly 1/100th the estimated lifetimes of molecular outflows ($\sim 10^5$ years; Fukui 1989).

3.8 CONCLUSIONS

Both HCO^+ J=3-2 and NH_3 (1,1) observations indicate the presence of dense, quiescent gas ahead of (south-east of) the optical knots that comprise HH2. This molecular region is split into two quite distinct features, as illustrated in the NH_3 channel maps: A tongue of material at $V_{LSR} \sim 5 - 7\text{km s}^{-1}$, 60 arcseconds (0.14pc) to the east and south-east of the optical knots that comprise HH2 — this feature may in fact correspond to a cavity wall extending down from the HH1/2 source VLA1, adjacent to the outflow that produces HH2. At higher velocities, $\sim 7 - 9\text{km s}^{-1}$, a further peak only 40 arcseconds (0.09pc) south-east of HH2 is observed. This latter clump is also seen in HCO^+ J=3-2, and since observable emission from the low-J states of HCO^+ requires relatively high densities in cool molecular environments ($n_{H2} \sim 10^6 - 10^7\text{cm}^{-3}$) this peak is likely to be of a higher density than the molecular tongue to the east. I calculate a gas density of $500 < n_{H2} < 5 \times 10^6$ cm^{-3} and a rotational temperature of 16($\pm$1)K towards this feature.

Of the three molecular tracers used in our study of HH2 (NH_3, HCO^+ and $C^{18}O$), the HCO^+ J=3-2 line illustrates most clearly the dense clump associated with HH2. The lack of a corresponding peak in $C^{18}O$ and in the NH_3 total integrated intensity map of HH2 is probably *not* due to chemical abundance variations (and particularly an enhancement in HCO^+) though a high-resolution, multi-wavelength study is required of this and other HH objects to verify this fact. Instead, the observed lack of correlation is most likely due to the differing excitation conditions required by each transition

observed; the $C^{18}O$ J=2-1 map in particular indicates an overall smooth distribution of gas column density over the HH2 region, whilst only the HCO^+ picks out dense clumping associated with the HH.

The HCO^+ observations thus illustrate the pre-shock, or *precursor* gas in HH2. Depending on whether the HCO^+ cloud is clumpy or uniform, I favour a "shocked cloudlet" or "light jet working-surface" model for HH2, though both models fail to account for the high proper motions observed in HH2. Some refinement of these models is thus required.

Chapter 4

A Near-IR Jet in L1448

SUMMARY: By imaging in the near-infrared (rather than at optical wavelengths) we may probe deeper into molecular cloud cores and so hope to observe evidence for stellar winds associated with heavily embedded sources. Moreover, unlike their unobscur ed optical counterparts, these embedded winds are more likely to produce molecular (CO) outflows via the entrainment of ambient cloud gas. Consequently, I present here such observations of the ro-vibrational H_2 emission from a high-velocity CO outflow in L1448. The coincidence of the observed H_2 jet structure with the CO bipolar outflow implies a strong association between the two phenomena. Also, mapping in HCO^+ J=3-2 and CS J=5-4 illustrates the ambient cloud environment in L1448. Cloud cores are clearly resolved which peak towards the source of the H_2 jet and CO outflow, and towards an additional infrared source labeled IRS3 to the north of this region.

4.1 INTRODUCTION

Within the dark cloud L1448 in Perseus, Bachiller *et al.* (1990) have recently discovered and mapped a striking example of a high-velocity molecular outflow. The flow is quite unique; their CO J=2-1 observations record a terminal velocity approaching 70 km s^{-1}, and an associated dynamical timescale $\sim$ 3500 years. The outflow thus seems to be one of the most rapid and "youngest" flows known (see the outflow characteristics listed in table 1.1). These observers have also detected high velocity CO clumps or "bullets", symmetrically placed either side of the mm-continuum source L1448-mm (the presumed exciting source for the outflow; Bachiller *et al.* 1991a). The most rapid bullets are found close to the source, whilst the slower clumps occur further out, $\sim$ 0.2pc ($\sim 130\hat{''}$) from L1448-mm; presumably some braking process occurs along the outflow. These bullets have also been identified in the J=2-1 line of v=0 SiO (Bachiller *et al.* 1991b). The authors note the similarity of these clumps with the molecular bullets proposed by Norman & Silk (1979) to account for HH objects.

I present here imaging of this outflow region in the v=1-0 S(1) line of molecular hydrogen. I also discuss HCO^+ J=3-2 and CS J=5-4 observations of the ambient molecular cloud in L1448, where a comparison is made with the lower resolution NH_3 (1,1) and (2,2) observations of Bachiller *et al.* (1990), and with recent CS 2-1 studies of dark cloud cores. Notably, the higher-J HCO^+ and CS observations presented here will probe deeper into cloud cores since the transitions require higher densities for excitation and the emission will be more optically thin.

4.2 OBSERVATIONS

The near-IR imaging was conducted on the UK 3.8-meter Infrared telescope (UKIRT) during July 1991 using the 1-5μ array camera IRCAM. At a scale of 0.62 arcseconds/pixel, the 62×58 InSb array provides a frame size of $37\hat{''} \times 35\hat{''}$; a mosaic of 8 frames was therefore needed to cover the extent of the molecular outflow. 300 second exposures were taken through a narrow band ($\Delta\lambda/\lambda \sim 1\%$) H_2 v=1-0 S(1) filter at 2.122μ and through the adjacent narrow-band continuum filter at 2.10μ. The bandpass (at 2μ) is equivalent to a velocity width of $\sim$ 3000 km s^{-1}, and so is sufficient to

include all the emission from shocked, velocity broadened H_2 lines. Sky frames were taken between each source frame (offset ~5 arcminutes). Dark frames were also taken periodically; this dark current was later subtracted from each source and sky frame. The source frames were then flat-fielded by dividing by the adjacent sky frame. We achieved an rms noise level of $\sim 10^{-19}$ W m^{-2} pixel^{-1}; calibration was conducted using observations of the IR standard star HD18881 (from which sky and dark frames were also removed). The pointing accuracy of the telescope $\sim 1''$ and the Full-Width at Half-Power of the standard star measured $\sim 1.5''$.

The sub-millimeter observations were made with the James Clerk Maxwell 15-meter telescope (JCMT) in late October 1991. The common-user heterodyne receiver A1 was used to access the HCO^+ J=3-2 (at 267.599 GHz) and CS J=5-4 (244.935 GHz) lines. The half-power beam width of the JCMT at these frequencies measures 21 arcseconds; the beam efficiency is 0.79. The resolution of the acousto-optic spectrometer used was 0.33 MHz ($\sim$ 0.3 km s^{-1}). System temperatures were typically 1300K for the CS observations and 2600K for the HCO^+. We integrated for 2 minutes on each on-source position, though some points were repeated to improve the signal-to-noise. Offsets (-3 arcminutes in RA) were observed after each on-source position and mapping was conducted at $15''$ spacings. Pointing checks were made every 1-2 hours (on W3(OH)) and so the rms error was restricted to $\sim 5''$. The distance to L1448 is judged to be $\sim$ 300 pc (Bachiller *et al.* 1990 and references therein).

4.3 RESULTS

4.3.1 The Remarkable H_2 Jet in L1448

The mosaic of frames in figure 4.1 (Davis *et al.* 1992) shows the spectacular "jet" structure in L1448. Moreover, the narrow-band continuum mosaic in figure 4.2 indicates that apart from the regions close to the source and IRS3 (at -35'', 75''), all of the emission in figure 4.1 is due to molecular hydrogen (there is no hint of the jet in our continuum images above an rms noise level of $\sim 4 \times 10^{-20}$ W m^{-2} pixel^{-1}; note that the grey-scale is the same in both figures 4.1 and 4.2). Hence, the continuum frames have not been subtracted from the H_2 frames since this would only serve to increase the noise level in

the H_2 image.

In figure 4.3 a comparison is made between the H_2 jet and the high-velocity CO outflow observed by Bachiller *et al.* (1990). The salient features are discussed here;

- The H_2 emission clearly extends along ~70% of the length of the blue-shifted CO lobe, and faint emission can be seen at the end of the red CO lobe. The lack of an H_2 jet in the red-shifted CO lobe may be due to extinction.

- The curvature of the northern lobe of the H_2 emission is also seen in the high-velocity CO morphology, although the CO lies mainly on the *outside* or eastern edge of the curve. The smoothness of the curve suggests that a large-scale phenomenon (such as a magnetic field or density gradient) is bending the jet, rather than localised ambient-cloud clumping. Also, the displacement of the CO outflow from the H_2 jet is consistent with models where molecular outflows are produced by the entrainment of ambient molecular material by a stellar wind (discussed by Lada [1985] and Fukui [1989]). One would certainly expect to see shocks on the inner edge of such a shell of outflowing molecular gas; the oblique shock angles would also favour H_2 excitation as opposed to dissociation, and so a near-IR rather than an optical jet would be expected.

- The lack of emission near the source suggests that either there are no shocks present *or* the H_2 is dissociated. Shock velocities greater than 20–25 km s^{-1} seem likely when one considers the high CO clump velocities near to the source (Bachiller *et al.* 1990). Moreover, J=3-2 and 5-4 v=0 SiO lines are particularly intense towards the source, indicating extreme excitation conditions (Bachiller *et al.* 1991b).

- The jet material is clumped on scales similar to those seen in optical jets, where typically the inter-knot spacing measures ~ 0.01 pc (a few arcseconds), equivalent to a few times the jet width (Reipurth 1989, Mundt *et al.* 1987). The jet also exhibits three apparent bow shocks equidistant along the flow, though whether these bow-shocks are associated with the CO/SiO bullets reported by Bachiller *et al.* (1990, 1991b) is unclear; higher-resolution mm/sub-mm observations are

Figure 4.1: (overleaf) A mosaic of 8 frames showing the H_2 v=1-0 S(1) emission associated with the CO outflow in L1448. The grey-scale ranges from 0 -1.5$\times 10^{-18}$ W m^{-2} pixel^{-1}. Offsets are from L1448-mm (marked with a cross), at RA(1950): $3^h22^m34^s.3$, DEC(1950): $30^o33'35''$.

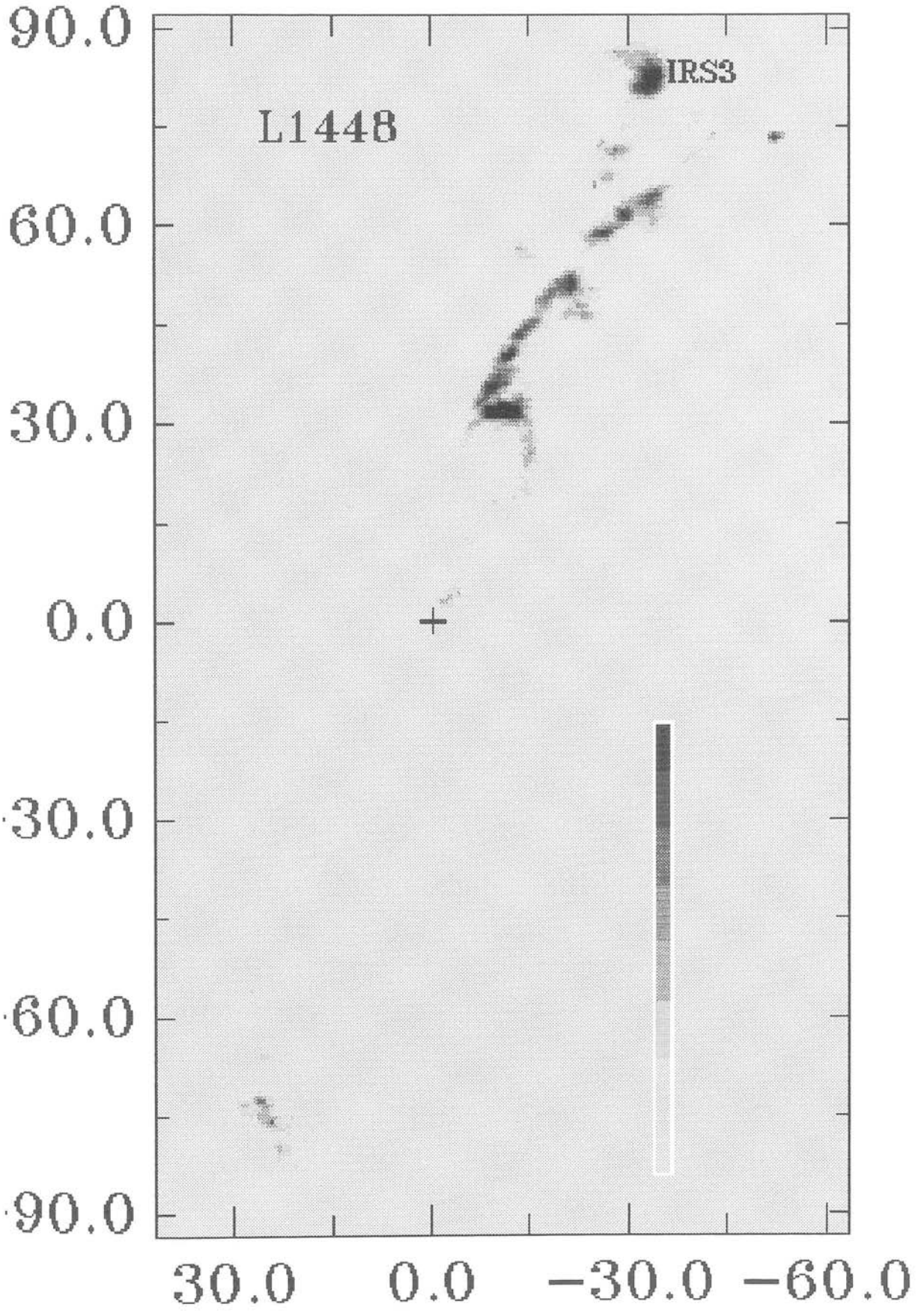
L1448
IRS3
90.0
60.0
30.0
0.0
30.0
60.0
90.0
30.0
0.0
−30.0
−60.0

Figure 4.2: (overleaf) 2.1μ continuum frames observed in L1448. The grey-scale is the same as that in figure 4.1.

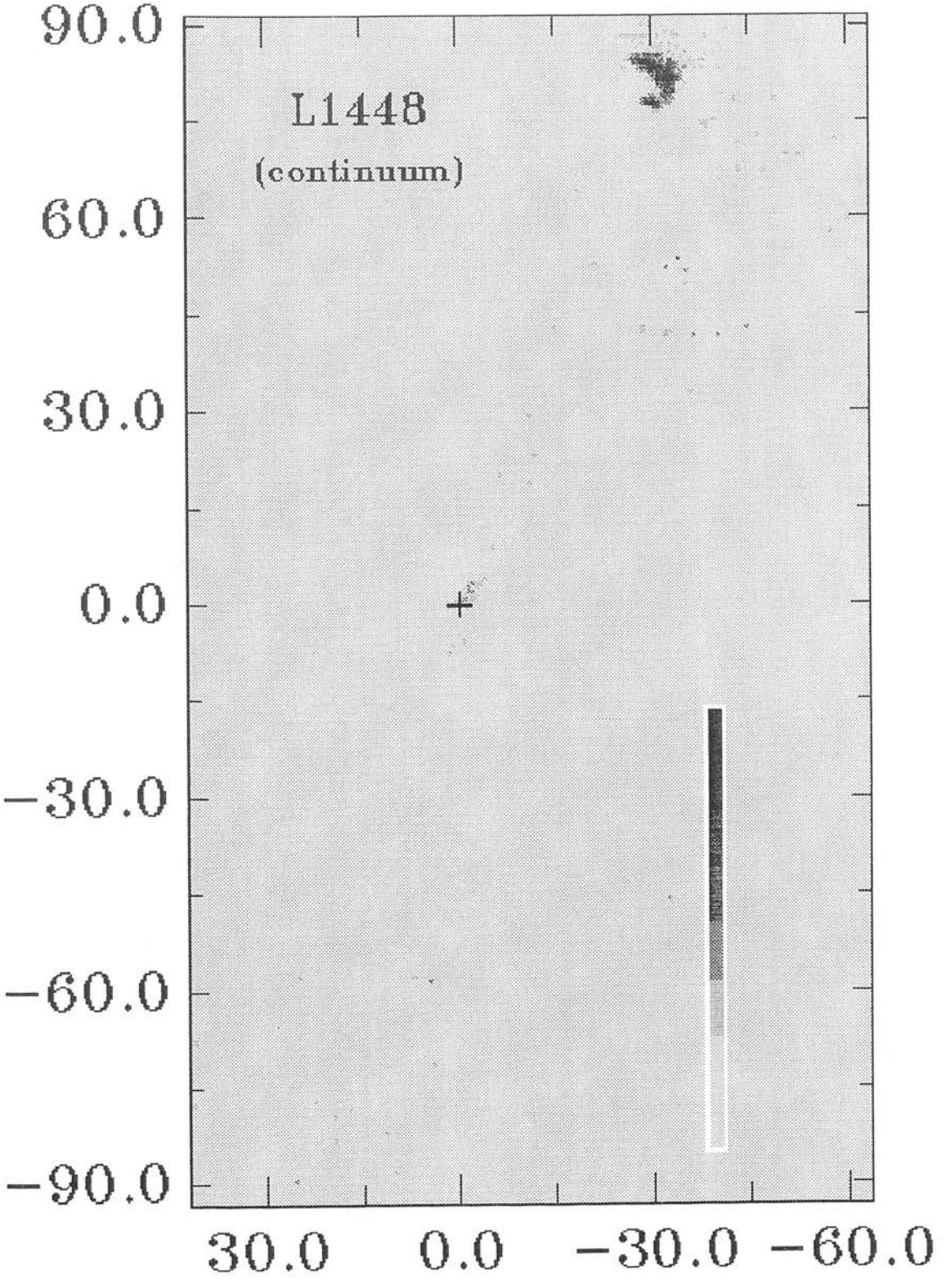
L1448
(continuum)
90.0
60.0
30.0
0.0
−30.0
−60.0
−90.0
30.0
0.0
−30.0
−60.0

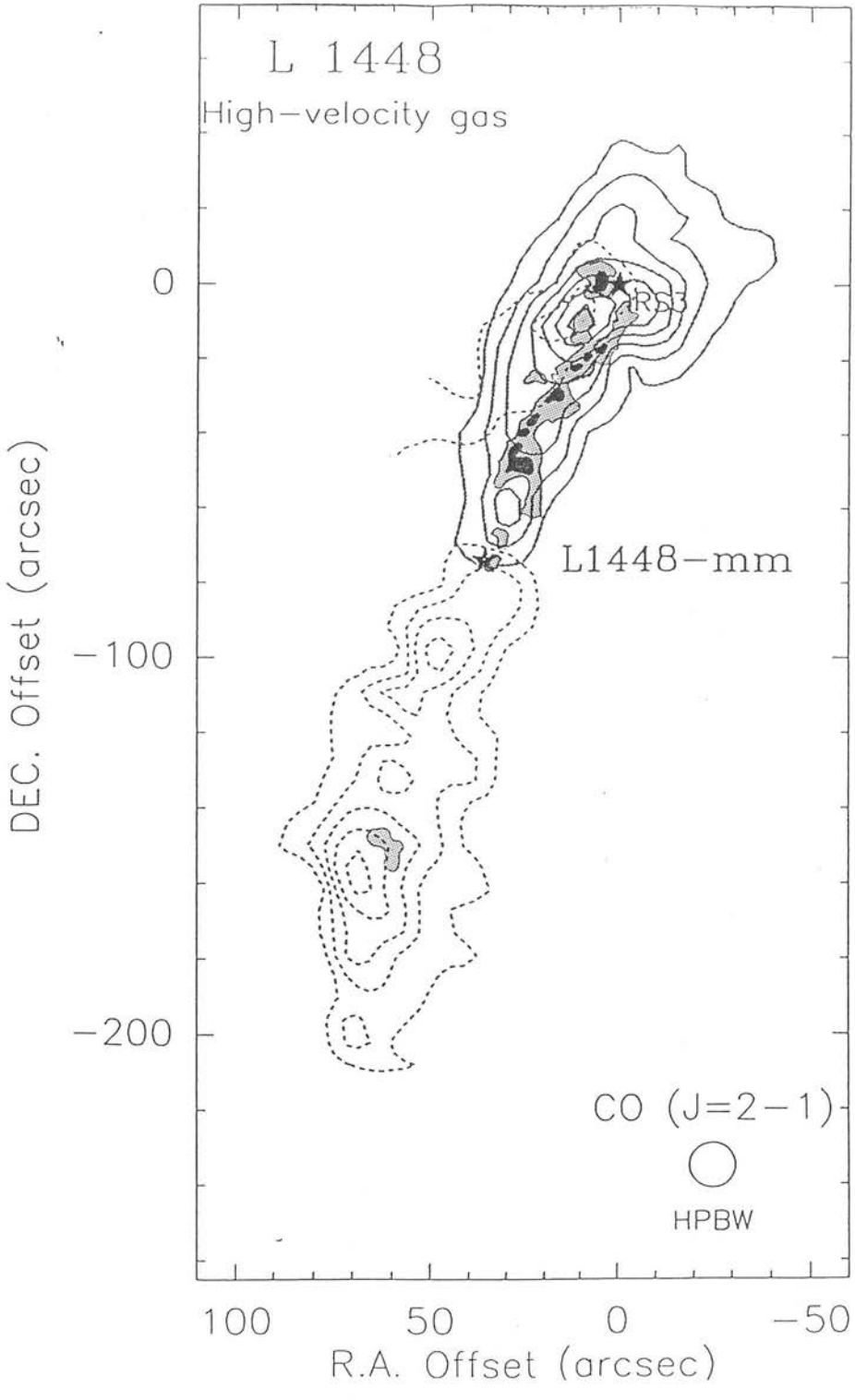

Figure 4.3: The H_2 jet sketched on to the CO 2-1 outflow (contours) of Bachiller *et al.* (1990).

required to establish a spatial coincidence. However, the decrease in bow-shock "size" is consistent with the deceleration of the CO bullets with increasing distance from the source.

Thus, the H_2 jet in L1448 appears to be physically associated with the CO outflow. Its characteristics are similar to those of optical jets, with regular clumps and bow shocks, though unlike many of these optical jets (e.g. HH34, HH111, HH110 etc.), the H_2 jet presented here bends smoothly through $\sim 15°$ over its observed length. A more detailed analysis of the H_2 jet structure is made in section 4.4.

4.3.2 HCO^+ and CS Observations of the Ambient Environment

The spectra in figure 4.4 and the contour plot in figure 4.5 show the distribution of HCO^+ J=3-2 emission in L1448. The distribution of CS J=5-4 is similarly illustrated in figures 4.6 and 4.7. Two distinct peaks are seen in both species, coincident with L1448-mm and the infrared source IRS3. These peaks also coincide with the clumps observed by Bachiller *et al.* (1990) in NH_3 (1,1) and (2,2). A weak ridge connects these two clumps and closely follows the jet direction; this feature is also seen in NH_3. Notably, a similar molecular ridge, traced in NH_3 and CS, is observed along the *optical* jet in the HH34 system (see chapter 5).

The size of the HCO^+/CS clumps shown here are consistent with the dense cores observed and resolved in the dark cloud surveys of Myers *et al.* (1991) and Lada *et al.* (1991). These authors measure CS core sizes of $\sim 0.1 - 0.5$ pc; for the northern clump in L1448 (hereafter L1448N) the FWHM size $\sim$ 0.1pc (HCO^+) and $\sim$ 0.07pc (CS); for the southern clump (L1448S) the FWHM size $\sim$ 0.1pc (HCO^+). Here, the HCO^+ 3-2 cores are slightly larger than the CS 5-4 cores because the CS requires higher densities to excite the observed transition.

Myers *et al.* (1991) find that elongation is a common characteristic among dense cloud cores. Myers *et al.* and Lada *et al.* (1991) report aspect ratios (major axis/minor axis) of on average $\sim$ 2. However, figures 4.5 and 4.7 show only a slight elongation of L1448S along the outflow direction (notably no elongation is observed perpendicular to the outflow direction, as would be expected from a disk structure around L1448-mm),

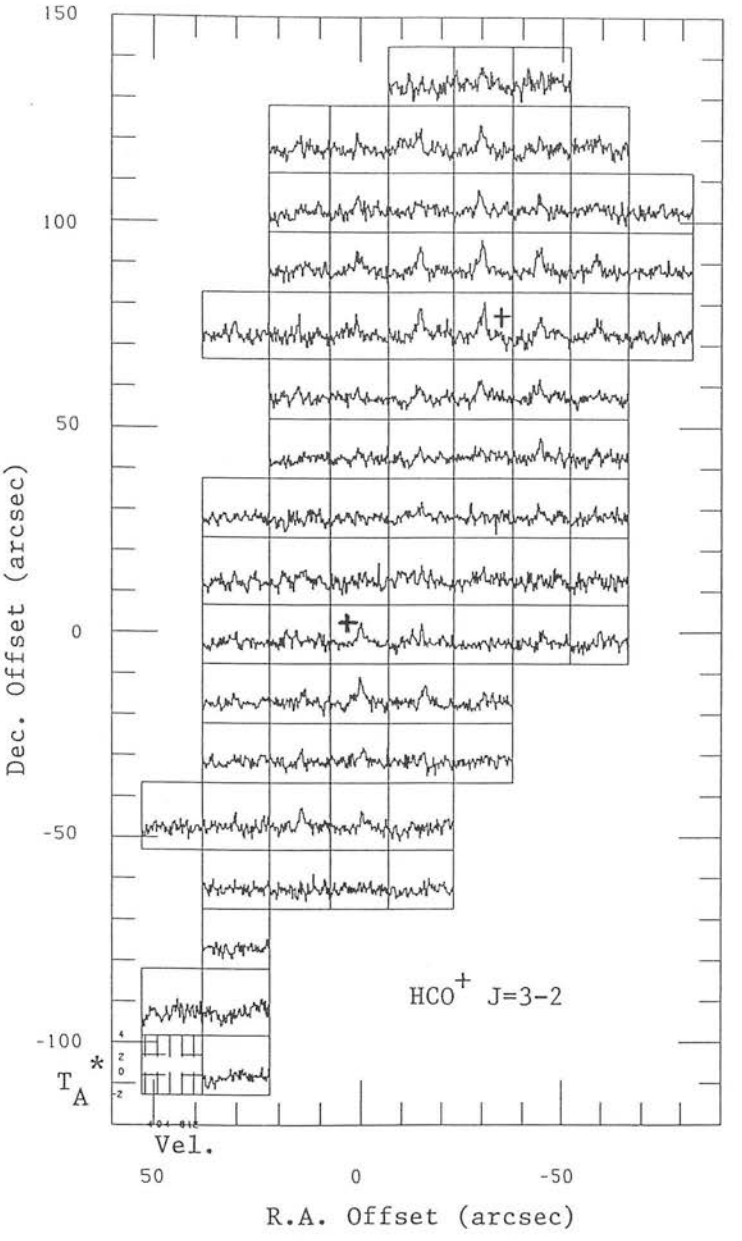

Figure 4.4: HCO^+ J=3-2 spectra in L1448. The central map position coincides with the L1448-mm source (marked with a cross), at RA(1950): $3^h22^m34^s.3$, DEC(1950): $30^o33'35''$. The infrared source IRS3 is also marked.

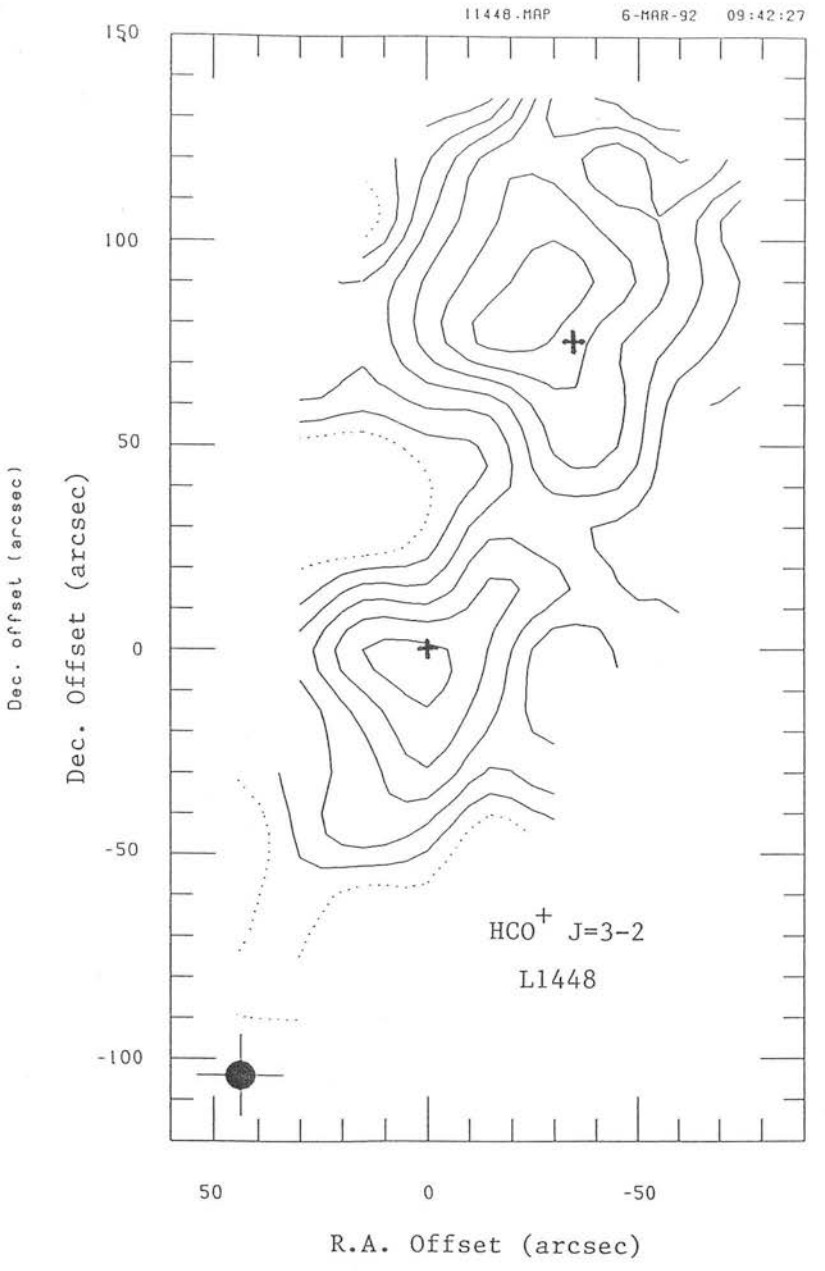

Figure 4.5: A contour plot of the HCO^+ 3-2 antenna temperature integrated from -5 to 15 km s^{-1}, taken from the spectra in figure 4.4. The contours increase in steps of 1 K km s^{-1} from a dotted base level of 0 K km s^{-1}. Map centre as for figure 4.4.

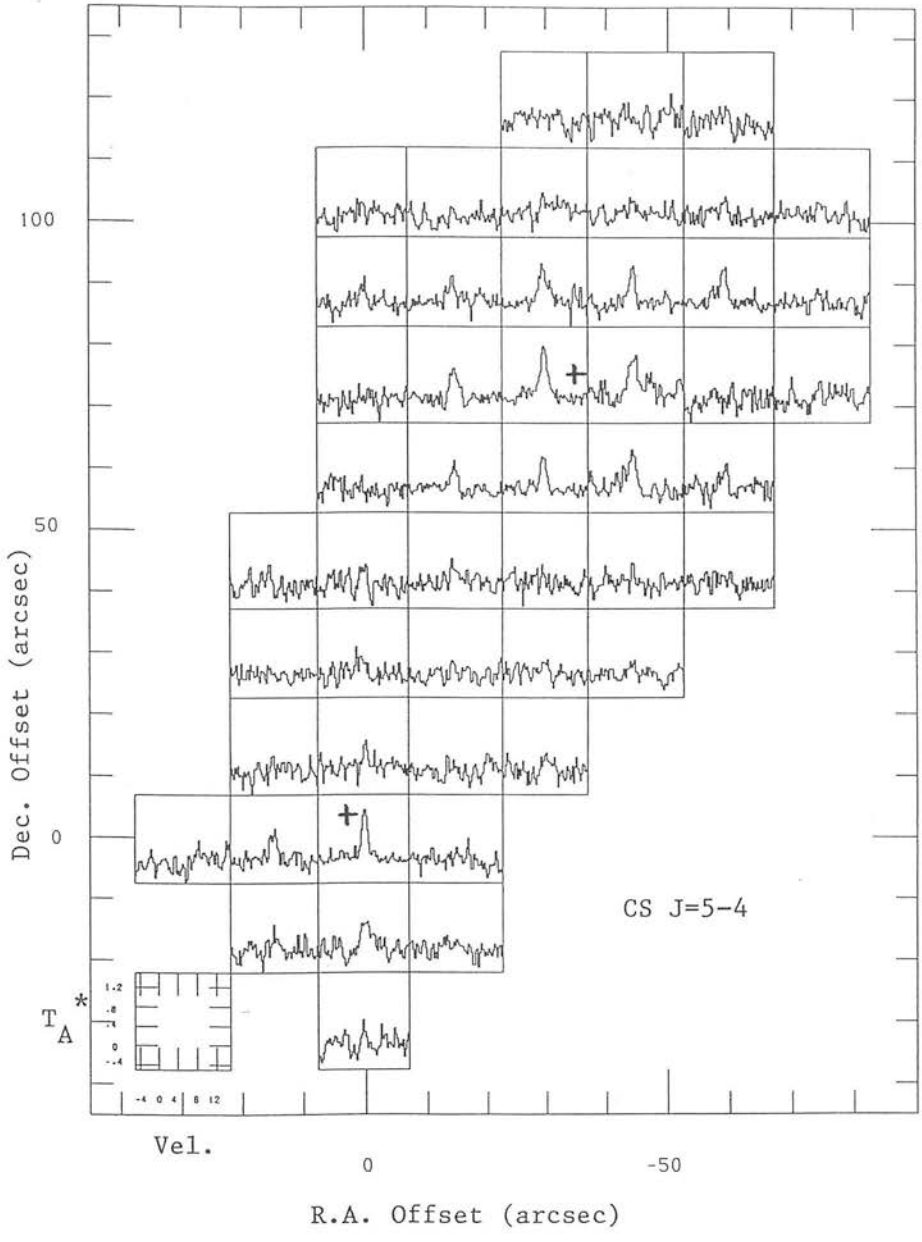

Figure 4.6: CS J=5-4 spectra in L1448. (0,0) as for figure 4.4; L1448-mm and IRS3 are marked with crosses.

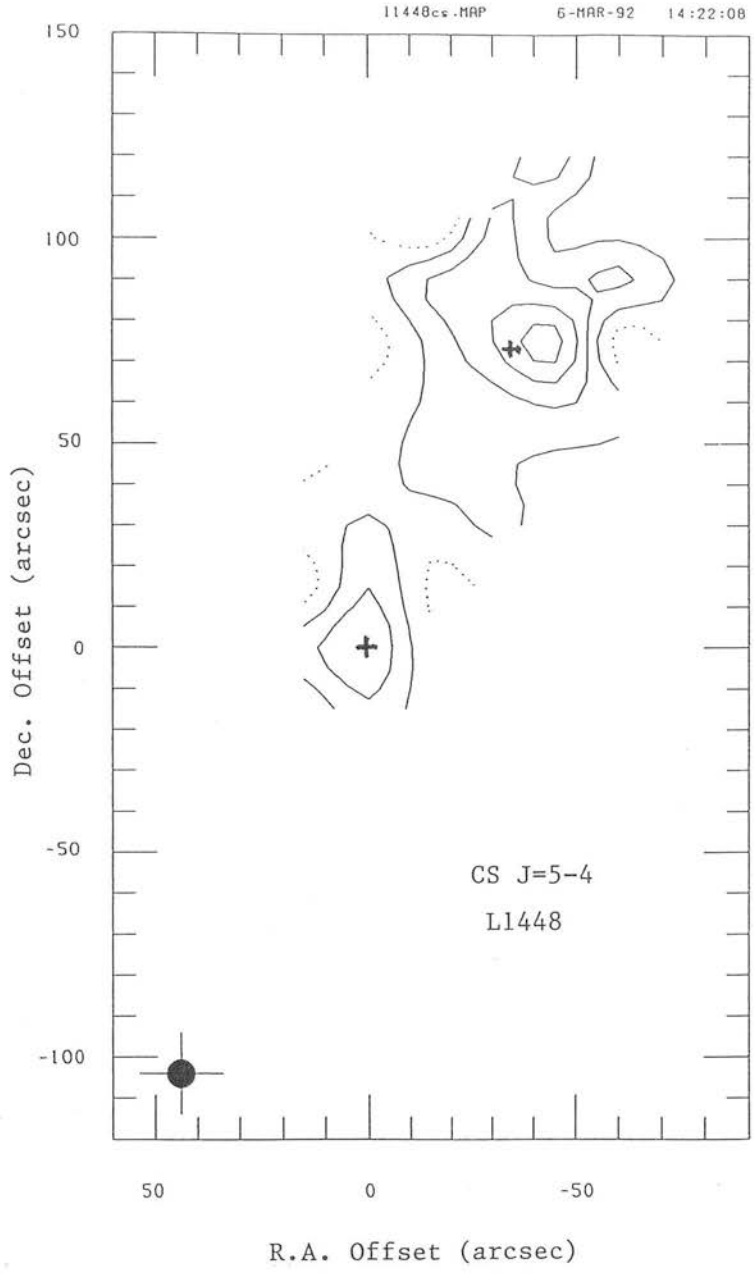

Figure 4.7: A contour plot of the CS 5-4 antenna temperature integrated from -5 to 15 km s^{-1}, taken from the spectra in figure 4.6. Again the contours increase in steps of 1 K km s^{-1} from a dotted base level of 0 K km s^{-1}. Map centre as for figure 4.4.

and there is no discernible elongation in L1448N. The aspect ratio of L1448S measured roughly from the FWHM contour in each figure is $\sim 1.2 - 1.4$.

The 5×5 grid of HCO^+ and CS spectra centred on IRS3 (these spectra constitute the clump L1448N) have been averaged and are shown in figure 4.8 (top). Similarly, figure 4.8 (bottom) shows the average of the 5×5 HCO^+ spectra and the 3×3 CS spectra around L1448-mm (this averaging serves to increase the signal-to-noise of the spectra). Myers *et al.* (1991) and Lada *et al.* (1991) record CS 2-1 line widths < 1 km s^{-1} in their studies of dark cloud cores (note that these quiescent cores do not *as yet* contain embedded sources but rather are thought to represent the initial conditions for star formation). Here the HCO^+ and CS spectra towards the peak positions in L1448N and S (figures 4.4 and 4.6) have line-widths $\sim 2.0(\pm 0.5)$km s^{-1}; the averaged spectra in figure 4.8 yield slightly greater FWHM values of $\sim 1.5 - 3.0$ km s^{-1}, the HCO^+ lines being marginally wider (the slight increase in the line widths of the averaged profiles over individual spectra is due to the velocity gradient across the L1448 region, discussed below). By comparison, the averaged HCO^+ 3-2 spectra in HH1 and HH2 (chapter 3) are slightly wider still; FWHM line widths ~ 2.6 and ~ 4.8km s^{-1} for HH1 and HH2 respectively. These increasing linewidths may be due to the mass motions associated with infall, in the case of L1448-mm and IRS3, or in the case of HH1/2 to the exciting outflow. However, whilst being wider than the dark cloud core linewidths of Myers *et al.* and Lada *et al.* they are still appreciably narrower than HCO^+ and CS profiles observed in the supernova remnant IC 443, by a factor of ~ 5 (Ziurys *et al.* 1989) and the shocked H_2 lines observed in HH objects (Zinnecker *et al.* (1989), by a factor of ~ 10.

The clump sizes and HCO^+/CS line-widths presented here for L1448 (and indeed also for HH2) do not support the power-law correlation measured by Larson (1981), Dame *et al.* (1986) and later Lada *et al.* (1991) in their studies of quiescent cloud cores. These authors record a relationship between cloud core size and internal velocity dispersion of the form $\Delta v \propto r^{0.4} \rightarrow r^{0.5}$. When compared to the log. log. plot presented by Lada *et al.*, for composite CS 2-1 profiles of clumps of similar sizes to L1448N and S (though clumps where no embedded sources are known to exist), the HCO^+ 3-2 and CS 5-4 linewidths from the averaged plots in figure 4.8 are too large, by a factor of a

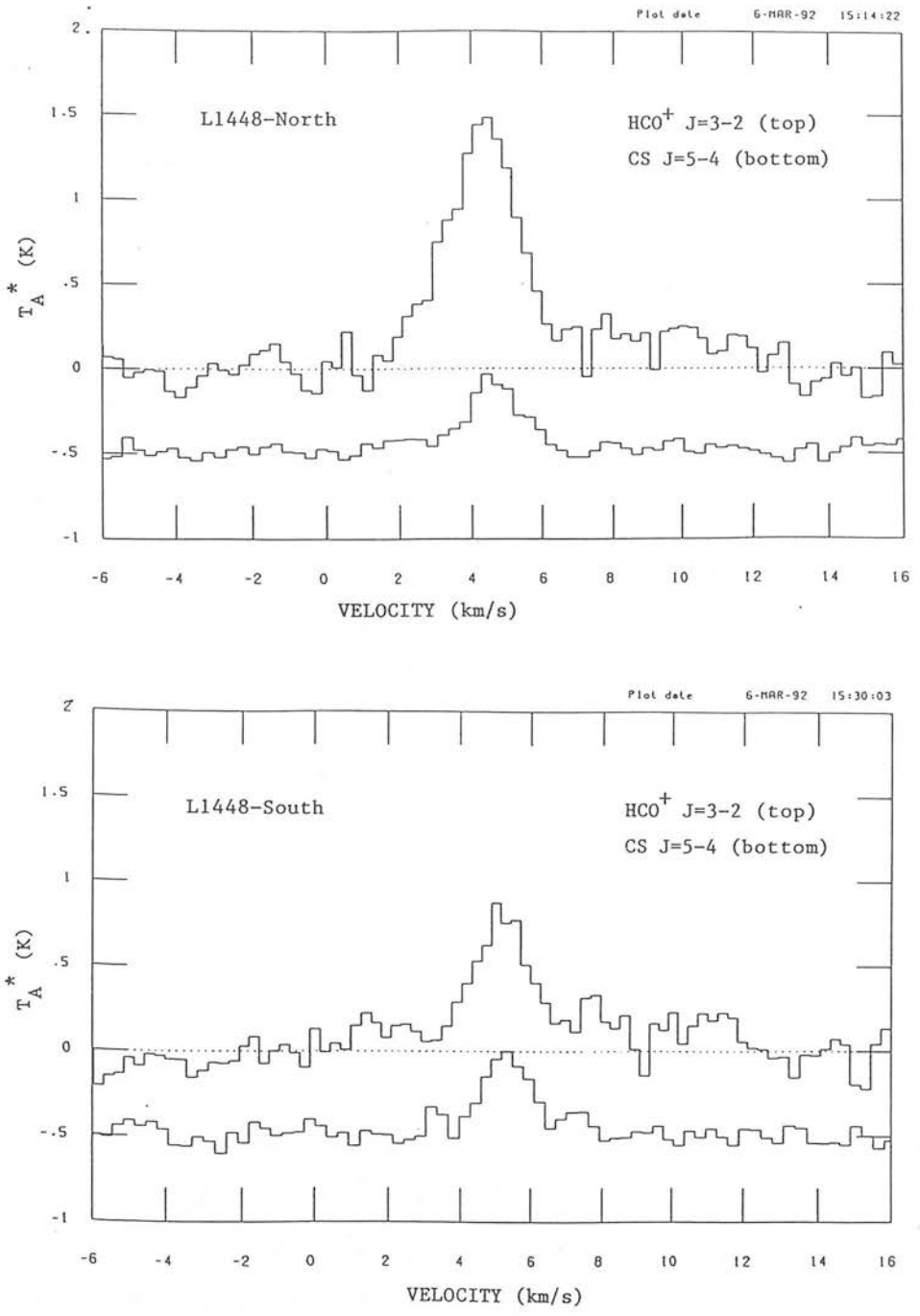

Figure 4.8: Average plots of the 5×5 HCO^+ and CS spectra that constitute the clump L1448N (*top*), centred on (-30,75), and average plots of the 5×5 HCO^+ and 3×3 CS spectra in L1448S, centred on (0,0).

few.

Figure 4.9 shows channel maps obtained from the HCO^+ J=3-2 observations of L1448. Bachiller *et al.* (1990) report signs of rotation in L1448N. The NH_3 emission at 4.3 km s^{-1} is shifted eastward from that at 4.8 km s^{-1}. Here we see no evidence for such east-west rotation. However, we do detect a north-south velocity gradient, across L1448N and down towards L1448S; the higher velocity gas occurs to the south of L1448N and extends progressively down (with increasing velocity) towards L1448S. This *smooth* north-south gradient is consistent with the rotation of a single cloud (the cloud envelope which encompasses both L1448N and L1448S) since one would expect an abrupt velocity change if these two clumps were independent and at different radial velocities.

In summary, because the peaks observed in CS and HCO^+ are coincidental and essentially equal in size, and because the CS and HCO^+ line widths are the same, then we may conclude that the HCO^+ and CS observations presented here trace the same colocated gas. The smooth velocity gradient observed in the channel maps of this region imply rotation of the L1448 parent cloud envelope (as opposed to rotation of the individual L1448N and S cloud cores). Furthermore, simple thermal broadening of the CS and HCO^+ spectra (at $T_k \sim 10 - 20$K) does not account for the observed linewidths, which may instead result from turbulence or indeed infall onto (or outflow from) the embedded sources IRS3 and L1448-mm.

4.3.3 Column Densities and Core Masses

From the spectra in figure 4.4 and 4.6 and the averaged plots in figure 4.8 we may calculate peak and average HCO^+ and CS column densities in L1448N and L1448S. Assuming thermalised level populations and optically thin emission then the HCO^+ and CS column densities are obtained from (appendix A);

$$N_{HCO+} = 1.79 \times 10^{11} \frac{\exp(12.8/T_{ex})}{(1 - \exp(-12.8/T_{ex}))} \int T_b.dv \qquad \text{for } J = 3 - 2$$

$$N_{CS} = 2.89 \times 10^{11} \frac{\exp(23.5/T_{ex})}{(1 - \exp(-11.7/T_{ex}))} \int T_b.dv \qquad \text{for } J = 5 - 4$$

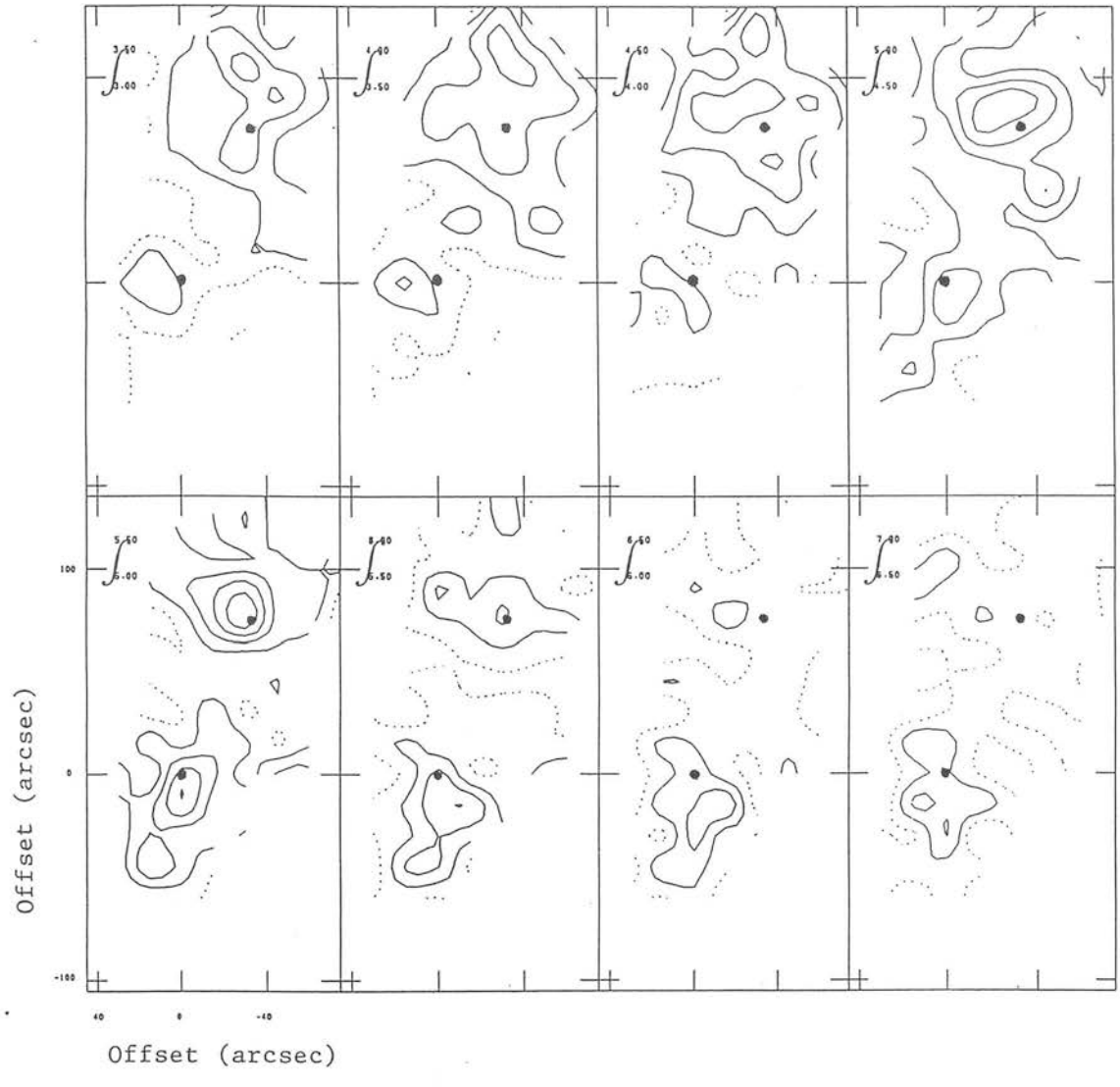

Figure 4.9: Channel maps of the HCO^+ J=3-2 emission in L1448. The velocity interval is 0.5 km s^{-1} and the contours increase from 0 K km s^{-1} (dotted) in steps of 0.3 K km s^{-1}. L1448-mm and IRS3 are marked on each plot.

where once again column densities are in cm^{-2} and integrated line brightness temperatures are in K km s^{-1}. Bachiller *et al.*'s (1990) NH_3 (1,1) and (2,2) observations of L1448, observations which resolve both L1448N and L1448S, yield kinetic temperatures of $T_k \sim 13K$ for each cloud core. I use this value here for the excitation temperature. Also, the integrated antenna temperatures are corrected for the JCMT beam efficiency and η_f is assumed to be unity. Peak column densities are thus calculated from the spectra in figures 4.4 and 4.6 at L1448-mm (0,0) and IRS3 (-30,75), and are listed in table 4.1. Also presented here are average core column densities, derived from the averaged HCO^+ and CS spectra in figure 4.8.

Table 4.1: Column Densities (in cm^{-2}) in L1448.

Source	N_{HCO+} (peak)	N_{CS} (peak)	....	Source	N_{HCO+} (average)	N_{CS} (average)
IRS3	5.5×10^{12}	8.7×10^{12}		L1448N	4.2×10^{12}	4.0×10^{12}
L1448-mm	4.5×10^{12}	7.6×10^{12}		L1448S	1.9×10^{12}	–

The HCO^+/CS column density ratios in both L1448N and L1448S ~ 1. This ratio is in accordance with the observations of dark cloud cores reported by Mann & Williams (1980) and with the later studies of the quiescent dark cloud TMC-1 and the Orion OMC1-Ridge (Irvine & Knacke 1988, Blake *et al.* 1987).

From the average HCO^+ column densities we may estimate core masses, where again the mass $M = 1.3 \times N_{HCO+} \times Area \times m_{H2}/X_{HCO+}$ (as used in section 3.3.1).

Here, the area is simply that covered by the averaged spectra; each 5×5 grid covers $60\widehat{''} \times 60\widehat{''}$ which at 300 pc is $(2.7 \times 10^{17}\mathrm{cm})^2$. An HCO^+ fractional abundance ratio of $X_{HCO+} = 2.3 \times 10^{-9}$, as determined from observations of the Orion OMC1-Ridge, is also used (Blake *et al.* 1987). I therefore derive core masses of $0.3\,M_\odot$ for L1448N and $0.1\,M_\odot$ for L1448S. These values should be regarded as lower limits because *i)* we have assumed optical thin emission, and *ii)* the excitation temperature used is likely to be an underestimate of that appropriate to the CS and HCO^+ lines observed (these transitions will probe deeper into each core than the NH_3 (1,1) and (2,2) lines of Bachiller *et al.*). Our mass estimate is also dependent on the HCO^+ fractional abundance ratio chosen.

From the H_2 column density to visual extinction ratio quoted by Bohlin *et al.* (1978) we may also estimate the extinction towards L1448-mm and IRS3: From an $N_{H2}/A_v \sim 2 \times 10^{21}$, and using the HCO^+ abundance ratio quoted above we arrive at an $A_v \sim 1$ for both L1448-mm and IRS3. By comparison, Bachiller *et al.* (1990) derive a value of ~ 5 from their NH_3 observations of this region. Notably, if this difference is due to our use of an incorrect (overestimated) HCO^+ abundance ratio and so an underestimated H_2 column density, then correcting X_{HCO+} in the above mass calculation (by this factor of 5) brings the mass estimates derived above for both L1448N and L1448S in line with the clump masses measured by Myers & Benson (1983) in their quiescent cloud surveys.

4.3.4 The Virial Mass

An upper limit to each core mass may be obtained by assuming that both cloud cores are in virial equilibrium. The virial theorem states that in hydrostatic equilibrium twice the kinetic energy of the cloud gas particles balances the total cloud potential energy. Ignoring surface pressure from gas outside the cloud, and magnetic and rotational energy contributions to cloud support, then the gravitational potential energy Ω is balanced by the thermal and turbulent kinetic energies;

$$2(E_{kin} + E_{therm}) + \Omega = 0 \tag{4.1}$$

For an ideal gas with $\gamma = C_p/C_v = 5/3$, the thermal energy contribution to cloud support

$$E_{therm} = \frac{3}{2}\frac{M}{\mu_H m_H}kT_k \tag{4.2}$$

where M is the cloud mass and $M/\mu_H m_H$ is the number of thermal gas particles. At a gas kinetic temperature $T_k = 10$K and mass $M = 1\,M_\odot$, $E_{therm} = 10^{34}$ Joules (note that at this temperature the sound speed is 0.2 km s^{-1}). By comparison, the bulk kinetic energy of the gas particles in 3-dimensions is

$$E_{kin} = \frac{3}{2}Mv_d^2 \tag{4.3}$$

where the velocity dispersion v_d is equal to the observed FWHM spectral line width σ , assuming gaussian line profiles. For a cloud mass $M = 1\,M_\odot$ and an emission line width ~ 2 km s^{-1}, $E_{kin} = 1.2 \times 10^{37}$ Joules; this is a factor of 10^3 greater than the thermal energy contribution to cloud support. Therefore, in deriving the virial mass we may neglect E_{therm} in equation 4.1.

The gravitational potential energy for a spherically symmetric mass distribution of constant density is (Dyson & Williams 1980, p. 178)

$$\Omega = -\frac{3}{5}\frac{M^2 G}{R} \tag{4.4}$$

and so from equations 4.1, 4.3 and 4.4 the virial mass is given by

$$M = \frac{5}{G}\frac{R\sigma^2}{} \tag{4.5}$$

Since the spectra averaged in figure 4.8 cover an area of $(2.7 \times 10^{17}$ cm$)^2$ a cloud radius of 1.4×10^{17} cm is used for both L1448N and L1448S. The line widths of these averaged spectra thus lead to virial masses of $\sim 3.60\,M_\odot$ (HCO^+) and $\sim 12.0\,M_\odot$ (CS) for L1448N, and $\sim 150\,M_\odot$ (HCO^+) for L1448S. Although these values are subject to the accuracy of the measured line-widths (an error of approximately 10-20%), they are clearly much

greater than those obtained from the HCO^+ column densities above and so appear to be over-estimated. It is likely that additional forms of cloud support (e.g. magnetic pressure or rotation) are required in the above equation for virial equilibrium (equation 4.4). However, this analysis does provide firm evidence that the observed line widths do not simply measure random gas motions which provide cloud support, but rather include rotation, turbulence and perhaps also infall or indeed outflow associated with each cloud core.

4.4 DISCUSSION

4.4.1 Canto's Steady Stellar Wind Model

It is perhaps tempting to identify the H_2 jet in figure 4.1 with the stellar wind model for HH objects proposed by Cantó *et al.* (1980, 1988). He has considered the expansion of an isotropic wind into an ambient environment through which there is a density gradient extending in one direction. The static configuration, produced when the ram pressure of the wind equals the gas pressure of the molecular cloud, results in the formation of an ovoidal cavity along which ambient gas may be entrained and eventually dumped at the focus of the cavity. Shocking along the cavity walls will produce hot-spots – HH nebulae (similar to the knots and bow-shocks observed here in L1448), though the brightest HH features will occur at the focus.

The H_2 jet shown here does resemble the curving shocked face of a cavity wall. The HCO^+ and CS maps of L1448S also show a density gradient extending radially away from the L1448-mm source, as required by the Cantó model. However, one would also expect to see the opposite cavity wall, curving in the opposite direction and to the west of the H_2 structure in figure 4.1, together with faint emission from the wall nearest to us; i.e. from the axis of the toroidal flow. The reader is referred to the observations of optical and infrared bipolar nebulae and to the optical jets where a cone of emission is clearly discern*i*ble (e.g. GGD27, Aspin *et al.* 1989; Cep A and Orion/IRC2, Lane 1989; HH1/2, Strom *et al.* 1985).

Assuming for the moment an ovoidal cavity structure for the H_2 jet in L1448, then from a simple geometrical argument (described in appendix B and shown here in figure

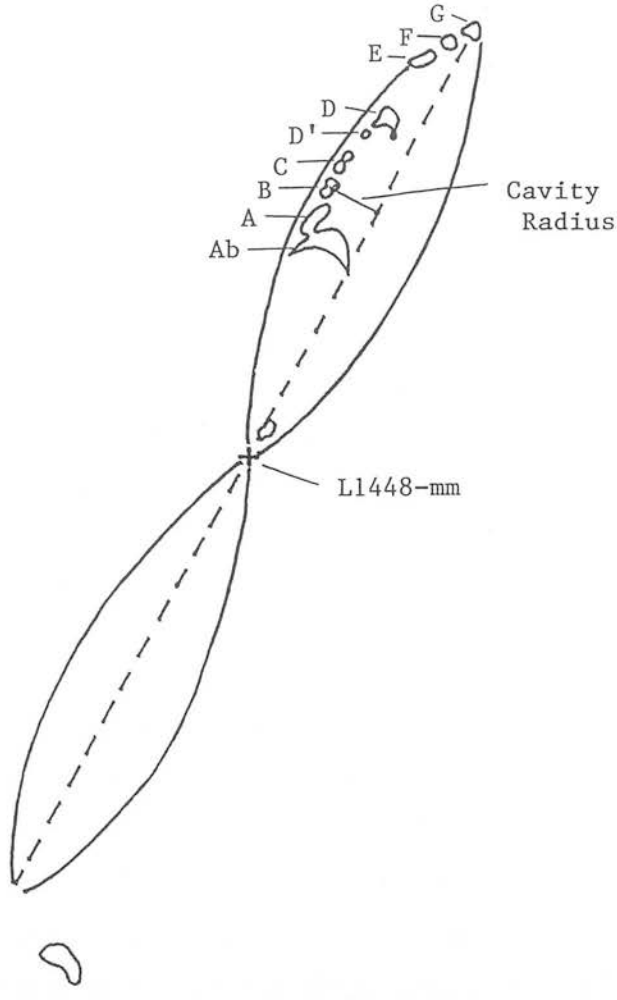

Figure 4.10: A drawing showing an ovoidal cavity structure similar to that proposed by Cantó (1980). The H_2 jet is included (drawn to scale).

4.10) we may calculate the expected ratio of near-IR fluxes that should be observed if the UKIRT beam is turned towards the eastern edge of the cavity wall and then to the axis of the cavity. This value may then be compared to the observed ratio; in this way we may check whether the emission from the axis of the flow is likely to be weaker than the noise level of the observations. Here I assume that the observed structure in figure 4.1 is the eastern cavity wall, and that the axis of the cavity lies along a line joining the source L1448-mm to the knot farthest from this position, knot G (though note that this axis does not point towards the southern H_2 feature, at ($30\widehat{''}$, -$75\widehat{''}$)). This axis is drawn on figure 4.10. Also, the H_2 emission is assumed to be uniform around a circular cross-section at any given distance along the axis. This emission is assumed to derive from the cooling flow over the cavity wall: From Cox (1972), Cantó (1980) points out that the thickness of this boundary layer d is of the order of 10^{16}cm (for a preshock wind density of 10-100 cm^{-3} and a shock velocity of 10-20km s^{-1}). This is indeed similar to the observed thickness. Finally, the radius of the cavity, from the axis to the H_2 knot labelled B in figure 4.10, is measured to be $\sim 9\widehat{''}$ (4×10^{16}cm) and is used in the calculation below.

As the pixel scale of the observations $b = 0.62\widehat{''}$ (3×10^{15}cm) is smaller than the thickness of the cooling flow (10^{16} cm), then from equation B.2 the flux density ratio should be ~ 6. If the rear face of the cavity is heavily obscured, this ratio may increase to ~ 12. However, the peak H_2 flux towards knot B measures 1.9×10^{-18} W m^{-2}pixel^{-1}; no emission is detected towards the axis above a noise level of 0.13×10^{-18} W m^{-2} pixel^{-1}. This leads to a lower limit for the edge/axial flux ratio of ~ 15, a value which is greater than would be expected from simple geometrical dilution. Clearly, if the H_2 structure in figure 4.1 does represent the eastern edge of an ovoidal cavity, we would expect to detect *faint* emission from the axis of the cavity above the noise level attained in these observations. Of course the lack of emission from the opposite (western) cavity wall also undermines this model. Therefore it does not seem likely that a *uniformly shocked* ovoidal cavity model is applicable here.

4.4.2 Confined Stellar Jet Models

Later modelling by Königl (1982), Dyson (1984), Raga (1989), Falle *et al.* (1987) and others has been motivated by observations of optical jets (detailed in Mundt *et al.* 1987). These models go some way to accounting for the knotty structure in these jets, though like Cantó's (1980) model, they are steady-state models and so fail to account for the high proper motions measured for the individual knots (Reipurth 1989). Clearly, proper motion studies of the H_2 jet presented here are warranted. Of particular interest are the bow-shocks observed along the flow (labelled knots Ab, D and G in figures 4.10 and 4.11 below). Whilst the knots along the jet may be steady-state phenomena, these bows may result from internal working surfaces in the flow produced by a variable wind-ejection velocity (Raga *et al.* 1989), or they may constitute "bullet" type HH objects and so possess high proper motions (Bachiller *et al.* 1991b, Norman & Silk 1979).

4.4.3 Interpretation of the L1448 Jet

However, ignoring these bow-shocks for the moment, then close scrutiny of figure 4.1 suggests that the remaining knots along the jet structure are not produced in the way described by the above authors. Instead, these shocks probably result from the impact of a supersonic stellar wind from L1448-mm on the ambient molecular cloud core L1448N, observed here in HCO^+ and CS and by Bachiller *et al.* (1990) in NH_3.

Notably, the clumps in L1448 are strongly asymmetrical (unlike the knots in optical jets; e.g. Mundt *et al.* 1990). Further, the major axes of these ovoidal clumps do not lie along the outflow direction, but rather are tilted through a small angle. By replacing each knot with an oblique molecular shock, the plane of which is parallel to the major axis of each clump, then we can immediately simulate quite accurately the overall smooth bend observed along the jet (though note that the section of the jet labeled E to G seems to be detached from the lower jet portion). This is shown in figure 4.11., where the angle of incidence (θ_1), between the flow streamlines and the shock plane, and the angle of refraction (θ_2), also measured between the (post-shock) flow streamlines and the shock plane, are related at each molecular shock by the simple

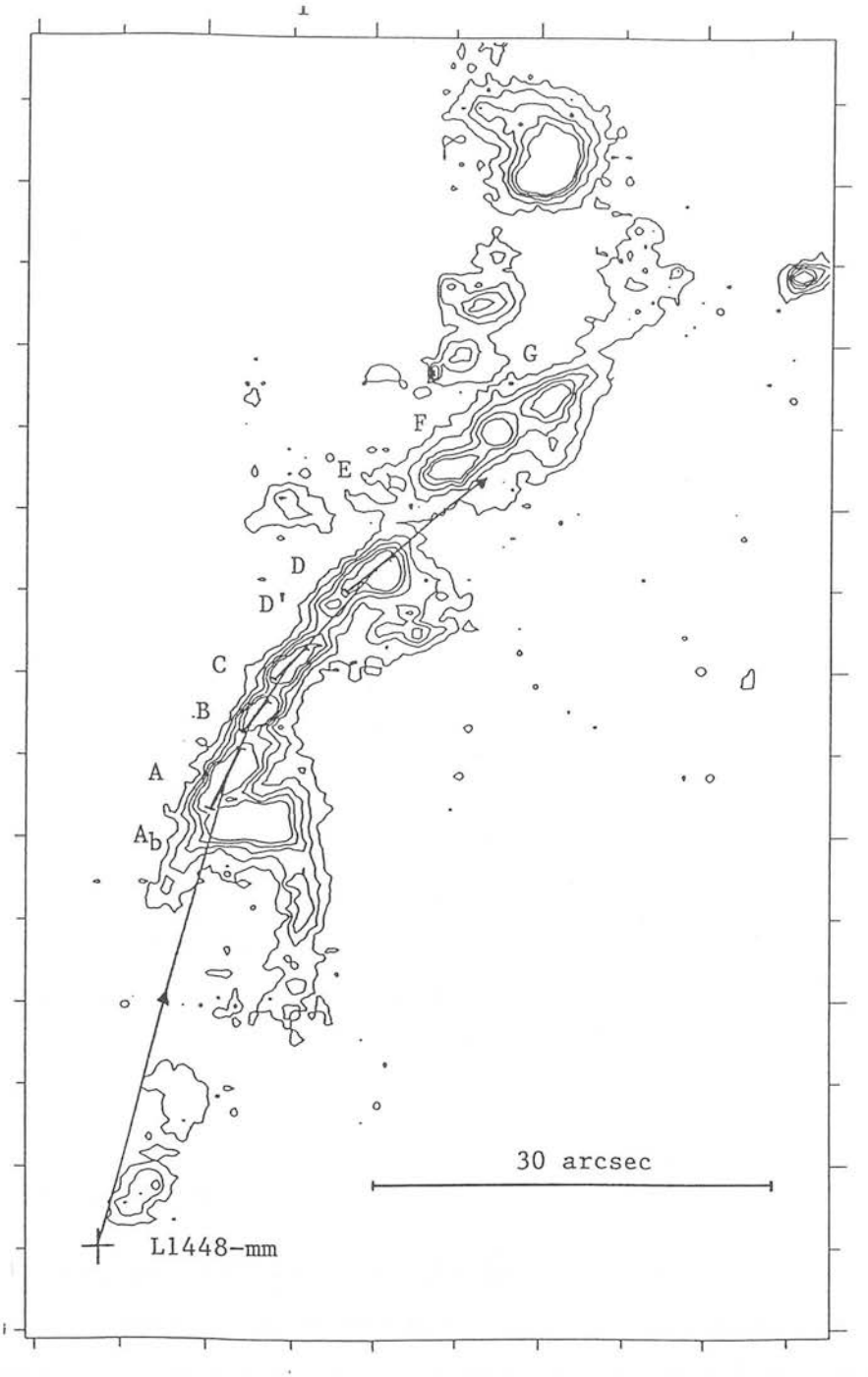

Figure 4.11: A contour plot of the northern lobe of the H_2 jet structure. Molecular shocks have been drawn in at an angle $\theta_1 = 10^o$. This angle produces quite well the curvature in the flow (shown by the arrowed line).

theoretical argument

$$\tan\theta_1 = 6 \times \tan\theta_2 \tag{4.6}$$

Equation 4.6 is obtained from equation 1.4 (for a molecular shock): As the flow passes through each shock, only the velocity component perpendicular to the shock plane is thermalised. Since the shocking is quite oblique (at each shock drawn in figure 4.11, $\theta_1 = 10^o(\pm 1^o)$), then this component is very small, at best $\sim 20 - 30$ km s^{-1} for an initial wind velocity of ~ 200 km s^{-1}. The wind velocity component parallel to the shock remains unaffected and so the flow remains highly supersonic after this and many later shocks (the speed of the post-shock flow behind knot A — assumed to be the first shock traversed by the flow — will be ~ 197 km s^{-1} for the quoted pre-shock wind velocity). Clearly, the wind may traverse a large number of these oblique shocks with little loss of energy. Moreover, these planar molecular shocks present a very efficient way of bending the flow from L1448-mm through the observed angle ($\sim 15^o$).

Finally, the CO high-velocity outflow, situated on the outside of the curving H_2 jet, presents further evidence that the H_2 shock structure results from the interaction of a stellar wind from L1448-mm with the molecular clump L1448N. One might expect entrainment of this ambient molecular gas by the stellar wind, and so hope to observe a molecular (CO) outflow lobe coincidental with the H_2 jet, such as is clearly detected here.

4.5 CONCLUSIONS

Imaging of the bipolar CO outflow in L1448 in H_2 v=1-0 S(1) at 2.12μ reveals a remarkable jet-like structure closely associated with the blue-shifted CO outflow lobe. The jet itself appears to consist of a series of planar shocks, together with three bow-shocks equally spaced along the jet length. The planar shocks are thought to produce the observed bend in the flow, which measures $\sim 15^o$ over the observed jet length. The shocks most probably result from the impact of a stellar wind from L1448-mm on the molecular cloud core situated to the north of the jet source. Moreover, this

interaction is thought to produce the northern lobe of the associated CO outflow via some entrainment process.

Conversely, the bow-shocks observed along the jet may result from individual dense clumps or bullets within the outflow or from a variable wind ejection velocity. Notably, the bow-shock sizes decrease with increasing distance from the source; this trend is consistent with the observed deceleration along the CO outflow.

I also report sub-millimeter observations of the L1448 ambient cloud envelope. Colocated HCO^+ J=3-2 and CS J=5-4 clumps peak towards the two embedded infrared sources in this region. Mass estimates derived for both cloud cores (labeled L1448N and L1448S here) from HCO^+ column densities are far smaller than virial masses obtained from HCO^+ and CS line widths. These latter virial mass estimates are believed to seriously over-estimate the true core masses. Core collapse, rotation and perhaps also outflow are thought to contribute to the observed molecular line widths; these processes have not been considered in the analysis.

Chapter 5

HH34: An Optical Jet System

SUMMARY: In the following chapter I discuss NH_3 observations of the molecular environment around HH34 and its exciting star. NH_3 (1,1) integrated intensity contours reveal two peaks, though neither is coincident with the HH34S bow-shock nor with the exciting source of the system. Instead, the northern peak is offset by ~ 40 arcseconds east of the source (HH34IRS), whilst a ridge of emission appears to follow the outflow direction. Towards HH34IRS the NH_3 column density is lower by a factor of ~ 10 than towards NH_3 peaks elsewhere in the HH34 system. On comparing the NH_3 morphology in HH34 with that seen in other young stars with outflows, this apparent underabundance occurs quite frequently: In many cases, there is no central NH_3 condensation, but rather this molecule is confined to a toroidal structure that surrounds the source. This scenario is discussed here. Also, a map showing the distribution of NH_3 (1,1) optical depth around HH34 reveals an additional optically thick, unresolved clump associated with the HH34S bow-shock. Remarkably, the column density is higher here than in any other position observed, even though the integrated line intensity contours clearly decrease towards this position.

5.1 INTRODUCTION

HH34 is certainly a clear-cut example of the association of Herbig-Haro shocks with optical jets and young stellar objects. Discovered independently by Reipurth *et al.* (1986) and Mundt (1986), the HH34 system lies at a distance of ~460pc in the south-east corner of the dark cloud L1640 in Orion. From the optically visible HH34 source (HH34IRS), a knotty 30 arcsecond long jet extends south towards the bow-shaped HH nebula, labeled HH34S by Bührke *et al.* (1988). The photograph in figure 5.1, obtained from an R-band UK Schmidt plate (no. OR 14052), shows this optical jet and bow-shock structure quite clearly. The more sensitive R-band imaging by Bührke *et al.* has also identified a similar, though fainter bow-shock equidistant from the source to the north. They label this feature HH34N. The close alignment of the apices of HH34N and S with the jet and source, and the high proper motions of each nebula all suggest that the HH objects are the "working surfaces" of a bipolar jet or outflow from the exciting young stellar object.

Photometric observations indicate a near-infrared excess towards the source of the HH34 system, HH34IRS (Reipurth *et al.* 1986). Whilst these authors recognise that a significant part of the luminosity is emitted in the far-IR, they never-the-less estimate a total luminosity of $0.5\,L_{\odot}$ for the source. From a low-resolution red spectrum they further estimate the extinction towards HH34IRS; $A_v \sim 5$.

Reipurth *et al.* (1986) also provide millimeter-wavelength observations of the HH34 molecular environment. Their ^{13}CO integrated intensity contours peak on the exciting source for the jet and HHs. ^{12}CO spectra however show no indication of high-velocity wings down to a $T_A^* \sim 50$mK (this lack of a molecular outflow counterpart to the optical jet has recently been confirmed by Matthews private communication 1991, who similarly observed the exciting star, jet and HH34S bow-shock, though in CO J=3-2 and with a 15 arcsecond beam). Observations of the region have also been made in NH_3 with the VLA (Anglada et al., 1991 – AERTCH). They report the detection of a ring of emission to the east of the central exciting source, plus a clump associated with the reflection nebula near the end of the optical jet.

I also present here NH_3 observations of the HH34 surroundings, though at a higher

sensitivity. The detection of both main and hyperfine components of the (1,1) transition allow us to examine the variation in optical depth around the region. I compare our data with the higher resolution VLA NH_3 results, as well as with other molecular studies where I discuss the often anomalous NH3 abundance as compared to other molecular gas tracers.

Figure 5.1: An R-band image of the jet and bow-shock in HH34. Image scale 2 arcsec/mm.

5.2 OBSERVATIONS

The NH_3 observations presented here were obtained with the Max-Plank-Institut für Radioastronomie 100 metre radio telescope located in Effelsberg, Germany during December 1989. We observed the (1,1) and (2,2) inversion transitions simultaneously, each at approximately 23.7GHz (1.3cm), using the 18 – 26 GHz maser receiver and auto-correlating spectrometer split into two 512 channel bands (though the signal to noise level obtained was not sufficient to detect the latter transition). At these frequencies the beamwidth measures 40 arcseconds FWHM (at 460pc, $40^{\widehat{\prime\prime}}$ ~0.1pc); the main beam efficiency is 0.4. In mapping the region a grid spacing of 20 arcseconds was used. We were also interested in obtaining velocity information and so observed with high spectral resolution (12.2 kHz or 0.15 km s^{-1}). Typically, the system temperature was ~65K. The on-source integration time for each point was 2 minutes, the only exception being towards HH34S, where we integrated for 6 minutes to reduce the noise. The observing technique consisted of integrations of 2 or 3 on-source positions followed by an observation of a reference position 30 arcminutes east of the map centre. Pointing checks were made every few hours, and so the error was less than 5 arcseconds rms.

5.3 RESULTS

5.3.1 NH_3 Total Integrated Intensity Map

In figure 5.2 I show a grid of the spectra observed towards the jet, the source and the HH nebula in HH34, together with in figure 5.3 a contour plot of the NH_3 (1,1) integrated line intensity (main component only). Sketched onto figure 5.3 is HH34S, the jet and the source HH34IRS. The ammonia emission is clearly restricted to the source and jet regions; notably the NH_3 also extends along the outflow direction, down from the east of the source to the west of HH34S. Two features are resolved, a peak ~ 40 arcseconds to the east of the source and a north-south "ridge" peaking ~ 20 arcseconds south of the end of the optical jet.

The peaks in this single-dish map of NH_3 emission are in close agreement with the compact VLA clumps observed by AERTCH; the eastern peak coincides with the partial shell-like structure seen at higher resolution, and the peak of the N-S ridge

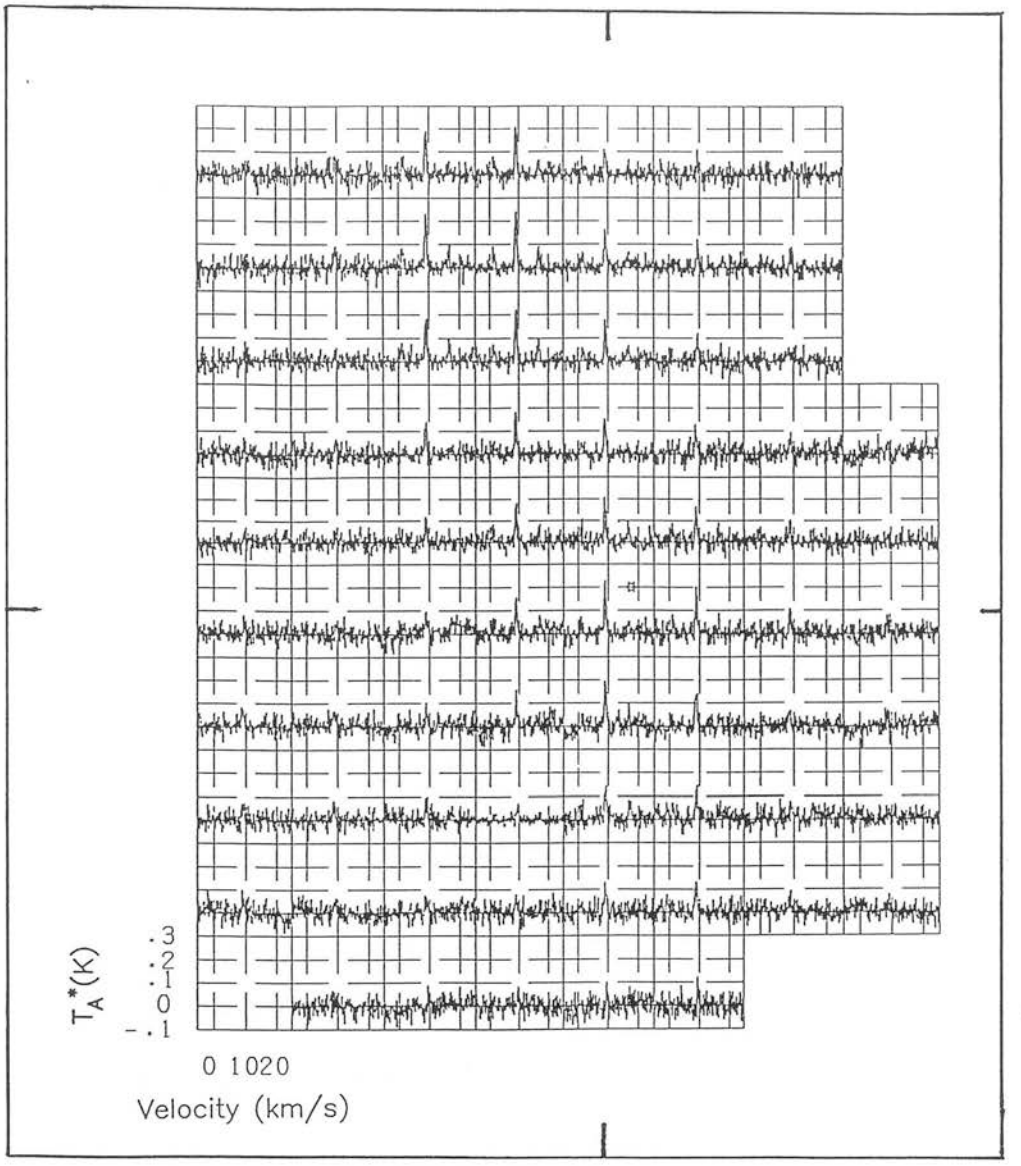

Figure 5.2: The NH_3 (1,1) spectra observed towards the HH34 system. Grid spacings are $20\widehat{''}$: The Effelsberg 100m telescope beam measures $40\widehat{''}$ at 23.7GHz. The map centre is at $\alpha(1950) = 5^h33^m03^s.9$, $\delta(1950) = -06°29'53"$.

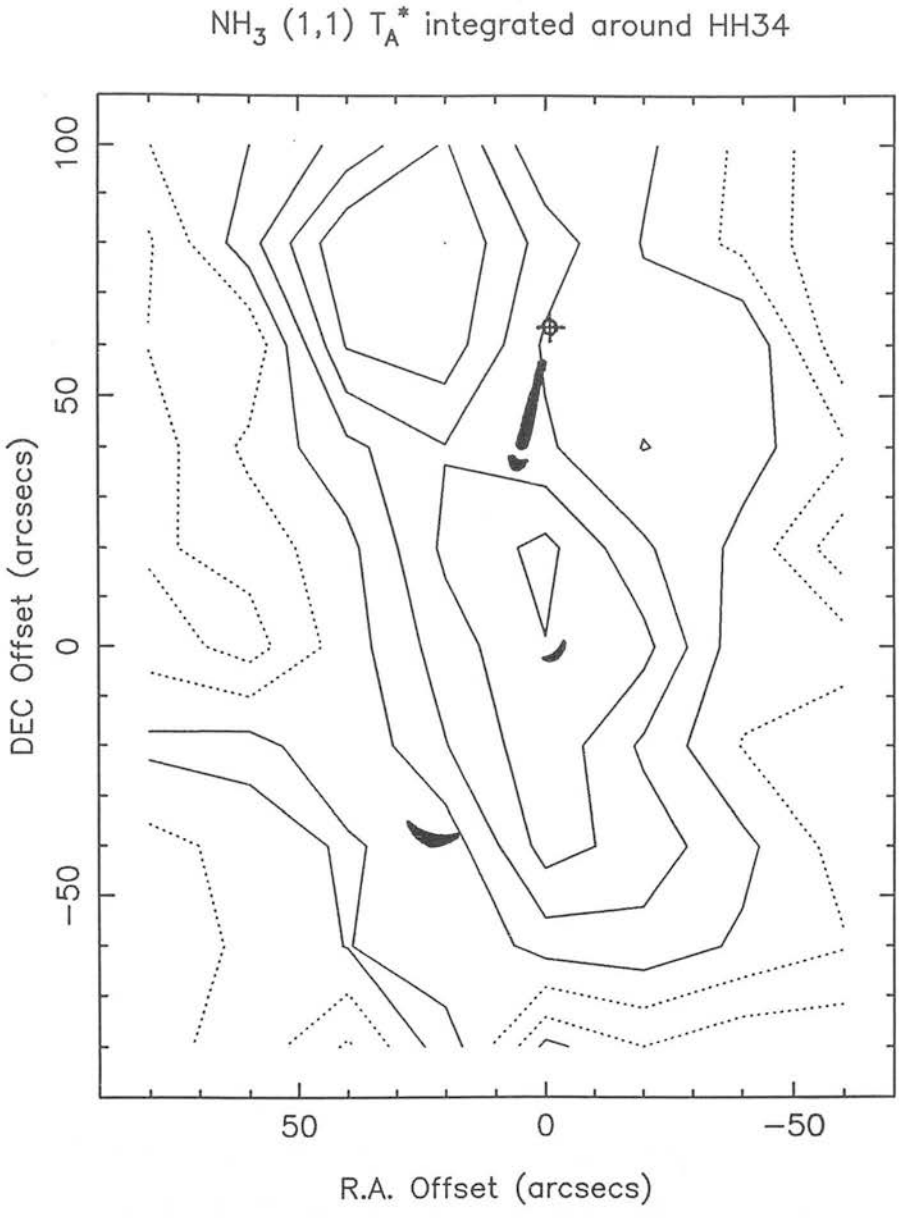

Figure 5.3: A contour plot of the NH_3 (1,1) antenna temperature, T_A^* integrated from 5 to 15 km s^{-1} around HH34. The full contours represent the higher levels; the maximum contour is at 0.21 K km s^{-1} and the levels decrease in steps of 0.03 K km s^{-1}. Sketched on are the HH34 source stellar object, at approx. $(0\widehat{''}, 60\widehat{''})$; the jet; HH34S at approx. $(20\widehat{''}, -40\widehat{''})$ and the reflection nebula from Bührke *et al.* (1988), at approx. $(0\widehat{''}, 0\widehat{''})$. Again, the map centre is at $\alpha(1950) = 5^h33^m03^s.9$, $\delta(1950) = -06°29'53"$.

coincides with the VLA clump near the optical reflection nebula, marked on figure 5.3 (see also Bührke *et al.*, 1988). Notably, neither NH_3 peak is coincident with the exciting source nor with the HH object.

The main beam brightness temperature ($= T_A^*/\eta_b$) of the Effelsberg data towards the northern clump is $\approx$ 0.4K (see figure 5.5, and note here the temperature scale is T_A^*). The VLA data give 0.7K (see the discussion below); since the clump, as determined by the VLA, fills $\sim 20 - 40\%$ of the Effelsberg ($40\widehat{''}$) beam, these results are consistent if beam dilution is taken into account. There is clearly no other major source of extended NH_3 emission near HH34IRS.

We may compare the Effelsberg NH_3 map to CS J=3-2 and J=2-1 observations (Cernicharo 1990, Cernicharo *et al.* 1991) and to ^{13}CO J=1-0 studies of the same region (Reipurth *et al.* 1986). In figure 5.4 I have superimposed the map produced by Cernicharo (1990) of the CS J=3-2/2-1 ratio onto the NH_3 contour plot of figure 5.3. As discussed in section 2.3.3, the ratio of antenna temperatures in LTE is related to the excitation temperature via $T_A^*(3-2)/T_A^*(2-1) \propto \exp(-h\nu_{32}/kT_{ex})$, where T_{ex} defines the relative populations of the J=3 to J=2 rotational levels via the Boltzmann equation. Large Velocity Gradient (LVG) models by Scoville & Solomon (1974) predict that for the rotational levels of CS T_{ex} is dependent on the gas density. Providing the emission is optically thin (not unreasonable for the 3-2 and 2-1 CS lines observed in HH34 since the jet, source and HH are optically visible), then Cernicharo (1990) also maintains that for a kinetic temperature of 10K, the CS(3-2)/(2-1) ratio is also *strongly* dependent on density. However, if the emission is thermalised then T_{ex} is sensitive to the gas kinetic temperature also. Thus, although Cernicharo attributes the observed peaks in the CS(3-2)/(2-1) ratio to high-density features, I add the cautionary note that gas heating may produce an additional enhancement in this ratio; the CS ratio is notably high towards the source, the optical jet *and* the HH object, regions where gas heating is likely to occur.

From the comparison of CS and NH_3 data in figure 5.4 then, notably the northern single dish (and VLA) NH_3 emission peak at relative position ($+20\widehat{''}, +80\widehat{''}$) does not coincide with the CS 3-2/2-1 peak at the central source. Nor do we see an NH_3 peak

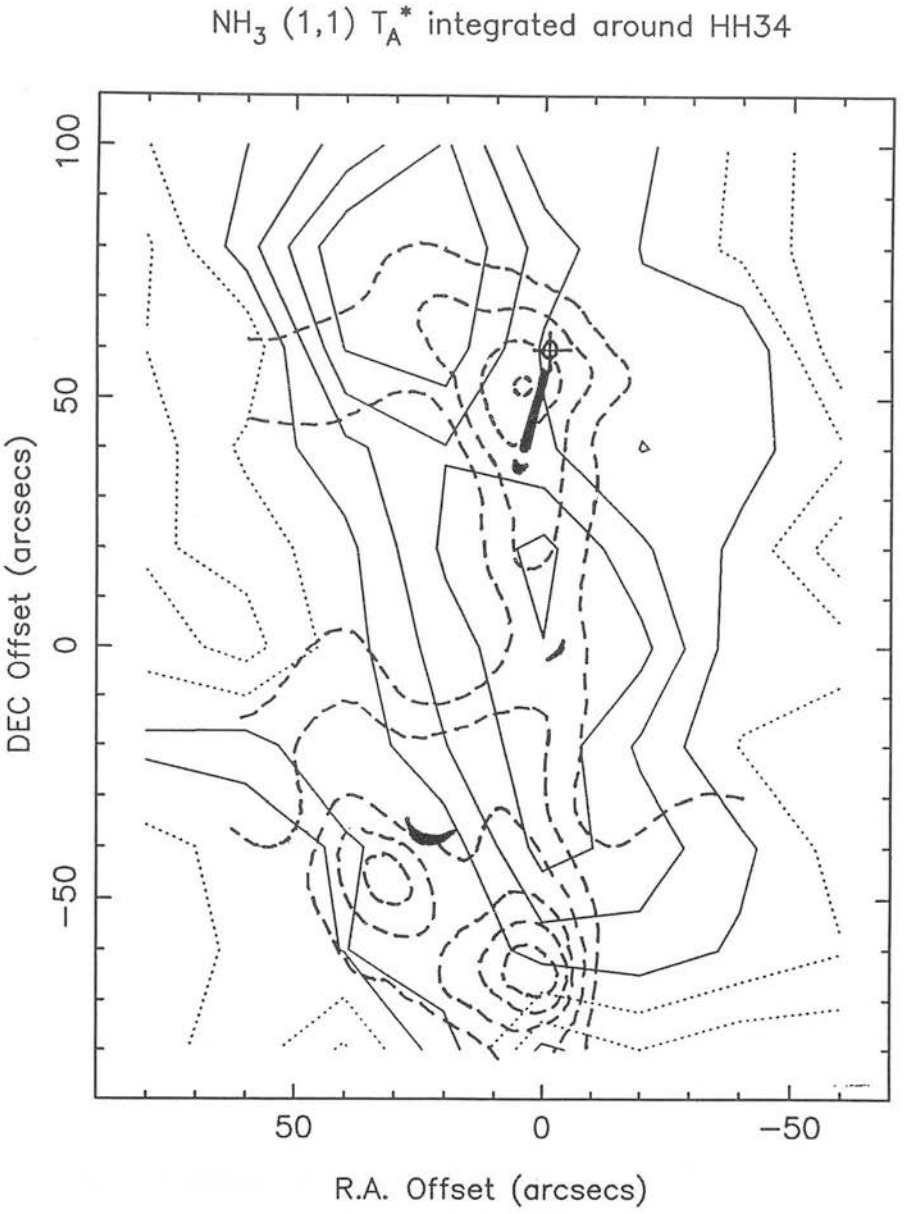

Figure 5.4: Contours of the CS J=3-2/J=2-1 ratio taken from Cernicharo *et al.* (1991) superimposed onto figure 5.3. The CS peaks towards the source and to the south of HH34S, and appears to show a ridge connecting these two peaks.

towards the two CS peaks below the HH34S bow-shock (this situation is similar to that in HH2, where the NH_3 peaks are offset from the molecular peak traced in HCO^+ J=3-2; see chapter 3 of this thesis). Equally, the weak CS ridge between the source and HH34S does not peak near the reflection nebula (marked on figures 5.3 and 5.4); the NH_3 contours clearly peak at this position. The CS does seem to follow the north-south extension of the NH_3 "ridge" however.

Lower resolution ^{13}CO observations conducted by Reipurth *et al.* (1986) also appear to differ from the NH_3 results. Reipurth *et al.* again observe a molecular peak towards the central source HH34IRS. The non-correlation with the NH_3 observations may however be due to the larger 100 arcsecond beam used for the ^{13}CO observations: From the NH_3 contour plot in figure 5.3 we see that a fully sampled ^{13}CO map, centred on HH34IRS with $50\widehat{''}$ spacings, would show a peak coincident with the source if the ^{13}CO emission coincides with the NH_3. Higher resolution ^{13}CO observations are clearly needed to establish whether the ^{13}CO is confined to a distinct clump centred on the source, or whether the ^{13}CO does in fact peak towards the NH_3.

In short, the low-resolution NH_3 results of figures 5.2 and 5.3 do not correlate well with the CS 3-2/2-1 ratio maps towards either the source or HH34S, though both the NH_3 and CS single dish observations do show the presence of a north-south ridge extending roughly along the outflow direction. The offset of the ^{13}CO peak from the northern NH_3 clump may conversely be due to the low resolution of the ^{13}CO observations.

5.3.2 NH_3 Column Density Estimates

From our observations we may estimate gas column densities in this HH system; towards the NH_3 peak situated $\sim$ 40 arcseconds east of the HH34 source, but also towards the source itself where the contours in figure 5.3 are decreasing. The NH_3 column density is once again given by (chapter 3);

$$N_{NH3} = 1.48 \times 10^{13} \frac{1 + \exp(-T_0/T_{1,1})}{1 - \exp(-T_0/T_{1,1})} \frac{\delta v \; \tau_{1,1}}{f_{1,1}}$$

where $T_0 = h\nu_{1,1}/k$, δv is in km s^{-1} and N_{NH3} is in cm^{-2}. Reipurth *et al.* (1986) estimate a value of 25K for the CO excitation temperature towards their molecular clump in HH34. Adopting this value for excitation temperature, $T_{1,1}$, then the fraction of NH_3 molecules in the (1,1) rotational state is $f_{1,1} = 0.44$ (Martin & Barrett 1978).

In figure 5.5 I show the spectrum towards the NH_3 intensity peak at ($40\widehat{''}$,$60\widehat{''}$). Although the line intensity appears to peak at approximately ($20\widehat{''}$,$80\widehat{''}$) in figure 5.3, in the discussion below we see that the optical depth and the column density is greatest towards ($40\widehat{''}$,$60\widehat{''}$). Also, the northern VLA peak observed by AERTCH is found at this position. Consequently, I choose to calculate N_{NH3} towards ($40\widehat{''}$,$60\widehat{''}$); via equation 1.19, $\tau_{1,1} = 1.2(\pm0.2)$, and since the line width is $\delta v = 1.0(\pm0.3)$ km s^{-1}, then the NH_3 column density is $N_{NH3} = 2.4(\pm0.6) \times 10^{15}$cm^{-2}.

Toward HH34IRS at ($0\widehat{''}, 60\widehat{''}$), the spectrum in figure 5.5 gives $\tau_{1,1} = 0.2(\pm0.04)$ and $\delta v = 0.6(\pm0.3)$ km s^{-1}, resulting in a lower column density of $N_{NH3} = 2.0(\pm1.1) \times 10^{14}$cm^{-2}. Ungerechts *et al.* (1980) suggest an abundance ratio ($[NH_3]/[H_2]$) of $\sim 10^{-7}$ in small dark clouds, though the interstellar cloud models of Viala (1986) predict a ratio of $\sim 2 \times 10^{-8}$. Similarly, Herbst & Klemperer (1973) favour a value of $\sim 10^{-8}$, whilst Marcaide *et al.* (1989) use a value of $\sim 3 \times 10^{-8}$ in their analysis of their observations of the HH1-2 system. Collectively, these values imply an H_2 column density of between $2.4 \times 10^{21} - 2.4 \times 10^{22}$cm^{-2} towards the NH_3 intensity peak at ($40\widehat{''}, 60\widehat{''}$), and a lower H_2 column density of between $2 \times 10^{20} - 2 \times 10^{21}$cm^{-2} towards HH34IRS.

From their CO data, Reipurth *et al.* (1986) also calculate the column density of gas towards the HH34IRS source. They arrive at a value not unlike that derived above, $N_{H_2} = 5 \times 10^{21}$cm^{-2}, though this of course is a mean value for the region covered by their larger $100\widehat{''}$ beam which when centred on HH34IRS also includes the northern NH_3 clump.

By smoothing the VLA map to the $40\widehat{''}$ resolution of the Effelsberg observations – using a deconvolved beam size of $\theta = \sqrt{40^2 - 4^2} \simeq 40\widehat{''}$, we may estimate the percentage of emission observed in the $40\widehat{''}$ beam towards HH34IRS that is due to the nearby dense clumps seen with the VLA. From the VLA contour plot of AERTCH I have obtained values for the NH_3 flux density at $8\widehat{''}$ spacings (twice the VLA beam size) and converted

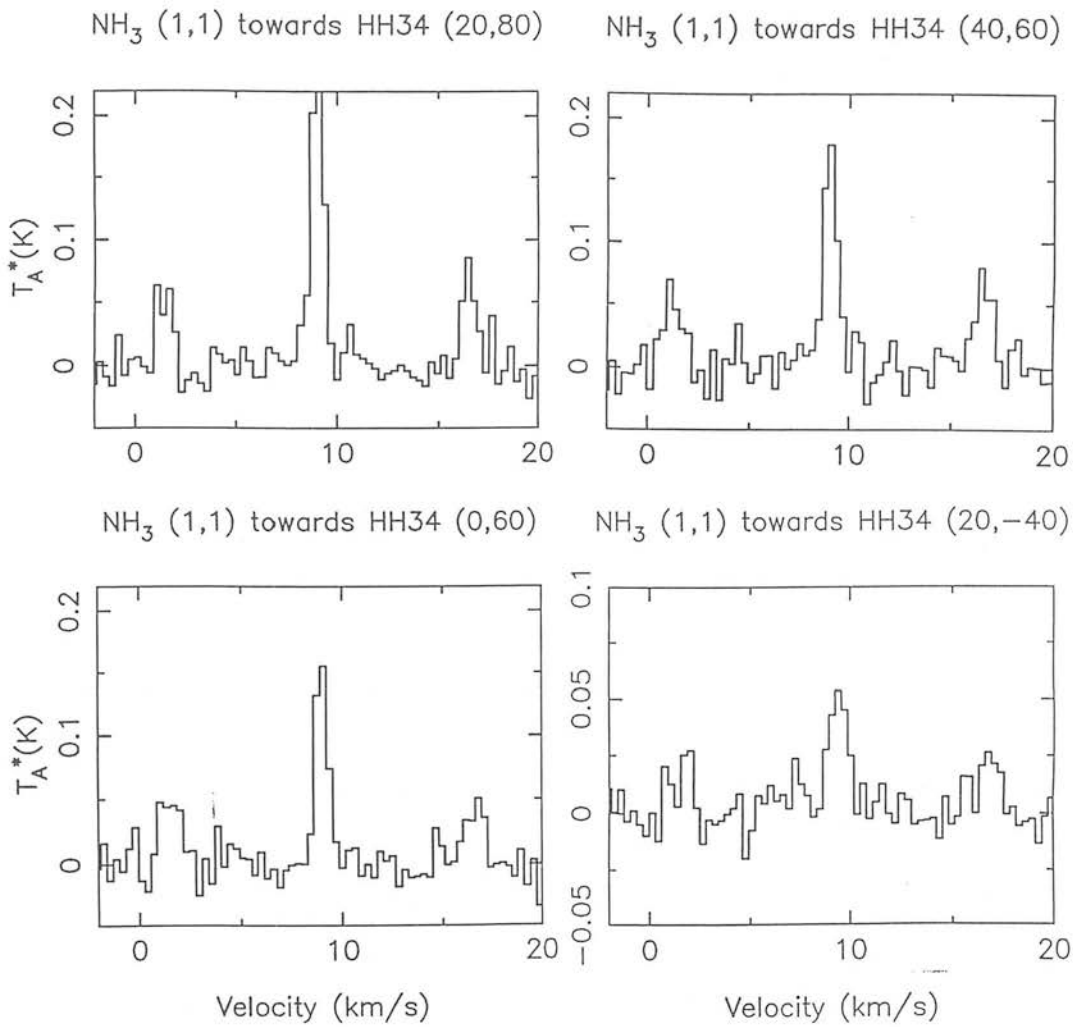

Figure 5.5: Spectra, each binned over two channels, taken from the NH_3 (1,1) map around HH34. The two inner hyperfine components are evident at $V_{LSR} \sim$ 1km s^{-1} and 17km s^{-1}. The temperature T_A^* has not been corrected for the telescope beam efficiency nor for the beam filling.

these to an equivalent (peak) brightness temperature, T_i from equation 1.13.;

$$\frac{T_i}{[\mathrm{K}]} = \frac{c^2}{2k\nu^2}\frac{1}{\Omega_m\ \Delta v}\int S_{0i}\ dv \times 10^{-29} = 0.037 \times \frac{\int S_{0i}\ dv}{[\mathrm{mJy.beam^{-1}.km.s^{-1}}]}$$

where S_{0i} is the VLA flux density, Δv the velocity range over which S_{0i} is integrated and Ω_m the synthesised VLA beam ($4.1\widehat{''} \times 3.5\widehat{''}$) in rad^2 . Assuming a gaussian beam profile for the Effelsberg antenna, and so using a gaussian weighting function, $W_i = \exp(-4\ \ln 2\ d^2/\theta^2)$, where d is the distance to each VLA cell position, we may obtain a value for the flux contribution from each VLA cell to the total flux within a $40\widehat{''}$ beam that is centred on HH34IRS. The main beam brightness temperature (in K) towards HH34IRS is then given by summing these weighted values;

$$T_b = \frac{\sum(W_i\ T_i)}{\sum W_i}$$

where the summation is over all cells to a distance of $30\widehat{''}$ from HH34IRS. We eventually arrive at a value $T_b = 0.08$K. This value is subject to the Effelsberg beam efficiency, $\eta_b = 0.4$, and so the contribution from nearby clumps to the equivalent antenna temperature that would be seen at Effelsberg is $T_A^* = 0.032$K. This compares to an observed $T_A^* = 0.16$K from the spectrum in figure 5.4: Evidently, only $\sim$20% of the emission towards HH34IRS in figure 5.4 is due to the nearby dense clumps; the column density estimate calculated above for HH34IRS is therefore an accurate measure of N_{NH3} towards the source and we may safely conclude that the NH_3 column density is a factor of $\sim$ 10 greater towards the northern peak, at ($40\widehat{''}$, $60\widehat{''}$), than towards HH34IRS.

5.3.3 NH_3 Optical Depth Map

Since the NH_3 and CS(3-2)/(2-1) peaks do not coincide (figure 5.4), there is some evidence that in HH34 the NH_3 (1,1) integrated intensity map does not fully illustrate the high-density features associated with not only the HH34 source, but also the optical jet and Herbig-Haro shocks: Is the NH_3 optically thick towards the density peaks traced in the CS(3-2)/(2-1) ratio?

I have produced in figure 5.6 a grey-scale map of the distribution in main line optical depth, $\tau_{1,1}$, calculated from the main to hyperfine line ratio using equation 1.19 (see

also Ho *et al.* 1983). Four of the spectra used are shown in figure 5.5. The complete set of optical depths used are listed in table 5.1. The optical depths measured increase from 0.0 (shaded grey) to a maximum value of 1.2 (shaded black). I have only calculated values towards positions where we made at least a 3-σ detection of each hyperfine component; consequently the white areas on the map represent regions where $\tau_{1,1}$ was not calculated. From the observed noise level, I estimate an error of between 12 and 20% in $\tau_{1,1}$ (the higher error being towards positions where the emission is weakest).

Table 5.1: Optical depths used to construct the map in figure 5.6.

Position	$\tau_{1,1}$	Position	$\tau_{1,1}$
(40,100)	0.14	(20,40)	>0.0
(20,100)	0.25	(0,40)	>0.0
(40,80)	0.90	(20,20)	0.46
(20,80)	0.47	(0,20)	0.90
(0,80)	0.40	(20,0)	0.80
(40,60)	1.18	(0,0)	>0.0
(20,60)	0.77	(-20,0)	0.27
(0,60)	0.20	(20,-40)	1.12

As one might expect, the optical depth is high towards the more northerly peak in figure 5.2b – particularly its eastern VLA rim at $(40\widehat{''}, 60\widehat{''})$, thus confirming that the "hole" toward the exciting star is not due to high optical depths. The VLA and single dish line intensity peak at $(0\widehat{''}, 20\widehat{''})$ is also coincident with optically thicker emission.

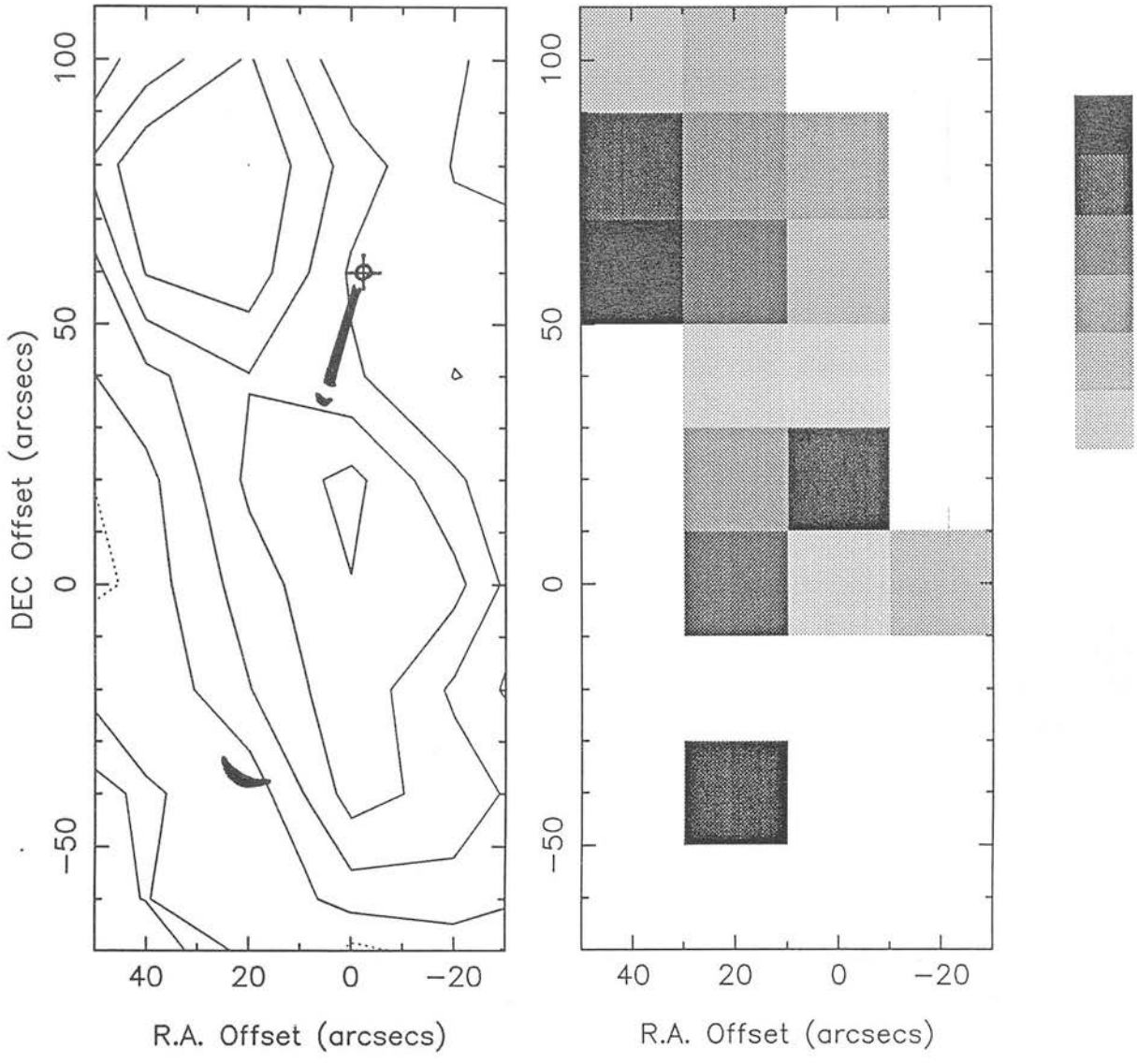

Figure 5.6: A grey scale map showing the variation in NH_3 (1,1) optical depth around HH34 compared to the contour plot in figure 5.3. The six shades of grey increase from $\tau_{1,1} = 0.0$ to 1.25 (black) in steps of 0.25. No measurements of $\tau_{1,1}$ were made towards the white background regions. Map centre as for Figure 5.2.

Conversely, the emission is optically thin towards $(0^{\widehat{m}}, 40^{\widehat{m}})$, coincident with the optical jet and a dip in the NH_3 contours, though towards HH34S $(20^{\widehat{m}}, -40^{\widehat{m}})$, where we also see a decrease in the NH_3 integrated intensity, $\tau_{1,1}$ is notably high. The 40 arcsec beam used in our NH_3 observations should be sufficiently small to resolve the CS clumps south of HH34S recorded by Cernicharo *et al.* (1991), but no corresponding NH_3 peak was detected. Thus, even though the NH_3 integrated intensity contours drop off towards HH34S, the NH_3 (1,1) emission is still optically thick; evidence for the existence of dense, though unresolved clumps. The primary beam of the VLA observations of AERTCH did not cover this region, so any proposed small clumps remained undetected. Such clumping has similarly been observed in the region of HH2 (Davis *et al.* 1992; discussed in chapter 3) and in HH7-11 (Rudolph & Welch 1988).

Finally, for comparison with the values calculated above we may similarly estimate the NH_3 column density towards HH34S and towards the Effelsberg and VLA peak at $(0^{\widehat{m}}, 20^{\widehat{m}})$; in the HH object HH34S $(20^{\widehat{m}}, -40^{\widehat{m}})$ where $\tau_{1,1} = 1.1(\pm 0.2)$ and $\delta v = 1.5(\pm 0.3)$ km s^{-1}, I calculate $N_{NH3} = 2.8(\pm 0.7) \times 10^{15}$cm^{-2}. Towards the NH_3 peak at $(0^{\widehat{m}}, 20^{\widehat{m}})$ $\tau_{1,1} = 0.9(\pm 0.2)$ and $\delta v = 1.0(\pm 0.3)$ km s^{-1}, I calculate $N_{NH3} = 1.8(\pm 0.8) \times 10^{15}$cm^{-2}. A comparison is made with column densities calculated earlier in table 5.2. Again both values are roughly a factor of 10 greater than towards the source; notably, in HH34S the NH_3 column density is highest towards the HH object.

5.4 DISCUSSION - ANOMALOUS NH_3 ABUNDANCES?

5.4.1 Is NH_3 Underabundant Towards the Exciting Stars of Outflows

The above observations show not only an offset in the NH3 peak from the exciting source in the HH34 system (by some 40 arcseconds), but also an apparent reduction, by a factor of ~ 10, in the NH_3 column density towards HH34IRS compared to other NH_3 peak positions and in particular compared to the HH bow-shock HH34S (table 5.2). Moreover, since the CS(3-2)/(2-1) line intensity ratio map of Cernicharo (1990) peaks

Table 5.2: Optical depths and column densities in HH34.

Position	coords (arcsecs)	T_A^* (K)	δv (km s^{-1})	$\tau_{1,1}$	N_{NH3} ($\times 10^{15}$cm^{-2})
Source	(0,60)	0.15	0.6	0.2	0.2
NH_3 peak (VLA peak)	(40,60)	0.18	1.0	1.2	2.4
NH_3 peak	(20,80)	0.24	1.0	0.5	1.0
NH_3 peak	(0,20)	0.20	1.0	0.9	1.8
HH34S	(20,-40)	0.06	1.5	1.1	2.8

towards the central star, it would appear that the NH_3 does not trace the underlying H_2 density towards HH34IRS. However, whilst a similar, seemingly anomalous NH_3 abundance in HH2 was believed to result from excitation effects, towards HH34IRS the NH_3 appears to be *underabundant.*

We may enquire as to whether NH_3 peaks are frequently offset from embedded outflow sources and associated molecular gas peaks. Low-resolution (1.4') NH_3 mapping by Anglada *et al.* (1989) has recently been conducted around suspected outflow sources. Of the 12 regions mapped, NH_3 peaks were detected towards only five of the suspected sources, *including HH34* (as well as Haro4-255 FIR, L43, RCrA and V1331Cyg). The observed NH_3 peaks were more frequently offset from the known IR sources in each field; in L1524 and HH38,43 for example the NH_3 peaks are approximately 3 arcminutes away from the proposed sources. The authors suggest that these clumps may indicate the true locations of the exciting sources associated with each system, though as we see here for HH34, it is equally likely that the NH_3 peaks are offset from the actual density peaks towards the known IR objects.

Earlier NH_3 studies by Torrelles *et al.* (1983) have produced similar results, with anomalies evident towards HH26 IR, Mon R2, V645 Cyg and perhaps most strikingly towards the visible bipolar nebula S106, where the double-maximum NH_3 structure peaks either side of the exciting source. The same double-peaked NH_3 structure has also been detected around SSV 59 (HH25-26) by Menten et al. (1987), whilst in the luminous outflow sources NGC2071 and G35.2N, Zhou *et al.* (1991) and Little *et al.* (1985) used high-resolution VLA observations to show the existence of "rings" of NH_3 emission around the central energy sources. Observations of mm-wavelength emission from dust in these latter objects showed no evidence of such rings; in both cases, there are unresolved cusps in the dust density distribution towards the central sources (Dent *et al.* 1989).

In LkHα234, the star is again offset from the NH_3 peak, though it is coincident with CS and dust emission peaks. The CS and dust observations suggest that the source is at a peak in the H_2 density (Gusten & Marcaide, 1986; Dent *et al.*, 1989). Similarly, in the well-studied bipolar outflow source L1551, VLA observations have detected no NH_3 emission towards the dust/CS core. Instead, two peaks are detected near HH-objects and along the CO outflow (Torrelles *et al.* 1985). We took an additional high-sensitivity NH_3 (1,1) spectrum of L1551 using the Effelsberg 40 arcsecond beam (figure 5.7) for comparison with published CS, $C^{18}O$ and HCO^+ data (Menton *et al.* 1989). These other molecules all peak near IRS5 and in velocity space all appear to have maxima at 6.5 km s^{-1}; from figure 5.7 however we see no corresponding component in NH_3 (in fact no emission is detected at all above the noise level $\sim$ 0.03K). The NH_3 therefore seems to trace a different molecular gas component to that seen in CS, HCO^+ or $C^{18}O$.

5.4.2 NH_3 Toroids

Clearly then, in outflows from young stars, NH_3 integrated line-intensity peaks do not coincide with peaks in dust and other molecular gas tracers, which themselves peak towards the outflow sources. Instead, the NH_3 is most often confined to clumps either side of the source whilst being depleted near to the star; this structure is usually interpreted not in terms of a disc, but rather as an NH_3 toroid which encircles the source (Rodriguez 1987). This scenario is further supported by the fact that the axis

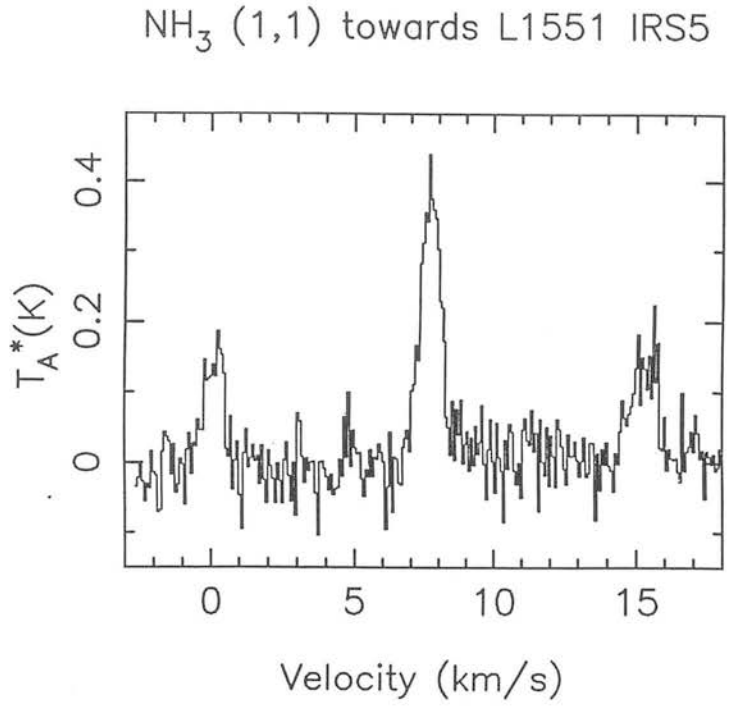

Figure 5.7: Spectrum of NH_3 (1,1) towards L1551 IRS5.

that connects the NH_3 peaks often lies perpendicular to the outflow direction. The sketch in figure 5.8 shows the proposed model.

The lack of CS, HCO^+ and HCN emission from the relatively *low*-density NH_3 toroid is thought to be due to excitation effects (see the discussion in chapter 3): The inversion lines of NH_3 observed here become thermalised above gas densities of $\sim 10^3 - 10^4$ cm^{-3} (at temperatures of a few 10s of K). At similar gas temperatures the rotational lines of CS, HCO^+ and HCN are sub-thermal. Consequently the emission will not peak towards these NH_3 toroidal features, but rather will illustrate the increasing gas density closer to the source, labeled the inner disc in figure 5.8. (Rodriguez 1987). The CS line ratio towards the source in HH34 implies a gas density $\sim 10^6$cm^{-3} (Cernicharo 1990).

However, excitation effects alone do not account for the *lack* of NH_3 in the inner disc. One would still expect to see emission from this higher density region (note that in HH34 we see a distinct reduction in the NH_3 column density towards the outflow source with regards to other NH_3 peak positions). Clearly, an additional process within

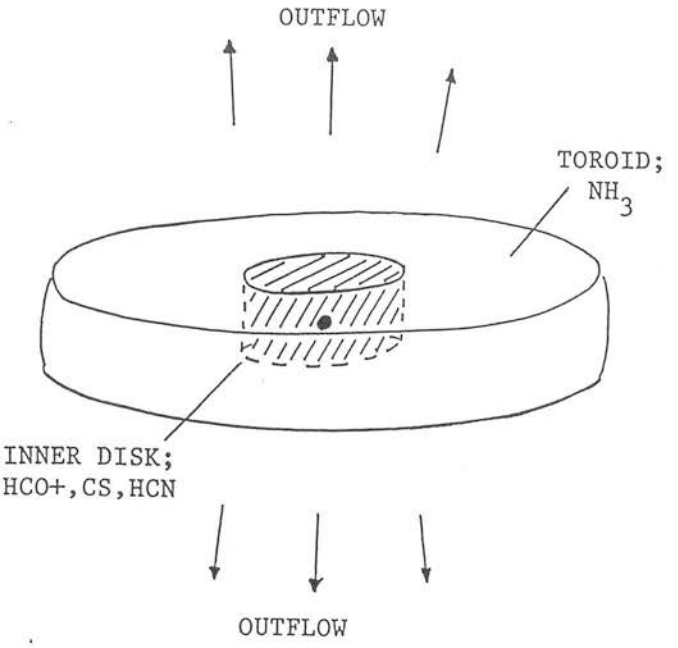

Figure 5.8: A toroid/disc model for outflow sources.

the inner disc is required to produce the apparent NH_3 depletion near to the source (and so the observed toroidal structure).

Possible mechanisms include the selective fractionation of NH_3, via shocking or photodissociation, or a restriction on the formation of NH_3. The former process seems unlikely since it requires a system that does not affect other molecules such as HCO^+, CS and HCN and yet depletes NH_3; the photodissociation cross-section for NH_3 is quite similar to the measured values for these other species (van Dishoek 1988). Also, the chemical models of Pineau des Forets *et al.* (1990), which consider the effects of low-velocity shocks (10 km s^{-1}) in dense clouds, predict no reduction in the NH_3 abundance but rather favour a slight enhancement, since NH_3 is thought to be formed through endothermic reactions involving nitrogen-bearing ions. Shocking will additionally enhance the NH_3 abundance through the desorption of dust grain mantles (Sweitzer 1978); Jones & Williams (1984) suggests that 5% of the mantle mass is NH_3. Indeed, NH_3 from grains is thought to contribute very significantly to the gas-phase abundance (Nejad *et al.* 1990).

It seems more likely therefore that the underabundance of NH_3 towards outflow sources is due to a restriction on formation. The synthesis of NH_3 in dark clouds is not well understood, though the decreased ionisation fraction in cloud cores is likely to result in a depleted NH_3 abundance (Herbst *et al.* 1987, Prasad *et al.* 1987). If this process does indeed account for the observed depletion, then the anti-correlation in CS and NH_3 maps in outflow regions is not a direct result of active star formation, but should also occur in quiescent, cold dark clouds. Notably, Sobolev & Sumina (1990) report such an anti-correlation in the dark cloud L183.

If the aforementioned NH_3 peaks do indeed represent toroids around dense, star-forming cloud cores — rather than simply a chance alignment of random clumps — then one would expect to see a relationship between the luminosity of the central source and the mass of the toroid. In table 5.3 I list parameters taken from the literature for outflows which derive from both low and high-luminosity sources, and for which high resolution NH_3 studies imply a toroidal structure. Single dish NH_3 observations are used to measure the NH_3 column density towards each source. These values are then converted to N_{H2} using an abundance ratio $N_{NH3}/N_{H2} = 10^{-7}$ (Ungerechts *et al.* 1980). We may therefore estimate the torus mass for each source ; $\propto N_{H2} \times R^2$ $(= n_{H2} \times R^3)$.

The plot in figure 5.9 shows a reasonable correlation, further evidence that the observed NH_3 peaks are linked to the star-formation process.

5.5 CONCLUSION

The observed NH_3 (1,1) integrated line-intensity peaks in the HH34 region do not coincide with peaks seen in the CS J=3-2/J=2-1 line ratio map of Cernicharo (1990). Instead, the NH_3 is confined to a peak $\sim 40''$ east of the source and a ridge which extends in a north-south direction and peaks $\sim 20''$ south of the end of the optical jet. Furthermore, towards HH34IRS the NH_3 column density is less by a factor of ~ 10 than towards other NH_3 peak positions in HH34. There is thus clear evidence that the NH_3

Table 5.3: IR-luminosities, ammonia disk radii and H_2 column densities (derived from NH_3 single-dish observations) towards IR/outflow sources.
References; 1. Mozurkewich *et al.* 1986 2. Torrelles *et al.* 1985 3. Little *et al.* 1985 4. Montalban *et al.* 1990 5. Menten *et al.* 1987 6. Zhou *et al.* 1991 7. Walker *et al.* 1986 8. Mundy *et al.* 1990 9. Lada *et al.* 1984 10. Torrelles *et al.* 1989 11. Reipurth *et al.* 1986 12. Anglada *et al.* 1991 13. Torrelles *et al.* 1991 14. Torrelles *et al.* 1983. 15. Takano *et al.* 1987 16. Marcaide *et al.* 1988 17. Dent *et al.* 1985 18. Mezger *et al.* 1987. 19. This paper.

Source	$(L/L_\odot)$	Radius (pc)	Beam (arcsec/pc)	N_{H2} (cm^{-2})	Log ($N_{H2}R^2$)	Refs.
L1551	29	0.02	$12''/0.01$	$8x10^{21}$	55.5	1,2,15
SSV59	40	0.08	$40''/0.1$	$4.8x10^{21}$	56.4	1,5,15
NGC2071	570	0.1	$10''/0.03$	$3x10^{21}$	56.4	1,6,15
Cep A	15,000	0.11	$12''/0.04$	$7x10^{21}$	56.9	1,2,15
S106	19,000	0.16	$40''/0.1$	$8x10^{21}$	57.2	1,18,18
Mon R2	28,000	0.5	$40''/0.2$	$1.8x10^{21}$	57.6	1,4,15
G35.2N	20,000	0.16	$7''/0.07$	$5x10^{22}$	58.1	17,3,3
HH1-2	50	0.03	$4''/0.01$	$6x10^{21}$	55.7	13,13,16
IRAS 16293-2422	27	0.012	$6''/0.005$	$2x10^{22}$	55.4	7,8,8
AFGL 2591	70,000	0.04	$6''/0.06$	$1.5x10^{21}$	55.3	9,10,15
HH34	0.5	0.1	$4''/0.01$	$2x10^{21}$	–	11,12,19

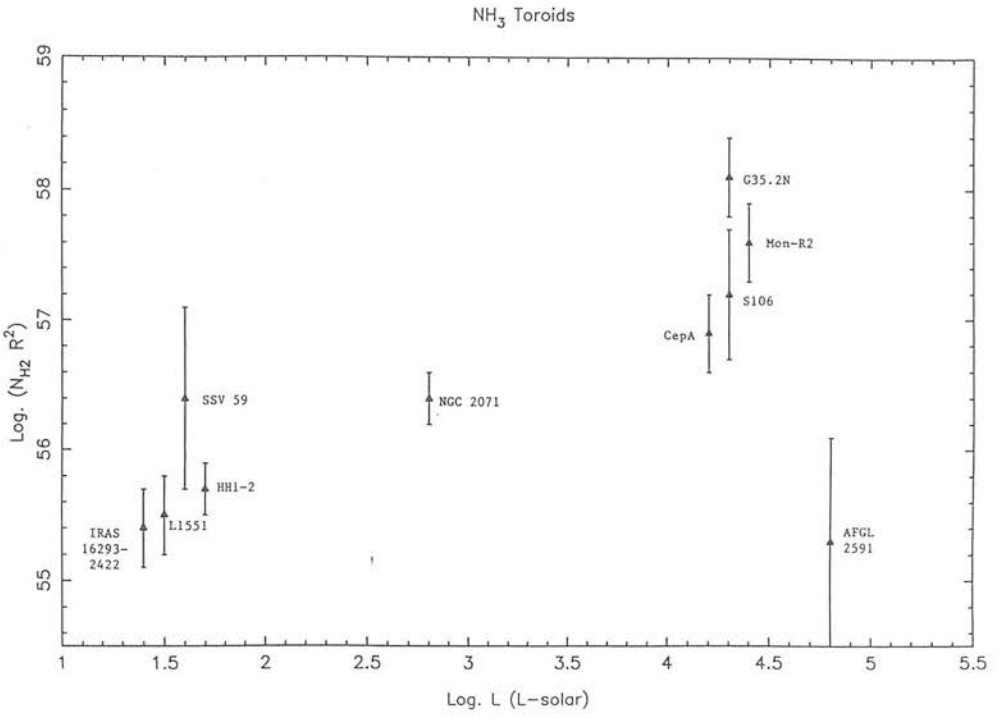

Figure 5.9: Plot of source bolometric luminosity against $N_H \times R^2$. The error bars represent the uncertainty in toroid radius due to the telescope beam size. Where a bolometric luminosity was not known, an IR luminosity was used.

is underabundant towards the central exciting star in HH34; caution should certainly be exercised when using NH_3 as a tracer of gas density towards outflow sources.

The observed offset in the NH_3 peaks from the source in HH34 (the clump observed in CS(3-2)/(2-1) and so presumably the underlying H_2 density) is not uncommon; NH_3 peaks are frequently observed either side of the source in outflow systems, whilst dust and other gas density tracers peak on the source position. This morphology is interpreted in terms of an outer, low-density toroid which encircles a higher-density inner disc; both are centred on the source and the polar axis of each is parallel to the outflow direction. The lack of CS, HCN and HCO^+ emission from the outer toroid is thought to be due to excitation effects, whilst the accompanying lack of NH_3 emission from the dense, inner disc is believed to result from a depleted NH_3 abundance (possibly the result of a suppressed rate of NH_3 synthesis in the inner disc).

z

Chapter 6

Conclusions

6.1 CONCLUSIONS

The research work presented in this thesis is largely concerned with studying the *molecular* structure of energetic outflows and stellar winds, Herbig-Haro (HH) objects and the ambient cloud in star-forming regions. Observations at millimeter and sub-millimeter wavelengths allow us to examine the structure and dynamics of the molecular cloud environment and precursor (or pre-shock) HH gas; conversely, studies at optical and infrared wavelengths probe only the hot, shocked or fluoresced gas in outflows and towards young stellar objects. Thus, the longer-wavelength observations are complementary to the erstwhile more common optical and infrared studies, providing a more complete picture of the star-formation process.

6.1.1 Molecular Outflows

Sub-millimeter observations of the outflow from GGD27 IRS in CO J=2-1, though not unusual, complement earlier CO J=1-0 observations (Yamashita *et al.* 1989) and further illustrate the need for care when analysing the data; particularly, mass and subsequent momentum and kinetic energy estimates for the outflow are found to be *strongly* dependent on the excitation temperature of the observed transition. Simply obtaining T_{ex} from the peak line brightness temperature, as is usually the case, is clearly not sufficient. Instead, sensitive multi-isotope and multi-wavelength observations are required to establish accurately the opacity, filling factor and then the excitation temperature in the high-velocity line-wings (the outflow gas). Only then may we be confident that estimates of outflow mass and energetics are accurate.

Detection of the CO 2-1 line-wings to high outflow velocities also allows us to ascertain the orientation of the flow: Here the outflow lies close to the plane of the sky since the rear side of the conical blue-shifted lobe is slightly red-shifted and vice-versa. Furthermore, the observed *molecular* outflow is not sufficiently powerful to excite the HH objects HH80/81. Instead, an associated atomic wind component to the outflow is the likely power source.

6.1.2 Herbig-Haro Objects

Attempts to observe dense, molecular features in Herbig-Haro objects have met with some success, even though the emission from the low-J transitions of density tracers such as HCO^+, CS and NH_3 is notoriously weak near HH objects. A quiescent, stationary molecular peak has been observed ahead of the rapidly moving HH shock in HH2. The narrow molecular line widths (observed in HCO^+ and NH_3) and the low peak LSR velocities imply that this well-defined clump does not represent a high-velocity bullet or a layer of swept-up gas but instead seems to be a stationary, shocked, dense clump within the ambient molecular cloud. Similar quiescent molecular emission has been observed towards other HHs (HH1, HH34). Moreover, this scenario does not fit into current popular jet-working-surface/bullet HH models, but rather favours *i)* a "shocked-cloudlet" HH model in which a stellar wind impacts small, quiescent, dense clumps of ambient cloud gas (the optical knots that comprise HH2 thus being shocks around individual dense clumps), or *ii)* a "light"-jet-working-surface scenario where the stellar wind impacts a much larger ambient cloud feature; a dense, stationary cloud *core*. Notably, the molecular clump in HH2 is of comparable size to cloud cores seen in dark cloud surveys. A more detailed analysis of this clump and a search for similar features in other HH objects is required. Further, observations of molecular bullets or swept-up layers will also be possible when more sensitive receivers and higher resolution imaging (sub-millimeter interferometry) become widely available. Are HCO^+ peaks common to many if not all HH objects, and does the HCO^+ accurately trace the underlying H_2 gas density?

6.1.3 Stellar Winds

A search for infrared counter-parts to optical stellar jets in molecular outflows has revealed a remarkable jet-like feature associated with the high-velocity CO outflow in L1448. The blue-shifted CO outflow lobe lies on the outer edge of the curved L1448 jet, imaged in the v=1-0 S(1) ro-vibrational line of H_2. This near-infrared emission seems to derive from oblique, planar shocks produced along a cavity wall which may well represent the interface between a stellar wind and a swept-up molecular shell (observed here in CO J=2-1). These observations certainly add credence to models in

which molecular outflows represent ambient material that is entrained by a collimated stellar wind. Indeed, HCO^+ and CS mapping of L1448 reveal a molecular cloud core to the north of the outflow source; a stellar wind impacting this cloud and entraining ambient gas would account for the H_2 shock-structure and the co-located high-velocity CO outflow.

We also see strong bow-shaped features, of decreasing size, and at equal intervals along the extent of the jet. These may be the result of high-velocity molecular "bullets" within the outflow, or else internal working surfaces along the flow, produced by a time-dependent outflow velocity. There is certainly evidence for such high-velocity clumps along the outflow from CO 2-1 observations and later J=2-1 v=0 SiO studies of this region (Bachiller *et al.* 1990, 1991b).

Clearly further imaging and spectroscopy of the above outflow/jet system is warranted, particularly to establish molecular line widths, proper motions and line ratios at various points along the jet length. Futhermore, with the advent of ever-more sensitive infrared array cameras, near-infrared imaging of other molecular outflows, situated deep within molecular clouds, will likely provide observations of similar "stellar jets" associated with most, if not all, CO outflows.

6.1.4 The Ambient Cloud; Chemistry

I have also investigated the *reliability* of a number of molecular gas tracers, commonly used to illustrate the underlying H_2 density and dynamical structure in clouds and outflows associated with young stellar objects. Notably, I observe a distinct lack of correlation between the spatial morphologies of HCO^+, NH_3 and $C^{18}O$ in HH1/2 and in other outflow/HH systems: Towards HH2, peaks in HCO^+ J=3-2 do not coincide with peaks in NH_3 (1,1), whilst the $C^{18}O$ J=2-1 emission appears evenly distributed throughout the HH region. The $HCO^+/C^{18}O$ anomaly is attributed to the different excitation conditions required by each observed transition, though the NH_3 distribution seems more difficult to explain: Is the NH_3 underabundant (with respect to other molecular species) in HH2? Shock models predict an increase in the NH_3 abundance, though in HH2 we see a distinct decrease in the NH_3 column density towards the optical HH nebula (the shock front) — where the HCO^+ clearly peaks. Further abundance

measurements of this and other species, in HH2 and in other HH objects, are plainly required.

Observations towards the HH34 jet and HH system again show that NH_3 integrated intensity peaks do not coincide with peaks seen in other molecules. Indeed, a search through the literature shows that this trend is observed towards many other outflows and associated exciting sources: Often two NH_3 peaks are observed either side of the source, whilst the emission from dust and other molecules peaks very precisely on the source. This curious NH_3 structure is believed to result from an underabundance of NH_3 towards outflow sources, the NH_3 being confined to a large scale outer toroid that encircles each source; observations of high-density gas tracers such as CS, HCO^+ etc. are required to probe the *inner*, high-density disc regions around young stellar objects. Hence, NH_3 is not deemed to be the best tracer of the underlying gas density towards sites of stellar formation.

In summary, sub-millimeter observations of the ambient molecular cloud/precursor gas in HH objects and along stellar "jets" complement earlier optical studies. Indeed they allow us to establish the true nature of the shock process in each case: In HH2 and HH34S the optical shock structure clearly precedes a dense ambient cloud core, and in L1448 shocking of the stellar wind is only observed where again the wind impacts a dense cloud core (no shocks are seen along the southern CO outflow lobe were the gas density decreases). From this one may conclude that the *brightest* shocks along an outflow from a young star, what are usually termed the HH objects, occur as the flow collides with a *density peak* in the surrounding cloud envelope. Moreover, it seems likely that this is the case in many, if not all bright HH objects.

6.2 FUTURE RESEARCH GOALS

Mass outflows from regions of star formation are observable via molecular tracers, typically CO rotational lines, and via the optical and infra-red emission produced in shocks within the outflow and as the flow interacts with the ambient surroundings. We know these shocks as the optical emission-line nebula, Herbig-Haro Objects (HHs), though

many HHs are now thought to be simply the brighter knots within more *continuous* high-velocity, highly collimated optical (stellar) jets.

A sizeable number of molecular outflows are now known to exist and a similar number of optical jets and HHs have also been identified. However, if we are to understand the outflow process, its origin and driving mechanism, the relationship between molecular outflows and optical jets and the interaction between energetic winds and the parent cloud we require additional *coherent* observational support: Whilst detailed studies of a relatively small number of flows exist (L1551, HH7-11, HH1-2, DR21 etc.), there are still many fundamental questions concerning *all* outflows that remain unanswered:

- **Are molecular outflows and stellar jets intrinsically linked?** Do both CO outflows and "optical" stellar jets occur *at the same time* in the early stages of a young stars evolution? High velocity jets have been observed towards a growing number of T-Tauri stars and embedded IR sources. However, whilst molecular outflows are more commonly associated with IR sources, stellar jets usually derive from T-Tauri stars (believed to be a later stage of a stars early development, when the star becomes optically visible). Indeed, towards the archetypal jets HH34 and HH1/2 no molecular counterpart has yet been traced (Matthews 1991 private communication, Davis *et al.* 1992). This is perhaps not surprising since towards the more heavily embedded sources, where molecular outflows are observed any optical emission from a jet (internal of a CO flow) will be heavily obscured. Clearly, the way forward is to search for the IR counterparts of optical jets within molecular outflows; sub-arcsecond imaging is now possible in the near-IR. Initially, the best candidate sources are those where *extremely* high velocity (EHV) CO wing emission has been discovered and mapped (where the line wings extend to > 50 km s^{-1}; e.g. Bachiller *et al.* 1990). IR jet counterparts are likely to derive from these outflows since the presence of EHV molecular gas implies the existence of a similarly energetic driving stellar wind. The more classic, less energetic CO outflows should however also be considered. Additional IR long-slit spectroscopy would provide complementary velocity information; for comparison with molecular outflow velocity data.

- **Are *all* molecular outflows actually hollow?** There is some evidence that molecular outflows represent a swept up shell of ambient molecular material, entrained by an energetic atomic/ionised wind. A number of outflows exhibit quite obvious "limb-brightening". However, many outflows do *not* appear hollow. This is probably due to a lack of angular resolution and signal-to-noise. A systematic survey of a number of known, CO outflows is needed, at highest possible spatial and velocity resolutions. A small number of points at positions across the width of each flow lobe, preferably in an optically thin CO isotope towards outflows where each lobe is clearly separated, would provide the necessary spatial/velocity information to distinguish between hollow or filled outflow models (high signal-to-noise observations may reveal the *rear edge* of the molecular shell, the edge that in flows in the plane of the sky is expanding away from us). With the advent of sensitive SIS receivers, this project is now possible.

- **Are molecular outflows driven by ionised/atomic energetic winds?** There is growing evidence that CO outflows are driven by stellar winds, not least the optical jets discussed above. However, the entrainment of ambient molecular gas should result in shocks along the interface between the stellar wind and the entrained molecular material; i.e. a shocked, cavity wall should be observable. There is some evidence for this at optical wavelengths, but again due to the high extinction towards CO outflows observations in the IR are preferable. The shock angles that result as a stellar wind entrains ambient gas will furthermore be *oblique*. The shock velocity component perpendicular to the stellar wind/molecular flow interface may thus be too low to produce strong optical recombination-line emission. Instead, ro-vibrational line emission from H_2, lines that occur in the near-IR, will result and may be imaged. Additional spectroscopy will provide velocity information and line ratios for comparison with current shock models. A survey of known molecular outflows is clearly needed, though once again Bachiller's detailed maps of EHV molecular outflows present excellent *initial* candidates for examining the entrainment process (via observations of the stellar wind/molecular outflow interface).

- **Are molecular outflows driven by accretion?** Accurate measures of optical

depths, gas temperatures and consequently outflow masses lead to accurate kinetic energy estimates for, again, known molecular flows (mapping of the entire flow would not be necessary). These may then be compared with estimates of the energy released by accretion (from accretion disk masses and ultimately *observed* mass infall rates). If outflows are driven by accretion, we would further expect the accretion time scale to be comparable to (or longer than) the dynamical time scale for outflow; would a plot of accretion period vs. outflow period for both low and high-mass star forming systems show a correlation?

- **What is the effect of the ambient cloud envelope on the outflow process?** We know little of the *detailed* structure of ambient cloud envelopes that surround star-forming systems. CO mapping suffers either from optical depth effects (simply probing the outer layers of the cloud) or excitation effects (the low-J rotational lines of CO are excited in relatively diffuse, cool environs – thus even CO isotopes do not trace the dense cores and clumps associated with star-forming regions, but simply illustrate the overall gas column density). Detailed mapping — obtainable with mm/sub-mm interferometers — in *reliable* density tracers; HCO^+, HCN, CS, dust etc. is required to search for density gradients or ambient clumps that may result in obscure HH nebulae (HHs that do not conform to the stellar jet/working surface scenario of Mundt 1988), or curved, obstructed or indeed ambipolar outflows. Additionally, it is becoming easier to observe high-velocity bullets or swept-up molecular layers in tracers other than CO, and this development should be followed up also.

Quite plainly, there is a wealth of information to be gleaned from molecular studies of outflows from young stars. In particular, line observations offer velocity information as well as detailed information on the spatial distribution of the molecular material. There is however a distinct need to consider radio and millimeter/sub-millimeter observations and infrared and optical studies together. Notably, when analysed separately they often yield quite different results.

REFERENCES

Anglada, G, Rodriquez, L.F., Torrelles, J.M., Estalella, R., Ho, P.T.P., Cantó, J., Lopez, R. & Verdes-Montenegro, V., 1989. *Astrophys. J.*, **341**, 208.

Anglada, G., Estalella, R., Rodriguez, L.F., Torrelles, J.M., Cantó, J. & Ho, P.T.P., 1991, In *Atoms, Ions & Molecules: New Results in Spectral Line Astrophysics*, ed. Haschick & Ho, (ASP: San Francisco), p. 279.

Aspin, C., McCaughrean, M.J., Casali, M. & Geballe, T.R., 1991. *Astr. Astrophys.*, **252**, 299.

Bachiller, R., Andre, P., & Cabrit, S., 1991a. *Astr. Astrophys. Letters*, **241**, L43.

Bachiller, R., Cernicharo, J., Martin-Pintado, J., Tafalla, M. & Lazareff, B., 1990. *Astr. Astrophys.* **231**, 174.

Bachiller, R. & Gomez-Gonzalez, J., 1991. *Astr. Astrophys. Review*, **3**, 257.

Bachiller, R., Martin-Pintado, J., & Fuente A., 1991b. *Astr. Astrophys. Letters* **243**, L21.

Bally, J., 1989. In proc. of ESO workshop on *Low-mass Star Formation & Pre-main Sequence Objects*, ed. Reipurth, München, p.1.

Bally, J. & Lada, C.J., 1983. *Astrophys. J.* **265**, 824.

Bally, J. & Lane, A.P, 1991. In *The Physics of Star Formation and Early Stellar Evolution*, NATO ASI series, eds. Lada & Kylafis, (Kluwer: Dordrecht), p. 329.

Barlow, M.J., 1978. *Mon. Not. R. Astr. Soc.*, **183**, 367.

Barrett, A.H., Ho, P.T.P. & Myers, P.C., 1977. *Astrophys. J. Letters.*, **211**, L39.

Benson, P.J. & Myers, P.C., 1983. *Astrophys. J.*, **270**, 589.

Blake, G.A., 1987. *Astrophys. J.*, **315**, 621.

Blake, G.A., Sutton, E.C., Masson, C.R. & Phillips, T.G., 1987. *Astrophys. J.*, **315**, 621.

Bohlin, R.C., Savage, B.D. & Drake, J.F., 1978. *Astrophys. J.*, **224**, 132.

Blondin, J.M., Königl, A. & Fryxell, B.A., 1989. *Astrophys. J. Letters*, **337**, L37.

Böhm, K.H., 1956. *Astrophys. J.*, **123**, 379.

Böhm K.H., Bührke T., Raga A.C., Brugel E.W., Witt A.N. & Mundt R., 1987. *Astrophys. J.*, **316**, 349

Böhm, K.H. & Solf, J., 1985. *Astrophys. J.*, **294**, 533.

Bowers, R. & Deeming, T., 1984. In *Astrophysics II: Interstellar Matter & Galaxies*, Vol. II, pubs: Jones & Bartlett.

Bührke, T., Mundt, R. & Ray, T.P., 1988. *Astr. Astrophys.* , **200**, 99.

Cabrit, S., 1989. In proc. ESO workshop on *Low Mass Starformation and Pre-Main Sequence Objects*, ed. Reipurth, Munchen, p. 119.

Cabrit, S., Goldsmith, P.F. & Snell, R.L., 1988. *Astrophys. J.*, **334**, 196.

Cantó, J., 1980. *Astr. Astrophys. J.*, **86**, 327.

Cantó, J. & Rodriguez, L.F., 1980. *Astrophys. J.*, **239**, 982.

Cantó, J., Tenorio-Tagle, G. & Rozyczka, M., 1988. *Astr. Astrophys.*, **192**, 287.

Chandler, C.J., 1990. *Ph.D. thesis*, Univ. of Edinburgh, Scotland.

Cernicharo, J., 1990. In *Physics of Star Formation and Early Stellar Evolution*, Nato ASI series, eds. Lada & Kylafis (Kluwer: Dordrecht), p. 287.

Cernicharo, J., Gonzalez-Alfonso, E. & Martin-Pintado, J., 1991. *in prep.*

Cox, D.P., 1972. *Astrophys. J.*, **178**, 158.

Cox, M.J., Scott, P.F., Andersson, M. & Russell, A.P.G., 1987. *Mon. Not. R. Astr. Soc.*, **226**, 703. Cohen, R. & Kuhi, 1979. *Astrophys. J. Supp.* **41**, 743.

Dame, R., Elmergreen, B., Cohen, R. & Thaddeus, P., 1986. *Astrophys. J.*,**305**, 892.

Danby, G., Flower, D.R., Valiron, P., Schilke, P. & Walmsley C.M., 1988. *Mon. Not. R. Astr. Soc.*, **235**, 229.

Davis, C.J., Dent, W.R.F. & Bell Burnell, S.J., 1990 *Mon. Not. R. Astr. Soc.*, **224**, 173.

Davis, C.J., Dent, W.R.F., & Matthews, H.E. 1992. submitted to proceedings of 6th O.A.C. workshop on *Stellar Jets & Bipolar Outflows*, held in Capri, Sept 1991.

Dent, W.R.F., Little, L.T., Sato, S., Ohishu, M. & Yamashita, T., 1985. *Mon. Not. R. Astr. Soc.*, **217**, 217.

Dent, W.R.F., Sandel, G., Duncan, W.D. & Robson, E.I., 1989. *Mon. Not. R. Astr. Soc.*, **238**, 1497.

Dickmann, R.L., 1978. *Astrophys. J. Suppl.*, **37**, 407.

Dopita, M.A., 1978. *Astrophys. J. Suppl.*, **37**, 117.

Dopita M.A., Schwartz R.D. & Evans I., 1982. *Astrophys. J. Letters*, **263**, L73.

Dyson, J.E.; 1984. In proc. Rutherford Appleton Lab. workshop on *Gas in the Inter-*

stellar Medium, eds. P.M. Gondalekhar, (RAL: Chilton), p.107.

Dyson, J.E., 1987 In *Circumstellar Matter*, IAU Symp. no. 122, eds. Appenzeller & Jordan, p.159.

Dyson, J.E. & Williams, D.A., 1980. In *The Physics of the Interstellar Medium*, Manchester University Press, p.126.

Edwards, S. & Snell, R.L., 1983. *Astrophys. J.*, **270**, 605.

Edwards, S. & Snell, R.L., 1984. *Astrophys. J.*, **281**, 237.

Elitzur, M., 1983. *Astrophys. J.*, **267**, 174.

Evans, N.J., 1980. In *Interstellar Molecules*, IAU Symp. no. 87, ed. Andrew, p.1.

Falle, S.A.E.G., Innes, D.E. & Wilson, M.J., 1987. *Mon. Not. R. Astr. Soc.*, **225**, 741.

Flower, D.R., 1990. In *Molecular Collisions in the Interstellar Medium*, Cambridge Univ. Press, p.45.

Fukui, Y, 1989. In *Low Mass Star Formation and Pre-Main Sequence Objects*, ESO workshop, ed Reipurth, München, p. 95.

Genzel, R., Downes, D., Ho, P.T.P., & Bieging, J., 1982. *Astrophys. J. Letters*, **259**, L103.

Genzel, R., Harris, A.I. & Stutzki J., 1988. In proc. 22nd Eslab sympos. on *IR Spectroscopy in Astronomy*, ed. Kaldeich, B.H.

Goldsmith, P.F., 1972. *Astrophys. J.*, **176**, 597.

Green, S. & Chapman, S., 1978. *Astrophys. J. Supp.*, **37**, 169.

Green, S. & Thaddeus, P., 1974. *Astrophys. J.*, **191**, 653.

Güsten,R. & Marcaide, J.M., 1986. *Astron. Astrophys.*, **164**, 342.

Haro, G., 1952. *Astrophys. J.*, **115**, 572.

Hartigan, P., 1989. *Astrophys. J.*, **339**, 987.

Hartigan, P., Raymond, J. & Hartmann, L., 1987. *Astrophys. J.*, **316**, 323.

Hartmann, L. & Raymond, J.C., 1984. *Astrophys. J.*, **279**, 560.

Harvey, P.M., Joy, M., Lester, D.F. & Wilking, B.A., 1986. *Astrophys. J.*, **301**, 346.

Heathcote, S, & Reipurth, B, 1989. *Astr. Astrophys.* , in prep.

Herbig, G.H., 1951. *Astrophys. J.*, **113**, 697.

Herbig, G.H., & Jones, B.F., 1981. *Astr. J.*, **86**, 1232.

Herbst, E., DeFrees, D.J., & McLean, A.D., 1987. *Astrophs. J.*, **321**, 898.

Herbst, E. & Klemperer, W., 1973. *Astrophys. J.*, **185**, 505.

von Hippel, T., Burnell, S.J., & Williams, P.M., 1988. *Astr. Astrophys. Supp.* **74**, 431.

Ho, P.T.P. & Townes, C., 1983. *Ann. Rev. Astr. Astrophys.*, **21**, 239.

Hollenbach, D.A. & McKee, C.F. 1989. *Astrophys. J.*, **342**,306.

Irvine, W.M. & Knacke, R.F., 1988 In *Origin & Evolution of Planetary & Satellite Atmospheres*, Univ. of Arizona press, Tucson, p. 3-34.

Jones, A.P. & Williams, D.A., 1984. *Mon. Not. R. Astr. Soc.*, **209**, 955.

de Jong, T., Dalgarno, A. & Boland, W., 1980. *Astr. Astrophys.* , **91**, 68.

Keene, J., Blake, G.A., Phillips, T.G., Huggins, P.J. & Beichman, C.A., 1985. *Astrophys. J.*, **299**, 967.

Khersonskii, V.K., 1989. *Astron. Nach.*, **310(5)**, 349.

Knee, L.B.G., 1992. *Onsala Space Observatory preprint.*

Königl, A., 1982. *Astrophys. J.*, **261**, 115.

Kraus, J.D., 1986. In *Radio Astronomy*, 2nd edition, (McGraw-Hill: Manchester), p.6-1.

Kutner, M.L., 1984. In *Fundamentals of Cosmic Physics*, Gordon & Breach Science, **9**, 233.

Kutner, M.L., Tucker, K.D., Chin, G. & Thaddeus, P., 1977. *Astrophys. J.*, **215**, 521.

Kutner, M.L. & Ulich, B.L., 1981. *Astrophys. J.*, **250**, 341.

Lada, C.J., 1991. In *The Physics of Star Formation and Early Stellar Evolution*, eds. Lada & Kylafis (Kluwer: Dordrecht), p.329.

Lada, C.J., 1985. *Ann. Rev. Astr. Astrophys.*, **23**, 267.

Lada, E.A., Bally, J. & Stark, A.A., 1991. *Astrophys. J.*, **368**, 432.

Lada, C.J. & Shu, F.H., 1990. *Science*, **248**, 564.

Lada, C.J., Thronson, H.A., Smith, H.A., Schwartz, P.R. & Glaccum, W. 1984. *Astrophys. J.*, **286**, 302.

Landau & Lifshitz, 1987. In *Fluid Mechanics*, 2nd Ed., Vol. 6, Pergamon Press, Oxford, chapter 9.

Lane, A.P., 1989. In *Low Mass Star Formation and Pre-Main Sequence Objects*, ESO workshop, ed. Reipurth, München, p. 331.

Larson, R.B., 1981. *Mon. Not. R. Astr. Soc.*, **194**, 809.

Little, L.T., Dent, W.R.F., Heaton, B., Davies, S.R. & White, G.J., 1985. *Mon. Not. R. Astr. Soc.*, **217**, 227.

Lizano,S., Heiles, C., Rodriguez, L.F., Koo, B., Shu, F.H., Hasegawa, T., Hayashi, S.S. & Mirabel, I.F. 1988. *Astrophys. J.* **328**, 763.

Liseau, R. & Sandell, G., 1986. *Astrophys. J.*, **304**, 459.

Loren, R.B., Wootten, A., Sandqvist, A., Friberg, P., & Hjalmarson, A., 1984. *Astrophys. J.*, **287**, 707.

Mann, A.P.C. & Williams, D.A., 1980. *Nature*, **283**, 721.

Margulis, M. & Lada, C.J., 1985. *Astrophys. J.*, **299**, 925.

Marcaide, J.M., Torrelles, J.M., Güsten, R., Menten, K.M., Ho, P.T.P., Moran, J.M. & Rodriguez, L.F., 1989. *Astr. Astrophys.*, **197**, 235.

Martin, R.N. & Barrett, A.H., 1978. *Astrophys. J. Supp.*, **36**,1.

Martin, R.N., Ho, P.T.P. & Ruf, K., 1982. *Nature*, **296**, 632.

Martin-Pintado, J. & Cernicharo, J., 1987. *Astr. Astrophys. Letters*, **176**, L27.

Menten, K.M., Walmsley, C.M., & Mauersberger, R. 1987. In *Circumstellar Matter*, IAU Symp. no. 122, ed. Appenzeller & Jordan, p179.

Menten, K.M., Harju, J., Olano, C.A. & Walmsley, C.M., 1989. *Astr. Astrophys.*, **223**, 258.

Mezger, P.G., Chini, R., Kreysa, E. & Wink. J., 1987. *Astr. Astrophys.* **182**, 127.

Mitchell, G.F. & Hasegawa, T.I. 1991. *Astrophys. J.*, **371**, L33.

Mitchell, G.F., 1987. In *Astrochemistry,* IAU Symp. no. 120, ed. Vardya & Tarafdar, p. 275.

Mitchell, G.F., Ginsberg, J.L. & Kuntz., P.J., 1978. *Astrophys. J. Supp.*, **38**, 39.

Montalban, J., Bachiller, R., Martin-Pintado, J., Taffalla, M. & Gomez-Gonzalez. 1990. *Astr. Astrophys.*, **233**, 527.

Monteiro, T., 1984. *Mon. Not. R. Astr. Soc.*, **210**, 1.

Moorhouse, A., 1990. *Ph.D. Thesis*, University of Edinburgh, Scotland.

Moran, J.M. & Rodriquez, L.F., 1988. *Astr. Astrophys.*, **197**, 235.

Moriarty-Scheiven, G.H. & Snell, R.L., 1989. *Astrophys. J.*, **338**, 952.

Mozurkewich, D., Schwartz, P.R. & Smith, H.A., 1986 *Astrophys. J.* **311**, 379.

Mundt, R., 1986. *Canadian J. Phys.* , **64**, 407.

Mundt, R., 1988. In *Formation & Evolution of Low Mass Stars*, Nato ASI series, eds. Dupree & Lago (Kluwer: Dordrecht), p.257.

Mundt, R., Brugel, E.W. & Buhrke, T. 1987 *Astrophys. J*, **275**, 303.

Mundt, R., Ray, T.P., Buhrke, T., Raga, A.C. & Solf, J., 1990 *Astr. Astrophys.*, **232**, 37.

Mundy, L.G., Wootten, H.A. & Wilking, B.A., 1990. *Astrophys. J.*, **352**, 159.

Myers, P.C., Fuller, G.A., Goodman, A.A. & Benson, P.J., 1991. *Astrophys. J.*, **376**, 561.

Myers, P.C. & Benson, P.J., 1983. *Astrophys. J.*, **266**, 309.

Nejad, L.A.M., Williams, D.A., & Charnley, S.B., 1990. *Mon. Not. R. Astr. Soc.*, **246**, 183.

Neufeld, D.A. & Dalgarno, A., 1989. *Astrophys. J.*, **340**, 869.

Norman, C. & Silk, J., 1979. *Astrophys. J.*, **228**, 197.

Norman, C. & Silk, J., 1980. *Astrophys. J.*, **238**, 158.

Osterbrock, D.E., 1958. *Pub. Astr. Soc. Pacific*, **70**, 399.

Panagia, N. 1988 In *Galactic & Extragalactic Star Formation*, NATO ASI series, eds. Pudritz & Fich (Kluwer: Dordrecht), p.25.

Pauls, T.A., Wilson, T.L., Beiging, J.H. & Martin, R.N., 1983, *Astr. Astrophys.*, **124**, 23.

Phillips, T.G. & Huggins, P.J., 1981. *Astrophys. J.*, **251**, 533.

Pineau des Forêts, G., Roueff, E. & Flower, D.R., 1990. *Mon. Not. R. Astr. Soc.*, **244**, 688.

Prasad, S.S., Tarafdar, S.P., Villere, K.R. & Huntress, W.T., 1987, In *Interstellar Processes*, eds. Hollenbach & Thronson (Reidel: Dordrecht), p.631.

Pravdo, S.H., Rodriguez, L.F., Curiel, S., Cantó, J., Torrelles, J.M., Becker, R.H., & Sellgren, K., 1985. *Astrophys. J. Letters*, **293**, L35.

Pudritz, R., 1986. *Pub. Astr. Soc. Pacific*, **98**, 709.

Raga, A., 1989. In proc. ESO workshop on *Low Mass Star Formation & Pre-Main Sequence Objects*, ed. Reipurth, München, p.281.

Raga, A.C., Barnes, P.J. & Mateo, M., 1990. *Astr. J.*, **99**, 1912.

Raga, A.C. & Bohm, K., 1985. *Astrophys. J. Supp.*, **58**, 201.

Raga, A.C., Canto J., Binette L. & Calvet N., 1990. *Astrophys. J.*, **364**, 601.

Raga, A.C. & Mateo, M., 1988. *Rev. Mexicana Astr. Astrophys.*, **16**, 13.

Raymond, J.C., 1979. *Astrophys. J. Supp.*, **39**, 1.

Reipurth, B. 1989. In proc. ESO workhop on *Low Mass Star Formation & Pre-Main*

Sequence Objects, ed. Reipurth, München, p. 247.

Reipurth, B., Bally, J., Graham, J.A., Lane, A.P. & Zealey, W.J., 1986. *Astr. Astrophys.* , **164**, 51.

Reipurth, B. & Graham, J.A., 1988. *Astr. Astrophys.*, **202**, 219.

Rodriguez, L.F., 1987. In: *Star Forming Regions*, IAU symp. no. 115, eds. Peimbert & Jugaku, p.293.

Rodriguez, L.F., Cantó, J., Torrelles, J.M., Anglada, G. & Ho, P.T.P., 1990a.In *Formation of Stars & Planets & the Evolution of the Solar System*, 24th ESLab Sympos., p. 179.

Rodriguez, L.F., Ho, P.T.P., Torrelles, J.M., Curiel, S. & Cantó, J., 1990b.*Astrophys. J.*, **352**, 645.

Rodriguez, L.F., Moran, J.M., Ho, P.T.P., & Gottlieb, E.W., 1980. *Astrophys. J.*, **235**, 845.

Rodriguez, L.F. & Reipurth, B., 1990. Submitted to *Rev. Mex. Astr. Astrophys.*.

Rohlfs, K., 1986. In: *Tools of Radio Astronomy* (Springer-Verlag: Berlin).

Rudolf, A. & Welch, W.J., 1988. *Astrophys. J. Letters*, **326**, L31.

Schinke, R., Engel, V., Buck, U., Meyer, H., & Diercksen, G.H.F., 1985. *Astrophys. J.*, **299**, 939.

Schwartz, R.D., 1978. *Astrophys. J.*, **223**, 884.

Scoville, N.Z. & Solomon, P.M., 1974. *Astrophys. J. Letters*, **187**, L67.

Seab, C.G. & Shull, J.M., 1983, *Astrophys. J.*, **275**, 652.

Shu, F.H. & Adams, F.C., 1987. In *Circumstellar Matter*, IAU Sympos. no. 122, eds. Appenzeller & Jordan, p.7.

Shull, J.M. & Draine, B.T., 1987. In *Interstellar Processes*, eds. Hollenbach & Thronson (Reidel: Dordrecht), p. 283.

Shull, J.M. & Beckwith, S., 1982. *Ann Rev. Astr. Astrophys.*, **20**, 163.

Shultz, A., Black, J.H., Lada, C.J., Ulich, B.L., Martin, R.N., Snell, R.L. & Erickson, N.J. 1989. *Astrophys. J.* **341**, 288.

Smith, M.D., 1991. submited to *Mon. Not. R. Astr. Soc.*

Snell, R.L. & Schloerb, F.P., 1985. *Astrophys. J.*, **295**, 490.

Snell, R.L., Scoville, N.Z., Sanders, D.B. & Erickson, N.R., 1984. *Astrophys. J.*, **284**, 176.

Sobolev, A.M. & Sumina, S.V., 1990. *Sov. Astr. J.*, **16**, 1.

Spitzer, L., 1978. In *Physical Processes in the Interstellar Medium,* John Wiley & Son, Chapter 6.

Sternberg, A., 1988. In Proc. 22nd Eslab Symp. on *IR Spectroscopy in Astronomy*, ed. Kaldeich, B.H., Salamanca, Spain, p. 269.

Strom,S.E., Strom,K.M., Grasdalen,G.L., Sellgren,K., Wolff,S., Morgan,J., Stocke,J. & Mundt,R., 1985. *Astr. J.*, **90**, 11.

Swade, D.A., Schloerb, F.P., Irvine, W.M. & Snell, R.L., 1985. In: *Masers, Molecules and Mass Outflows in Star Forming Regions,* ed. Haschick, A.D., Westford, Massachusetts, p. 73.

Sweitzer, J.S., 1978. *Astrophys. J.*, **225**, 116.

Takano, T., Stutzki, J., Fukui, Y. & Winnewesser, G., 1987. In *Star Forming Regions*, IAU sympos. no. 115., Ed: Peimbert & Jugaku, pub: Reidel, Dordrecht, Holland, p. 361.

Tenorio-Tagle, G. 1989. In *Structure & Dynamics of the Interstellar Medium*, IAU Colloqium no 120., eds. Tenorio-Tagle, Moles & Melnick, (Springer-Verlag: Berlin), p.264.

Thompson, R.I., 1981. In *Infrared Astronomy*, IAU Symp. no. 96., eds. Wynn-Williams & Cruikshank, p.153.

Tielens, A.G.G.M. & Hollenbach D., 1985. *Astrophys. J.*, **291**, 722.

Torrelles, J.M., 1991, In *Atoms, Ions & Molecules: New Results in Spectral Line Astrophysics*, eds. Haschick & Ho (ASP: San Francisco), p. 257.

Torrelles, J.M., Cantó, J., Rodriguez, L.F., Ho, P.T.P. & Moran, J.M., 1985. *Astrophys. J. Letters*, **294**, L111.

Torrelles, J.M., Rodriguez, L.F., Cantó, J., Carral, P., Marcaide, J., Moran, J.M. & Ho, P.T.P., 1983. *Astrophys. J.*, **274**, 214.

Torrelles, J.M., Ho, P.T.P., Rodriguez, L.F. & Cantó, J., 1985. *Astrophys. J.*, **288**, 595.

Torrelles, J.M., Ho, P.T.P., Rodriguez, L.F. & Cantó, J., 1989. *Astrophys. J.*, **343**, 222.

Townes, C.H. & Schawlow, A.L., 1975. In *Microwave Spectroscopy,* Dover Publications Inc.

Ungerechts, H., Walmsley, G.M.& Winnewisser, G., 1980. *Astr. Astophys. J.*, **88**, 259.

van Dishoeck, E.F., 1988. In: *Rate Coefficients in Astrochemistry*, eds. Millar & Williams, (Kluwer:Dordrecht), p.49.

Viala, Y.P., 1986. *Astr. Astrophys. Supp.*, **64**, 391.

Walmsley, C.M. & Ungerechts, H., 1983. *Astr. Astrophys.*, **122**, 164.

Walker, C.K., Lada, C.J., Young, E.T., Maloney, P.R., Wilking, B.A. 1986. *Astrophys. J. Letters*, **309**, L47.

Williams D.A., 1982. In *Galactic & Extragalactic IR Spectroscopy*, Eslab sympos. no. 16, eds. Kessler & Phillips, (Reidel:Dordrecht).

Williams, D.A. & Hartquist, T.W., 1990. *Quart. J. R. Astr. Soc.*, **31**, 593.

Williams, D.A. & Hartquist, T.W., 1984. *Mon. Not. R. Astr. Soc.*, **210**, 141.

Wolf, G.A., Lada, C.J. & Bally, J., 1990. *Astr. J.* **100**, 1892.

Wolfire, M.G., & Königl, A., 1988. *Bull. Amer. Astr. Soc.*, **20**, 1094.

Wootten, A., Loren, R.B., Sandqvist, A., Friberg, P., & Hjalmarson, A., 1984. *Astrophys. J.*, **279**, 633.

Yamashita, T., Sato, S., Nagata, T., Suzuki, H., Hough, J.H., McLean, I.S., Garden, R. & Gatley, I., 1987. *Astron. Astrophys.*, **177**, 258.

Yamashita, T., Suzuki, H., kaifu, N., Tamura, M., Mountain, C.M. & Moore, T.J., 1989. *Astrophys. J*, **347**, 894.

Zhou, S., Evans, N.J. & Mundy, L.G., 1991. *Astrophys. J.*, **355**, 159.

Zinnecker, H., Mundt, R., Geballe, T.R. & Zealey, W.J., 1989. *Astophys. J.*, **342**, 337.

Ziurys, L.M., Snell, L.S. & Dickman, R.L., 1989. *Astrophys. J.*, **341**, 857.

Appendix A

Gas Column Densities from Radio & Millimeter Observations

The absorption coefficient κ_ν is directly related to the gas density, n_{tot} and optical depth τ_ν and so may be used to establish a relationship between these two quantities. The following treatment is outlined in Rohlfs (1986, Chapter 13), and Chandler (1990).

For a transition in the rotational ladder of a linear molecule, $i \rightarrow j$ (j being the upper rotational level), κ_ν is related to the occupancy of the two levels (n_i and n_j) and the rates for stimulated transitions between these levels (B_{ji} and B_{ij});

$$\begin{aligned} \kappa_\nu &= \frac{h\nu_{ji}}{4\pi}\left[n_i B_{ij} - n_j B_{ji}\right]\phi \\ &= \frac{h\nu_{ji}}{4\pi} n_i B_{ij}\left[1 - \frac{n_j B_{ji}}{n_i B_{ij}}\right]\phi \end{aligned}$$

where ϕ is the line profile function (discussed below). Now, in thermodynamic equilibrium, B_{ij} and B_{ji} are related to the spontaneous transition rate, A_{ji} by

$$g_i B_{ij} = g_j B_{ji} = \frac{c^3}{8\pi h \nu_{ji}^3} g_j A_{ji}$$

Also, since the level populations n_i and n_j are related to the statistical weights g_i and

g_j by the Boltzman equation

$$\frac{n_j}{n_i} = \frac{g_j}{g_i} \exp\left(\frac{-h\nu_{ji}}{kT_{ex}}\right) \tag{A.1}$$

then our equation for κ_ν becomes

$$\kappa_\nu = \frac{c^2}{8\pi\nu_{ji}^2} A_{ji} \left(n_i \frac{g_j}{g_i}\right) \left[1 - \exp\left(\frac{-h\nu_{ji}}{kT_{ex}}\right)\right] \phi \tag{A.2}$$

At this point we must substitute for $(n_i g_j / g_i)$. From the Boltzmann equation, A.1, above, we may estimate the *fraction* of molecules excited to level i

$$\frac{n_i}{n_{tot}} = \frac{g_i}{Q} \exp\left(\frac{-h\nu_{i0}}{kT_{ex}}\right) \tag{A.3}$$

where $h\nu_{i0}$ is the energy of level i above the ground level and Q is the partition function, which for the rotational states of a linear molecule is given by (Rohlfs 1986 p.279)

$$Q = \sum_{j=0}^{\infty} (2j+1) \exp\left(\frac{-h\nu_{j0}}{kT_{ex}}\right)$$

In the *low-temperature* environment of molecular clouds, molecules will only populate the lower lying J-states (up to about $h\nu = kT$). For simplicity, we shall evaluate the sum as an integral and further assume that T_{ex} is the same for all J-levels, and that $h\nu_{j0} \ll kT_{ex}$. Substituting also for the molecular *rotational constant*, $B_e = \nu_{j0}/[j(j+1)]$ (a constant for each molecule; here j is the higher rotational state) then the above reduces to

$$Q \simeq \frac{kT_{ex}}{hB_e}$$

Substituting for Q in equation A.3, multiplying both sides by g_j/g_i and rearranging gives

$$n_i \frac{g_j}{g_i} = \frac{g_j}{g_i} g_i n_{tot} \left(\frac{hB_e}{kT_{ex}}\right) \exp\left(\frac{-hB_e i(i+1)}{kT_{ex}}\right)$$
$$= (2j+1) n_{tot} \left(\frac{hB_e}{kT_{ex}}\right) \exp\left(\frac{-hB_e i(i+1)}{kT_{ex}}\right)$$

I have here also substituted for the statistical weight, which for linear molecules is given by $g_j = 2j + 1$. Thus, equation A.2 becomes

$$\kappa_\nu = \frac{A_{ji} c^2}{8\pi \nu_{ji}^2} (2j+1) n_{tot} \left(\frac{hB_e}{kT_{ex}}\right) \exp\left(\frac{-hB_e i(i+1)}{kT_{ex}}\right) \left[1 - \exp\left(\frac{-h\nu_{ji}}{kT_{ex}}\right)\right] \phi \quad \text{(A.4)}$$

Finally, since κ_ν is related to the optical depth by

$$\tau_\nu = \int \kappa_\nu dx \simeq \kappa_\nu L$$

where L is the depth into the molecular region, and of course with the column density of the gas $N = n_{tot} L$, then equation A.4 becomes

$$\boxed{\tau_\nu = \frac{A_{ji} c^2}{8\pi \nu_{ji}^2} (2j+1) \left(\frac{hB_e}{kT_{ex}}\right) \exp\left(\frac{-hB_e i(i+1)}{kT_{ex}}\right) \left[1 - \exp\left(\frac{-h\nu_{ji}}{kT_{ex}}\right)\right] \phi N \quad \text{(A.5)}}$$

This relates the **optical depth** to the **column density** of gas, though because of the value of Q chosen, the above only applies to low-J transitions in linear molecules (e.g. CO, HCO^+, HCN, CS etc.) in the *cool* environments typical of interstellar molecular clouds.

EXAMPLE 1: $\tau \ll 1, h\nu \ll kT, T_{ex} > T_{bb}$

To finally measure the column density N, we must establish a relationship between N and the brightness temperature (derived from T_A^*). Now, at radio, mm and sub-mm wavelengths, the optical depth of an observed line is not always known. However,

it may often be assumed to be < 1. The source brightness temperature is given by equation 1.14 (chapter 1), and in the optically thin limit

$$T_b \simeq \tau_\nu (T_{ex} - T_{bb}) \simeq \tau_\nu T_{ex}$$

The observed line profile is determined by Doppler broadening. Consequently, $\phi.dv$ is the fraction of molecules whose radial velocity lies within the range $dv = (c/\nu)d\nu$ (Spitzer 1978 p.36). Over the whole line $\int \phi.dv$ normalises to unity. Thus, substituting for τ_ν in equation A.5 and integrating relates T_b to N

$$\int \frac{T_b}{T_{ex}}.dv = \frac{A_{ji}c^3}{8\pi\nu_{ji}^3}(2j+1)\left(\frac{hB_e}{kT_{ex}}\right)\exp\left(\frac{-hB_e i(i+1)}{kT_{ex}}\right)\left[1-\exp\left(\frac{-h\nu_{ji}}{kT_{ex}}\right)\right] N \int \phi.dv$$

and finally re-arranging

$$N = \left(\frac{8\pi k}{c^3 h}\right)\frac{\nu_{ji}^3}{A_{ji}}\frac{1}{(2j+1)B_e}\frac{\exp\left(\frac{hB_e i(i+1)}{kT_{ex}}\right)}{\left[1-\exp\left(\frac{-h\nu_{ji}}{kT_{ex}}\right)\right]}\int T_b.dv \qquad \text{(A.6)}$$

$$= \left(1.94\times10^{-14}\right)\frac{\nu_{ji}^3}{A_{ji}}\frac{1}{(2j+1)B_e}\frac{\exp\left(\frac{hB_e i(i+1)}{kT_{ex}}\right)}{\left[1-\exp\left(\frac{-h\nu_{ji}}{kT_{ex}}\right)\right]}\int T_b.dv \qquad \text{(A.7)}$$

EXAMPLE 2: $\tau \geq 1$, AND A KNOWN QUANTITY

Once again, from the equation that relates optical depth to the gas column density, equation A.5 becomes

$$\tau_\nu \Delta v = \frac{A_{ji}c^2}{8\pi\nu_{ji}^2}(2j+1)\left(\frac{hB_e}{kT_{ex}}\right)\exp\left(\frac{-hB_e i(i+1)}{kT_{ex}}\right)\left[1-\exp\left(\frac{-h\nu_{ji}}{kT_{ex}}\right)\right]\phi\left(\Delta\nu\frac{c}{\nu}\right)N$$

We have here multiplied both sides by the FWHM line width Δv, substituted $\Delta\nu = (\nu/c)\Delta v$ on the right-hand side and again assumed the following

$$\int \phi.d\nu \simeq \phi\Delta\nu = 1$$

Re-arranging again leads to

$$N = \left(\frac{8\pi k}{c^3 h}\right)\frac{\nu_{ji}^3}{A_{ji}}\frac{T_{ex}}{(2j+1)B_e}\frac{\exp\left(\frac{hB_e i(i+1)}{kT_{ex}}\right)}{\left[1-\exp\left(\frac{-h\nu_{ji}}{kT_{ex}}\right)\right]}\tau_\nu\Delta v \quad \text{(A.8)}$$

$$= \left(1.94\times10^{-14}\right)\frac{\nu_{ji}^3}{A_{ji}}\frac{T_{ex}}{(2j+1)B_e}\frac{\exp\left(\frac{hB_e i(i+1)}{kT_{ex}}\right)}{\left[1-\exp\left(\frac{-h\nu_{ji}}{kT_{ex}}\right)\right]}\tau_\nu\Delta v \quad \text{(A.9)}$$

Appendix B

Emission from an Ovoidal Shell.

Figure B.1 shows a cross-sectional cut through an ovoidal shell of shocked gas similar to that proposed by Canto (1980). If the shell is spherically symmetric about the axis along the outflow direction (here the outflow is directed out of the page), and the emission is uniform throughout the shell, then the ratio of shell volumes covered by the telescope beams pointing towards the edge of the shell and towards the centre, V_1 and $V_2 + V_3$, will equal the ratio of observed brightnesses.

I. If the telescope beam b (the full width at half power) is greater than the thickness of the shell, d: The angle θ is given by

$$\cos\theta = \frac{R - b/2}{R}$$

where R is the shell radius. The volume of the cylindrical shell V_1 covered by the telescope beam is then

$$V_1 = 2 \times \frac{\theta}{360^o}[\pi(R + d/2)^2 - \pi(R - d/2)^2]\ d$$

Substituting for θ gives

$$V_1 = \left(\frac{\cos^{-1}\left(\frac{R-b/2}{R}\right)}{180^o} \right) [\pi(R + d)^2 - \pi(R - d/2)^2]\ d$$

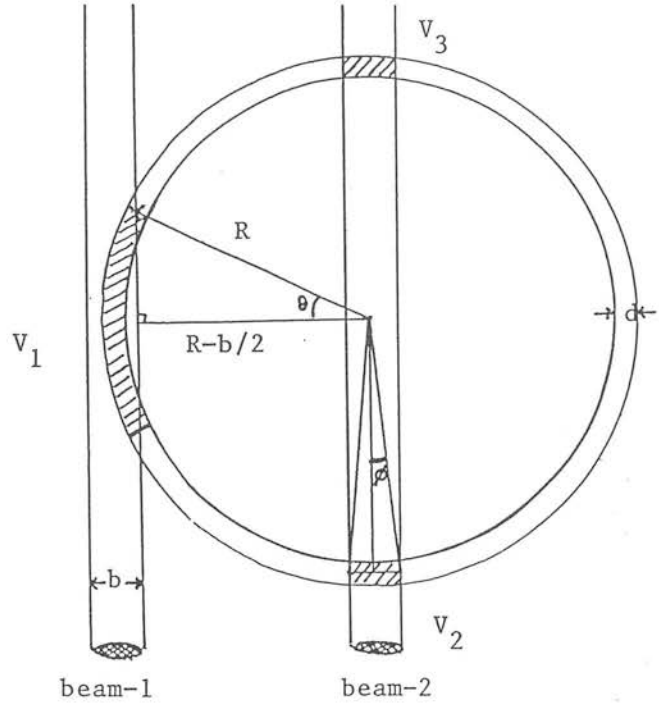

Figure B.1: Cross-section through an ovoidal shell.

Similarly, ϕ and so V_2 are obtained from

$$\sin\phi = \frac{b/2}{R}$$

$$V_2 = \left(\frac{\sin^{-1}\left(\frac{b/2}{R}\right)}{180^o}\right)[\pi(R+d)^2 - \pi(R-d/2)^2]\,d$$

The ratio of volumes covered by beams 1 and 2 is thus given by;

$$\frac{V_1}{V_2+V_3} = \frac{\cos^{-1}\left(\frac{R-b/2}{R}\right)}{2\times\sin^{-1}\left(\frac{b/2}{R}\right)} \qquad \text{(B.1)}$$

II. If b is less than the shell thickness d then from figure B.2

$$V_1 = 2l\times\pi\left(\frac{b}{2}\right)^2 = 2[R^2+(R+d/2)^2]^{1/2}\times\pi\left(\frac{b}{2}\right)^2$$

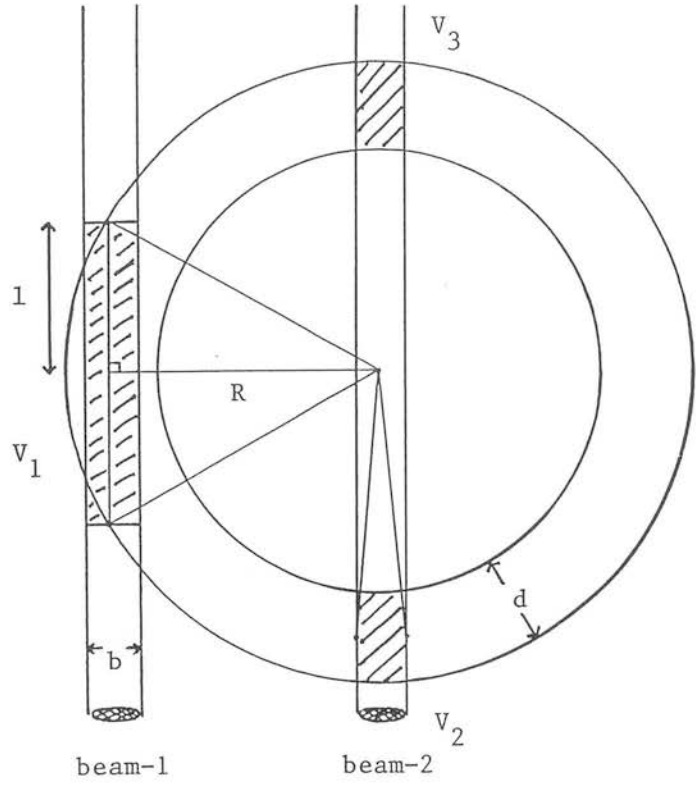

Figure B.2: As for figure B.1, but with a larger source/beam size ratio.

and

$$V_2 = d\pi \left(\frac{b}{2}\right)^2$$

Thus

$$\frac{V_1}{V_2 + V_3} = \frac{2[R^2 + (R + d/2)^2]^{1/2}}{2d} \tag{B.2}$$

If the extinction towards the rear cavity wall is high then the emission from this surface is ignored and the factor of 2 in the denominator dropped from equations B.1 and B.2.

Mon. Not. R. astr. Soc. (1990) **244**, 173–178

HCO^+ observations of the Herbig–Haro objects 1 and 2

C. J. Davis
Department of Astronomy, University of Edinburgh, Blackford Hill, Edinburgh, EH9 3HJ

W. R. F. Dent and S. J. Bell Burnell
Royal Observatory, Blackford Hill, Edinburgh, EH9 3HJ

Accepted 1989 November 14. Received 1989 November 14, in original form 1989 June 27

SUMMARY

Recent observations, made in the $J=3-2$(267.557 GHz) rotational line of HCO^+ of the HH1–2 bipolar outflow region, have detected the presence of a dense, stationary, ambient clump of HCO^+ associated with the Herbig–Haro object HH2. HCO^+ was also detected around HH1 and the probable central exciting object, VLA1. The *downwind* offset of the clump of HCO^+ in HH2 from the peak optical, bremsstrahlung and molecular hydrogen $v=1-0$ $S(1)$ emission, together with the low HCO^+ radial velocity measured (essentially $V_{LSR}-V_{amb}\sim 0$) and narrow FWHM line widths, imply that HH2 represents a 'shocked cloudlet'.

1 INTRODUCTION

Over the past ten years or so a number of models have been proposed to explain the semi-stellar emission nebulae, first observed independently by Herbig and Haro nearly 40 years ago (Herbig 1951; Haro 1952), that appear to reside near regions of star formation. The brightness of these Herbig-Haro objects in low-excitation forbidden lines such as [O I], [S II], [N I] and [Fe II], together with observations at infra-red and millimetre wavelengths of molecular hydrogen and other molecular species leave us with little doubt that they are the direct result of some process of shock excitation that occurs as a wind or outflow, driven by a young star, interacts with the ambient surroundings (Schwartz 1983).

Proper motion studies, together with the bow-shaped structure often seen in HH objects (HH1, HH34), have led many observers to believe that the HH phenomenon represents the head or 'working surface' of a wind or outflow as it ploughs into the ambient medium, or a dense 'bullet' driven by the wind that similarly shocks the surrounding material (Norman & Silk 1979; Böhm & Solf 1985; Hartigan, Raymond & Hartmann 1987; Blondin, Königl & Fryxell 1989). Recent observations, however, have detected the presence of dense, stationary clumps of HCO^+ associated with four of the five HHs that comprise the HH7–11 system (Rudolph & Welch 1988). These clumps were all found to be downwind of the optical HH objects and essentially stationary with respect to tiie ambient surroundings. The results were in direct contrast with existing 'jet' models (Blondin *et al.* 1989) and earlier 'bullet' models (Norman & Silk 1979), instead implying that the HHs in HH7–11 represented stationary cloudlets that were shocking the wind. Consequently, the impetus behind the project presented in this paper was to determine whether such stationary clumps of HCO^+ are present in other HH objects and indeed a feature common to all such objects.

We report here observations made of the bright HH objects 1 and 2, and also the central radio source, VLA1 (first identified as the probable exciting source for the HH objects by Pravdo *et al.* 1985) in the $J=3-2$ rotational line of the HCO^+ ion. Recent studies have been made of this outflow region in the (1,1) and (2,2) inversion lines of NH_3 (Torrelles *et al.* 1985; Martín-Pintado & Cernicharo 1987; Marcaide *et al.* 1988) and in molecular hydrogen at 2.12 μm $v=1-0$ $S(1)$ (Harvey *et al.* 1986). Previous attempts by Edwards & Snell (1983, 1984) to observe this region in the $J=1-0$ rotational lines of ^{12}CO and ^{13}CO have failed to detect any line emission that must obviously be associated with either HH1 or HH2. A distance of 500 pc is assumed throughout (Torrelles *et al.* 1985).

2 OBSERVATIONS

The observations were made using the 15-m James Clerk Maxwell Telescope (JCMT) on Mauna Kea, Hawaii, during 1988 October. With a beamwidth of 19 arcsec and beam efficiency of 0.79, grid maps of HH1 and HH2 were taken with a 15-arcsec spacing using the RxA heterodyne receiver and a wide band acousto-optic spectrometer (bandwidth 500 MHz with a resolution of 1.0 MHz or 1.1 km s^{-1}). The HCO^+ $J=3-2$ rotational transition lies at 267.557 GHz. Typical SSB system temperatures were 800–1000 K. An integration time of 10 min was required for each spectrum. For each spectrum, linear baselines were removed and inte-

grated line intensities then calculated using the SPECX data-handling package.

3 RESULTS

3.1 HCO^+ observations

We obtained HCO^+ spectra around the outflow regions known as HH1 and HH2. A spectrum was also taken towards the central continuum source, VLA1, now thought to be the driving force for the outflows (Pravdo *et al.* 1985). All the plots obtained for HH1 and HH2 were averaged to give the top two spectra shown in Fig. 1. These plots thus represent the large-scale HCO^+ emission in the two HH regions. Also shown is the single spectrum recorded for VLA1 (Fig. 1c). From these, the peak LSR radial velocities have been measured and recorded in Table 1. A comparison is made here with the velocities of various molecular lines, as measured by other authors. Table 3 shows the HCO^+ FWHM velocities and the line widths (ΔV_{max}) measured at 0.1 K.

It is interesting to note at this point the discrepancy in the peak velocities, especially between the ammonia data, as

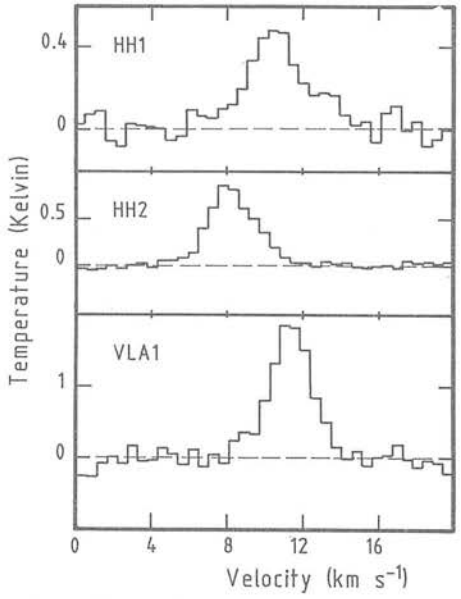

Figure 1. The $HCO^+ J = 3-2$ emission from HH1, HH2 and VLA1. The three spectra represent (a) the *average* of the seven spectra shown in the grid map of the HH1 region, (b) the *average* of the 18 spectra shown in the grid map of the HH2 region, and (c) the HCO^+ emission from the probable central exciting source for the HH1–2 system, VLA1.

Table 1. A comparison of the peak LSR radial velocities for HH1, HH2 and VLA1. HH2 optical and H_2 velocities correspond to the HH2A clump. Note that the Hβ velocities quoted are heliocentric and *not* LSR. All velocities are in km s^{-1}. References: (a) Torrelles *et al.* 1985, (b) Schwartz 1978, (c) Zinnecker *et al.* 1989.

Object	HCO^+ V_{LSR}	[a] NH_3 V_{LSR}	[c] H_α V_{LSR}	[b] H_β V_{LSR}	[c] H_2 V_{LSR}
HH1	10.5	8.5	-6	1	5
HH2	8.0	6.9/9.5	7	17	7
VLA1	11.0	8.1/9.9	–	–	–

recorded by Torrelles *et al.* (1985) and the HCO^+ velocities presented in this paper (Table 1). Within HH1 and VLA1, the HCO^+ velocities are markedly larger than those associated with the NH_3 emission. For HH2 however, the *two* NH_3 peaks (see the discussion below) measured are fairly symmetrical about the single HCO^+ line. The HCO^+ velocity in HH2 is in fact very nearly equal to the velocity of the ambient material, $V_{amb} \sim 8$ km s^{-1} (Edwards & Snell 1983). The HCO^+ found in HH2 thus appears to be essentially stationary ($V_{LSR} - V_{amb} \sim 0$).

We also note that the remarkable splitting of the central NH_3 peak, found by Torrelles on his spectrum of VLA1 and especially his HH2 plot, is not apparent on any of our HCO^+ spectra, though the red wing found on the HH1 plot, extending 4 km s^{-1} from line centre, could be due to two separate overlapping velocity components. This becomes more evident if we consider the individual spectra of the HH1 grid map (Fig. 2a). We note here that the velocity maxima corresponding to the two HCO^+ peaks on HH1 ($T_A \sim 0.44$ K and 0.16 K, respectively), $V_{LSR} = 10.5$ km s^{-1} and 13.5 km s^{-1}, are again both significantly higher than those obtained from Torrelles' NH_3 data.

Turning our attention to HH2, we see even less evidence of such line splitting, though a red wing extending 3 km s^{-1} from line centre is discernible. This contrasts with the NH_3 results where the splitting of the (1,1) inversion line obtained by Torrelles is very clear, resulting in two peaks of near equal magnitude split by 2.6 km s^{-1}. Edwards & Snell (1983) have also found a similar red wing on a CO $J = 1-0$ spectrum of HH2 recorded in 1983, though surprisingly little other CO emission seems to have been detected around either HH1 or HH2. In their paper they comment on the wing being "weak, but definite, extending 8 km s^{-1} from line centre".

It should be noted at this point that the beamsize of 19 arcsec used with the JCMT for the results presented here is much smaller than the 1.4-arcmin beam used by Torrelles to obtain the NH_3 data. The average HCO^+ spectra (Fig. 1) correspond to beamsizes of approximately 1.25 arcmin for HH2 and 0.75 arcmin for HH1, smaller than the NH_3 beamsize. Also, the grid maps cover areas "leeward" of the optical HH coordinates, beyond the lobes of highest (optical) excitation, where velocities may be lower. However, the discrepancy between the HCO^+ 1.25-arcmin beam and the NH_3 1.4-arcmin beam used by Torrelles is *not* so great as to result in such drastically different line profiles. Nor can the NH_3 splitting be a result of an optical depth effect, as the hyperfine lines also show double peaks. This phenomenon may instead be a result of two clumps of dense NH_3 gas moving at different velocities in the HH2 region. The less distinct line splitting observed in HCO^+ for HH1 and the red wing seen on the HH2 HCO^+ spectrum could then be due to two or *a number* of clumps, of varying densities, also being accelerated to different velocities. It is, however, clear that the motions of the NH_3 and HCO^+ clumps associated with HH1 and HH2 are in effect independent of each other.

3.2 Calculation of HCO^+ column densities and source masses

From the HCO^+ data presented in this paper it is possible to calculate column densities, N_{HCO^+}, and masses for HH1, HH2 and VLA1.

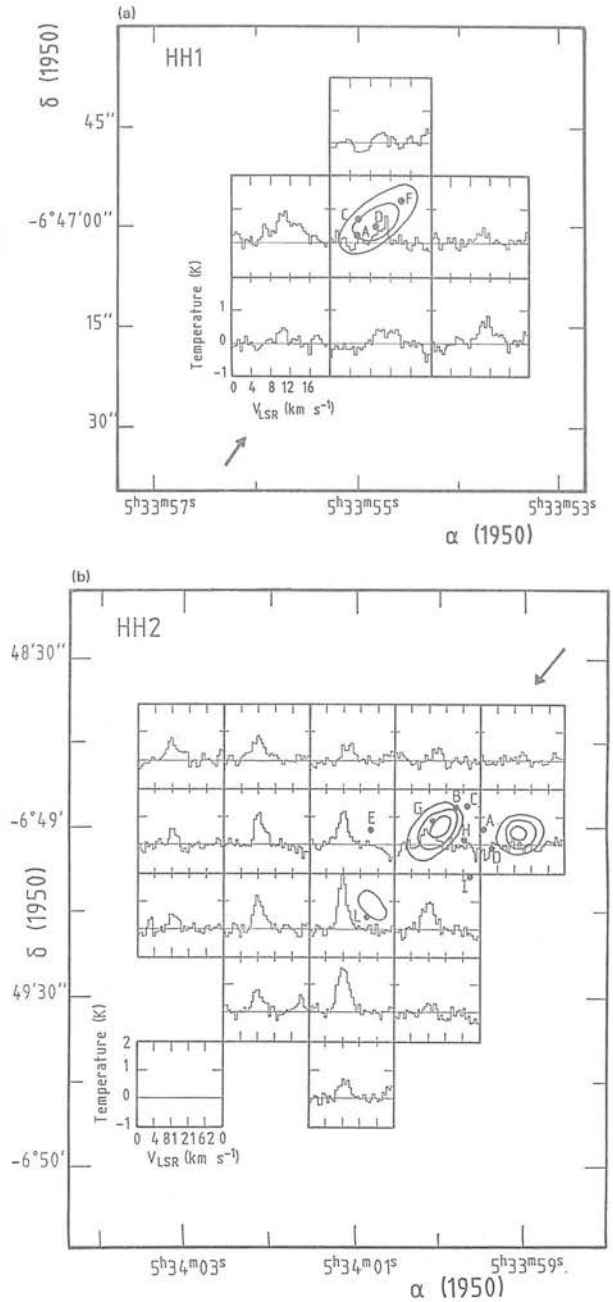

Figure 2. (a) A grid map showing the distribution of HCO^+ in HH1. The points correspond to the peaks of optical emission and the contours to molecular hydrogen at 2.12 μm. The arrow shows the direction of the assumed outflow from VLA1. (b) A grid map showing the distribution of HCO^+ in HH2. The points and contours again correspond to optical and molecular hydrogen emission, with the arrow indicating the direction of the outflow.

Using a dipole moment of 4.07 debye (Cox *et al.* 1987), which gives a squared value for the dipole matrix element of 9.93 debye^2 for the $J=3-2$ rotational transition of the HCO^+ ion (Townes & Schawlow 1975), and assuming optically thin emission, the following equation can be used to calculate the column density (Dickman 1978):

$$N_{HCO^+} = \frac{1.79\times10^{11}\int T_b dv}{(1-e^{-12.8/T_{ex}})e^{-12.8/T_{ex}}}. \quad (1)$$

From the line temperatures recorded by Edwards & Snell (1983), kinetic temperatures of 17 K for HH1 and 16 K for HH2 can be calculated (Evans 1980), whilst Martín-Pintado & Cernicharo (1987) give a rotational temperature of 23 K from their NH_3 observations (assumed to be a lower limit for the excitation temperature, Walmsley & Ungerechts 1983). Throughout the calculation an excitation temperature, T_{ex}, of 25 K is assumed. It is then a simple matter to obtain the integrated line intensities, $\int T_b dv$, corrected for a 0.79 beam efficiency, from the two average plots for HH1 and HH2 and the VLA1 plot (Fig. 1) and so calculate the column densities *averaged* over the map areas.

For HH1, $\int T_b dv = 2.33$ K km s^{-1};

so $N_{HCO^+} = 1.74\times10^{12}$ cm^{-2}.

For HH2, $\int T_b dv = 3.27$ K km s^{-1};

so $N_{HCO^+} = 2.42\times10^{12}$ cm^{-2}.

The map sizes of the HCO^+ sources observed were taken to be $(45\hat{''}\times30\hat{''})+(15\hat{''}\times15\hat{''})$, giving at 500 pc a total area of 8.8×10^{34} cm^2 for HH1, and $(75\hat{''}\times45\hat{''})+(15\hat{''}\times60\hat{''})$, giving at the same distance a total area of 23.8×10^{34} cm^2 for HH2.

The *peak* column densities are also calculated, from the individual spectra recorded at the coordinates of peak HCO^+ emission (Fig. 2). For HH1 the coordinates of the spectrum used were $\alpha(1950)=5^h\,33^m\,56^s$, $\delta(1950)=-06°\,47'00''$, and for HH2, $\alpha(1950)=5^h34^m01^s$, $\delta(1950)=-06°49'30''$.

For HH1, $\int T_b dv = 4.14$ K km s^{-1};

so $N_{HCO^+} = 10.08\times10^{12}$ cm^{-2}.

For HH2, $\int T_b dv = 6.35$ K km s^{-1};

so $N_{HCO^+} = 15.45\times10^{12}$ cm^{-2}.

For VLA1, $\int T_b dv = 6.43$ K km s^{-1};

so $N_{HCO^+} = 15.65\times10^{12}$ cm^{-2}.

Following Rudolph & Welch (1988) the *average* HCO^+ column densities can now be used to estimate overall masses for the 'large-scale' HH1 and HH2 regions. The mass of each object is calculated from $M = 1.3\times\mathcal{N}_{HCO^+}\times m_{H_2}/X_{HCO^+}$, where $\mathcal{N}_{HCO^+}$ is the number of HCO^+ ions (note the difference between this and N_{HCO^+}, which is the HCO^+ column density), X_{HCO^+} is the abundance of HCO^+ relative to H_2, and m_{H_2} is the mass of an H_2 molecule. The factor of 1.3 here takes into account the mass contribution of elements other than hydrogen found in interstellar gas. Assuming a value of 2.3×10^{-9} for X_{HCO^+} (Blake *et al.* 1987) the masses of each emission region are thus calculated to be 0.14 ($\pm$0.08) $M_\odot$ for HH1 and 0.55 ($\pm$0.14) $M_\odot$ for HH2.

For comparison, an upper limit to the mass of either HH object can be calculated from the NH_3 data obtained by Martín-Pintado & Cernicharo (1987). For HH1 and HH2, the NH_3 column density was given an upper limit of $N_{NH_3}\leqslant9\times10^{13}$ cm^{-2} (using a 40-arcsec beam). Assuming the abundance of NH_3, $X_{NH_3}\sim10^{-7}$ (Benson & Myers 1983), then following the method described above, an upper limit to the mass of either HH1 or HH2 is found to be 0.1 $M_\odot$ (note that the FWHM beam size and not the deconvolved source size was used in this calculation, and N_{NH_3} is also very much an upper limit). This result is consistent with that obtained from the HCO^+ data.

4 DISCUSSION

The individual HCO^+ spectra obtained for HH1 and HH2 are presented as grid maps in Fig. 2(a) and (b). The optically visible knots (Herbig & Jones 1981; coordinates from von Hippel, Burnell & Williams 1988) are included as points, as are contour lines of molecular hydrogen $v=1-0$ $S(1)$ emission (Harvey *et al.* 1986). In addition, 6-cm continuum peaks (Pravdo *et al.* 1985) are found to be coincident with the optical knots.

A consideration of the maps presented here may help us to pin down a Herbig–Haro model applicable to this system. Papers by Hartigan *et al.* (1987) and Böhm & Solf (1985) support Norman & Silk's 'interstellar bullet' (1979) or Dyson's later (1984) 'jet' model for HH1. In both cases, bow shocks are directed away from the exciting source (assumed to be VLA1), the shocking being a result of either (i) a dense clump or bullet of material ploughing into the ambient cloud, or (ii) the head or 'working surface' of an outflow jet burrowing into the surrounding medium producing the observed emissions – the HH objects. Both models require high radial velocities, the optical emission representing either high-velocity bullet or jet material that is shocked as it impacts the ambient surroundings. As later discussed by Blondin *et al.* (1989), the 'jet' model specifies a two-shock system, the bow shock accelerating ambient material in its path and preceding a jet shock where deceleration of the jet itself takes place. As a result, radiative cooling occurs within the high-density gas between these two shocks producing the observed HH phenomena. The 'bullet' model shows a similar bow shock feature, though here the jet shock is replaced by a *cloudlet* or *bullet* shock that travels through the bullet shocking the dense gas.

When we consider CCD images of HH1 it does seem to have a bow-shaped structure that fits the requirements of either the jet or the bullet model (Herbig & Jones 1981). Also, proper motion studies conducted by Herbig & Jones have assigned velocities ranging from 150 to over 350 km s^{-1} for the individual knots that comprise the HH1 object. It is, however, difficult to fit the HCO^+ observations presented here for HH1 to either model, though the low LSR radial velocities and narrow FWHM line widths do suggest that the HCO^+ observed in HH1 is essentially stationary and quiescent. Two peaks of HCO^+ are observed north-west and south-east, and slightly *upwind* of HH1, though the signal-to-noise is low (see the individual spectra in Fig. 2a). The grid map obtained for the HH2 region does, however, contain more positive information.

The peak HCO^+ emission in HH2, shown in Fig. 2(b), is found to be clearly downwind of the optical knots, the H_2 peaks and the 6-cm bremsstrahlung continuum emission peak. The HCO^+ results therefore tend to support a third model, Schwartz's 'shocked cloudlet' model (1978), see Fig. 3. Here an *inverted* bow shock is produced on the *windward* side of a dense, stationary clump of ambient material by the impact of a high-velocity outflow; a second cloudlet shock propagates into the clump itself, resulting in a general heating of the cloudlet gas. Such a model is essentially the inverse of Norman & Silk's interstellar bullet, though now we expect the HCO^+ to be stationary. We also expect to observe shock-ionized wind gas, stopped at the *head* of the cloudlet but also flowing around the sides of the

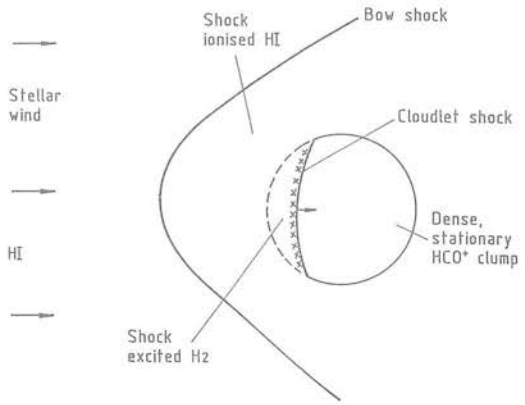

Figure 3. The shocked cloudlet model for HH objects, initially proposed by Schwartz (1978), that seems to be applicable to HH2.

Table 2. A comparison of the FWHM line widths for HH1 and HH2. All line widths are in km s^{-1}. References: (a) Torrelles *et al.* 1985, (b) Schwartz 1978, (c) Zinnecker *et al.* 1989.

Object	HCO^+	[a] NH_3	[c] $H\alpha$	[b] $H\beta$	[c] H_2
HH1	2.6	1	50	81	38
HH2	4.8	-	120	72	44

Table 3. Velocity data obtained from the HCO^+ observations for the HH objects and the central exciting object, VLA1. All velocities are in km s^{-1}, with ΔV_{max} measured at 0.1 K.

Object	HCO^+ ΔV_{max}	HCO^+ V_{FWHM}	HCO^+ V_{LSR}
HH1	5.9	2.6	10.5
HH2	4.5	4.8	8.0
VLA1	5.9	2.1	11.0

cloudlet. This would explain the large FWHM line widths and low mean velocities seen in $H\alpha$ and $H\beta$ (see Tables 1 and 2), if the outflow is nearly perpendicular to the line-of-sight.

Whilst Schwartz (1978) envisaged his cloudlets to be only a few arcseconds across (at 500 pc), the clump of HCO^+ seen in HH2 extends over nearly 1 arcmin. This larger cloudlet may, however, consist of many smaller clumps, too small to be resolved by the 20-arcsec beam used in these observations. Optical photographs of HH2 show it to be highly clumpy. Alternatively, we may be seeing *ablation* of the shocked face of a larger cloudlet, i.e. pieces being 'chipped off' and similarly individually shocked by the wind. Further more, it may be these individual condensations, shocked separately and accelerated to high velocities that explain the high (and varied) proper motions observed in HH2 by Herbig & Jones (1981). As described above, we would expect the optical bow shock around a stationary cloudlet to be at rest, and so the apparent high optical velocities seen cannot be explained by a simple, single-shocked cloudlet.

Post-shock H_2 (cloudlet gas) may also be seen on the windward edge of a stationary, shocked cloudlet. Down the sides

of the cloudlet, where lower shock velocities result because of oblique shock angles, the H_2 may not be dissociated, instead being shock excited. This shocked gas may therefore be visible in the infrared. Also, H_2 will reform – in excited states – in the cooling, post-shock gas behind the cloudlet shock. This gas may similarly be observable. If we assume a pre-shock cloudlet density of $\sim 10^5$ cm^{-3} and a cloudlet shock velocity of the order of 50 km s^{-1} (Wolfire & Königl 1989; Schwartz 1978; see also the discussion below), then radiative cooling of the post-shock cloudlet material will become possible very rapidly, and so the hot, post-shock gas will cool sufficiently to enable H_2 reformation in only a few days (Blondin *et al.* 1989; Spitzer 1978). Consequently, it will be impossible to resolve the region *between* the cool, high-density cloudlet gas – the observable H_2 – and the cloudlet shock itself (Fig. 3), and so the H_2 emission in the HH2 and HH1 clumps will thus show the position of the cloudlet shock (Fig. 2a). H_2 with a low mean velocity is certainly observed windward of the HCO^+ clump in HH2. H_2 is also seen in HH1.

Does the HCO^+ observed in HH1 and HH2 represent pre- or post-shock cloudlet material? The contrasting structures seen in these two HH regions suggest we are studying two different mechanisms. The HCO^+ seen in HH2, found downwind of the optical and H_2 peaks, may represent gas that has not yet 'seen' the shock. The HCO^+ associated with HH1 may, however, be high-density, post-shock material, although the signal-to-noise ratio is low. It is clearly difficult to arrive at a firm conclusion.

At present only the HCO^+ molecule shows a clump that is clearly associated with HH2 or HH1. NH_3 seems to be distributed over the entire outflow region (Torrelles *et al.* 1985) and no CS data are yet available. HCO^+ has, however, recently been detected in another HH system. Observations of the HH7–11 system conducted by Rudolph & Welch (1988) have detected HCO^+ clumps downwind of four of the five HHs. Further studies though, using CS as a density tracer, have failed to detect any compressed regions coincident with the HCO^+ clumps.

Such results suggest that HCO^+ is unique in some way. Possibilities are (i) it represents shocked material and has been enhanced due to formation in the shock front by collisions within the shock-impacted gas, (ii) it has not been shocked and is instead enhanced by a process of UV pumping [Wolfire & Königl (1989) have suggested that the gas ahead of an advancing shock-front in HH regions may be fluoresced rather than shocked], or (iii) the HCO^+ excitation temperature within the cloudlet has been enhanced, possibly because of the high ionic fraction in the shock (Elitzur 1983). The 6-cm continuum observations by Pravdo *et al.* (1985) of HH1 and 2 clearly show peaks coincident with both HH objects, indicating a high abundance of hot electrons. If this is the case, clumps of other ionic species, such as N_2H^+ and HCS^+ should be observed in HH1 and 2.

Whether X_{HCO^+} is in fact enhanced, reduced or unchanged in shocks is, however, still unresolved. Wootten *et al.* (1984) concluded that there was no real enhancement in the abundance of HCO^+ in the shocked region of NGC 2071, and that ionization levels were similar in both accelerated and ambient cloud regions. Loren *et al.* (1984) reported similar findings, whilst Mitchell (1987), in his study of the chemistry found in low-temperature clouds ($\sim$10–20 K) excited by low-velocity shocks (shock velocity $\sim$5–20 km s^{-1}), predicts a reduction in the abundance of HCO^+.

Finally, it may be possible to obtain a crude estimate of the *lifetime* of the cloudlet in HH2. As described by Schwartz (1978), it is possible to estimate the velocity of the cloudlet shock in HH2 from the equation

$$V_{cs} = \frac{V_w}{1+(\rho_c/\rho_w)^{1/2}}, \qquad (2)$$

where V_w, ρ_w, ρ_c and V_{cs} are the wind velocity, the wind and cloudlet densities and the cloudlet shock velocity respectively. Using values of $V_w \sim 300$ km s^{-1} (Pravdo *et al.* 1985), $\rho_c \sim 10^5$ cm^{-3}, and $\rho_w \sim 4000$ cm^{-3} (Wolfire & Königl 1989; Schwartz 1978), a $V_{cs} \sim 50(\pm 16)$ km s^{-1} is calculated. The temperature of the post-shock material behind such a shock will be of the order of 56 000 K (Dyson & Williams 1980) – hot enough to dissociated HCO^+ and so perhaps also to destroy the clump. Assuming the clump *is* dissociated behind the advancing cloudlet shock, then the lifetime of HH2 may be estimated from the time it takes the cloudlet shock to traverse the length of the HCO^+ clump. Assuming a diameter of $\sim$45 arcsec (3×10^{15} m) for the HCO^+ clump, an approximate lifetime of 2000 yr is calculated for HH2.

5 CONCLUSIONS

From the HCO^+ observations presented here, we come to the following conclusions.

(i) There is HCO^+ emission associated with the regions collectively known as HH1 and HH2. HCO^+ has also been detected from the central exciting source, VLA1.

(ii) A comparison has been made with spectra of the NH_3 (1,1) inversion transition as measured by Torrelles *et al.* (1985) for the HH1–2 outflow region. There appears to be no relation between the HCO^+ peak and the NH_3 peak LSR radial velocities for HH1 or HH2. However, the HCO^+ clump within HH2 does appear to be at rest with respect to the ambient surroundings.

(iii) Definite red wings are found on both HH1 and HH2 spectra, though the HH1 red wing may be the result of two quite separate overlapping peaks corresponding to two independent, dense clumps of HCO^+ moving at different velocities.

(iv) The HCO^+ data obtained for HH2 support the 'shocked cloudlet' model for the HH phenomenon. H_2, optical and bremsstrahlung emission originates on the *windward* edge of dense, stationary ambient clumps of HCO^+. The presence of the observed emission may be explained as due to enhancement of either the HCO^+ abundance or the excitation temperature. It is possible that shock compression of the ambient, stationary clumps to a density above that required for the excitation of HCO^+ may be occurring, though the absence of co-located NH_3 and, in the case of HH7–11, CS (Rudolph & Welch 1988) suggests that this is less likely.

ACKNOWLEDGMENTS

CJD wishes to thank Dr P. M. Williams, Dr P. W. J. L. Brand and many others at the Royal Observatory, Edinburgh for their many useful comments and suggestions. Special thanks are

due also to Mrs M. Fretwell for assistance in completing the figures. CJD also acknowledges a SERC studentship. The JCMT is operated by the Royal Observatory, Edinburgh on behalf of the United Kingdom Science and Engineering Research Council, the Netherlands Organisation for Pure Research and the National Research Council of Canada.

REFERENCES

Benson, P. J. & Myers, P. C., 1983. *Astrophys. J.*, **270,** 589.
Blake, G. A., Sutton, E. C., Masson, C. R. & Phillips, T. G., 1987. *Astrophys. J.*, **315,** 621.
Blondin, J. M., Königl, A. & Fryxell, B. A., 1989. *Astrophys. J.*, **337,** L37.
Böhm, K. H. & Solf, J., 1985. *Astrophys. J.*, **294,** 533.
Cox, M. J., Scott, P. F., Andersson, M. & Russell, A. P. G., 1987. *Mon. Not. R. astr. Soc.*, **226,** 703.
Dickman, R. L., 1978. *Astrophys. J. Suppl.*, **37,** 407.
Dyson, J. E., 1984. In: *Gas in the Interstellar Medium, Proc. Rutherford Appleton Lab. Workshop*, p. 107, ed. Gondhalekar, P. M., RAL-84-101, Chilton, Didcot.
Dyson, J. E. & Williams, D. A., 1980. In: *The Physics of the Interstellar Medium*, p. 126, Manchester University Press, Manchester.
Edwards, S. & Snell, R. L., 1983. *Astrophys. J.*, **270,** 605.
Edwards, S. & Snell, R. L., 1984. *Astrophys. J.*, **281,** 237.
Elitzur, M., 1983. *Astrophys. J.*, **267,** 174.
Evans, N. J., 1980. *Interstellar Molecules, IAU Symp. No. 87*, p. 1, ed. Andrew, B. H., Reidel, Dordrecht.
Haro, G., 1952. *Astrophys. J.*, **115,** 572.
Harrigan, P., Raymond, J. & Hartmann, L., 1987. *Astrophys. J.*, **316,** 323.
Harvey, P. M., Joy, M., Lester, D. F. & Wilking, B. A., 1986. *Astrophys. J.*, **301,** 346.
Herbig, G. H., 1951. *Astrophys. J.*, **113,** 697.
Herbig, G. H. & Jones, B. F., 1981. *Astr. J.*, **86,** 1232.
Loren, R. B., Wootten, A., Sandqvist, A., Friberg, P. & Hjalmarson, A., 1984. *Astrophys. J.*, **287,** 707.
Marcaide, J. M., Torrelles, J. M., Güsten, R., Menten, K. M., Ho, P. T. P., Moran, J. M. & Rodríguez, L. F., 1988. *Astr. Astrophys.*, **197,** 235.
Martín-Pintado, J. & Cernicharo, J., 1987. *Astr. Astrophys.*, **176,** L27.
Mitchell, G. F., 1987. *Astrochemistry, IAU Symp. No. 120*, p. 275, eds Vardya, M. S. & Tarafdar, S. P., Reidel, Dordrecht.
Norman, C. & Silk, J., 1979. *Astrophys. J.*, **228,** 197.
Pravdo, S. H., Rodríguez, L. F., Curiel, S., Cantó, J., Torrelles, J. M., Becker, R. H. & Sellgren, K., 1985. *Astrophys. J.*, **293,** L35.
Rudolph, A. & Welch, W. J., 1988. *Astrophys. J.*, **326,** L31.
Schwartz, R. D., 1978. *Astrophys. J.*, **223,** 884.
Schwartz, R. D., 1983. *Ann. Rev. Astr. Astrophys.*, **21,** 209.
Spitzer, L., 1978. In: *Physical Processes in the Interstellar Medium*, p. 143, John Wiley & Son, Chichester.
Torrelles, J. M., Cantó, J., Rodríguez, L. F., Ho, P. T. P. & Moran, J. M., 1985. *Astrophys. J.*, **294,** L117.
Townes, C. H. & Schawlow, A. L., 1975. In: *Microwave Spectroscopy*, p.34, Dover Publications Inc., New York.
von Hippel, T., Burnell, S. J. & Williams, P. M., 1988. *Astr. Astrophys. Suppl.*, **74,** 431.
Walmsley, C. M. & Ungerechts, H., 1983. *Astr. Astrophys.*, **122,** 164.
Wolfire, M. G. & Königl, A., 1988. *Bull. Am. astr. Soc.*, **20,** 1094.
Wootten, A., Loren, R. B., Sandqvist, A., Friberg, P. & Hjalmarson, A., 1984. *Astrophys. J.*, **279,** 633.
Zinnecker, H., Mundt, R., Geballe, T. R. & Zealey, W. J., 1989. *Astrophys. J.*, **342,** 337.